

Fall 12-20-2019

The Development of Hyaluronan-Based Contract Agents for the Intraoperative Detection of Pancreatic Tumors

Bowen Qi
University of Nebraska Medical Center

Follow this and additional works at: <https://digitalcommons.unmc.edu/etd>

 Part of the [Pharmaceutics and Drug Design Commons](#)

Recommended Citation

Qi, Bowen, "The Development of Hyaluronan-Based Contract Agents for the Intraoperative Detection of Pancreatic Tumors" (2019). *Theses & Dissertations*. 403.
<https://digitalcommons.unmc.edu/etd/403>

This Dissertation is brought to you for free and open access by the Graduate Studies at DigitalCommons@UNMC. It has been accepted for inclusion in Theses & Dissertations by an authorized administrator of DigitalCommons@UNMC. For more information, please contact digitalcommons@unmc.edu.

**THE DEVELOPMENT OF HYALURONAN-BASED CONTRAST
AGENTS FOR THE INTRAOPERATIVE DETECTION OF
PANCREATIC TUMORS**

by

Bowen Qi

A DISSERTATION

Presented to the Faculty of
the University of Nebraska Graduate College
in Partial Fulfillment of the Requirements
for the Degree of Doctor of Philosophy

Pharmaceutical Sciences Graduate Program

Under the Supervision of Professor Aaron M. Mohs

University of Nebraska Medical Center
Omaha, Nebraska

November, 2019

Supervisory Committee

Graca Almeida-Porada, M.D., Ph.D.

David Oupicky, Ph.D.

Michael A. Hollingsworth, Ph.D.

Joseph A. Vetro, Ph.D.

ACKNOWLEDGEMENTS

First and foremost I want to thank my advisor Dr. Aaron Mohs. It has been an honor to be his Ph.D. student. He has taught me, both consciously and un-consciously, how good experimental pharmaceuticals is done. I am extremely grateful for him trusting my academic potential as a researcher and nominating me for F99/K00 applicant in UNMC. I appreciate all his contributions of time, ideas, and funding to make my Ph.D. experience productive and stimulating. The joy and enthusiasm he has for his research was contagious and motivational for me, even during tough times in the Ph.D. pursuit. I am also thankful for the excellent example he has provided as a successful pharmaceutical scientist and professor.

The members of the Mohs group have contributed immensely to my personal and professional time at UNMC. The group has been a source of friendships as well as good advice and collaboration. I am especially grateful for the fun group of original Mohs lab members who stuck it out in grad school with me: William Payne, Nicholas Wojtynek, Deep Bhattacharya, Dr. Denis Svechkarev. I would like to acknowledge honorary group member Megan Holmes, Dr. Joshua Soucek and Dr. Tanner Hill who was here a couple years ago. I worked with Megan on tuning the biodistribution for the optimal tumor imaging efficacy, and I very much appreciated her enthusiasm, intensity, willingness to do frequent image-guided surgery, and amazing ability to do animal dissection and organ storage. I worked with Josh on determining the synergistic apoptosis observed when combining taxane drugs and a lab-developed nanoformulation of Orlistat for the treatment of taxane-resistant prostate cancer cells. I also worked with Tanner on synthesizing and

characterizing the modified HA, as well as determining biodistribution of contrast agents in breast tumor models. Other past and present group members that I have had the pleasure to work with or alongside of are grad students Maddie Olson, Paul Lovell, Aishwarya Bapat; Dr. Joe Gerald Jesu Raj and Dr. Liu Xiang; and the numerous summer and rotation students who have come through the lab.

I would express my special gratitude to William Payne, who contributed a lot in helping me polish the UNMC fellowship application, F99/K00 application package and more than thirty cover letters for postdoc application. Will shared with me some tips he picked up in his external fellowship application experience, and shared some of his expert in grant writing skills with me. For the wording in manuscripts and conference abstracts, Nick, AJ, Maddie, Paul and Lucas also provide assistance. I would also like to acknowledge the UNMC Tissue Science Core Facility where the organ tissue were embedded, sectioned, stained and scanned.

The tumor imaging studies discussed in this dissertation would not have been possible without the primary pancreatic tumor models and hepatic metastatic models introduced with the help from the group of Dr. Tony Hollingsworth from the Eppley Cancer Center in UNMC. I have appreciated their collaboration and the impressive tumor implantation skills of Ayrienne Crawford, Thomas Caffrey, Kelly O'Connell who helped with the tumor surgery.

For the tumor intraoperative efficacy study, Megan and AJ made significant contributions to the experiments. In my attempted measurements of plasma protein association, I thank the following people for helpful discussions with us: Tom Bargar, Dr. Nicholas Woods, Dr. Romanova Svetlana. For the confirming the protein association with

SDS-PAGE, I am especially grateful for conversations with Dr. Joshua Soucek and also Dr. Dragana Lagundzin, as we strived to determine the proteomic profile of associated proteins.

For this dissertation I would like to thank my reading committee members: Dr. David Oupicky, Dr. Michael (Tony) Hollingsworth, Dr. Joseph Vetro and Dr. Graca Almeida-Porada, for their time, interest, and helpful comments. I would also like to thank them for their time and insightful questions for my oral defense.

I have appreciated the local expertise of the LI-COR Biosciences for supplies of IRDye800 derivatives, as well as the Curadel group for technical support of FLARE-imaging system. I am grateful to our group's current administrative assistant Renee Kaszynski and former assistant Katina Winters who kept us organized and were always ready to help.

I gratefully acknowledge the funding sources that made my Ph.D. work possible. I was funded by the Chinese Scholarship Counsel fellowship for my first 4 years and was honored to be a UNMC Graduate Fellow for years 3 & 4. My work was also supported by the sponsored by National Institutes of Health [grant numbers R00CA153916, R01EB019449, CAP50CA127297, U01CA210240, 1S10RR17846, 1S10RR027940, and P30CA036727 (Fred and Pamela Buffett Cancer Center at UNMC)], the Nebraska Cattlemen's Ball Development Fund, and the Nebraska Research Initiative.

My time at UNMC was made enjoyable in large part due to the many friends and groups that became a part of my life. I am grateful for time spent with Yaqing Wang, as my backpacking buddies and our memorable trips into the Wisconsin, for Yuhong Yang, Yang Peng, Di Wen's hospitality as I first came into this university, and for many other

people and memories. My time at UNMC was also enriched by the American Association of Pharmaceutical Sciences, Woman Scholar in World Molecular Imaging Network and the UNMC Orchestra group.

Lastly, I would like to thank my family for all their love and encouragement. For my parents who raised me with a love of science and supported me in all my pursuits. For the presence of my mother at UNMC for two of my years here and support me through tough times. And most of all for my loving, supportive, encouraging mother Shuling Wang whose faithful support during the final stages of this Ph.D. is so appreciated. Thank you.

Bowen Qi

University of Nebraska Medical Center

September 2019

ABSTRACT

Pancreatic ductal adenocarcinoma is highly lethal and surgical resection is the only potential curative treatment for the disease. Tumor-specific intraoperative fluorescence imaging could improve staging and surgical resection, thereby improving prognosis. In the first study, hyaluronic acid derived NPs with physico-chemically entrapped indocyanine green, termed NanoICG, were utilized for intraoperative near infrared fluorescence detection of pancreatic cancer. NanoICG accumulated significantly in an orthotopic pancreatic ductal adenocarcinoma model with safety profile both *in vitro* and *in vivo*. To maximize tumor signal, while minimizing signal in healthy pancreas and RES capture of macromolecules, in the next study, we describe the rational development of a series of hyaluronic acid (HA) conjugates that vary in molecular weight and are conjugated to near-infrared fluorescent (NIRF) dyes that have differences in hydrophilicity, serum protein binding affinity, and clearance mechanism. We systematically investigated the roles of each of these properties on tumor accumulation, relative biodistribution, and the impact of intraoperative imaging of orthotopic, syngeneic pancreatic cancer. Overall, each HA-NIRF conjugate displayed intra-pancreatic tumor enhancement compared to uninvolved pancreas at 24 and 96 h. Regardless of HA molecular weight, Cy7.5 conjugation directed biodistribution to the liver, spleen, and bowels. Conjugation of IRDye-800 to 5 and 20 kDa HA resulted in low liver and spleen signal, while preserving tumor contrast enhancement up to 14-fold compared to healthy pancreas. When IRDye800 was conjugated to 100 kDa HA, the conjugate preferentially distributed to RES organs. When assessing the imaging efficacy of HA-based conjugates in hepatic metastases, those that accumulated to the liver utmost (HA_{100k}-Cy7.5, HA_{100k}-IRDye800, NanoICG) turned to aid the identification of

hepatic malignancy with hypo-contrast. These studies demonstrate that by tuning HA molecular weight and the physicochemical properties of the conjugated moiety, in this case a NIRF probe, peritoneal biodistribution can be substantially altered to achieve optimized delivery to tumors with robust contrast enhancement for intraoperative imaging to abdominal tumors. Aside from assisting the accurate delineation of primary tumor, HA-NIRF conjugates demonstrated potential for identification of occult metastases in the intraoperative setting, as a versatile tool for accurate staging.

Key words: Pancreatic ductal adenocarcinoma, hyaluronic acid, fluorescence guided surgery, biodistribution, serum protein binding, Indocyanine green, splenic metastasis

TABLE OF CONTENTS

Acknowledgements.....	I
Abstract.....	V
Table of contents.....	VII
List of figures.....	XI
List of tables.....	XIII
List of abbreviations	XIV
Chapter 1: Introduction.....	1
1.1 Current preoperative imaging tools for PDAC.....	7
1.1.1 Transabdominal and Endoscopic US.....	7
1.1.2 Improving the specificity of US with molecularly targeted contrast agents.....	8
1.1.3 CT and CT Perfusion	9
1.1.4 Improving the specificity of CT by using encapsulated contrast medium– targeting biomarkers	10
1.1.5 Endoscopic retrograde cholangiopancreatography (ERCP)	11
1.1.6 MRI, diffusion-weighted MRI and MR spectroscopy	11
1.1.7 Potential improvements of MR imaging with molecularly targeted contrast agents	13
1.1.8 ¹⁸ F Fluorodeoxyglucose positron emission tomography (¹⁸ FDG PET).....	14
1.1.9 Improving sensitivity and specificity of PET with new radiotracers.....	15
1.2 Current intraoperative imaging tools	16
1.3 The need for advanced molecular imaging in PDAC	17
1.4 Tumor-targeted molecular imaging strategies for PDAC.....	19
1.4.1 Small molecules.....	22
1.4.2 Peptides	22

1.4.3 Aptamers	23
1.4.4 Antibodies	24
1.4.5 Nanoparticles (NPs)	24
1.4.6 Multimodality imaging probes	26
1.5 Physiologic concerns for developing NP imaging probes	26
1.5.1 Vascular delivery	27
1.5.2 Renal clearance	29
1.5.3 Hepatic clearance	32
1.6 Intraoperative molecular imaging techniques: potential for improved intraoperative performance	34
1.6.1 Fluorescence molecular imaging	34
1.6.2 Molecular-targeted agents for fluorescent molecular imaging	35
 Chapter 2: Nanoformulation of ICG for the intraoperative probing of pancreatic tumor and metastases with reduced toxicity	 38
2.1 Introduction	38
2.2 Methods	41
2.2.1 Materials	41
2.2.2 Preparation and characterization of NanoICG	42
2.2.3 Cytotoxicity	42
2.2.4 Chemotaxis	43
2.2.5 Phagocytosis	44
2.2.6 Tumor model induction	44
2.2.7 Near-infrared fluorescence imaging	45
2.2.8 Histological analysis	46
2.2.9 <i>In vivo</i> toxicology	47
2.2.10 Statistical analysis	47
2.3 Results	48
2.3.1 Characterization of NanoICG	48
2.3.2 Cytotoxicity	49
2.3.3 Chemotaxis	50
2.3.4 Phagocytosis	51
2.3.5 Detection of ICG and NanoICG in tumor-bearing mice with IGS	53
2.3.6 <i>Ex vivo</i> analysis of fluorescence accumulation of pancreatic tumor	55
2.3.7 Relative biodistribution of ICG and NanoICG in PDAC	57
2.3.8 <i>In vivo</i> toxicology	60
2.4 Discussion	63
 Chapter 3: Tuning HA for the delivery of pancreatic cancer with multifactorial control	 68
3.1 Introduction	68

3.2 Methods.....	70
3.2.1 Materials	70
3.2.2 Conjugation and characterization of Cy7.5 or IRDye800 HA Conjugates.....	71
3.2.3 Determination of nonspecific serum protein binding.	71
3.2.4 Tumor model induction.....	72
3.2.5 Biodistribution of HA-Dye conjugates as measured by fluorescence.	73
3.2.6 Simulated fluorescence guided imaging of PDAC	73
3.2.7 Histological analysis	74
3.2.8 Statistical Analysis.....	75
3.3 Results.....	75
3.3.1 Synthesis and photochemical properties of HA-NIRF conjugates	75
3.3.2 <i>In vitro</i> assessment of protein association	79
3.3.3 Biodistribution of HA-NIRF.....	84
3.3.4 Background interference	87
3.3.5 IGS of HA-NIRF in PDAC-bearing mouse model.....	91
3.4 Discussion.....	106
 Chapter 4: Probing capability of HA-based contrast agents for identification of pancreatic cancer metastases	 114
4.1 Introduction.....	114
4.2 Methods.....	115
4.3 Results.....	116
4.4 Discussion	118
 Chapter 5: Discussion	 120
5.1 Research proposed for the near future	
5.1.1 Preclinical investigation of in vivo performance for HA20k-Cy7.5 and HA20k-IRDye800 with PK study	121
5.1.2 Characterization of CD44-mediated cancer cell uptake and subcellular localization of HA-based contrast agents	122
5.1.3 Gel separation and proteomic analysis of associated proteins of HA20k-dye conjugates	123
5.1.4 Expected results/Potential problems/Alternatives	124
5.2 New strategies proposed for PDAC therapy	125
5.2.1 To determine the optimized delivery strategies for hyaluronidase, collagenase	128
5.2.2 To decide the time frame of matrix modeling for ICB perfusion	129
5.2.3 To investigate the delivery efficiency for the antitumor immunotherapy	129
5.2.4 Exploration of genetic targeting of fibrosis with ICB	130
5.2.5 Expected results:	131
5.2.6 The challenges and alternatives	132

5.3 Challenges translating new molecularly targeted contrast agents into the clinic	134
5.4 Novel imaging of molecular targets is an emerging area crucial to the development of targeted drugs.....	136
5.4.1 Imaging of target expression.....	138
5.4.2 Tissue pharmacokinetics	140
5.4.3 Measuring target inhibition.....	141
5.4.4 Assessment of tumor response to therapy.....	142
Bibliography	ERROR! BOOKMARK NOT DEFINED.
Curriculum vitae	195

LIST OF FIGURES

Figure 1. Schematic illustration of the key imaging modalities used for the diagnostics and potential intraoperative modalities for pancreatic cancer.	16
Figure 2. A schematic overview of the principle of tumor-targeted imaging in pancreatic cancer, showing the most promising imaging modalities for early diagnosis and improved surgical treatment, and most promising targets for this purpose.	20
Figure 3. Physical characterization of NanoICG.	50
Figure 4. CCK-8 assay.	51
Figure 5. Chemotaxis and phagocytic assay.	53
Figure 6. Schematic of FIGS and Surgical Navigation of PDAC with NanoICG.	55
Figure 7. <i>Ex vivo</i> analysis of ICG and NanoICG accumulation in pancreatic tumor.	57
Figure 8. Histological examination of splenic metastasis of PDAC.	58
Figure 9. Quantification of biodistribution of ICG and NanoICG in PDAC mice based on NIRF images at 24 h post contrast agent administration.	59
Figure 10 Hematology and blood biochemistry assessments of the vehicle (black), low dose (0.39 mg/kg ICG equivalent, red) and high dose (2 mg/kg ICG equivalent, green) of NanoICG.	61
Figure 11. H&E stained tissue slides (liver, spleen, kidney and lung) of C57BL/6 mice after intravenous injection of vehicle (<i>top row</i>), low dose NanoICG (0.39 mg/kg ICG equivalent, <i>middle row</i>) and high dose NanoICG (2 mg/kg ICG equivalent, <i>bottom row</i>).	62
Figure 12. Characterization of HA-dyes with different HA MW _N	77
Figure 13. Absorption and fluorescence emission pattern of different MW of HA conjugated dyes in ultrapure H ₂ O and 50/50 DMSO/H ₂ O.	78
Figure 14. TEM images of HA _{20k} -Cy7.5 (A) and HA _{20k} -IRDye800 (B) with negative staining, scale bar represents 500 nm.	79
Figure 15. BSA interacts with HA-dyes to different extents due to dye hydrophobicity.	81
Figure 16. Validation of the presence of BSA in fixed fragmentation of chromatographic elution.	82
Figure 17. TEM images of BSA (A), BSA mixed with HA _{20k} -Cy7.5 (B), BSA mixed with HA _{20k} -IRDye800 (C) with negative staining.	83
Figure 18. <i>In vitro</i> exploration of cellular uptake as a result of protein association.	84
Figure 19. Varied biodistribution between HA-Cy7.5 and HA-IRDye800 in WT C57BL/6 mice 24 h post <i>i.v.</i> injection.	86
Figure 20. The biodistribution of HA-dye in PDAC-bearing mice and quantification of background interference.	89
Figure 21. Images from surgical navigation of PDAC with contrast enhancement due to HA-dye and dye 24 h post <i>i.v.</i> injection.	92
Figure 22. Quantification and quantification of signal from NIR channel that corresponds to Figure 19.	94
Figure 23. Images from surgical navigation of pancreatic tumor contrast-enhanced with HA-dye 96 h post <i>i.v.</i> injection.	95
Figure 24. <i>Ex vivo</i> analysis of HA-dye accumulation within the pancreases from WT C57BL/6 (A, C) and tumor-bearing mice (B, D, E).	98

Figure 25. <i>Ex vivo</i> analysis of HA-dye accumulation within the pancreases from WT C57BL/6 and tumor-bearing mice 96 h post injection.....	99
Figure 26. Representative whole-body images of PDAC bearing mouse injected with HA _{20k} -NIRF conjugates.	100
Figure 27. Probing capability of HA _{20k} -IRDye800 on the intraperitoneal metastases of PDAC-bearing mice.....	102
Figure 28. Comprehensive biochemical and hematological assessments for WT C57BL/6 mice injected with HA _{20k} -NIRF (equivalent to 20 nmol of free dye/mouse) or vehicle control for the acute toxicology study..	104
Figure 29. Representative images for the histological assessments of vital organs harvested from WT C57BL/6 mice injected with HA _{20k} -NIRF.....	105
Figure 30. Schematic summarization of the HA MW and dye hydrophilicity affect the PDAC contrast in tumor-bearing mice..	111
Figure 31. <i>In vitro</i> exploration of cellular uptake supporting the PDAC specificity.	112
Figure 32. CD44 expression in PDAC cells <i>ex vivo</i> and <i>in vitro</i>	113
Figure 33. <i>Ex vivo</i> analysis of hepatic metastases.	117
Figure 34. Mesoscopic correlation between the scanned H&E and NIRF of liver harboring metastases that were treated with different contrast agents/time points.	118
Figure 35. Mesoscopic correlation between the scanned NIRF (a) and H&E (b) of superficial splenic metastases that were treated with HA _{5k} -Cy7.5 (A) and HA _{100k} -Cy7.5 (B).	119
Figure 36. Mesoscopic correlation between the scanned NIRF (a) and H&E (b) of superficial splenic metastases that were treated with HA _{5k} -Cy7.5, HA _{20k} -Cy7.5 and HA _{100k} -Cy7.5.	119

LIST OF TABLES

Table 1. Calculated characteristic parameters of HA-dye conjugates	80
Table 2. NP tracking analysis of BSA and BSA with/without HA-dye conjugates	84
Table 3. Ratio of HA-Cy7.5-treated pancreas or PDAC fluorescence divided by signal of surrounding organs 24 h post injection.....	91
Table 4. Ratio of HA-IRDye800-treated pancreas or PDAC fluorescence divided by signal of surrounding organs 24 h post injection.....	91

LIST OF ABBREVIATIONS

ADC, apparent diffusion coefficient; ALB, albumin; ALP, alkaline phosphatase; ALT, alanine aminotransferase; AMY, amylase; ATF, amino-terminal fragment; AU, arbitrary unit; BUN, blood urea nitrogen; BSA, bovine serum albumin; CAM, Calcein AM; CCK-8, cell counting kit-8; CEA, carcinoembryonic antigen; CM, complete medium; CNR, contrast-to-noise ratio; CT, computed tomography; Cy7.5, Cyanine 7.5; DMSO, dimethyl sulphoxide; DW, diffusion-weighted; EDC, 1-Ethyl-3-(3-dimethylaminopropyl)-carbodiimide; EES, extravascular extracellular space; EGF, epidermal growth factor; EPR, enhanced permeability and retention; FC, flow cytometry; FDG, fluorodeoxyglucose; FIGS, fluorescence image-guided surgery; GBM, glomerular basement membrane; GI tract gastrointestinal tract; GLOB, globulin; GLUT-1, glucose transporter 1; HA, hyaluronic acid; HA-PBA, HA-aminopropyl-1-pyrenebutanamide; HCT, hematocrit; HGB, hemoglobin; HMW, high molecular weight; HP, healthy pancreas; HPNE, human pancreatic nestin-expressing epithelial; HD, hydrodynamic diameter; H&E, hematoxylin and eosin; ICG, indocyanine green; IFSC, intraoperative frozen-section analysis; KPC, LSL-Kras^{G12D/+};LSL-Trp53^{R172H/+};Pdx-1Cre; LMW, low molecular weight; MMP, matrix metalloproteinases; MRI, magnetic resonance imaging; MW_N, molecular weight; NanoICG, HA-derived NPs with physico-chemically entrapped ICG; NHS, N-hydroxysuccinimide; NIR, near infrared; NIRF, near infrared fluorescence; PanNET, pancreatic neuroendocrine tumor; PDAC, pancreatic ductal adenocarcinoma; PEG, polyethylene glycols; PET, positron emission tomography; PK, pharmacokinetic; PLT, platelet; PPE, primary pancreatic epithelial; RBC, red blood cells; RES, reticuloendothelial; ROI, region of interest; SD, standard deviation; SEC, size exclusion chromatography; SM,

starving medium; SNR, signal to noise ratio; Thy1, thymocyte antigen 1; TP, total protein; TPC, theoretical plasma concentration; UP, uninvolved pancreas; uPA, urokinase plasminogen activator; US, ultrasonography; VEGF, vascular endothelial growth factor; WBC, white blood cells; WT, wide type.

CHAPTER 1: INTRODUCTION

Pancreatic cancer is an intractable malignancy and the third leading cause of cancer deaths in the USA [1]. It is likely to become the second most frequent cause of cancer-associated mortality within the next decade [2]. The disease has a relatively low occurrence yet falls within the most common causes of cancer-related deaths [3]. It often presents at an advanced stage, which contributes to the poor five-year survival rates of 2%-9%, ranking firmly last amongst all cancer sites in terms of prognostic outcomes for patients. Better understanding of the risk factors and symptoms associated with this disease is essential to inform both health professionals and the general population of potential preventive and/or early detection measures [4].

A slight difference in pancreatic cancer incidence among genders as well as a significant different geographic distribution was observed: It is more common in men (5.5 per 100,000, 243,033 cases) than in women (4.0 per 100,000, 215,885 cases) [5]. The age-standardized rate incidence was highest in Europe (7.7 per 100,000 people), followed by North America (7.6 per 100,000 people). The lowest rate was observed in Africa with an estimated incidence of 2.2 per 100,000 people [6]. Despite advancement in the knowledge of potential risk factors that cause pancreatic cancer and newly available tools for early diagnosis, its incidence is estimated to increase and will include 355,317 new cases before 2040 [6].

Most of the global variation in the incidence of pancreatic cancer has been attributed to exposure to known or suspected risk factors related to lifestyle or the

environment [7], [8]. Tobacco smoking is likely to explain the gender differences [9], some findings indicated that obesity and dietary style may have some effects as well [8], [10]. Additionally, aging and hereditary might play a role. On the other hand, diagnostic tools and diagnostic modalities vary between developed and undeveloped geographic areas, which affects the management and prognosis of patients [6].

Pancreatic cancer is mainly divided into two types: pancreatic adenocarcinoma (PDAC), which is the most common (85% of cases) arising in exocrine glands of the pancreas, and pancreatic neuroendocrine tumor (PanNET) , which is less common (less than 5%) and occurs in the endocrine tissue of the pancreas [11]. Based on the clinical stage of the tumor, pancreatic cancer is classified into four types: I (no spread or resectable), the cancer is limited to the pancreas and has grown 2 cm (IA) or greater than 2 cm but less than 4 cm (IB); II (local spread or borderline resectable), the cancer is > 4 cm and is limited to the pancreas, or there is spread locally to the nearby lymph nodes; III (wider spread or unresectable), cancer may have expanded to the nearby blood vessels or nerves, but has not metastasized to distant sites; IV (metastatic), cancer has spread to distant organs [12]. Because PDAC and the other less common exocrine cancers are typically diagnosed at a late stage (III or IV), it has a very poor prognosis compared to PanNET.

PDAC has a very poor prognosis. It usually lacks symptoms at its early stages. After diagnosis, only 24% of people survive 1 year, the 5-year survival rate is 9% for pancreatic cancer with combined stages [13]. Over the period 2014-2018, the United States National Cancer Institute data for pancreatic cancer in both sexes and all races showed that 10% of people diagnosed at the local stage had a 5-year survival rate of 32%. If the cancer

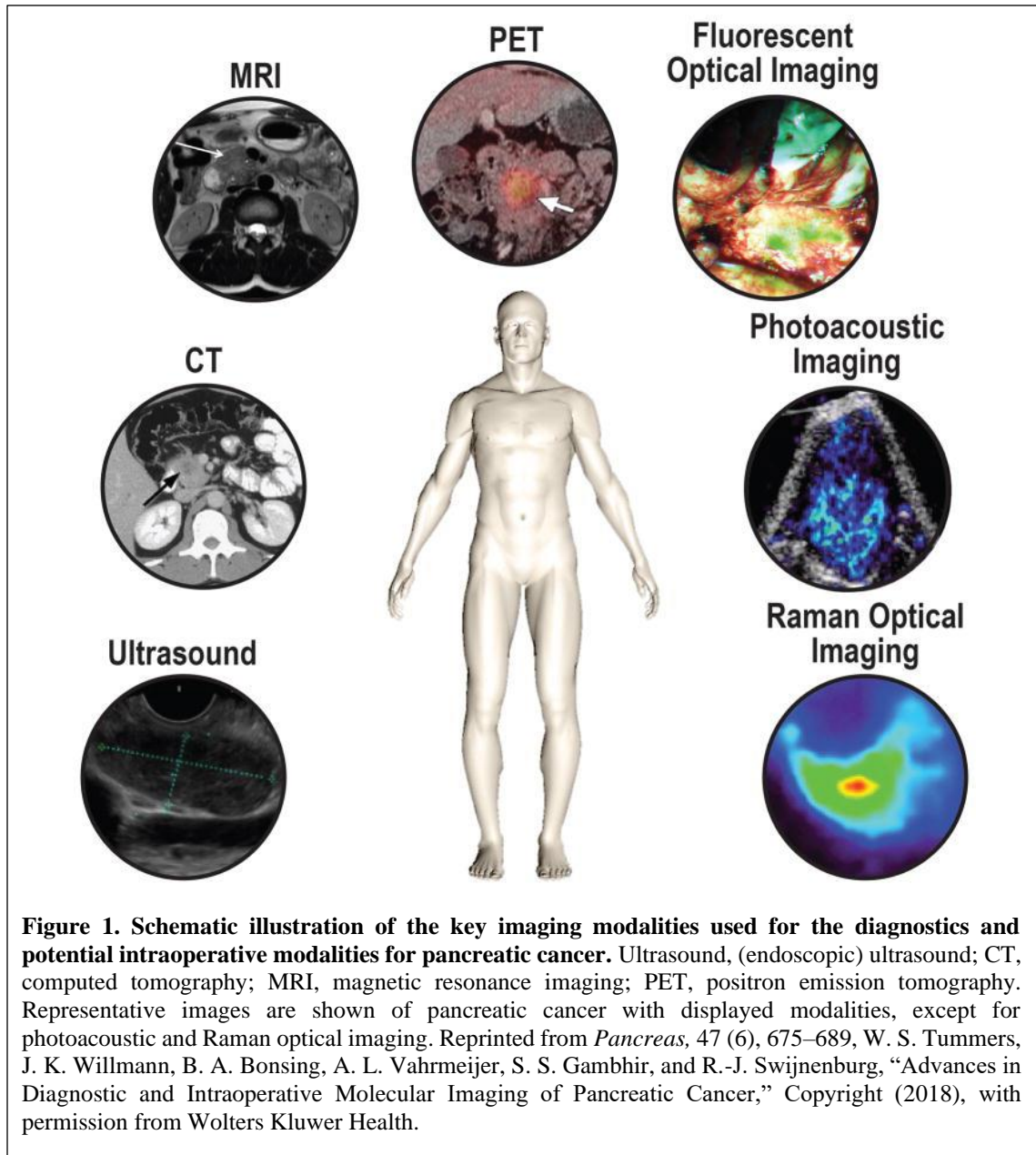
is at stage III, the 5-year survival rate is 12%. More than half (52%) of people were diagnosed at stage IV and had a 5-year survival rate of 3% [6].

In contrast to the steady increase in survival observed for most cancer types, advances have been slow for lung and pancreatic cancers [13], [14]. Even at high volume specialty centers, where the survival rate is higher than that of the general population, disease recurrence is still a major problem [15]. Treatment and clinical management of pancreatic cancer are often determined by the clinical stage of the patients' disease and are usually focused on the question of disease resectability. Patients who have resectable tumor are eligible for surgery and thus have a significantly improved prospect for long-term survival [15]. Because advanced and distant metastatic disease are excluded for surgical treatment, only a minority of patients are presented to be eligible for surgical resection [16].

More than two-thirds of PDAC occur in the head of the pancreas. Hence, abdominal pain, jaundice, pruritus, dark urine, and alcoholic stools may be presented as symptoms. Nevertheless, in the early stages of the disease these symptoms may be subtle and easy to be ignored [17]. In the symptomatic patients, abdominal ultrasonography (US) is a reasonable first imaging test. If US is not diagnostic or pancreatic cancer is highly suggested by clinical examination, then pancreas protocol computed tomography (CT) is the standard for diagnosis and staging [18], [19]. Abdominal CT provides an assessment of local and regional disease extent, which determines resectability, and also evaluates the possibility of distant metastatic spread. If CT is not possible because of lack of availability or allergy to contrast media, magnetic resonance imaging (MRI) with contrast media can be used for the diagnosis and staging of pancreatic cancer. MRI as well as magnetic

resonance cholangiopancreatography, can be performed as an adjunct to CT in detecting extrapancreatic disease (**Figure 1**). If a pancreatic mass is identified, subsequent endoscopic US and fine-needle aspiration are indicated [12]. Aside from the detection of tumor masses, serum tumor marker cancer antigen 19-9 (CA 19-9) can be used to confirm the diagnosis and to predict prognosis and recurrence. However, CA 19-9 is not tumor-specific. It has a limited sensitivity of 50% to 75% and specificity of 80% to 85%, and cannot distinguish between cancer and chronic pancreatitis and possibly other disease states with chronic inflammation [12], [20]. Thus CA19-9 is not sufficient as individual screening tool for asymptomatic patients. Despite advances in imaging technologies as well as *in vitro* diagnostic testing methods, the median size of PDAC at the time of diagnosis is ~3.1 cm, which have not changed in the past three decades [21].

After diagnosis of PDAC, patients are selected for surgical resection, which is the only potential curative treatment for PDAC. However, only 15% to 25% of patients are eligible for surgery at their initial diagnosis [22], [23]. Preoperative imaging evaluation determines candidacy for resection. Absolute contraindications to resection include the presence of metastases in the liver, peritoneum, any extra-abdominal site or vascular invasion [4]. Specifically, hepatic metastases seen on multiple detector CT (MDCT) or Positron emission tomogram (PET) /CT is a defining characteristic of unresectability based on the consensus-based guidelines from the National Comprehensive Cancer Network (NCCN) [24]. More precise detection methods can lead to improved patient stratification for the most optimal primary treatment modality-either surgery or systemic (neoadjuvant) therapy. This stratification can prevent patients from undergoing resections without any oncologic benefit.



Currently available imaging techniques are highly accurate at predicting unresectable disease, but they fall short in predicting resectability of disease, mainly because of limited sensitivity for small-volume metastatic disease. Radiographically occult metastases (<1 cm in diameter) on the surface of the liver or peritoneum, which are rarely visible by CT, MRI, or transabdominal US, may be visualized laparoscopically. Diagnostic staging laparoscopy (DSL) has shown to complement the preoperative assessment of

radiographic imaging, which has limitations for identifying regional extension of the primary tumor and/or metastatic disease, such as peritoneal involvement [24]. The case reported by Pandit et al. [24] clearly suggests that MDCT and PET-CT which are part of treatment algorithm for pancreatic cancer still miss distant small metastasis. Intraoperative US is superior to other imaging studies in characterizing hepatic metastases, but does not improve detection of liver metastases in resectable pancreatic cancer [25].

Tumor margin-positive (R1) resections occur in up to 70% of PDAC cases, leading to a high number of loco-regional recurrence [26], [27]. This means that for all patients diagnosed with PDAC, only 15% of these patients will receive a radical, tumor-margin negative (R0) resection and have a chance for prolonged survival. Therefore, improved tools for diagnosis, accurate staging, and more effective, tumor-margin negative pancreatic surgeries are crucial for improving surgical intervention outcomes. However, this process is challenging at multiple stages during the surgical procedure: detection of occult distant metastases, assessment of the extent of the primary tumor, peritumoral lymph nodes (LN), and the resection margins. Surgeons address two critical decisions during the procedure that will determine the long-term survival of pancreatic cancer: the absence of metastatic and regional disease and cancer-free margins [28], [29]. However, margin-positive (R1) resections are a frequent phenomenon (which occurs up to 70% of cases) [30], as is the emergence of distant metastases soon after surgery [31]. Failure to identify small tumor extensions during surgery is not surprising, due to the growth pattern of the tumor and the inability of the surgeon to differentiate between tumor and (peritumoral) inflammation.

In summary, resection of pancreatic malignancies is hindered by high rates of local and distant recurrence from positive margins and unrecognized metastases. Early distant

recurrences following margin-negative resection highlight the likelihood of unrecognized metastases at the time of surgery [32]. Accurate staging drives proper treatment of patients with pancreatic cancer, particularly when selecting patients for surgical resection.

1.1 Current preoperative imaging tools for PDAC

1.1.1 Transabdominal and Endoscopic US

Transabdominal US is often the initial investigation performed in patients presenting with upper abdominal pain or jaundice. However, the sensitivity of transabdominal US for detecting PDAC varies widely depending on the size of the tumor, ranging from 95% in tumors larger than 3 cm to 50% in tumors smaller than 1 cm [33]. Furthermore, it is difficult to differentiate adenocarcinoma from focal inflammatory masses secondary to chronic pancreatitis [34]. The introduction of contrast medium increases the diagnostic accuracy of transabdominal US, which can provide dynamic information regarding the macro- and microcirculation of focal lesions and of normal parenchyma. However, the US evaluation of the pancreas can be limited by its deep location within the upper abdomen, as well as intervening bowel gas and subcutaneous fat.

Endoscopic US overcomes these limitations by utilizing a transducer placed within the stomach and duodenum that's in close proximity to the pancreas. With its high spatial resolution, endoscopic US is able to identify focal lesions as small as 2-3 mm, potentially enabling the early detection. Moreover, endoscopic US provides an excellent tool for sampling suspicious lesions by fine needle aspiration or a biopsy needle. Nevertheless, in addition to the high number of false-positive findings, endoscopic US is invasive, operator dependent and is associated with poor inter-observer consensus for differentiating pancreatitis from malignant pancreatic lesions, even in highly specialized centers [35], [36].

Therefore, improving the specificity of US techniques would greatly increase the usefulness of this imaging modality for the early detection and characterization of pancreatic lesions.

1.1.2 Improving the specificity of US with molecularly targeted contrast agents

The use of molecularly targeted contrast microbubbles has the potential to improve the sensitivity and specificity of contrast-enhanced US. Targeted microbubbles are created by attaching ligands for disease-specific biomarkers to the microbubble shell surface [37]. These ligands promote the selective targeting and retention of the acoustically active microbubbles at the sites of disease, thereby providing contrast with adjacent non-diseased tissue. The microbubbles remain within the vascular space after intravascular administration, which reduces the possibility to target to molecules that are overexpressed on the surface of endothelial cells of the tumor vasculature. Despite this apparent limitation, multiple biomarkers crucial for angiogenesis are overexpressed in the vasculature of many malignant tumors, including pancreatic cancer [38]. The best examples are the receptors of vascular endothelial growth factor (VEGF). Several studies have shown successful US imaging of VEGF receptor 2 in animal models of breast, colon, prostate and pancreatic cancer [39]–[41]. Pysz *et al.*[40] developed a VEGF receptor 2-targeted US imaging platform for the reliable detection of small foci of pancreatic cancer (< 3 mm), with a 31-fold increased imaging signal intensity compared with that of normal pancreatic parenchyma in a genetically engineered pancreatic cancer mouse model. Foygel *et al.* [42] discovered and validated thymocyte antigen 1 (Thy1) as a new PDAC-associated molecular imaging target overexpressed on the neovasculature of pancreatic cancer. Subsequent *in*

vivo imaging studies in a genetically engineered mouse model showed 4-5.5-fold increase in the signal of pancreatic cancer foci as compared that in normal parenchyma [42]. Human toxicity and feasibility studies on VEGF receptor-targeted microbubbles are currently ongoing and will determine the sensitivity and efficacy of this novel imaging approach [43]. Integration of molecular imaging with endoscopic US may further show enhanced visibility of early-stage PDAC in future clinical trials and may increase inter-observer agreement of endoscopic US examinations.

1.1.3 CT and CT Perfusion

MDCT with intravenous contrast medium is the preferred diagnostic test for suspected pancreatic lesions. CT features of PDAC are variable. The majority of PDAC are hypo-attenuating relative to the surrounding pancreatic parenchyma, a small percentage (~ 5%) are iso-attenuating [44]. Several secondary signs of PDAC have been described to improve the diagnostic accuracy of CT, including pancreatic ductal dilatation, interruption of the pancreatic duct, and distal parenchymal atrophy. Ahn *et al.* [45] reported the sensitivity and specificity of focal pancreatic tumor, pancreatic duct dilation, interruption of the pancreatic duct, and distal parenchymal atrophy to be 75% and 84%, 50% and 78%, 45% and 82%, and 45% and 96%, respectively. While MDCT can be popular for diagnosis and staging of pancreatic malignancies, the diagnostic accuracy is limited for small (< 1 cm) lesions. There are also growing concerns regarding the increased risk of developing cancer after repeated exposure to imaging radiation. Furthermore, contrast agents currently used for CT are limited in their applicability in patients with reduced renal function.

In CT perfusion, functional information regarding the blood perfusion within the tumor is obtained in addition to the anatomic or morphologic information from the conventional CT [46]. During CT perfusion, the transit of an intravenous CT contrast medium is monitored as it passes through a region of interest. Physiologic parameters of the tissue can then be evaluated, including capillary permeability, fractional intravascular blood volume, blood flow and tissue interstitial volumes. Several studies have evaluated the use of CT perfusion imaging for the assessment of PDAC [47], [48]. CT perfusion imaging enables detection of altered perfusion parameters and will likely translate to improved treatment monitoring. However, it is a conspiracy that whether CT perfusion imaging is sensitive enough for the early detection of pancreatic cancer. CT perfusion imaging is also associated with even higher doses of radiation than conventional CT, making it unsuitable for widespread use as a screening modality. Other techniques, such as dual-energy CT, are being developed to increase the conspicuity of lesions at CT. However, additional clinical experience is needed for better characterization of the lesions [49].

1.1.4 Improving the specificity of CT by using biomarker-targeted contrast medium

A promising alternative for the nonspecific contrast media is the contrast agents that have been encapsulated in liposomes, which are highly biocompatible and associated with less toxicity. Studies have demonstrated the feasibility of using iodinated liposomes with micro-CT, including the ability to detect submillimeter microvessels [50], [51]. Similar to the design of tumor specific microbubbles, attempts have been made to improve the specificity of the technique by inserting targeted ligands into the liposomal membranes [52]. To date, the use of CT as a molecular imaging modality has yet to be fully defined.

The low sensitivity and the need for relatively large quantities of contrast medium currently limits wider application of molecularly-targeted CT imaging [52].

1.1.5 Endoscopic retrograde cholangiopancreatography (ERCP)

ERCP is an invasive technique but remains the procedure of choice for high-resolution assessment of biliary and pancreatic ductal anatomy. Contrast material is injected directly into the pancreatic ducts under fluoroscopic guidance. Because PDAC is of ductal origin, ERCP is very sensitive (78%–95%) and specific (88%–95%) for detecting pancreatic malignancies [53], [54], though not as sensitive as endoscopic US. Moreover, ERCP is not suitable as a screening tool given its invasiveness and associated complications (the risk of acute pancreatitis), which are not encountered with other noninvasive imaging modalities. Thus, ERCP is usually reserved for situations in which a therapeutic intervention could be required, such as stent placement, when performing the diagnostic evaluation [53].

1.1.6 MRI, diffusion-weighted MRI and MR spectroscopy

Relative to CT, MRI has the advantage of improved soft-tissue contrast resolution and no reliance on ionizing radiation. Currently, PDAC is best detected by using non-enhanced T1-weighted fat-suppressed gradient-recalled-echo imaging followed by contrast-enhanced imaging with gadolinium-based contrast agents [55], [56]. Normal pancreatic tissue has high signal intensity on non-contrast T1-weighted fat-suppressed images because of the presence of aqueous protein in the pancreatic parenchyma. Normal pancreatic tissue demonstrates a uniform capillary blush immediately after contrast enhancement and fades to iso-intense signal on interstitial phase images. In contrast, pancreatic cancer has a relatively abundant fibrous stroma and sparse tumor vascularity,

which expressed as a low signal intensity on non-contrast T1-weighted fat-suppressed images and less enhancement than the surrounding normal pancreatic tissue [57]. Recent reports of sensitivity and specificity of MR imaging for the diagnosis of pancreatic cancer are 85%–93% and 72%–79%, respectively [58], [59].

Diffusion-weighted (DW) MRI is the only imaging method that can be used to evaluate the diffusion process *in vivo*. DW imaging is increasingly being used within the abdomen [60], [61]. Various malignant tumors demonstrate high signal intensity on DW images, likely reflecting high cellularity and/or a long T2 relaxation time [62]. Several investigators have used DW imaging to detect PDAC. Muraoka *et al.* [63] reported that the apparent diffusion coefficient (ADC) in PDAC correlates with tumor fibrosis rather than with tumor cellularity. Ichikawa *et al.* [61] reported a very high sensitivity (96.2%) and specificity (98.6%) for detecting PDAC using DW imaging alone. Recent studies claimed that pancreatic cancer exhibits a high signal intensity on DW images with a significantly decreased ADC value compared with that of normal in parenchyma. ADC has also proven to be helpful for differentiating pancreatic cancer from mass-forming focal pancreatitis [64], [65]. While the results of these studies indicate that DW imaging is useful for characterizing pancreatic lesions, it has yet to be shown for the detection of pancreatic cancer at an earlier stage. It is also unclear about the improvement of diagnostic accuracy when DW imaging is added to MR protocols. Kartalis *et al.* [66] found similar diagnostic accuracy for pancreatic cancer when comparing their conventional MR protocol to the same MR protocol with DW imaging added.

MR spectroscopy provides a noninvasive measurement of biochemical information *in vivo* [67]. Several investigators have described the use of MR spectroscopy to characterize pancreatic neoplasms [68], [69]. When compared with normal pancreas, choline-containing compounds, fatty acids, and lipids were all decreased in PDAC [67]. The authors hypothesized that the hypo-perfusion and hypo-metabolism of PDAC relative to the surrounding pancreatic parenchyma contribute to these metabolic changes. MR spectroscopy is a promising method for improving the sensitivity for the diagnosis of PDAC. However, metabolic molecular information is currently limited by the relatively low magnetic field and signal strength associated with MR spectroscopy for clinic use [67].

1.1.7 Potential improvements of MR imaging with molecularly targeted contrast agents

MR imaging is associated with excellent soft-tissue contrast, but low sensitivity, which makes the development of molecular probes more challenging compared with other modalities such as positron emission tomography (PET), US, and optical imaging. Contrast agents based on nanoparticulate probes with a high payload of contrast-generating metals have been developed to overcome the low sensitivity. Tumor-targeted MR imaging has been performed by using gadolinium (III)-containing micelles and liposomes, superparamagnetic iron oxide NPs, and manganese (II) chelates [57], [70]–[72]. At present, superparamagnetic iron oxide NPs are the most attractive due to their chemical stability and biocompatibility, with an overall hydrodynamic diameter of less than 50 nm, much smaller than a cell (normally 10–30 μm) [72]. The incorporation of targeted biomarkers such plectin-1 [73] or EGFR [34], which are overexpressed in pancreatic cancer, have been published. Targeted contrast agents were developed by attaching peptide or single-chain

antibodies to iron oxide NPs [74], [75]. Results of these studies using tissue specimens and animal models demonstrated the feasibility of using targeted NP probes for both *ex vivo* and *in vivo* MR imaging. Molecular MR imaging for earlier detection of PDAC has not yet been translated into clinical trials. Greater adoption of MR imaging is likely challenged by the higher spatial resolution, lower cost, and greater availability of MDCT.

1.1.8 ^{18}F Fluorodeoxyglucose positron emission tomography (^{18}F FDG PET)

Elevated uptake of 18 fluorine (^{18}F) fluorodeoxyglucose (FDG) has been demonstrated in most primary malignant tumors because of increased metabolism of glucose [76]. Early studies demonstrated quantitative and selective overexpression of glucose transporter 1 (GLUT-1) in malignant pancreatic lesions [77], while normal pancreatic tissue has low glucose utilization due to reduced GLUT-1 density. Studies have demonstrated that ^{18}F FDG PET has a relatively high sensitivity (88%–94%) but variable specificity (60%–94%) for differentiating benign from malignant pancreatic masses [78]–[80]. Compared with CT and MRI, ^{18}F FDG PET is more sensitive for the detection of small tumors [81] and recurrent pancreatic cancer [82], [83]. However, PET has been reported with a high rate of false-positive results, particularly in patients with mass-forming pancreatitis [84]. With the development and combination of PET and CT, the ability of ^{18}F FDG PET imaging to provide accurate anatomic localization has greatly improved [85], [86]. Currently, the relatively low specificity, high cost, limited availability, and ionizing radiation all hinder the use of PET or PET/CT as a front-line diagnostic tool for pancreatic cancer. PET/CT can help establish the diagnosis of PDAC in patients suspected of having

pancreatic cancer in whom CT fails to identify a discrete tumor mass or in whom fine needle aspirations are non-diagnostic [86].

1.1.9 Improving sensitivity and specificity of PET with new radiotracers

^{11}C -acetate PET, which is thought to be metabolized by entering the lipid synthesis pathway [87], may be useful for the diagnosis of malignant tumor. As the cellular uptake of acetate is not affected by glucose metabolism, ^{11}C -acetate may provide superior detectability over ^{18}F FDG for malignancy and is expected to be comparably effective even in hyperglycemic states. In a recent study, Zhao *et al.*[88] reported the earlier detection of PDAC xenografts with ^{11}C -acetate PET than with ^{18}F FDG PET, but the ratio of accumulated radiotracer between tumor and non-tumor in ^{11}C -acetate PET was lower than that in ^{18}F FDG PET during the same period. Another radiotracer, ^{18}F -fluoroethyl-D-glucopyranose (^{18}F FEDL), which is overexpressed in peri-tumoral pancreatic acinar cells, was reported to be helpful for the detection of small pancreatic cancer lesions [89]. Further studies are needed to evaluate the performance of new radiotracers for detecting and characterizing PDAC specifically.

With recent advances in nanoparticle (NP) engineering, radiolabeled antibody or gene-based probes have been developed that target specific proteins or genes overexpressed on the surface or inside tumor cells (or vascular endothelial cells). These targeted probes demonstrated promise to increase diagnostic specificity. For example, the epithelial cell surface receptor $\alpha\beta 6$ is overexpressed in many cancers. Hausner *et al.* [90] have demonstrated the feasibility of targeting $\alpha\beta 6$ *in vivo* by using PET and a new radiotracer. With the new probes they were able to achieve excellent tumor retention and

fast clearance of nonspecifically bound tracer, which resulted in the signal ratio of tumor-pancreas greater than 23:1 in a mouse model of PDAC. Uptake of the radiotracers by integrin $\alpha\text{v}\beta\text{6}$ -expressing tumors was fast and intensive, contributing to the minimized off-target background.

Finally, given that 95% of patients with PDAC carry 12th codon activating mutations in their KRAS2 oncogenes, attempts have been made to image mutated KRAS2 mRNA activation by using PET and nucleic acid of mutant KRAS2 peptide: by using IGF1R (insulin-like growth factor 1 receptor)-overexpressed AsPC-1 pancreas cancer xenografts, a [^{64}Cu]KRAS-IGF1 radio-hybridization probe resulted in improved tumor contrast on PET, with an 8.6-fold increase in signal intensity within the human pancreas cancer xenografts when compared with the contralateral muscle [91].

1.2 Current intraoperative imaging tools

A major limitation of the aforementioned imaging techniques, such as CT, MRI or PET, is that they cannot be applied in intraoperative setting due to the altered positioning of the body and tissue manipulation by the surgeon [92]. For brain cancer surgery, the use of MRI-guided resection has become standard practice in most cases [93]. Unfortunately, this method is time-consuming, costly with limited acceptance. Therefore, chances are limited that MRI-guided resection will be widely-implemented outside the field of brain tumor surgery. Currently, the only tools available for the surgeon to ensure complete tumor resection are visual and tactile information, frozen-section analysis by a pathologist, and intraoperative US.

The clinical standard-of-care for achieving negative margins have severe limitations. Visual inspection is limited in detecting small tumors. Palpation is limited in sensitivity and is increasingly not used due to the utilization of robotic laparoscopic surgery. Intraoperative frozen section analysis is limited to certain tissue types, and is time-consuming and prone to sampling error. Frozen section analysis is discrepant with permanent pathology in 5–15% of cases [94].

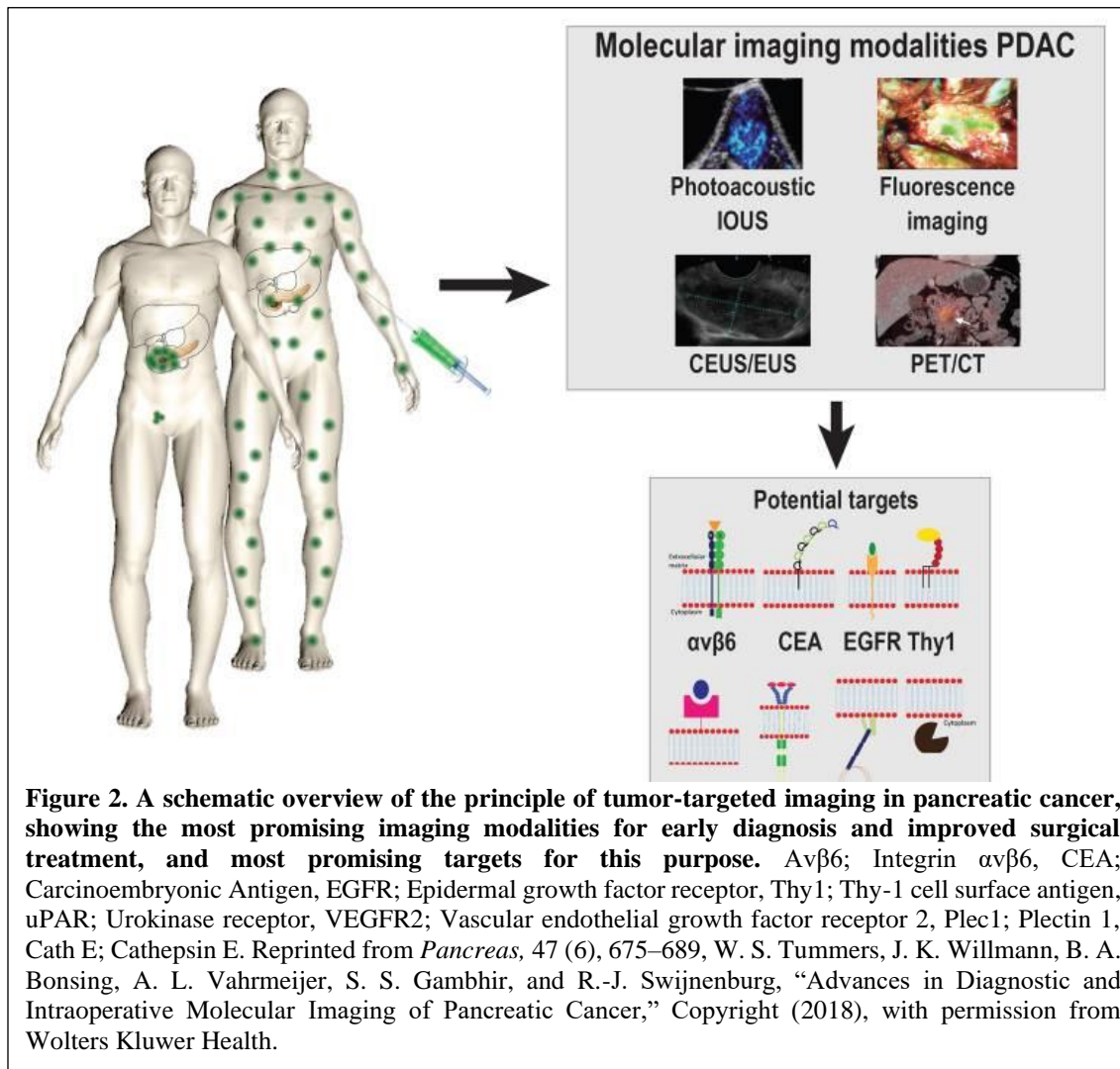
Currently, the only intraoperative imaging technique that can help the surgeon delineate PDAC from its surrounding tissue is anatomical intraoperative US. The ability to provide high resolution real-time imaging, along with accurate lesion detection, has established its role in PDAC surgery. Intraoperative US can be used for surgical guidance and localization of lesions, for determining resectability, surgical planning, differentiation between cystic and non-cystic lesions, and metastatic survey [95], [96]. However, it also has disadvantages as being less reliable to detect superficial and small lesions [97]. Another disadvantage is operator dependence: substantial training and experience are needed for generating and interpreting useful images for intraoperative surgical decision-making.

1.3 The need for advanced molecular imaging in PDAC

To improve detection and patient stratification for treatment, it is imperative to develop and improve imaging methods that specifically recognize cancer. In current practice, the accurate identification of tumors is mainly subjective and relies heavily on the surgeon's experience leading to a significant variability in surgical outcomes [98]. This inability to exactly identify tumors intraoperatively could result in: 1) incomplete resection of tumors that could otherwise have been resected completely; 2) attempts to resect tumors

which should have been identified as locally advanced tumors; 3) incomplete lymph node removal due to lack of knowledge of the involved or potentially involved lymph nodes, and 4) resection of the primary tumor in the presence of visually occult micrometastases. In each of these situations, patients undergo operations with little or no oncological benefit, but with a high risk of deteriorated life quality due to surgeries in their end stage of life. There are two other challenges a surgeon might face. First, both the benign pancreatitis and malignant PDAC have abundant stroma, and therefore both entities are difficult to distinguish using conventional imaging techniques. Second, the introduction of neoadjuvant treatment regimens such as FOLFIRINOX (a combination of chemotherapy drugs fluorouracil, leucovorin, irinotecan and oxaliplatin) was reported to increase the tumor resectability by 51% after 4 months of treatment [99]. However, conventional preoperative imaging modalities are often not able to differentiate between viable tumors and chemoradiation-induced tumor necrosis and fibrosis [100]. Neotreatment effects make differentiation between (vital) tumor and fibrotic pancreatic tissue even harder for surgeons during the operation.

Tumor-targeted molecular imaging could provide crucial information in these situations (**Figure 2**). Molecular imaging can either be performed by using conventional imaging techniques in combination with tumor-specific imaging agents, or by the development of novel imaging techniques, such as fluorescent, photoacoustic and Raman optical imaging. Currently, several first-in-human clinical trials are conducted using these techniques in pancreatic cancer patients.



1.4 Tumor-targeted molecular imaging strategies for PDAC

A molecular imaging approach using imaging agents that target molecular features of cancer could lead to more precise diagnoses [101]. The common consensus is that PDAC evolves from precursor lesions and transform into invasive carcinoma through a multistep process, which involves the progression from pancreatic intraepithelial neoplasia (PanIN) into PDAC [102]. Genetic alterations, such as mutations in the KRAS oncogene or p53, DPC4, and BRCA2 tumor suppressor genes affect a core group of signaling pathways. The processes that are altered in PDAC lead to the expression of specific biomarkers, and these

changed biomarkers may serve as targets for tumor-specific imaging [103]. Potential biomarkers for tumor-specific targeting must possess certain characteristics such as diffuse upregulation through tumor tissue, strong upregulation compared to the expression in normal and surrounding tissue, and localization on the cellular membrane [104], [105]. An effective molecular imaging agent needs to demonstrate a high ratio of specific to non-specific binding to make sure the signal truly reflects the molecular imaging target.

A molecular imaging agent is typically comprised of a targeting component and a signaling component. The main purpose of a molecular imaging agent is to interrogate and report back about a specific target (or targets) of interest during the course of a molecular imaging study. It is important to note that there are some molecular imaging techniques such as Raman Spectroscopy (RS) and coherent anti-stokes Raman scattering microscopy [106] that do not necessitate the introduction of an exogenous agent for visualizing certain biochemical targets and pathologies. In most other cases, a molecular imaging agent designed to specifically interact with one or more molecular targets needs to be first introduced to study biochemical processes. For the most part, the development of such an agent is not straightforward and is therefore a key rate-limiting step in molecular imaging.

Ideally, a molecular imaging agent should have the following characteristics: good ratio of specific to non-specific binding, high selectivity for biochemical target/process of interest, suitable pharmacokinetics, excellent *in vivo* stability (metabolism should not negatively affect functional binding), good safety profile (lack of toxicity to subject), potential for clinical translation, time and cost effective synthesis, signal amplification, and multiplexing capabilities [107].

For an effective imaging agent, the ratio of specific to nonspecific binding needs to be high. In the case of imaging low-density receptors, this ratio should be >3 [108]. High selectivity is also an important factor, whereby the imaging agent should possess the greatest affinity for, or functional interaction with, the intended binding site/process, but only negligible interaction with other sites/processes [109]. Nonspecific binding occurs due to the adhesion of an imaging agent to proteins and lipids. Although it is a challenge to predict the extent *in vivo*, it is generally believed that the lipophilicity of an imaging agent is proportional to the degree of nonspecific binding [108]. Therefore, lipophilicity is an important aspect to consider whilst designing an imaging agent.

A molecular imaging agent should display suitable pharmacokinetics (PK) for visualizing the biochemical target/process of interest. The rate of absorption and delivery to the target site, metabolism, excretion, and whether it will be reabsorbed in the enterohepatic circulation all factored in. Ideally, an imaging agent would be preferred to have rapid and specific interaction with its target, fast blood clearance, urinary excretion, and persistent, high accumulation at the target site. Size, charge and hydrophilicity play an important role in determining the PK profile [107], [110]. Generally, one aims to match the half-life of an imaging agent's signaling component to its PK process of interest.

There are numerous categories of available molecular imaging agents including small molecules, peptides, aptamers, antibodies, engineered protein fragments, NPs, or micro-sized contrast agent. Each of these types of agents is different in size and thus possesses different PK characteristics.

1.4.1 Small molecules

Small molecules play an important role in molecular imaging. The small size of chemical entities that are <500 Da means they can access and identify a large range of molecular targets (including intracellular and CNS targets). In addition, they are generally less likely to suffer from unfavorable biodistribution-related issues than those with large molecular weight (MW). Typically, small molecules can escape the vasculature easily, either passively or actively through biological barriers, interact with their targets, and clear from circulation in a short period of time [111]. The main drawback is the time-consuming process to discover, synthesize, and validate, and often does not afford many successful imaging agents. Also, due to their small size, there are limitations concerning the type of signaling component that can be attached (and hence modality that can be used). For example, one cannot usually conjugate a large fluorophore to a small molecule without altering the PK and targeting properties of the molecule.

1.4.2 Peptides

Peptides have emerged as a prominent class of molecular imaging agents. The application of solid-phase peptide synthesis and phage display libraries have led to rapid high-throughput synthesis and screening of peptide-based molecular imaging agents [112]. Peptides are easily modified, fairly small in size (up to 15 amino acids), and rapidly clearable. They have a number of advantages over small molecules, including superior selectivity and specificity, and tolerable for chemical modifications without altering binding properties or kinetics [113]. Although peptides generally display a lower affinity when compared to antibodies, they are more stable at room temperature and penetrable to tissues/tumors [114]. Additionally, peptides are less likely to induce immunogenic

reactions [115] compared with antibodies and are more cost effective to produce, as peptide synthesis is much cheaper than recombinant production techniques.

Peptide imaging agents have been reported to visualize a range of targets, including integrins [107], [116], matrix metalloproteinases [117], [118], caspases [119], [120] somatostatin receptors [121], [122], and gastrin releasing peptide receptors [123], [124]. The main disadvantage of using peptides as target moiety is that they are prone to rapid proteolytic degradation *in vivo* with a short plasma half-life. In addition, peptides used for PET and SPECT imaging mostly require prosthetic groups [125] for radioisotope labelling, which increased the complexity and time for synthesis, and might altered the structure necessary for efficient binding.

1.4.3 Aptamers

Aptamers are defined as single-stranded DNA or RNA oligonucleotides that bind to their targets with a high degree of specificity and selectivity [126]. The superior targeting capabilities of aptamers, comparable to that of antibodies, along with their relative ease of synthesis [127], high diversity, and inexpensive production, have made these 5-15 kDa chemical entities attractive candidates for molecular imaging. There are several published articles describing the labeling of aptamers with either fluorophores or radioisotopes imaging purpose [128], [129]. However, these agents have not yet been evaluated in living subjects. There are a few key limitations associated with using aptamers as molecular imaging agents, including 1) low *in vivo* stability due to serum degradation, 2) poor membrane passage due to their size and charge (*i.e.*, PK is rather variable and difficult to predict), 3) small size leading to short half-life.

1.4.4 Antibodies

Monoclonal antibodies (mAbs), also known as immunoglobulins, are highly specialized, ~150 kDa, Y-shaped proteins [130]. Unlike small molecules and peptides, mAbs are not restricted to interacting with binding pockets or active sites, but instead can bind adhesion molecules, activation markers, antigens, and receptors [131]. Currently, there are over 20 FDA-approved mAb therapeutic agents and greater than 8 radiolabeled mAbs approved for SPECT molecular imaging [132]. Current efforts in the field of antibody-based molecular imaging agents are focused towards developing chimeric, humanized, or fully human mAb imaging agents (to eradicate immunogenicity issues) both from a diagnostic and therapeutic standpoint. Although there are many promising mAb-based molecular imaging agents emerging for a range of different imaging platforms, their versatility and usefulness has remained fairly limited due to their long residence in blood and restricted ability to transverse biological barriers (*e.g.*, the blood-brain barrier and cell membranes).

1.4.5 Nanoparticles (NPs)

In terms of imaging agents, NPs are emerging as an exciting new set of diagnostic tools, capable of both passive and active targeting. Since there exist a wide range of different shaped NPs of varied size and composition with unique surface properties and reactivities, it is not surprising that NPs are among the most flexible imaging agents with respect to the types of imaging modalities they are compatible with. Although there is no fixed size constraint for the NP, people typically consider them to be on the order of ~10-100 nm, and no larger than 1000 nm. Generally, NPs are larger than many proteins and small molecules, yet smaller than cells. Their relatively large size (compared with small

molecules and many proteins) means they are often taken up by the reticuloendothelial system (RES). Polymer-coated “stealth” NPs, on the other hand, can avoid entrapment by the RES from hours to days [133]. Due to their high surface area-to-volume ratio, many NPs are able to carry substantial payloads of targeting and/or signaling moiety. This means that for each NP bound to a target, there can be signal magnification compared with the signal from singular molecular imaging agent. This multivalent mode is known as avidity and is particularly important in cases where sensitivity of the imaging modality is the main limitation (*e.g.*, MRI). Also, due to the high density of targeting moieties that are attached to the NP surface, they have a greater chance to bind to the target. However, the advantages of NPs come at the cost of fewer particles being delivered to the target site, comparing to the delivery of small molecules. This is because NPs rapidly accumulated in liver, spleen, and bone marrow following their administration, and thus less of the dose is “available” for targeting/delivery. Key types of NPs that are currently reported in molecular imaging such as: single-walled carbon nanotubes [134], quantum dots [135], gold NPs [136], superparamagnetic iron oxide NPs [137].

As exciting as NP-based imaging agents are, the limitations should be noted. The size can be a key factor concerning their nature of polydispersity. Delivery of sufficient concentration remains a challenge, primarily due to competition of RES uptake. Other issues including slow clearance, thereby making it difficult to distinguish NPs that bound to the target(s) from unbound NPs. Also, heterogeneity make it challenging to predict bio-performance as it is for small molecules, in specific aspects of characterization, toxicological study and potential translation. Whereas the growing number of approved therapeutic NPs [138] (such as Doxil, a liposome drug delivery system used to treat AIDS-

related Kaposi's sarcoma and ovarian cancer) is currently serving as a template for the clinical translation of functionalized NPs for molecular imaging purposes, thus accelerating progress in this area.

1.4.6 Multimodality imaging probes

Multimodality probes are imaging agents capable of being detected *via* two or more different imaging modalities simultaneously. Since these types of probes have the potential to generate multiple readouts concerning the same biological phenomenon, they could be of great value for numerous clinical and basic research applications. Multimodality probes are predominately NP-based (*e.g.*, superparamagnetic iron oxide, gold nanospheres/nanorods, single/multi-walled carbon nanotubes, quantum dots (QDs)); however, there are also examples of engineered proteins [139], peptides [140], and small molecule-based probes [141]. Typical probes include MRI/optical, MRI/PET, MRI/SPECT, PET/optical, SPECT/optical, and photoacoustic imaging (PAI)/Raman imaging. The main challenge involved in developing and using multimodality imaging probes is that some modalities (such as PET and MRI) differ in their sensitivities by more than three orders of magnitude [142]. Hence, a combined probe can lead to a compromise compared with using each component separately [143].

1.5 Physiologic concerns for developing NP imaging probes

NPs and nano-sized molecules (NMs) possess enormous potential as diagnostic imaging agents and hold promise for the development of multimodality agents with both imaging and therapeutic capabilities [110]. Currently, some of the most promising NPs that are under investigation contain heavy metals, which not only pose risks for systemic

toxicity, but prolonged particle retention that may interfere with imaging and diagnostic tests. Creating particles with optimal clearance characteristics will minimize toxicity risks and disease concerns by reducing the duration of exposure to these agents. Given that many types of NPs possess easily modifiable surface chemistry, if characteristics of NPs and NMs associated with optimal clearance were well established, it would be feasible to create agents with more favorable clearance properties. Properties known to affect clearance include particle composition, size, shape, surface chemistry and charge – all of which are tunable for specific applications.

1.5.1 Vascular delivery

Upon intravenous administration, NPs and NMs enter the vascular system and are distributed to the organs and peripheral tissues of the body. Within the vascular compartment these particles or molecules encounter blood cells, platelets, coagulation factors and plasma proteins. Depending on the size and charge, NPs and NMs may undergo adsorption or opsonization by serum proteins. In addition to enhancing particle recognition by the host immune system, adsorption/opsonization alters the effective size of the particle and results in a particle diameter referred to as the *in vivo* hydrodynamic diameter (HD), which may be considerably larger than the *in vitro* diameter. The HD affects blood clearance and therefore blood half-life and whole body half-life. The HD is inversely related to rate of glomerular filtration and is directly related to blood and whole body half-life.

The vascular endothelial cell monolayer acts as a dynamic and semi-selective barrier that regulates transportation of fluid and macromolecules between the vascular

compartment and the extravascular space [144]. Although the structure of the endothelial layer varies throughout the body, the effective pore size in normal intact endothelium is approximately 5 nm [145]. NMs with an HD less than 5 nm achieve rapid equilibrium with the extravascular extracellular space (EES), whereas larger particles experience prolonged circulatory times due to slow transport across the endothelium. For example, intravenously administered human IgG (HD:11 nm) requires 24 h to equilibrate between the vascular compartment and the EES [145], [146]. By contrast, smaller molecules such as the radiocolloid dextran-Techneium 99 (HD < 4 nm) could establish rapid equilibration with the EES owing to penetration of capillary fenestrae [147]. Similar behavior has also been observed in the lymphatic vessels with NPs. Although the lymphatic vessel endothelial layer is more permeable than that of the vascular endothelium because of its role in clearance of macromolecules from the EES, particles up to or smaller than 6 nm in diameter can flow easily into and out of the lymphatic vessels [148]. Therefore, the threshold of nano-size diffusion from the lymphatics is slightly larger than the capillaries, yet still comparable.

Modification of NP/NM characteristics such as size and surface chemistry can significantly alter *in vivo* kinetic properties. For instance, PEGylation, the process of molecularly attaching polyethylene glycols (PEG) with different MWs to the particle surface groups, is one of the most widely used methods for improving particle pharmacokinetic behavior [149]. The primary effects of PEGylation include prolongation of plasma half-life, alteration of tissue distribution and particle elimination [149].

1.5.2 Renal clearance

The kidney is capable of rapidly removing molecules from the vascular compartment with their original form. Renal excretion represents a desirable pathway for NP/NM clearance as is the minimal involvement of intracellular catabolism. This route reduces the possibility of retention and cytotoxicity as compared with the hepatobiliary system, in which intracellular enzymatic modification is standard. Thus renal clearance is thought to be the preferred clearance route to minimize toxicity and agent retention. Renal clearance of intravascular agents is a multifaceted process involving glomerular filtration, tubular secretion and finally elimination of the molecule through urinary excretion. Glomerular filtrate flows through the fenestrated, across the glomerular basement membrane (GBM) and through the filtration slits. Among the key nanostructural dimensions is the slit diaphragm, whose diameter is approximately 43 nm [150]. However, after considering the combined effects of each layer of the glomerular capillary wall, the functional or physiologic pore size is significantly smaller—only 4.5-5 nm in diameter [151].

Glomerular filtration is highly dependent on the molecule size and is referred to as the filtration-size threshold [150]. Molecules with an HD of less than 6 nm are typically filtered, while those more than 8 nm are not typically capable of glomerular filtration. Filtration of molecules within the intermediate range (6-8 nm in HD) depends upon both size and charge of the particle. The filtration-size threshold for globular proteins has been well studied and is generally accepted to be less than 5 nm in HD. For example, inulin (HD: 3 nm) achieves 100% renal filtration with a blood half-life of only 9 minutes [152]. The relationship between protein size and clearance is further demonstrated by antibody clearance data. The stabilized V-region fragment of an antibody (HD: 4 nm) demonstrates

100% renal filtration with a serum half-life of 5 minutes [153], as compared with the antibody's Fab' fragment (HD: 6.0 nm), which achieves only 9% of effective filtration with a serum half-life of 28 min [154]. Additionally, clearance of antibody fragments is more rapidly than that of the intact antibody, which is not efficiently filtered and has a circulation half-life up to days.

Renal filtration of globular proteins as a function of size provides an important framework for the understanding of general properties of renal clearance. Nevertheless, the physical properties of NPs differ from those of proteins in several ways: NP shape, surface chemistry and interior charge is distinct; in addition, NPs can be synthesized with a near-spherical shape and identical surface chemistry [155]. Such differences may lead to distinct renal handling of NPs compared with protein molecules. To evaluate the effect of these characteristics on size threshold of filtration, clearance studies of poly(aminoamine) dendrimer-based NPs with homogenous chemical properties and near-spherical shape were conducted. Results showed that poly(aminoamine) dendrimers with the average diameter of 5.4 nm demonstrated effective filtration [156]. This filtration-size threshold is similar to that of conventional macromolecules. Additionally, renal clearance studies in mice using QDs revealed that renal excretion was observed for those with HDs ranging from 4.36 to 5.52 nm [145]. QDs larger than 8 nm (HD: 8.65 nm) did not demonstrate renal filtration but instead exhibited uptake in RES and lung [145]. The relationship between HD, renal clearance and total body retention was determined to be sigmoidal with the 50% point for total body clearance at 4 h achieved with an HD of 5.5 nm [145]. These results also suggested that the size threshold for renal filtration of NPs may be comparable to proteins and other NMs. With this in mind, it is reasonable to conclude that NPs capable of being

synthesized with a diameter of less than 8 nm, such as dendrimers, carbon nanotubes, silica particles and QDs, can undergo renal clearance if other modifiable parameters (surface charge and chemistry) are optimized for this excretion pathway.

In addition to size, surface charge is also an important determinant of the renal handling of NP/NMs. The effect of molecular charge on renal filtration is due to at least two factors: potential interactions between charged molecules and serum proteins, resulting in increased HD [145], as well as the electrostatic interactions between charged molecules and fixed charges within the glomerular capillary wall [150]. Studies using QDs as the model for *in vivo* NP clearance revealed that purely anionic or cationic charge was associated with serum protein adsorption [145]. Adsorption resulted in an increase in HD to more than 15 nm, dramatically reducing renal filterability [145], [157], [158]. Neutralization of the NP surface *via* PEGylation was shown to be effective in preventing serum protein adsorption. However, it was reported that synthesizing PEGylated QDs with an HD of less than 10 nm was not possible [145]. Therefore, PEGylation also dramatically reduces particle renal filtration. Interestingly, zwitterionic coatings were shown to prevent serum protein adsorption and were associated with the highest solubility and smallest HD [145].

Studies evaluating the effect of molecular charge on glomerular filtration of similarly sized molecules have shown that filtration is the greatest for cationic molecules, followed by neutral molecules, while anionic molecules are least readily filtered [150]. Direct comparison of varied charged molecules about the glomerular filtration has been studied using charge-modified Fab' fragments (HD: 6 nm). Weakly anionic Fab showed

drastically less filtration compared with those that are weakly cationic [159]. Charge-selective filtration is attributed to fixed negative charges within the capillary wall [150]. It is worth mentioning that molecular charge is of particular significance for the filtration of molecules within the 6-8 nm range, as these particles are not small enough to undergo charge-independent filtration, yet may still be filtered if molecular charge is favorable.

The final step in renal processing occurs at the proximal tubule where filtered molecules may be resorbed from the tubular fluid and previously unfiltered molecules may be actively secreted into proximal tubule lumen. Particle behavior at the proximal tubule is an important consideration because some molecules, such as glucose, achieve 100% reabsorption thus negating the effects of glomerular filtration. While other agents, such as heavy metals, are highly toxic to proximal tubule cells and may potentially cause renal damage including acute tubule necrosis, interstitial nephritis and even renal failure. Research evaluating NP/NM reabsorption at the proximal tubule is currently limited. Studies by Kobayashi *et al.* [159] indicate that some polyamine dendrimers may undergo proximal tubule reabsorption, but further investigation of this issue is needed to gain insight into the renal toxicity profile of NP. Evaluation of agent behavior at each step in renal processing might lead to agents with optimal biocompatibility and clearance properties.

1.5.3 Hepatic clearance

The hepatobiliary system represents the primary route of excretion for particles that do not undergo renal clearance. Liver provides the critical function of catabolism and biliary excretion of blood-borne particles, serves as an important site for the elimination of foreign substances and particles through phagocytosis [160]. Those NPs and NMs that are

excreted *via* the biliary system are catabolized first through hepatocytes. All physical or chemical catabolites must be accounted for when considering total hepatic clearance. Therefore, the hepatic clearance is more complex than renal clearance. Phagocytic Kupffer cells have ciliated borders and stellate branches that serve as highly adapted mechanical traps for the removal of unwanted substances from the blood including foreign colloidal or particulate substrates [160]. Kupffer cells possess numerous receptors for selective endocytosis of opsonized particles (receptors for complement proteins and for the Fc part of IgG) [160]. Hepatocytes play an important role in liver clearance through endocytosis and enzymatic breakdown of foreign particles. Although the phagocytic capacity of hepatocytes is much less than that of Kupffer cells, these cells represent an important physiologic pathway for foreign particle processing and are potential sites for induced toxicity [160]. Furthermore, hepatocytes are within the pathway for biliary excretion and therefore particles processed by these cells are potentially excreted into the bile. Kupffer cells are part of the RES and rely exclusively on intracellular degradation for particle removal. Similar to all phagocytic cells of the RES, particles that are not broken down by intracellular processes will remain within the cell and will therefore be retained longer in the body.

Liver is functionalized to efficiently capture and eliminate particles on the scale of 10-20 nm for the clearance of viruses and other small particles. As a result of this adaptation, agents within this size range often undergo rapid liver uptake [145]. To achieve adequate retention times, NPs may require modification to prevent or reduce opsonization. Molecular modification *via* PEGylation is a widely used mechanism to decrease first-pass extraction and extend NP circulation. Interestingly, although uptake of particles from the

blood to the liver may occur relatively fast, hepatic processing and biliary excretion of these particles are pretty slow, which contributes to the prolonged retention of NPs within the liver parenchyma itself [145].

1.6 Intraoperative molecular imaging techniques: potential for improved intraoperative performance

1.6.1 Fluorescence molecular imaging

Over the last few years, intraoperative imaging technologies using near-infrared (NIR) fluorescence have made enormous progress. The volume of publications in this field has increased by eight-fold in the literature in the last 10 years [161]. Benefit of fluorescence imaging using NIR fluorescent is the ability to image in real-time without impeding the current clinical workflow. If surgeons were able to resect tumors and preserve normal structures more easily, time of surgery could be shortened, thereby reducing anesthesia time and associated risks. Furthermore, this could subsequently lower the rates of recurrence and complications, which would improve patient outcomes and even save costs [92]. Fluorescence imaging has already been established as a powerful tool for guiding precise intraoperative positioning in multiple types of cancer such as liver metastases [162], breast cancer [163], ovarian cancer [164], sentinel lymph node in melanoma [165], vulvar cancer [166], [167], and cervical cancer [168], [169]. However, only the non-specific dyes methylene blue (MB) and indocyanine green (ICG) are approved for clinical use by FDA. Second window ICG [170] accumulates in the invasive pancreatic malignancies and provides real-time feedback during pancreatectomy [32]. NIR imaging could help to assess the tumor response to neoadjuvant therapy as well [32]. ICG was also found to identify residual disease during anterior mediastinal tumor resection

[171], and allows location of pulmonary, pleural and thoracic malignancies during surgery [172].

In order to improve clinical benefit of fluorescent imaging, incorporation of tumor-specific imaging agents will be essential. Recently, two first-in-human clinical studies have been reported to use tumor-specific intraoperative imaging as the visual aid for the resection of PDAC. They are antibody-based contrast agents including targeting carcinoembryonic antigen (CEA) with SGM-101 [173] and EGFR with cetuximab-IRDye800 [174]. In both cases successful PDAC imaging could be appreciated as well as the specific identification of abdominal metastases. These trials show the proof-of-concept that this imaging technique is possible for aiding the resection of PDAC, despite the idea that the dense stroma of PDAC will restrict the access of targeted-imaging agents and therapeutics [175].

1.6.2 Molecular-targeted agents for fluorescent molecular imaging

As described above, only agents targeting the CEA and EGFR receptor have been reported to be used in clinical trials for specific NIR fluorescent imaging of PDAC. With cetuximab-IRDye800, it was even possible to identify PDAC from peri-tumoral inflammation [176]. Nevertheless, only preclinical work is performed for the identification of tumor-specific targets. Gao *et al.* [177] synthesized an integrin $\alpha\beta6$ -targeted NIR fluorescent dye-labeled contrast agent and investigated it for targeted theranostics. The image probe bound to integrin $\alpha\beta6$ *in vitro* and *in vivo* with high affinity, and when used for surgical guidance, completely secured the tumor removal. Additionally, small size conferred its easy extravasation and fast excretion. Zhang *et al.* [178] reported an optical

imaging agent that's suitable for both fluorescent and photoacoustic imaging. The imaging probe consists of a cysteine knottin targeting $\alpha v \beta 6$ that conjugated to the NIRF dye, which is detectable in integrin $\alpha v \beta 6$ -positive tumors both *in vitro* and *in vivo* by photoacoustic and fluorescence imaging.

Aside from developing passive and active targeting probes, site-activatable contrast agents were also reported. Cathepsin E is a tumor-associated intracellular non-lysosomal aspartic proteolytic enzyme which presents in PanIN lesions and PDAC but not in normal pancreatic tissue [179]. Cathepsin E-activatable imaging probes are fluorescence quiescent in native state, but become fluorescent upon Cathepsin E cleavage [179], [180]. Activatable imaging probes demonstrate several advantages. The native state of the probe is optically silent, thereby minimizing background fluorescence and enhancing tumor-to-background ratio. Moreover, probes can be designed to be activated by varied proteases according to the tumor histological characterization [181], [182]. The first-in-human trial was reported by Whitley *et al.* [183], who assessed the imaging efficacy of protease-activatable fluorescent imaging probe for the detection of soft tissue sarcoma and breast cancer, thus demonstrated the potential of activatable probes for clinical translation.

Here, we report the preclinical screening of a series of HA-based macromolecular NIRF contrast agents, for the specific detection of PDAC and associated metastases. HA platforms utilize a natural polymer with a tropism to a receptor (CD44) overexpressed in many cancers, and thus these carriers do not require separate targeting with an antibody or peptide, which may translate into a lower cost of the treatment and a more stable formulation compared to the antibody-based contrast agents. The hypothesis is, by

investigating the effects of HA molecular weight and NIRF properties, the leading contrast agents will reduce the contrast agents in non-specific organs and improve probe specificity for malignancy detection.

CHAPTER 2: NANOFORMULATION OF ICG FOR THE INTRAOPERATIVE PROBING OF PANCREATIC TUMOR AND METASTASES WITH REDUCED TOXICITY

2.1 Introduction

Pancreatic ductal adenocarcinoma (PDAC) is highly lethal due to the advanced stage at diagnosis, with a median overall survival of 15 months and 5-year survival rate of 13% [184]. Detection and surgical resection at earlier stages increases 5-year survival to 31.7 ± 3.6 months [185]. Enhanced contrast can aid surgeons to confirm suspected pancreatic masses and elucidate positive margins [186]. Therefore, improved tumor imaging techniques that can better recognize cancerous lesions are essential to improve complete removal of PDAC and subsequent survival. At present, tumor localization and assessment of disease extension are made with visual inspection and palpation [187], which can lead to incomplete resection or unnecessary removal of healthy tissue. Using tumor-specific contrast agents, image-guided surgery facilitates real-time, intraoperative, and visual identification of pancreatic tumors with improved discrimination of malignant and normal tissue [92].

Clinically available preoperative imaging modalities, such as computed tomography (CT), magnetic resonance imaging (MRI), and positron emission tomography (PET), are critical to surgical planning. However, translating these results to the operating room is difficult due to altered body positioning, tissue manipulation, and lack of sensitivity to detect microscopic lesions [188]. Therefore, an intraoperative imaging technique with

high accuracy and sensitivity is needed to fill the gap between preoperative and intraoperative reality. Current techniques that are used to assess pancreatic tumor extension intraoperatively, such as ultrasonography (US) and intraoperative frozen-section analysis (IFSC), have limitations. Substantial experience is required to generate and interpret useful US images during pancreatic cancer surgery [188]. Although IFSC is useful in ensuring negative margins, it has a negative predictive value of 50% for examining pancreatic lesions that could result in poor histological diagnosis and determination of resectability.

Clinically available preoperative imaging modalities, such as CT, MRI, and PET, are critical to surgical planning. However, translating these results to the operating room is difficult due to altered body positioning, tissue manipulation, and lack of sensitivity to detect microscopic lesions.[188] Therefore, an intraoperative imaging technique with high accuracy and sensitivity is needed to fill the gap between preoperative and intraoperative reality. Current techniques that are used to assess pancreatic tumor extension intraoperatively, such as US and intraoperative frozen-section analysis (IFSC), have limitations. Substantial experience is required to generate and interpret useful US images during pancreatic cancer surgery [188]. Although IFSC is useful in ensuring negative margins, it has a negative predictive value of 50% for examining pancreatic lesions that could result in poor histological diagnosis and determination of resectability [189].

Fluorescence imaging offers a potential method to detect pancreatic cancer intraoperatively to maximize malignant tissue resection. FIGS can detect fluorescent contrast agents with high sensitivity and spatial resolution, which minimizes contrast agent dose and allows real-time determination of tissue status.[190], [191] For example, AlexaFluor488 conjugated CA19-9 antibody was used to detect primary tumor and splenic

and liver metastases of pancreatic cancer during surgical navigation.[192] Furthermore, near infrared (NIR) FIGS can minimize interference caused by tissue auto fluorescence, scattering, and absorption, allowing relatively deep detection of contrast agent [193], [194]. Metidi *et al.* [195]demonstrated usage of MMP-2 and MMP-9 cleavable peptides conjugated Cy7 for accurate labeling of pancreatic tumors with FIGS in an orthotopic human xenograft mouse model, this resulted in a lower metastatic burden and decreased distant recurrence compared with resection surgery under standard bright light. Yang *et al.* [196] used magnetic iron oxide NPs modified with Cy5.5 conjugated ATF (amino-terminal fragment) of uPA (urokinase plasminogen activator) for surgical detection of pancreatic cancer lesions. Combined, fluorophore conjugated monoclonal antibody probes were used in animal models of pancreatic cancer with improved specificity, however, their efficacy was limited by naturally existing cellular targets that are often heterogeneously expressed in tumors and possibly in low abundance compared to background signals.[197] Therefore, a more generally applicable NIR fluorescent (NIRF) probe could have potential for NIR FIGS for reducing PDAC tumor burden.

Hyaluronic acid (HA), the principal ligand for CD44, possesses many attractive features, including acting as a capping agent to achieve targeted and controlled payload release, prolonging the blood circulation time, and increasing the physiological stability and biocompatibility of drugs [198]–[200]. Incorporation of HA into a delivery system can reduce plasma protein adsorption and immunogenicity of associated protein upon *i.v.* administration, further highlighting potential as biocompatible and safe drug carrier [201]–[204].

Here, we report the use of a HA nanoformulation of ICG, termed NanoICG, for tumor detection in an orthotopic, syngeneic model of pancreatic cancer. ICG is an FDA-approved NIR fluorophore that can be detected through up to 8 mm of tissue [205]–[207]. On the other hand, HA is a major component of extracellular matrix that participates in cell proliferation, wound healing, and cancer metastasis [208]. With modifiable chemical groups such as carboxylate, N-acetylglucosamine, hydroxyl, and acetyl moieties, HA is readily available for chemical conjugation [209], [210]. Recently, we reported that NanoICG increased NIR tumor signal by 2.28- and 2.25-fold compared to ICG in MDA-MB-231 xenograft [211] and 4T1 syngeneic orthotopic [206] breast tumor models, demonstrating potential for sensitive tumor detection. In this study, NanoICG was compared to ICG as a NIR FIGS contrast agent for the intraoperative detection and contrast-enhancement of pancreatic cancer in a syngeneic, orthotopic model. Results from *in vitro* and *in vivo* studies indicated that NanoICG is a safe contrast agent that can potentially be used in pancreatic tumor detection and surgical resection.

2.2 Methods

2.2.1 Materials ICG, luminol, and zymosan A were purchased from Sigma-Aldrich (St. Louis, MO). 10-20 kDa sodium hyaluronate was purchased from Lifecore Biomedical (Chaska, MN). HPNE cell line was provided by Dr. Michel J. Ouellette from University of Nebraska Medical Center, while the KPC cell line was shared by Dr. Hollingsworth. HL-60 cells were purchased from ATCC (Manassas, VA). HPNE cells were grown in 70% DMEM with 25% medium M3, 5% FBS, 20 ng/mL human recombinant EGF, 1% penicillin/streptomycin; KPC cells were grown in DMEM with 10% FBS and 1%

penicillin/streptomycin, HL-60 was maintained in IMDM with 20% FBS. Cell counting kit-8 (CCK-8) was purchased from Dojindo Molecular Technologies Inc. (Rockville, MD). Calcein AM was purchased from Invitrogen (Carlsbad, CA). 10-week-old female C57BL/6J mice were purchased from Jackson Laboratories (Bar Harbor, ME). 5.0 chromic gut and 5.0 nylon surgical sutures were purchased from Johnson & Johnson (Somerville, NJ). Comprehensive diagnostic profile reagent rotor was purchased from Abaxis (Union City, CA). All the other chemicals were purchased and used at analytical grade.

2.2.2 Preparation and Characterization of NanoICG The synthesis of amphiphilic HA-aminopropyl-1-pyrenebutanamide (HA-PBA), preparation of NanoICG from the entrapment of ICG during HA-PBA self-assembly, and quantification of ICG in NanoICG were performed based on the literature.[206], [211]

The mean hydrodynamic diameter and zeta-potential of NanoICG was determined using a Zetasizer Nano instrument (Malvern, Worcestershire, UK). NanoICG was prepared at 0.34 mg/mL for size determination and 0.06 mg/mL for the determination of UV-visible absorption and fluorescence emission. An Evolution 220 spectrophotometer (Thermo Fisher Scientific, Madison, WI, USA) was used for scanning absorbance spectra (600–900 nm) and a FluoroMax-4 spectrofluorometer (Horiba, Edison, NJ, USA) was used for quantifying fluorescent intensity of ICG, NanoICG, and disassembled NanoICG.

2.2.3 Cytotoxicity The cytotoxicity of NanoICG and empty NP (self-assembled HA-PBA) were tested using the CCK-8 assay (Dojindo; Rockville, MD). HPNE and KPC cells were seeded in 96-well plates at a density of 25,000 cells/well and allowed to adhere for 24 h. Empty NP and NanoICG were dissolved in DMEM at different concentrations (0,

0.01, 0.05, 0.1 mg/mL) and 200 μ L was added to each well. Cells were treated for 24 h and washed twice with PBS. Next, 100 μ L of 10% CCK-8 reagent in DMEM was added to each well and incubated at 37 °C. After 50 min, absorbance of each well was measured at 450 nm using a Synergy HTX multi-mode plate reader (BioTek, Winooski, VT, USA). Relative viability was calculated as the absorbance of wells from treated cells divided by the absorbance from wells with untreated cells.

2.2.4 Chemotaxis A chemotaxis assay was adapted from procedures from the National Cancer Institute's Nanotechnology Characterization Laboratory (NCL) (<https://ncl.cancer.gov/resources/assay-cascade-protocols>): ITA-8. Briefly, HL-60 cells were suspended in serum-free IMDM (SM) and incubated overnight prior to use. 1×10^6 viable cells/mL (as determined by trypan blue) were dispersed onto a MultiScreen filter plate with 3 μ m polycarbonate membrane (Merck Millipore, Germany) at 50,000 cells/well. Test samples (150 μ L) were added in the feeding tray. The filter plate and feeding tray were gently assembled and incubated for 4 h. After incubation, Calcein AM (CAM) working solution was added to appropriate wells and incubated for 1 h. The solution was then transferred to the optical bottom plate (Thermo Fisher Scientific, Rochester, NY, USA) on a fluorescent plate reader with 485 nm excitation/535 nm emission. Fold increase of chemotaxis was calculated as follows:

$$\text{Background Chemotaxis} = \text{Mean } FU_{SM/CAM} - \text{Mean } FU_{SM/PBS}$$

$$\text{Sample Chemotaxis} = \text{Mean } FU_{TS/CAM} - \text{Mean } FU_{SM/PBS}$$

$$\text{Fold Increase of Chemotaxis} = \text{Sample Chemotaxis} / \text{Background Chemotaxis}$$

where Mean $FU_{SM/CAM}$ = fluorescence units of HL-60 treated with SM and CAM, Mean $FU_{SM/PBS}$ = fluorescence units of HL-60 treated with SM and PBS, and Mean $FU_{TS/CAM}$ = fluorescence units of HL-60 treated with test samples and CAM.

The theoretical plasma concentration (TPC) of ICG and NanoICG was calculated based on the dose administered to mice below.[212] Calculating formula was adapted from NCL Method ITA-8. TPC of empty NP were based of the mass ratio of HA matrix in NanoICG. The concentrations for $10 \times$ TPC, $1 \times$ TPC, $1/5 \times$ TPC and $1/25 \times$ TPC of ICG were 5.1 μ M, 0.51 μ M, 0.10 μ M, 0.02 μ M, respectively; the concentrations for $10 \times$ TPC, $1 \times$ TPC, $1/5 \times$ TPC and $1/25 \times$ TPC of NanoICG were 38 μ g/mL, 3.8 μ g/mL, 0.76 μ g/mL, 0.15 μ g/mL, respectively. The same concentrations were used in the phagocytosis assay.

2.2.5 Phagocytosis Phagocytosis was assessed according to NCL ITA-9. The multi-mode reader and 96-well plate were pre-warmed to 37 °C. HL-60 cell concentration was adjusted to 1×10^7 viable cells/mL (as determined by trypan blue) with complete medium. 100 μ L of cell suspension was added per well. 100 μ L of controls or test samples were added to pre-warmed wells, followed by 100 μ L of luminol working solution (250 μ M in PBS). A positive control was prepared by reconstituting zymosan A in PBS with 20% pooled normal human AB serum (Innovative Research, Novi, MI, USA) to a concentration of 2 mg/mL. After mixing, 100 μ L of cell suspension was added in sample wells and mixed thoroughly. The kinetic reading process was 1.5 h with 2.1 min reading intervals. The area under the curve (AUC) for each kinetic reading curve from each well was calculated as phagocytic potential.

2.2.6 Tumor model induction All animal studies were performed under an approved

UNMC Institutional Animal Care and Use Committee protocol and procedures followed were in accordance with the institutional guidelines per the Guidelines on the Care and Use of Animals for Scientific Purposes. To preclinically evaluate contrast-enhancement of pancreatic cancer by ICG and NanoICG, mature C57BL/6 mice were selected for orthotopic tumor challenge using 10,000 LSL-Kras^{G12D/+};LSL-Trp53^{R172H/+};Pdx-1Cre (KPC)-derived PDAC syngeneic cells per mouse. As described previously,[213] once anesthetized, an approximately 5 mm incision was made into the skin and peritoneum on the abdomen between the hip and rib. This allowed for the spleen to be exteriorized for injection of PBS cell suspension into the body of the pancreas. The peritoneum and skin were then secured using an internal dissolving chromic gut and a 5.0 nylon surgical suture respectively. Animals were warmed, hydrated, and monitored through recovery. Within two weeks of introduction of tumor cells, palpable tumors were detected in all challenged mice.

2.2.7 Near-infrared fluorescence imaging ICG (10 nmol per mouse) or NanoICG (10 nmol ICG per mouse) in 80 μ L ultrapure water was intravenously injected into mice via a tail vein ($n = 5$ mice per group). Mice were euthanized 24 h post injection. Prior to imaging, the liver and spleen were removed to minimize strong ICG fluorescence due to hepatobiliary clearance and to evaluate the ability of ICG and NanoICG to distinguish pancreatic tumor from healthy pancreas. A custom-designed FIGS system was employed to detect contrast enhancement of ICG and NanoICG in the pancreatic tumors. The imaging system utilizes a handheld fiber-coupled spectroscopic unit that excites ICG and collects wavelength-resolved NIR emission (DeltaNu; Laramie, WY, USA). The spectroscopic unit also serves as the excitation source for a real-time wide-field imaging system (Spectropath; Atlanta, GA, USA) that merges a NIR channel (800-950 nm) and a visible color channel

for spatial orientation of the NIR signal. The overall design and integration of these systems has been previously reported.[214], [215] A laser power of 80 mW at 785 nm was used for wavelength-resolved (800-950 nm) and widefield imaging.

After FIGS, all mice were necropsied. The pancreas was removed *en bloc* to preserve the anatomical integrity of the primary, stromal, and healthy tissues for fluorescence imaging and histological sectioning. Dissected organs were imaged on a Pearl Trilogy small animal imaging system (LI-COR Biosciences, Lincoln, NE, USA). The fluorescence intensity of each organ was collected with the 800 nm channel and analyzed by Image Studio Ver. 5.0 software (LI-COR Biosciences, Lincoln, NE, USA). The periphery of each organ was identified free-handed to define the region of interest (ROI). Average pixel intensity was used to calculate signal to noise ratio (SNR), which is defined by average tissue intensity per pixel in an ROI/standard deviation of background ROI. Fluorescence intensity plots of representative pancreases were analyzed with ImageJ 1.49v software (National Institutes of Health, Bethesda, MD, USA). To compare against the spectroscopic analysis of each pancreas that was obtained during surgery, a straight line was drawn longitudinally across the pancreas to include as many acquisition points as possible after whole pancreas imaging. The NIR fluorescence intensity along the line was quantified with the *plot profile* function in ImageJ.

2.2.8 Histological analysis Tumor tissue and organs of metastatic interest were embedded in OCT mounting media gel and were frozen rapidly in liquid nitrogen. Pancreatic tissue was positioned to obtain a maximal footprint for both diseased and healthy pancreases. These samples were cut using Cryostat (Leica Biosciences, Buffalo Grove, IL, USA) at a thickness of 8 μm . Sections from each mouse were stained with

hematoxylin and eosin (H&E) or left unstained for NIR fluorescence microscopy. Representative slides were imaged with an IX73 Inverted Microscope with a xenon excitation source and captured with a DP80 Digital Camera and displayed by CellSens Dimension 1.13 software (all from Olympus, Japan). H&E stained slides were visualized and imaged with a bright-field filter, unstained slides were imaged for autofluorescence with a FITC filter cube, and NIR fluorescence with an ICG filter cube. Exposure time of ICG and NanoICG were constant throughout all the samples.

2.2.9 *In vivo* toxicology To evaluate the systemic toxicity of NanoICG, 15 mature C57BL/6J mice were divided into vehicle control group, low dose group (equivalent to 10 nmol of ICG per mouse) and high dose group (equivalent to 51.6 nmol of ICG per mouse) (5 mice each group). High dose was calculated based of FDA recommended upper limit dosage of ICG. The mice were treated correspondingly by *i.v.* injection. 72 h after the injection, whole blood was collected into lithium heparin coated blood collection tubes (BD Vacutainer, Franklin Lakes, NJ, USA) and K₂EDTA coated blood collection tubes (BD Microtainer, Franklin Lakes, NJ, USA) by heart puncture. Comprehensive diagnostic profile of the blood samples were determined by chemistry analyzer (Abaxis, Union City, CA, USA) and complete blood count was determined by hematology analyzer (Abaxis, Union City, CA, USA). Livers, lungs, spleens and kidneys were collected, fixed, sectioned and HE-stained for pathological examination.

2.2.10 Statistical analysis Data was analyzed in Prism 7 software (Graphpad, La Jolla, CA, USA). Cytotoxicity was analyzed using 2-way ANOVA with Tukey's multiple comparisons test; chemotaxis and phagocytosis were analyzed using a 1-way ANOVA and

Tukey's multiple comparisons test; biodistribution was analyzed using multiple t tests. *In vivo* toxicity was analyzed with Kruskal-Wallis test. All data is shown as Mean \pm Standard Deviation (SD).

2.3 RESULTS

2.3.1 Characterization of NanoICG The number mean hydrodynamic diameter of NanoICG was 70.96 ± 13.63 nm with the average polydispersity index of 0.240 ± 0.017 ($n = 6$). The average zeta-potential of NanoICG was (-21.4 ± 0.289) mV. According to TEM image (Figure 1B), the average diameter of spherically shaped NanoICG is around 40 nm. Absorption spectra for intact NanoICG was indicative of ICG being tightly packed within amphiphilic HA (Figure 3C). In comparison, dissolved ICG and disassembled NanoICG (in 50/50 DMSO/H₂O), has strong NIR absorbance around 785 nm, 6-fold higher than NanoICG at the same wavelength. Correspondingly, fluorescence emission is minimized (5-fold lower) due to packing of ICG and is indicative of ICG entrapment in the self-assembled NP (Figure 3D), which is consistent with previous reports by us and others.[211], [216] The quenched fluorescence of NanoICG becomes activated in serum and tissue interaction due to nonspecific interaction with protein hydrophobic domains.[206]

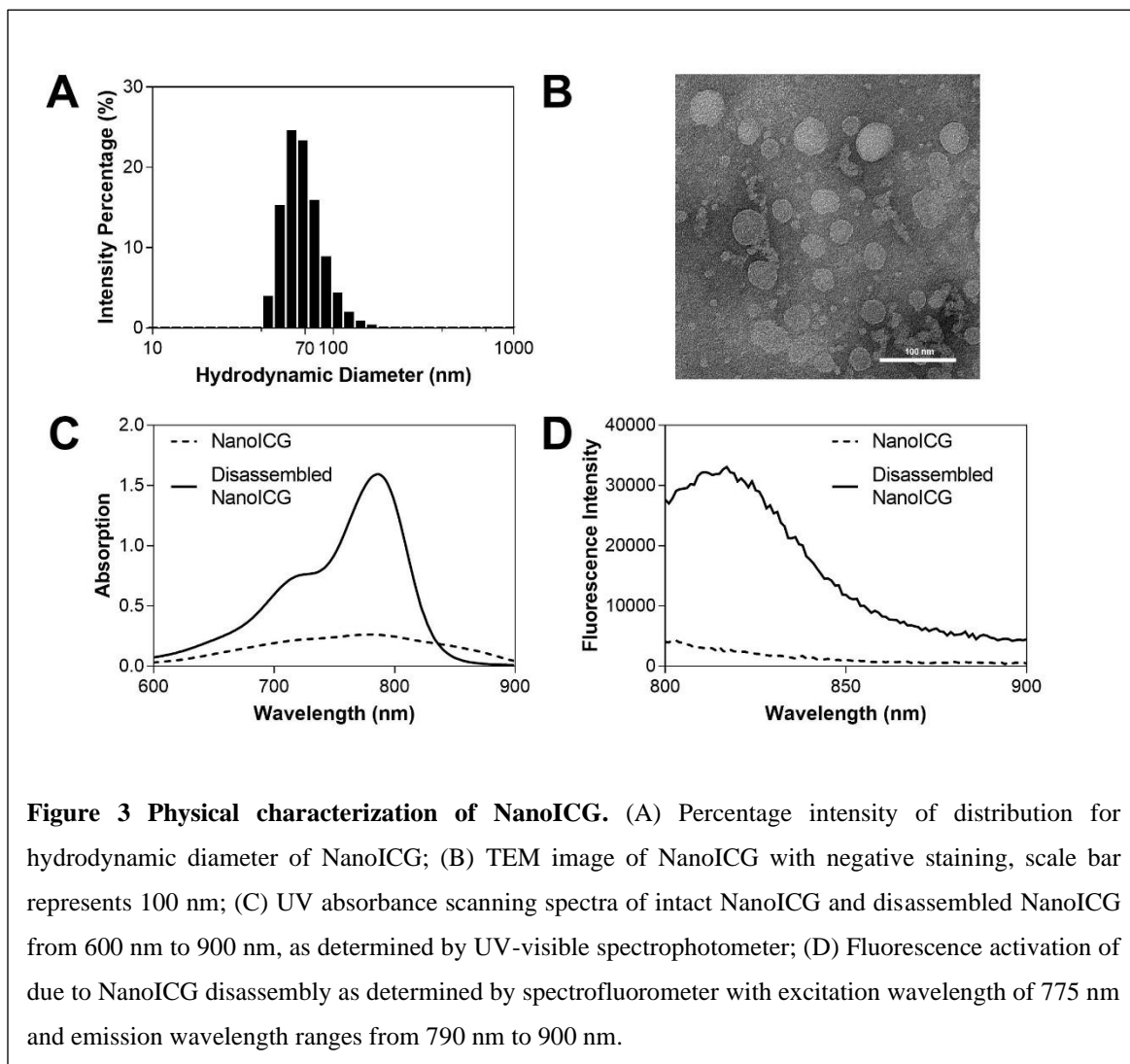
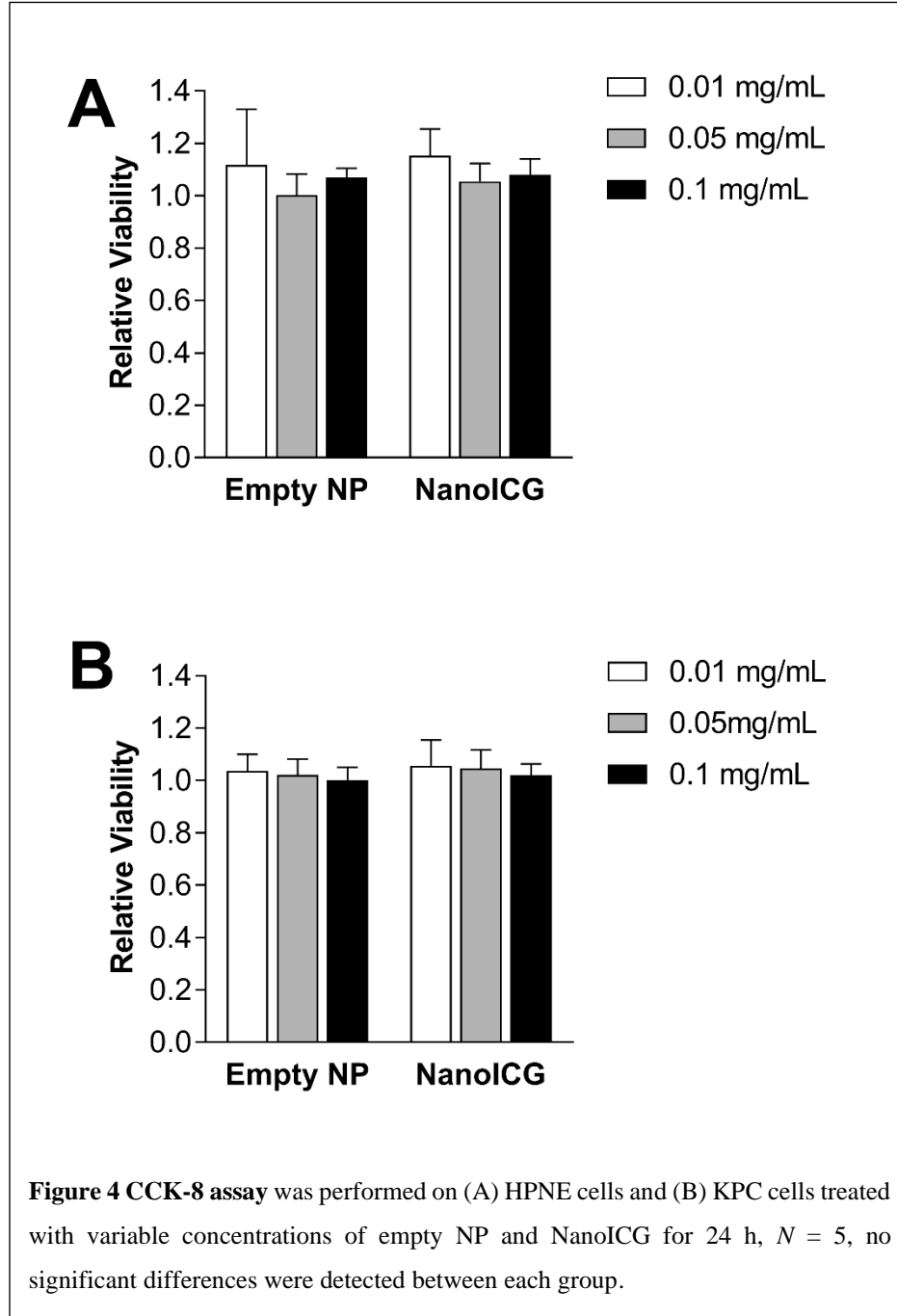


Figure 3 Physical characterization of NanoICG. (A) Percentage intensity of distribution for hydrodynamic diameter of NanoICG; (B) TEM image of NanoICG with negative staining, scale bar represents 100 nm; (C) UV absorbance scanning spectra of intact NanoICG and disassembled NanoICG from 600 nm to 900 nm, as determined by UV-visible spectrophotometer; (D) Fluorescence activation of due to NanoICG disassembly as determined by spectrofluorometer with excitation wavelength of 775 nm and emission wavelength ranges from 790 nm to 900 nm.

2.3.2 Cytotoxicity The relative viability of HPNE and KPC cells were calculated by normalizing to untreated cells. Overall, the relative viability of HPNE and KPC cells, which were treated with empty NP and NanoICG, was close to 1. No significant differences were observed between 0.1, 0.01 and 0.001 mg/mL (**Figure 4**). Additionally, no significant difference was detected between empty NP and NanoICG. Empty NP and NanoICG did not impair the metabolic activity of healthy pancreatic epithelial cells.



2.3.3 Chemotaxis There was a 6.79-fold induction of chemotaxis towards complete medium (positive control) as compared to PBS. In contrast, ICG, NanoICG and empty NP ($p < 0.0001$) showed relative values (as compared to PBS) of 0.63 ± 0.02 for $10 \times$ TPC of

ICG, 0.63 ± 0.04 for $10 \times$ TPC of NanoICG and 0.60 ± 0.01 for $10 \times$ TPC of empty NP ($n = 3$) (**Figure 5A**). The lowest concentration ($1/25 \times$ TPC) of ICG, NanoICG and empty NP showed relative chemotaxis induction (as compared to PBS) of 0.85 ± 0.02 , 0.87 ± 0.03 , and 0.81 ± 0.01 times, respectively ($n = 3$). These results demonstrate that NanoICG and empty NP have no significant chemoattractant properties.

2.3.4 Phagocytosis HL-60 displayed low phagocytic activity toward PBS, ICG, NanoICG, and empty NP, regardless of test sample concentrations (**Figure 5B**). In comparison, zymosan A was internalized to a significantly higher extent ($p < 0.0001$), with AUC values 1.87, 1.83 and 1.93 times higher than $10 \times$ TPC for ICG, NanoICG and empty NP, respectively. There was no significant effect of $10 \times$ TPC of ICG, NanoICG and empty NP on phagocytosis as compared to PBS [1.03 ± 0.02 , 1.03 ± 0.01 and 1.00 ± 0.01 respectively. ($n = 6$)].

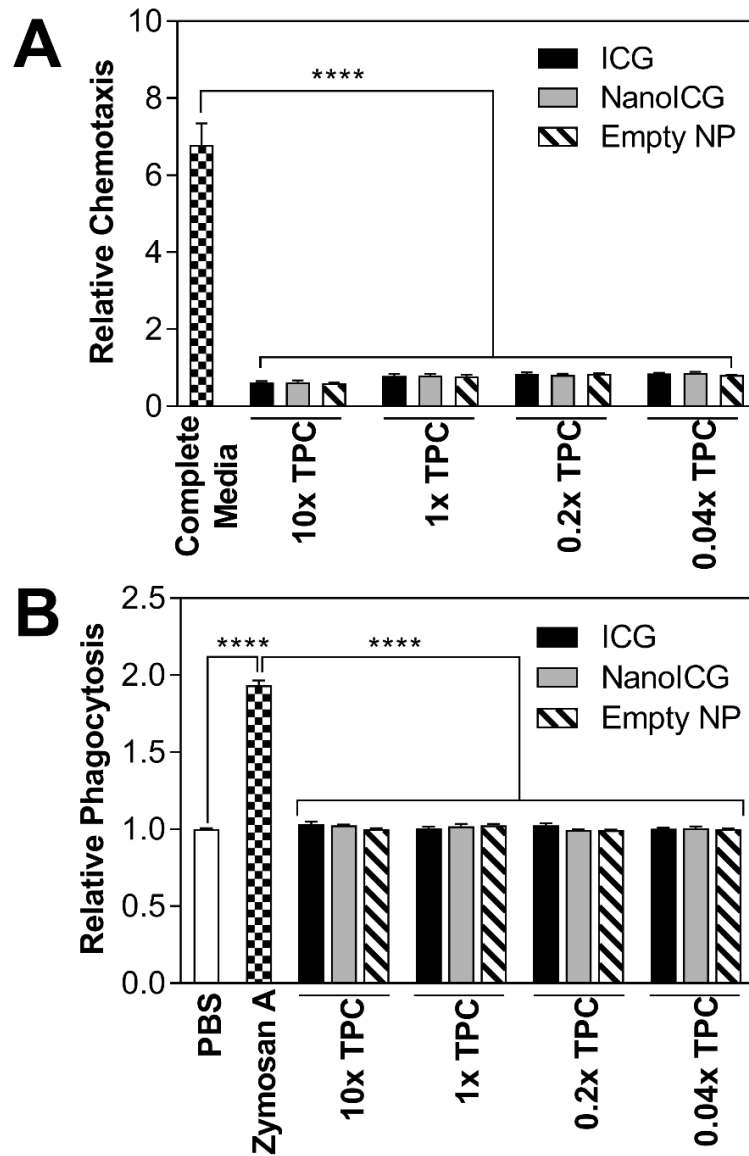


Figure 5 Chemotaxis and phagocytic assay. (A) Chemotaxis assay of HL-60 with ICG, NanoICG and empty NP at varied concentrations based of theoretical plasma concentration (TPC) at 4 h time point. Complete medium is IMDM with 20% FBS. Fluorescent spectra of calcein AM was collected at 485 nm excitation/535 nm emission; (B) Phagocytic assay of NanoICG in HL-60. Zymosan A served as the positive control while PBS was the negative control. Luminescence reading was monitored for 1.5 h with 2.1 min intervals and AUC of fluorescent signal was quantified as chemotactic response. **** $p < 0.0001$.

2.3.5 Detection of ICG and NanoICG in tumor-bearing mice with IGS

ICG and NanoICG were examined for suitability for IGS as schematically depicted in Figure 5A. Intraoperative imaging demonstrated that NanoICG and ICG could both be detected by IGS in pancreatic tumors; however, NanoICG resulted in more complete and intense enhancement of the tumor when compared to ICG under identical experimental conditions (both were excited with 80 mW power at a constant distance from the tumor) (**Figure 6, bottom**). Spectra collected from these regions are in close agreement with the NIR fluorescence detected in wide-field imaging channel, indicating stronger NIR fluorescence in mice injected with NanoICG (**Figure 6, middle**); at the peak emission wavelength of 814 nm, the fluorescent signal of NanoICG treated pancreatic tumor is 2.03 times of that in ICG group. The IGS images demonstrated an improved contrast profile with NanoICG in orthotopic PDAC detection.

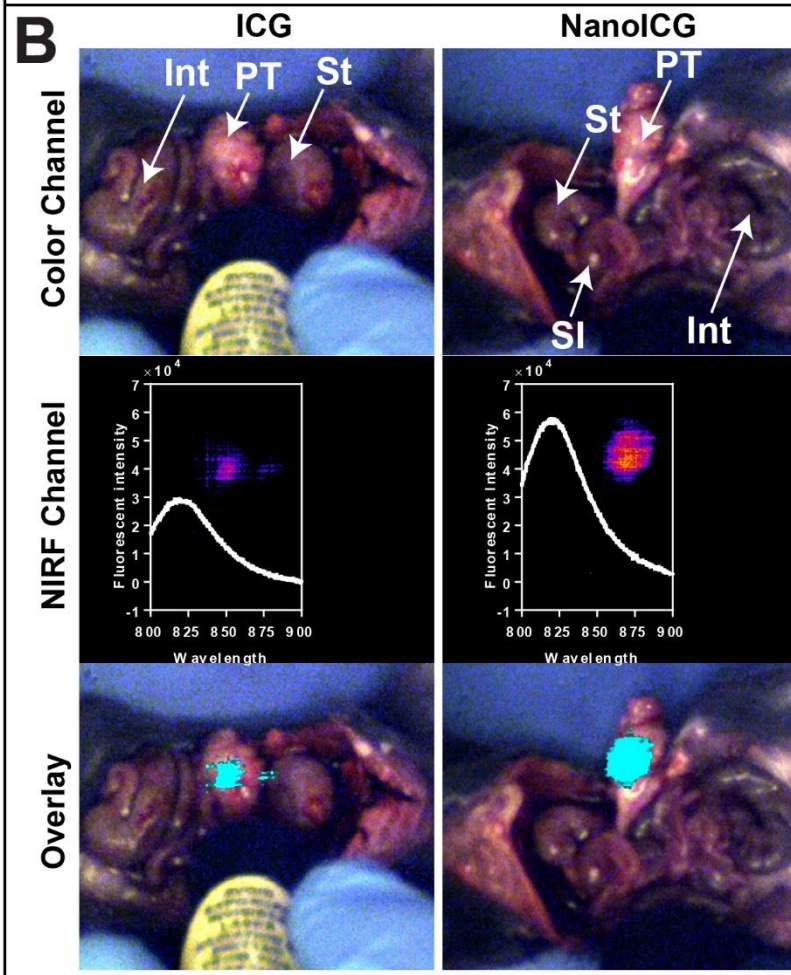
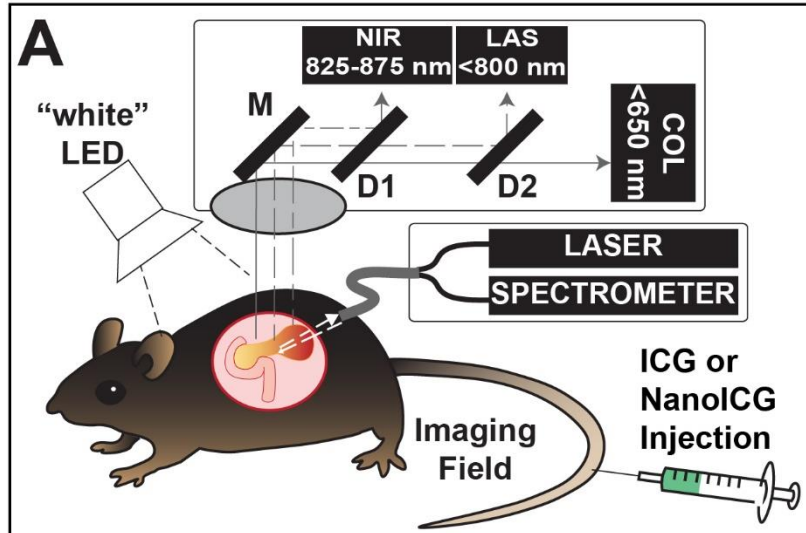
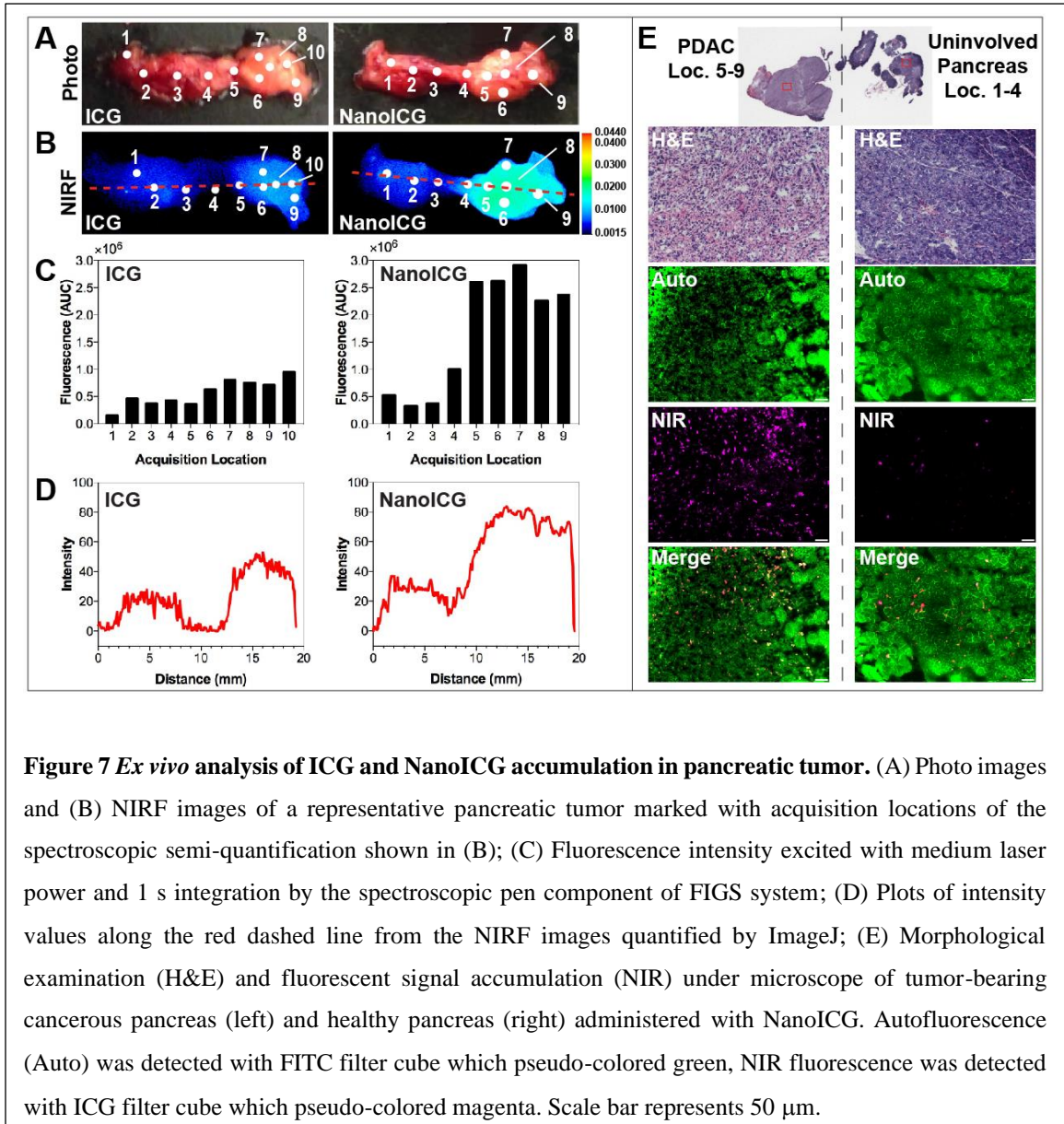


Figure 6 Schematic of FIGS and Surgical Navigation of PDAC with NanoICG. (A) Schematic of the image-guided surgery system utilized to detect orthotopic PDAC. As described in the text, the system utilizes both wavelength-resolved NIR spectroscopic measurements and a wide-field, multi-detector video camera for real-time surgical guidance that uses the hand-held spectroscopic pen as an excitation source. (B) Images from surgical navigation of pancreatic tumor contrast-enhanced with ICG (left) or NanoICG (right) 24 h post *i.v.* injection. Livers and spleens were removed due to high background signal from ICG clearance. Int = large intestine, PT = pancreatic tumor, St = stomach, SI = small intestine; (Top) Color images show orthotopic PDAC and the location of the handheld spectroscopic pen, which provides NIR spectral information and serves as an excitation source for a widefield imaging system. (Middle) Pseudo-colored signal in the NIR channel of the widefield imaging system and the spectroscopic signal from within the contrast-enhanced region; (Bottom) NIR signal overlaid (cyan) onto the color image shows robust enhancement of syngeneic, orthotopic pancreatic cancer. Contrast enhancement can be observed with both ICG and NanoICG, with NanoICG having stronger signal (see inset middle row).

2.3.6 *Ex vivo* analysis of fluorescence accumulation of pancreatic tumor

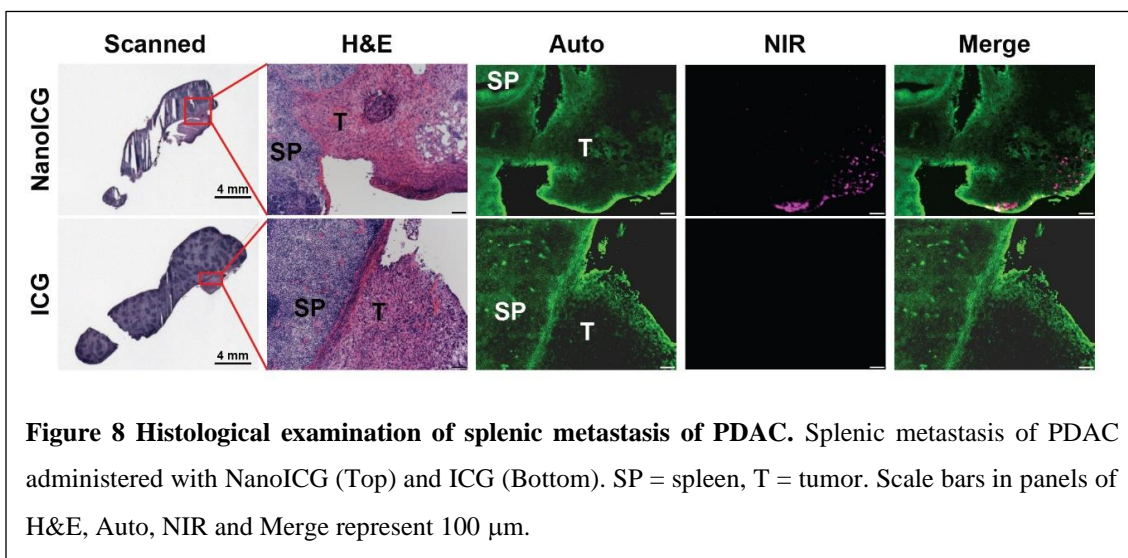
NIRF images of the pancreas showed higher accumulation of fluorescent signal in the tumor portion of NanoICG treated pancreas compared with that of ICG, as shown in **Figure 7B** (7A is a bright field photograph of the pancreas for spatial reference). **Figure 7C** shows the quantified fluorescence intensity from the spectroscopic pen at acquisition locations across the pancreas to determine the NIR signal and tumor contrast. Spots in the pancreatic tail, which correspond to the location where the KPC PDAC cells were implanted, were brighter compared with the head and body. The point spectroscopic measurements were consistent to whole pancreas NIR images as shown in **Figure 7D**, where a line was drawn across the pancreas image to obtain as many data points as possible from non- and contrast-enhanced regions, which depicted healthy tissue and PDAC, respectively. The average fluorescent intensities of the healthy and tumor portions of the pancreas were 0.35 ± 0.12 AU and 0.77 ± 0.12 AU, respectively, for ICG. In comparison, the average fluorescence

intensity of the healthy and tumor portions were 0.41 ± 0.10 AU and 2.30 ± 0.67 AU, respectively, for NanoICG. The average fold-increases of the tumor portion of the pancreas compared with the healthy portion of the pancreas were 2.20 and 5.61 for ICG and NanoICG, respectively.



During sectioning, the surfaces of the solid tumors were visually observed to be light yellow in color, which is indicative of a high-degree fibrosis [217]. H&E stained tumor slides displayed characteristic poorly differentiated adenocarcinoma with high stroma content (**Figure 7E**, *left*). Normal pancreatic morphology was shown in a slide from benign pancreatic tissue (**Figure 7E**, *right*). A higher level of NIRF signal was observed throughout the tumor portion of pancreas treated with NanoICG compared with those treated with ICG (**Figure 7E**).

The borders of splenic metastasis and healthy spleen tissue were identified by H&E



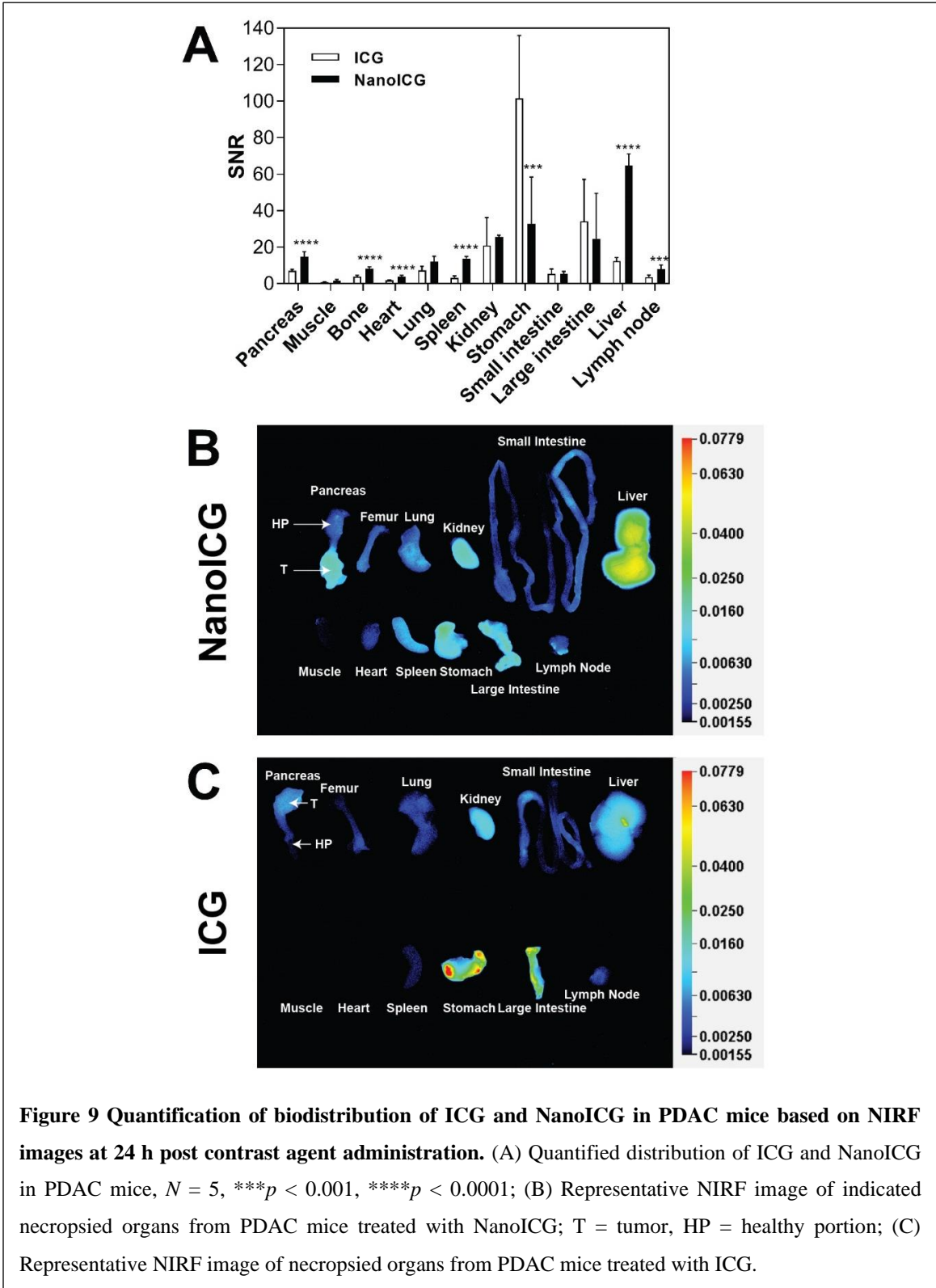
stained slides as shown in **Figure 8**. Fluorescent signal was detected along the borderline of tumor in the NanoICG treated group but not in the ICG treated group.

2.3.7 Relative biodistribution of ICG and NanoICG in PDAC

The fluorescence intensity of ICG and NanoICG was evaluated among organs harvested from the mice with the orthotopic PDAC model. Overall, higher SNR signal was observed in pancreas in the NanoICG-treated group compared with ICG-treated group with $p < 0.0001$ (**Figure 9A**). Between organs, significantly higher signals were seen in the liver, spleen, pancreas, bone, heart and lymph node in the NanoICG treated group, which were 5.3, 4.4,

2.1, 2.1, 2.3, 2.2-fold higher compared with ICG treated group respectively. On the other hand, ICG displayed a great propensity to be cleared by the GI tract as determined by semi-

quantified NIRF images (**Figure 9C**), whereas for NanoICG, increased liver and spleen signal, suggestive of RES clearance (**Figure 9B**).



2.3.8 *In vivo* toxicology to make a comparative study on the potential toxic effect of NanoICG on the treated mice, we carried out blood biochemistry and hematology analysis. **Figure 10** shows the levels of standard hematological markers, such as white blood cell (WBC), red blood cell (RBC), hemoglobin (HGB), hematocrit (HCT) and platelet (PLT); The WBC is sensitive to the physiological response, the mean value of vehicle control was in the normal range. There is a slight decrease in the number of WBC for NanoICG-treated groups, but this decrease is not significantly different, and close to the anticipated value provided by the animal supplier [50]. All the other parameters in the NanoICG-treated groups appear to be normal compared with the control group, and be within the normal ranges. In addition, we present the biochemistry results of the mice including albumin (ALB), alkaline phosphatase (ALP), alanine aminotransferase (ALT), amylase (AMY), blood urea nitrogen (BUN), total protein (TP) and globulin (GLOB). Fluctuation was observed in ALP, ALT and GLOB for NanoICG-treated group compared with vehicle control, but still remained within the normal ranges; no difference was observed between NanoICG doses or with the vehicle control. The results of blood biochemistry and hematology analysis suggest no obvious toxicity even with upper limit dose of NanoICG.

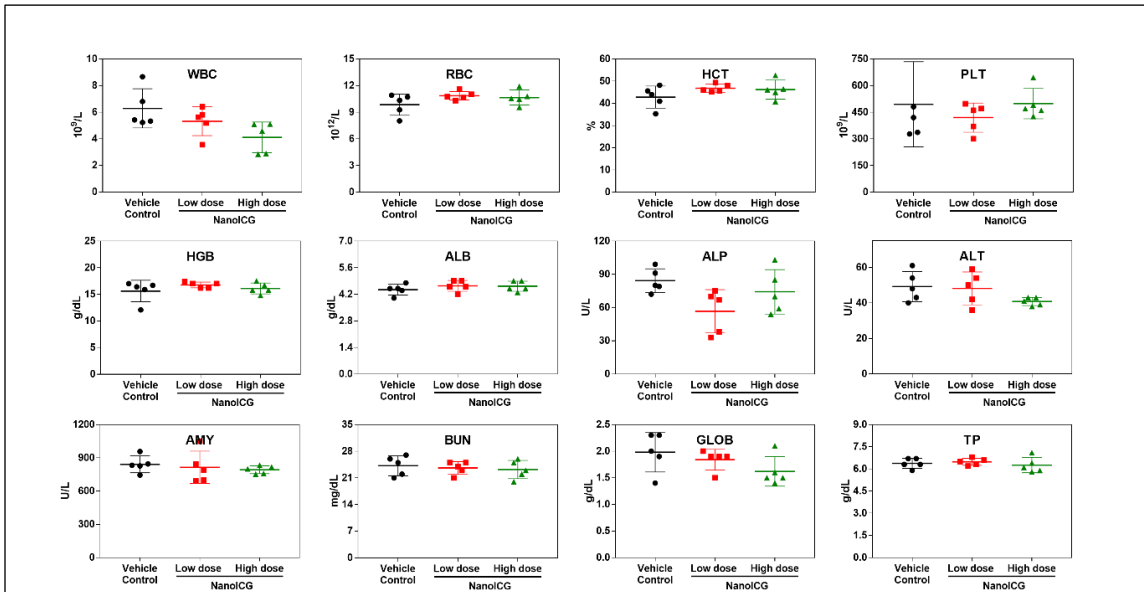
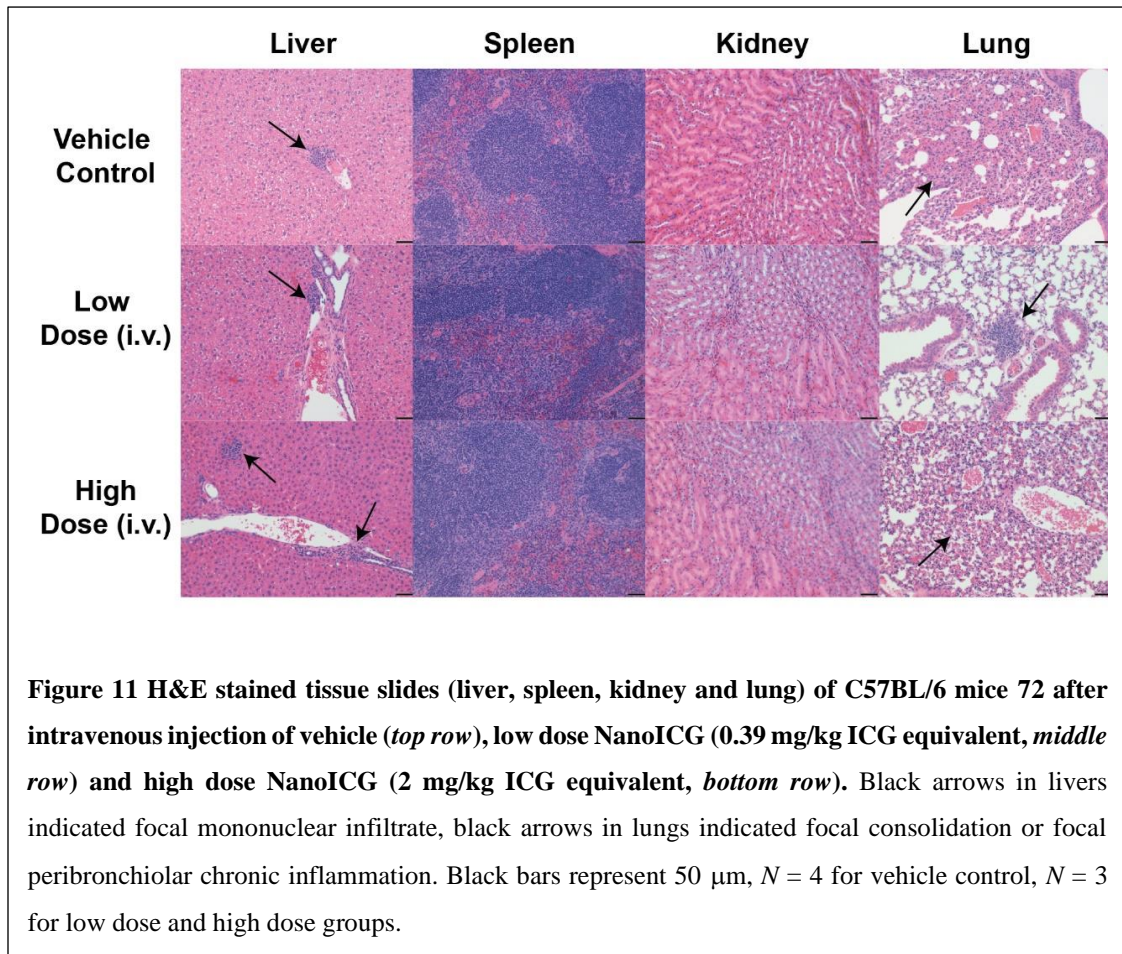


Figure 10 Hematology and blood biochemistry assessments of the vehicle (black), low dose (0.39 mg/kg ICG equivalent, red) and high dose (2 mg/kg ICG equivalent, green) of NanoICG treated mice 72 h after intravenous injection. The results show mean and standard deviation of white blood cells (WBC), red blood cells (RBC), hemoglobin (HGB), hematocrit (HCT), platelet (PLT), albumin (ALB), alkaline phosphatase (ALP), alanine aminotransferase (ALT), amylase (AMY), blood urea nitrogen (BUN), total protein (TP), globulin (GLOB). $N = 5$.

To further investigate the *in vivo* toxicity of NanoICG, histological analysis of major organs including liver, spleen, lung and kidney were performed 72 h after intravenous administration of different doses of NanoICG, examined by board-certified pathologist (SMC), and the results are shown in **Figure 11**. The spleens from all animals were normal. This indicates that there was no overall effect on the immune system as there was excellent preservation of the lymphoid white pulp of the spleen. The kidneys showed no evidence of toxicity, either in the glomeruli, tubules, papilla, vessels, or pelvis. Thus, there is no evidence of nephrotoxicity. In the livers, there were occasional animals with focal mononuclear infiltrate (as indicated by the black arrows), but this was not associated with any evidence of necrosis or regeneration. There was no consistent zonal area involved. There was only 1 animal in the vehicle control group with this finding, none in the low

dose group, and 2 of the 3 animals in the high dose group had this finding. Thus, this may reflect a low level of hepatotoxicity. However, these results contradict biochemical analysis that had normal levels of ALT and AST for the vehicle control, low dose, and high dose of NanoICG (**Figure 10**). In the lung, there was 1 animal in the vehicle control group that showed focal consolidation of the alveoli without inflammation, 1 animal in the low dose group that showed focal peribronchiolar chronic inflammation, and 1 animal in the high dose group that also showed focal alveolar focal peribronchiolar and alveolar inflammation (as indicated by black arrows). It is most likely that these lung changes reflect the intravenous administration of the material and not related to the material that was injected.



2.4 Discussion

The formulation of HA-derived NPs has advantages, most notably overcoming poor aqueous solubility of therapeutic or imaging agents [218]. Second, HA-derived NPs exhibit prolonged circulation and low toxicity to healthy tissues [219]–[221]. Third, the possibility of tumor targeting, including by specific binding of CD44 [222] and through the enhanced permeability and retention (EPR) [218] effect, makes it promising for cancer imaging and therapy. In this study, HA polymers were conjugated with PBA to obtain amphiphilic HA, which readily entrapped amphiphilic ICG in aqueous solution. By incorporating ICG into an HA-derived NP contrast agent, ICG accumulation in tumor was increased (**Figure 6, 7 and 9**), potentially due to the so-called EPR effect [218], [223], while mitigating potential toxicity from the innate immune system (**Figure 5**).

Overcoming the immune system barrier is a key step for targeted delivery of contrast agents. Gallagher *et al.* reported that HL-60 cells exhibited responsiveness to chemoattractant and phagocytic activity that were commensurate with the proportion of mature granulocytes [224]. Others have reported that HA species of molecular weights from 792 to 3×10^6 Da all stimulated phagocytic and chemotactic function of polymorphonuclear leukocytes, and, 10 kDa HA was reported as a potent stimulator of the innate immune system [225], [226]. However, for HA derived nanosystems, different molecular weight of HA modified liposomes did not cause complement or macrophage activation [227]. In the *in vitro* studies reported here, no significant immunotoxicity was observed except a slight inverse dose-dependency in chemoattractant potential of test samples. The possible explanation is that the volume ratio of SM, a potent chemoattractant for HL-60, increased proportionally as test samples were diluted.

Contrast enhancement within whole pancreas was observed both in ICG and NanoICG treated groups (**Figure 7, 9**). ICG is a small, amphiphilic dye molecule. After injection, ICG is bound immediately with albumin and other serum proteins and then liberated into liver and cleared out in bile resulting in a half-life of less than 20 min in healthy humans [223]. NIR images of S-180 tumor were reported with obvious contrast 2 h to 48 h post ICG injection, likely from the EPR effect of ICG bound albumin [223]. In Figure 4B, a slight accumulation of ICG was observed in pancreatic tumor, which is comparable to mice with S-180 tumors [223]. In comparison, a more apparent contrast enhancement between healthy and diseased portions of pancreas was observed in NanoICG recipients (Figure 5B). Qhattal and colleagues [228] reported that tumor targeting benefited extensively from long systemic circulation of nanosystems, while Han *et al.* [229] assert that HA performs like PEG by increasing plasma half-life while displaying limited immunotoxicity. Thus, accumulation of NanoICG in tumor could be due to prolonged circulation of HA based nanosystems.

Bouvet *et al.* reported that metastatic lesions of an orthotopic pancreatic cancer model were detected in spleen, bowel, and omentum, as visualized by implanting GFP transfected BxPC-3 cells. By inspecting intravitaly, tumor and metastatic area were quantified for growth monitoring [230]. Wang *et al.* [196] reported a dual optical and MR imaging agent, denoted by Cy5.5-ATF-IO, was able to detect intraperitoneal metastatic lesions of PDAC as small as 0.5 mm^3 in optical NIR imaging. Furthermore, optical NIR imaging could detect as little as 1×10^4 tumor cells, which was 1/10 of that which can be detected by MRI [196]. Another study showed that CA19-9 conjugated AlexaFluor488 were potent at detecting micrometastases of PDAC including splenic, peritoneal and liver

[192]. In this study, microscopic lesions of splenic metastasis were obviously visualized by NanoICG (**Figure 8**) and mostly accumulated at the lesion periphery.

An important limitation for targeted delivery of HA-decorated NP is preferential uptake by RES system [218]. On one hand, it has been empirically shown that NPs with size less than 100 nm, neutral or anionic charge, and lower complement binding can avoid RES uptake after *i.v.* administration [227]. Additionally, Qhattal *et al.* found that high molecular weight (HMW) HA grafted liposomes were cleared much faster than low MW HA [228], because HMW HA had a higher affinity with HARE or LYVE-1, which were widely expressed in normal sinusoidal endothelial cells of the liver, spleen, and activated tissue macrophages [231]. Consequently, NPs that derived with 10 kDa HA could accumulate to a lower degree in liver in that scenario. However, in **Figure 9A**, NanoICG displayed marked accumulation in liver and spleen ($p < 0.0001$) compared with ICG, which was indicative of increased RES uptake. Further studies are ongoing to determine an optimized HA MW for formulation of NanoICG for pancreatic tumor delivery balanced with minimized RES uptake.

Endogenous HA may play an important role in the biology of pancreatic cancer [232], as expression of high and low molecular weight forms of HA have been reported to inhibit or enhance malignant properties of pancreatic cancer cells in experimental models. Careful analysis of human samples suggests that HA is expressed by greater than 85% of human pancreatic cancers [233]. However, its expression is not correlated with improved or worse outcome in humans. HA is also the target of therapeutic approaches in which its targeted degradation by PEGylated hyaluronidase is used to improve drug delivery [234], or alternatively, HA complexes are being developed as drug delivery agents [235], [236].

Taken together, our results presented here and the existing and emerging literature strongly support further investigation into the biology and use of HA as delivery vehicle and/or a targeting agent in pancreatic cancer.

In terms of *in vivo* safety, results from healthy C57BL/6J mice after vehicle or one of two NanoICG doses were in concordance with others. For example, HA-derived amphiphilic polymers were reported to demonstrate a protective effect against cisplatin or doxorubicin-induced hepatotoxicity and nephrotoxicity [237], [238], which demonstrates that the self-assembled drug carriers-constructed by HA conjugated hydrophobic moiety-are effective at reducing systemic toxicities. On the other hand, Rao *et al.* reported that HA-derived nanocarriers can control the release of drug payload, depending on the reversible interaction of HA-containing carriers and drugs [239]. This is consistent with the recent results of Hill *et al.*, which showed controlled dye release rate from amphiphilic HA nanostructures. Accordingly, we hypothesize that negligible toxicity from NanoICG could be due to a combination of several factors: imaging agent was administered with singular and low dose; ICG was entrapped in a stable state through π - π stacking with PBA [211], which could affect ICG release, and released ICG is an FDA-approved medical diagnostic agent with low inherent toxicity.

NanoICG, an HA-derived NP that physico-chemically entraps ICG, displayed a nontoxic safety profile *in vitro* and *in vivo* and provided significant NIR signal for guidance for intraoperative detection of PDAC *in vivo*. The fluorescence intensity of NanoICG was higher compared to ICG both in pancreas and splenic metastasis, which was confirmed by NIRF imaging, FIGS and microscopic analysis. In conclusion, NanoICG exhibited improved efficacy at detecting pancreatic tumors in an orthotopic pancreatic cancer model

with negligible NP-derived toxicity, suggesting that NanoICG is a promising potential contrast agent for guiding pancreatic tumor removal.

CHAPTER 3: TUNED NEAR INFRARED FLUORESCENT HYALURONIC ACID CONJUGATES FOR DELIVERY TO PANCREATIC CANCER FOR INTRAOPERATIVE IMAGING

3.1 Introduction

Surgical resection remains a promising treatment for improving prognosis of cancer patients as it is potentially curative for primary tumors and local metastases [240]. Currently, surgery is performed without contrast-enhanced image guidance to identify tumor margins and small occult metastases due to the absence of clinically available optical contrast agents [92], [187], [188]. Contrast-enhanced optical imaging could provide real-time guidance during tumor resection with highly sensitive, rapid, and non-radioactive NIRF tracers to highlight the areas of extension of the malignancy [241]. NIRF is promising for *in vivo* optical imaging due the relative biological transparency at wavelengths between 700 nm and 1000 nm [92], [242], [243]. To date, however, FIGS of tumors has not reached its full potential, in part due to contrast agents lacking high intensity, water solubility, biocompatibility, and tissue-specific targetability [244].

Attaining high contrast-to-noise ratio (CNR: signal in region of interest relative to neighboring region) and signal-to-noise ratio (SNR: signal in the region of interest relative to background noise) is important for specific visual guidance of tumor detection and removal. Sufficient CNR and SNR are achieved primarily if specific binding of the fluorophore to the target tissue occurs, while unbound fluorophore is rapidly cleared from the background tissue [245]. Nevertheless, most dyes are not tumor-specific and *in vivo*

performance can be complicated by non-specific biological interaction, *e.g.* membranes, pharmacokinetic process including absorption, distribution, metabolism and excretion, and optical properties of the dye and tissue [246]. For instance, cyanine-based NIRF probes with hydrophobic core structures and high surface charge bind to plasma proteins, which results in RES organ sequestration and hepatobiliary clearance *in vivo*, which can compromise tumor contrast.[247]–[250] Useful strategies for improving CNR and SNR include, among others, utilizing tumor or tumor microenvironment specific biomarkers [246] and altering excretion from the liver (hepatobiliary) to the kidneys (urinary) [145], [251], [252]. Pancreatic cancer CNR was found to be significantly increased by targeting somatostatin [253], [254] or tumor cell antigens [255] or utilizing cell-penetrating peptides [117] for tumor-specific enhancement. Reported by Choi *et al.* [242], [243], [247], [250], improved tumor SNR was achieved by using zwitterionic fluorophores, which increased renal filtration and reduced overall background. Hence, we hypothesize that optimized pancreatic tumor contrast could be achieved by combining tumor-specific targeting and facilitating minimized intraperitoneal organ accumulation.

Previously, we reported the development of tumor-selective delivery of the FDA-approved NIR fluorophore, ICG, by physically entrapping the dye in HA-derived nanoformulations, termed NanoICG, in models of breast, prostate, and pancreatic cancer [206], [211], [256], [257]. NanoICG resulted in significant pancreatic cancer contrast relative to a muscle reference and uninvolved pancreas, but also gave rise to strong signal in intraperitoneal organs, especially the liver and spleen [256]. To maximize PDAC contrast enhancement and to minimize RES capture, we now specifically examine the role of HA molecular weight and NIRF dye properties. Compared to our previous study of using

hydrophobically-modified HA to drive NP self-assembly and physicochemical entrapment of dye, two dyes, Cy7.5 (relatively hydrophobic) and IRDye800 (hydrophilic dye), are directly conjugated to HA of three different molecular weights (MW_N), including $MW_N = 5, 20, \text{ and } 100$ kDa. The effects of HA MW_N and physiological properties of NIR dyes on tumor specificity and biodistribution were investigated to determine a lead agent for PDAC enhancement in minimized RES uptake. These select agents would ideally be useful for detection of intraperitoneal metastatic pancreatic cancer or other tumor types that required surgical intervention in the abdominal cavity.

3.2 Methods

3.2.1 Materials Cy7.5 amine was purchased from Lumiprobe (Hallandale Beach, FL); IRDye800CW trifluoroethylamine was purchased from LI-COR (Lincoln, NE); 5 kDa, 20-30 kDa, and 100 kDa sodium hyaluronate were purchased from Lifecore Biomedical (Chaska, MN). Lyophilized powder of bovine serum albumin (BSA) was purchased from Sigma (St Louis, MO). Sephadex G-25 PD-10 desalting column was purchased from GE Healthcare (Pittsburgh, PA); KPC cells were obtained from the diseased pancreas of LSL-Kras^{G12D/+}; LSL-Trp53^{R172H/+}; Pdx-1Cre (KPC) mice which were shared by Dr. Hollingsworth. 10-week-old female C57BL/6J mice were purchased from Jackson Laboratories (Bar Harbor, ME). 5.0 chromic gut and 5.0 nylon surgical sutures were purchased from Johnson & Johnson (Somerville, NJ). FITC-labeled CD44 antibody, purified rat mouse BD Fc blocker, propidium iodide (PI) staining solution and flow cytometry (FC) staining buffer was purchased from BD Bioscience (San Jose, CA). All other chemicals were purchased from Fisher Scientific and used at analytical grade.

3.2.2 Conjugation and characterization of Cy7.5 or IRDye800 HA

Conjugates. Sodium hyaluronate (3.3-6.9 mg, $MW_N = 5$ kDa; 9.5-10.7 mg, $MW_N = 20$ -30 kDa; 10.2-12.7 mg, $MW_N = 100$ kDa) were completely dissolved in 2 mL of water. 1-Ethyl-3-(3-dimethylaminopropyl)-carbodiimide (EDC) and N-hydroxysuccinimide (NHS) (both 10× molar ratio to amine group), were then dissolved in the HA solution. After 15 min of activation, the pH was raised to 7.2, and Cy7.5-NH₂ (dissolved in DMSO) or IRDye800-NH₂ (dissolved in ultrapure water) – both at 3× molar ratio to disaccharide units per HA_{5k} and HA_{20k} chain and 9× for HA_{100k} chain – were each added dropwise to each of the activated HA solutions under constant stirring. The reaction was allowed to stir for 24 h at room temperature (rt). The reaction contents were then transferred to dialysis tubing (MWCO = 3500 Da for HA_{20k}- and HA_{100k}-dye conjugates; MWCO = 1000 Da for HA_{5k}-dye conjugates, Spectrum Laboratories, Rancho Dominguez, CA): HA-Cy7.5 conjugates were dialyzed against 1:1 EtOH:H₂O for 24 h followed by H₂O for an additional 48 h. HA-IRDye800 conjugates were dialyzed against H₂O for 24 h. The HA-dye conjugates were removed from the dialysis tubing, purified by PD-10 column, followed by lyophilization, and storage at -20 °C. Dye content and overall HA-dye conjugate optical properties were determined relative to dye solutions using absorbance and fluorescence spectroscopy. Specifically, an Evolution 220 spectrophotometer (Thermo Fisher Scientific, Madison, WI) was used for scanning absorbance spectra (600-900 nm) and a FluoroMax-4 spectrofluorometer (Horiba, Edison, NJ) was used for quantifying fluorescent intensity of dye, HA-dye, disassembled and BSA-associated HA-dye.

3.2.3 Determination of nonspecific serum protein binding. 50 μM bovine

serum albumin (BSA; Sigma-Aldrich, MO) was incubated with HA_{20k}-Cy7.5/IRDye800 (4

μM dye equivalent) in phosphate buffer (0.01 M, pH 7.4) for 1 h at rt. 1 mL of mixture or corresponding control was filtered through 0.22 μm filter before loading onto an AKTA Pure 25 L Chromatography system (GE Healthcare, Sweden) that was equipped with Superdex200 Increase 10/300 GL column, UV monitor (fixed wavelength at 280 nm), and a fraction collector. For kinetic fluorescence measurements, an outlet portal was connected to micro cuvette (Starna, Atascadero, CA) for monitoring the fluorescence of elution using the fluorescence spectrophotometer. Sample was eluted at flow rate of 0.45 ml/min and elution time period was 60 min. Kinetic monitoring of fluorescence was collected for 4000 s with 5 s integration time for HA_{20k}-Cy7.5 (slit width was 20 nm, $\lambda_{\text{ex}} = 775$ nm, $\lambda_{\text{em}} = 820$ nm) and HA_{20k}-IRDye800 (slit width was 10 nm, $\lambda_{\text{ex}} = 770$ nm, $\lambda_{\text{em}} = 790$ nm).

3.2.4 Tumor model induction All animal studies were performed under a protocol approved by the UNMC Institutional Animal Care and Use Committee. Procedures were followed in accordance with institutional guidelines per the Guidelines on the Care and Use of Animals for Scientific Purposes. The guidelines were followed to ensure humane care of the animals. Orthotopic, syngeneic PDAC induction was performed as described in previous studies [213], [256]. Briefly, mature female C57BL/6 mice were selected for orthotopic tumor challenge using 10,000 KPC-derived PDAC syngeneic cells per mouse. Once anesthetized, a ~ 5 mm incision was made into the skin and peritoneum on the abdomen between the hip and rib. This allowed for the spleen to be exteriorized for injection of PBS cell suspension into the body of the pancreas. The peritoneum and skin were then secured using an internal dissolving chromic gut and a 5.0 nylon surgical suture, respectively. Animals were warmed, hydrated, and monitored until consciousness was regained. Within two weeks of introduction of tumor cells, palpable tumors were detected

in all challenged mice.

Cells will be mixed with complete media or serum-free media, both containing HA-dyes, at 4°C for 30 min. Next, cells will be incubated with contrast agent-free complete growth media to allow internalization of surface-bound HA-dyes, which can then be quantified by flow cytometry.

3.2.5 Biodistribution of HA-Dye conjugates as measured by fluorescence.

Dye (1 nmol per mouse) or HA-dye (1 nmol dye/mouse equivalent) in 80 µL ultrapure water was intravenously injected into wild type (WT) C57BL/6 mice or PDAC-bearing mice via a tail vein ($N = 5$ mice/group). Mice were euthanized 24 h or 96 h post injection. WT mice were completely necropsied to examine overall fluorescence distribution of dye or dye conjugates. Dissected organs were imaged on a Pearl Trilogy small animal imaging system (LI-COR Biosciences, Lincoln, NE). The fluorescence intensity of each organ was collected with the 800 nm channel and analyzed with Image Studio Ver. 5.0 software (LI-COR Biosciences, Lincoln, NE). The periphery of each organ was identified by defining the region of interest (ROI) with free-hand. Average pixel intensity was used to calculate signal to noise ratio (SNR), which is defined by average tissue intensity per pixel in an ROI: standard deviation of background ROI.

3.2.6 Simulated fluorescence guided imaging of PDAC

Using the aforementioned dose, time, and contrast agents, mice were administered NIR fluorophore or HA-NIRF dye conjugates. After euthanasia, but prior to intraoperative imaging, the liver and spleen were removed to expose the pancreas and minimize background interference of those contrast agents cleared by the RES. A custom-designed FIGS system was employed

to detect contrast enhancement of dye and HA-dye in the pancreatic tumors. The imaging system utilizes a handheld fiber-coupled spectroscopic unit that excites 785 nm and collects wavelength-resolved NIR emission (DeltaNu; Laramie, WY). The spectroscopic unit also serves as the excitation source for a real-time widefield imaging system (Spectropath; Atlanta, GA, USA) that merges a NIR channel (800-950 nm) and a visible color channel for spatial orientation of the NIR signal. The overall design and integration of these systems has been previously reported [214], [215]. A laser power of 80 mW at 785 nm was used for wavelength-resolved (800-950 nm) and widefield imaging.

After FIGS, all mice were necropsied. The pancreas was removed *en bloc* to preserve the anatomical integrity of the primary, stromal, and healthy tissues for fluorescence imaging (using the method described for WT mice) and histological sectioning. To compare against the intraoperative imaging analysis of each pancreas that was obtained during surgery, a straight line was drawn longitudinally across the pancreas in the image obtained by the Pearl Trilogy imaging system. The NIRF intensity along the line was quantified with the *plot profile* function in ImageJ 1.49v software (National Institutes of Health, Bethesda, MD). Tumor bearing pancreas were directly compared against WT pancreas for all contrast agents.

3.2.7 Histological analysis Tumor tissue was embedded in OCT mounting media gel and was rapidly frozen in liquid nitrogen for staining with H&E or left unstained for NIR fluorescence microscopy. Pancreatic tissue was positioned to obtain a maximal footprint for both diseased and healthy pancreases. These samples were cut using a Cryostat (Leica Biosciences, Buffalo Grove, IL) at a thickness of 8 μm . For immunohistological staining, the pancreas was fixed with 4% paraformaldehyde solution for 24 h followed with 70%

ethanol. Samples were embedded in wax and sectioned sequentially for immunohistological and H&E staining. Anti-CD44 antibody (Abcam, Cambridge, MA) was applied at a dilution of 1:100. Representative unstained slides were scanned with Odyssey Clx imaging system (LI-COR, Lincoln, NE) with 800 nm channel. Exposure time was consistent among each group (HA-Cy7.5 and HA-IRDye800). H&E-stained slides were scanned with Panoramic 250 flash series digital scanner (3DHistech, Hungary). Representative microscopic photos for IHC and H&E were imaged and captured with an IX73 Inverted Microscope equipped with a DP80 Digital Camera and displayed by CellSens Dimension 1.13 software (all from Olympus, Japan).

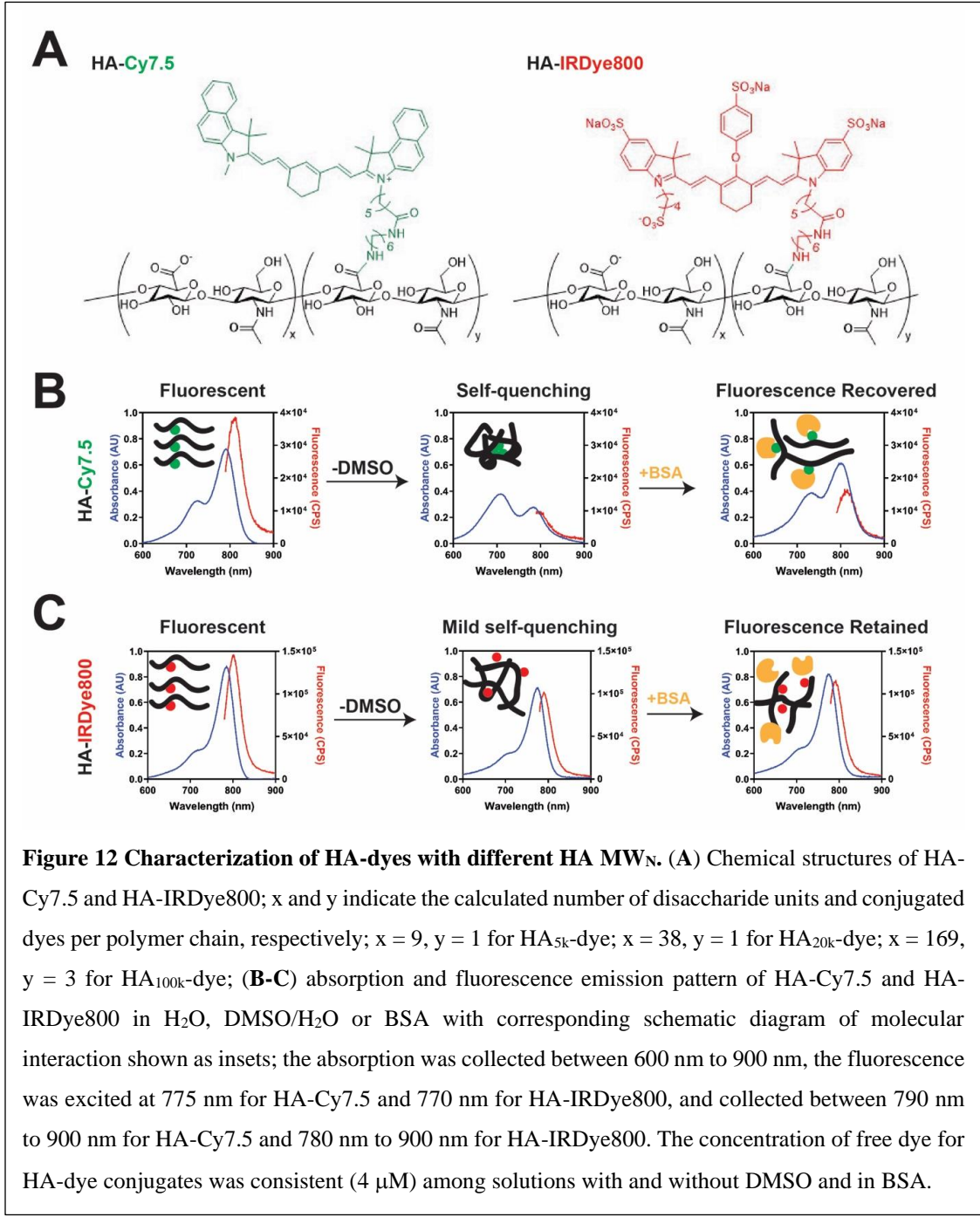
3.2.8 Statistical Analysis Data was analyzed in Prism 7 software (Graphpad, La Jolla, CA). Biodistribution and background interference were analyzed using a 2-way ANOVA and Dunnett's multiple comparisons test; *ex vivo* analysis of contrast within pancreas was analyzed using one way ANOVA with Tukey's multiple comparisons test; all data is shown as mean \pm standard deviation (SD).

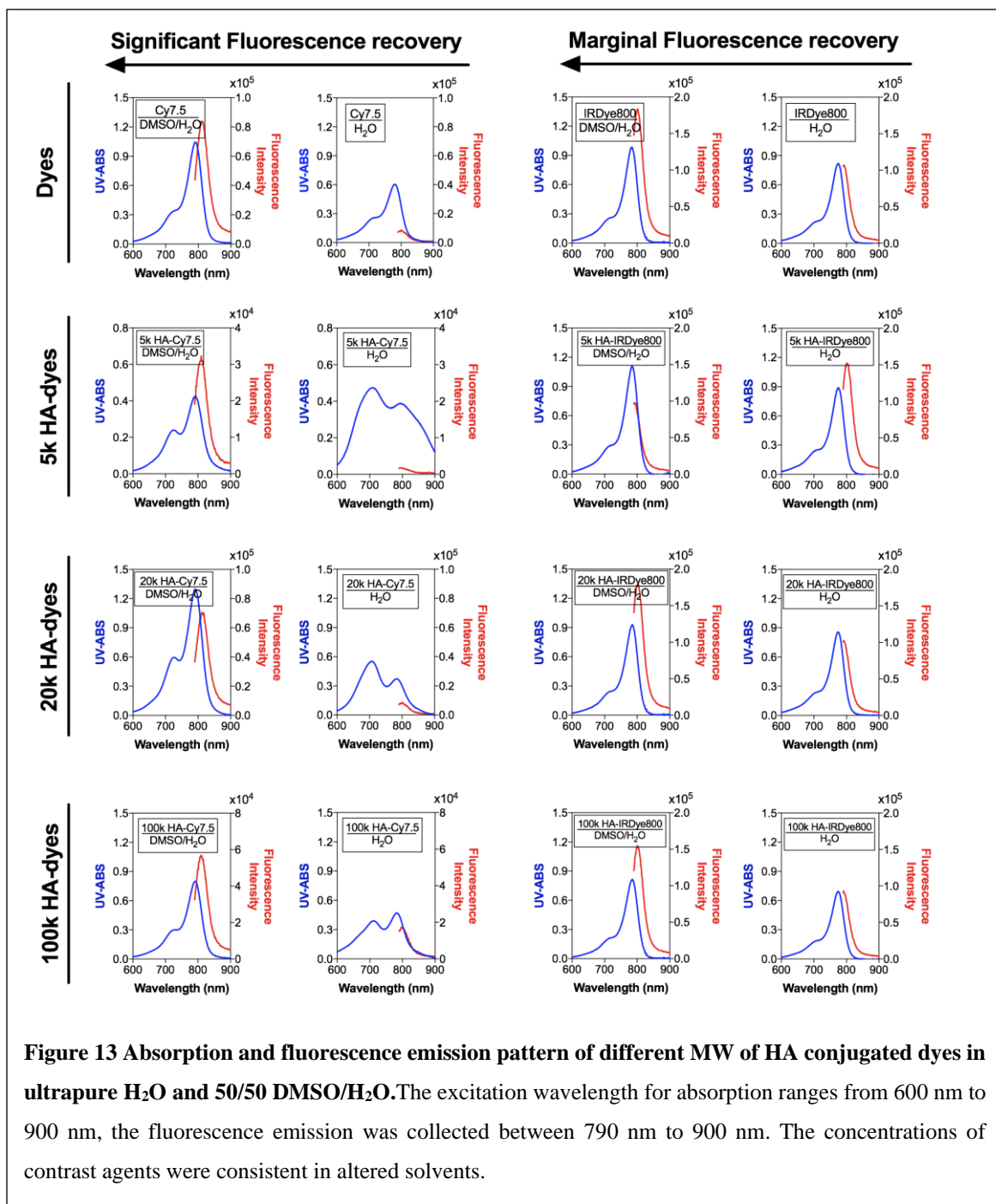
3.3 Results

3.3.1 Synthesis and photochemical properties of HA-NIRF conjugates

HA-Cy7.5 and HA-IRDye800 conjugates were synthesized with 1-Ethyl-3-(3-dimethylaminopropyl)-carbodiimide (EDC)/N-hydroxysuccinimide (NHS) coupling chemistry. The physicochemical and optical properties of HA-Cy7.5 and HA-IRDye800 are summarized in **Figure 12-13, Table 1**. HA-Cy7.5 conjugates displayed distinct, solvent-dependent spectral properties: In H₂O, the extinction spectral fluorescent peaks were "flat" and broad compared to dissociation in DMSO, indicating self-assembly and self-quenching, which is consistent with nanoformulation of Cy7.5 [258]. Cyanine dyes

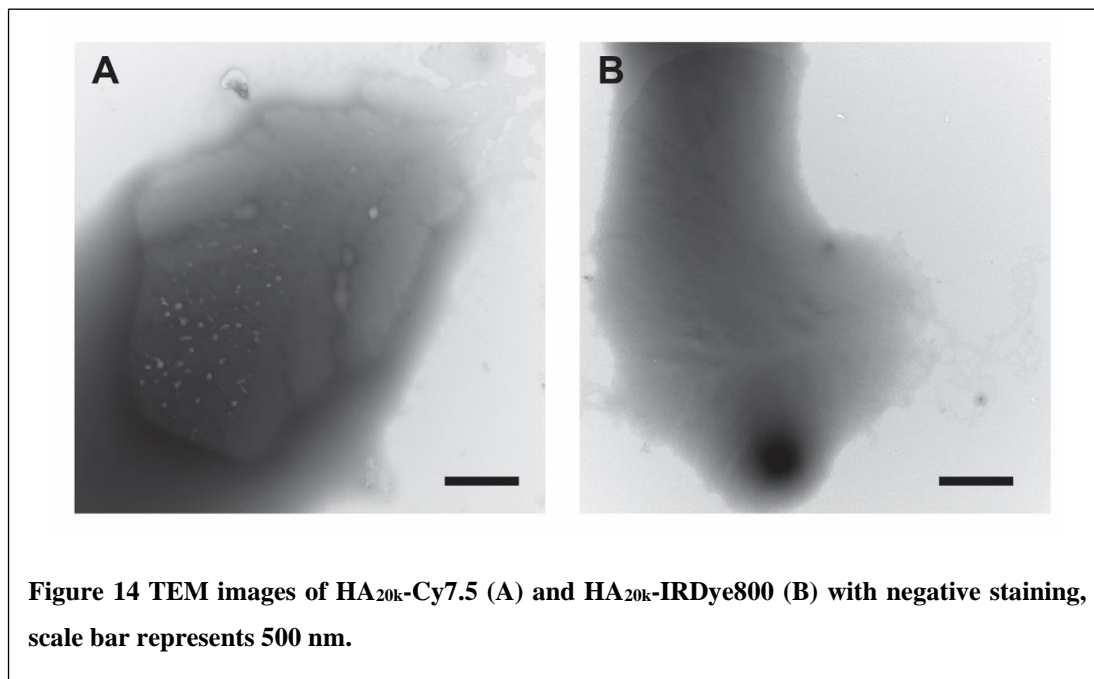
are capable of forming H-aggregates by hydrophobic interaction, which is characterized with hypsochromic absorption and weak fluorescence emission. As shown in Figure S1, the absorption wavelength blue-shifted 80 nm for HA_{5k}, HA_{20k} conjugated Cy7.5, while a blue shift of only 10 nm was observed for HA_{100k}-Cy7.5 conjugate in H₂O. Furthermore, upon disassembly in DMSO, the fluorescence emission intensity exhibited a red-shifted to 810 nm, and a 21.3-, 9.8- and 4.0- fold increase in fluorescence intensity for HA_{5k}-, HA_{20k}- and HA_{100k}-dye conjugates, respectively. In comparison, hydrophilic IRDye800 displayed a limited tendency to interact with other IRDye800 molecules as opposed to interacting with polar solvent (**Figure 12C, 13**). The negative charge also prevents close interaction of the heterocyclic rings between dyes, compromising pi-pi interaction. Therefore, conjugation of HA to IRDye800 had minimal impact on spectral properties of IRDye800 (**Figure 12C**). It is worth noting that HA_{20k}-dye conjugates are not nanoparticles in aqueous phase. In addition, BSA monomer is spherically shaped with a diameter of ~10 nm (**Figure 14A**). When mixed with HA_{20k}-Cy7.5, BSA morphologically changed to irregular shape with sizes range from 10-70 nm (**Figure 14B**). In comparison, BSA monomer remains ~10 nm in the presence of HA_{20k}-IRDye800. In summary, when conjugated with hydrophobic Cy7.5, HA-dye tends to aggregate and self-quench, but the fluorescence is recovered upon disassembly, or partially upon BSA interaction. No fluorescence quenching was observed in HA conjugated to the hydrophilic IRDye800, HA-IRDye800 conjugates conserved spectral properties.





The morphology of HA-dye conjugates were examined with negative staining. It is worth mentioning that HA_{20k}-dye conjugates are not NPs in aqueous phase, they formed irregular shape of aggregates at the range of micrometers (**Figure 14**).

	HA _{5k} - Cy7.5	HA _{20k} - Cy7.5	HA _{100k} - Cy7.5	HA _{5k} - IRDye800	HA _{20k} - IRDye800	HA _{100k} - IRDye800
Weight ratio (g/g) dye/polymer	0.57	0.15	0.10	0.26	0.05	0.02
Dyes per chain	1.23	1.15	0.56	1.18	0.69	1.40
Conjugating efficiency (%)	77.1	88.8	78.9	57.8	27.8	18.4
Yield (%)	37.3	33.3	21.8	45.6	68.5	75.5



3.3.2 *In vitro* assessment of protein association Plasma proteins association can have a significant impact on *in vivo* size and solubility, which can potentially alter its pharmacokinetic properties and tissue specificity [259]. To prove that hydrophobicity of

contrast agents implies strong non-specific protein association, the mixture of HA-dye and BSA were chromatographically eluted for BSA recognition while being monitored for NIRF to identify the presence of HA-dye. ICG+BSA was used to test the applicability of chromatography-spectrofluorometer system (data not shown), elution histogram was exhibited after the void volume (determined by FITC labeled dextran2000), delay volume between UV detector and spectrofluorometer was 5.55 ± 0.18 mL (determined by FITC labeled dextran2000 and ICG+BSA) and normalized in **Figure 15**.

BSA monomer was eluted maximally at 27 min when monitoring absorbance at 280 nm (**Figure 15A**), whereas minimal peaks were observed in NIRF at that time (**Figure 15B-C**, blue trace). The NIRF of HA_{20k}-Cy7.5 is undetectable due to self-quenching, whereas HA_{20k}-IRDye800 exhibits 2 peaks which likely correspond to aggregate and dispersed polymer conjugate (**Figure 15B-C**, red trace). Interestingly, an apparent NIRF peak was detected that corresponds to BSA for HA-Cy7.5 (**Figure 15B**, green trace) and is consistent with the fluorescence recovery displayed spectrofluorometrically (**Figure 12B**), while a corresponding peak from HA-IRDye800 attributed to BSA binding was minimally present (**Figure 15C**, green trace). In order to confirm the presence of BSA, fractionated elutions of interest from HA-dye + BSA were collected for Bradford assay, the NIRF peak fractions were strongly positive after Bradford dye staining, indicating that NIRF peak of HA-Cy7.5 corresponds to BSA elution (**Figure 16**).

We also determined the size of particle distribution for BSA with/without HA-dye conjugates with NP tracking analysis (< 30 nm to > 1 μ m). The concentration of HA_{20k}-Cy7.5 was 3 times lower than that of HA_{20k}-IRDye800, indicating more of HA_{20k}-Cy7.5 formed aggregates that are larger than 1 μ m (**Table 2**).

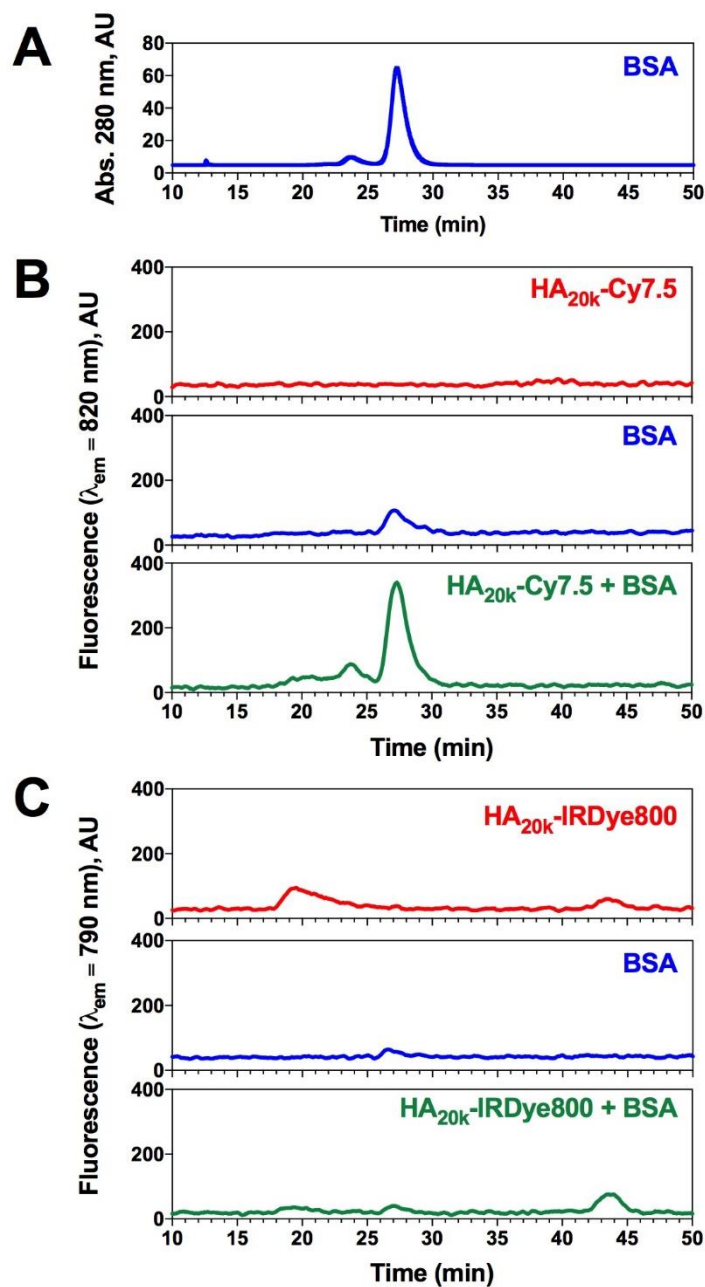


Figure 15 BSA interacts with HA-dyes to different extents due to dye hydrophobicity. (A) Elution histogram of 50 μ M BSA monitored at 280 nm absorption; (B) fluorescent histogram of elution of HA_{20k}-Cy7.5 (4 μ M Cy7.5 equivalent, red), BSA (50 μ M, blue) or the mixture (green) monitored at 820 ± 10 nm and integrated by 5 s; (C) fluorescent histogram of elution of HA_{20k}-IRDye800 (4 μ M IRDye800 equivalent, red), BSA (50 μ M, blue) or the mixture (green) monitored at 790 ± 5 nm and integrated by 5 s; samples were eluted by AKTA pure 25L Chromatography system, monitored with absorption motif at fixed wavelength of 280 nm and NIRF spectrofluorometer. All the samples were run at least three times.

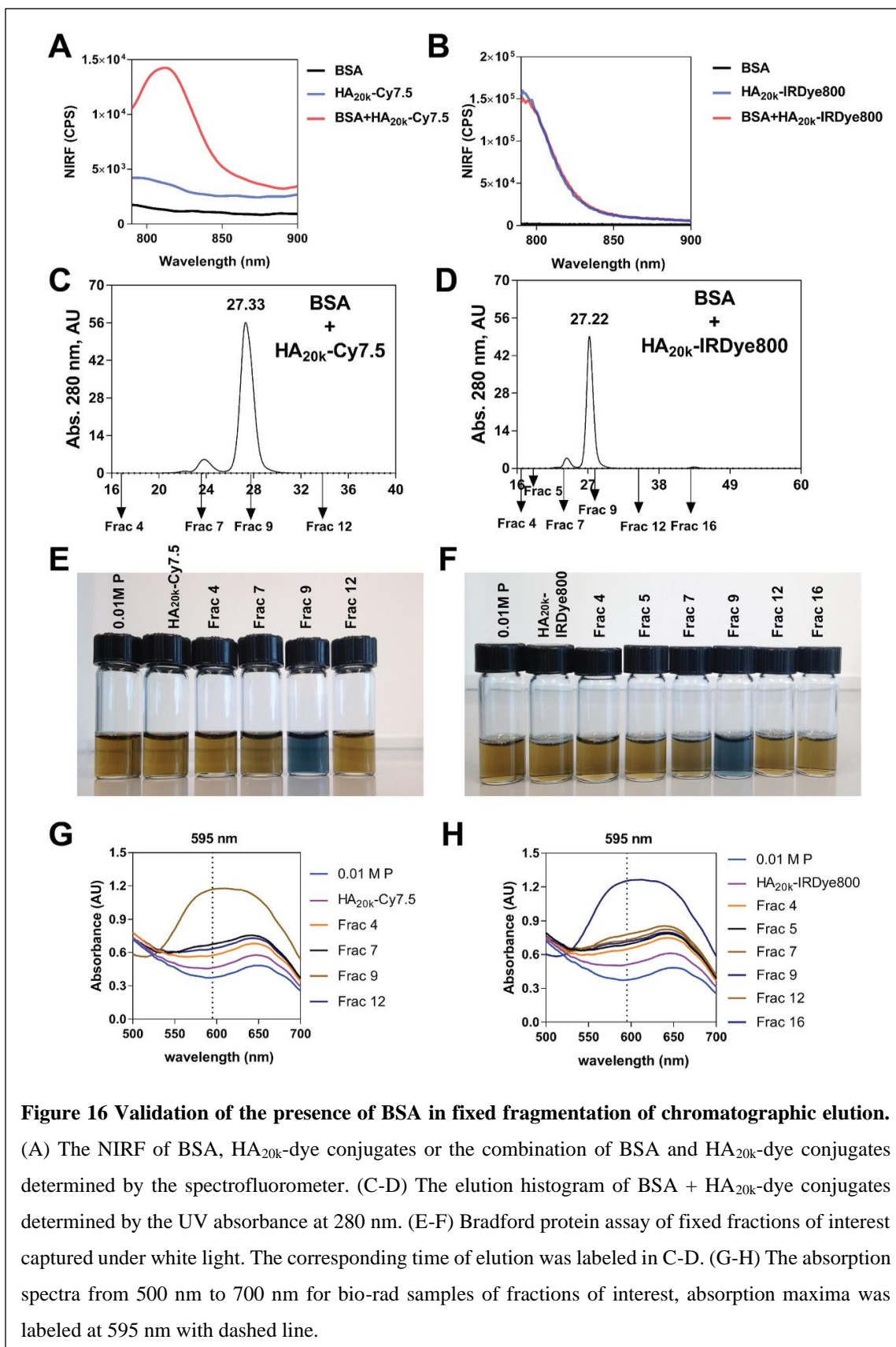
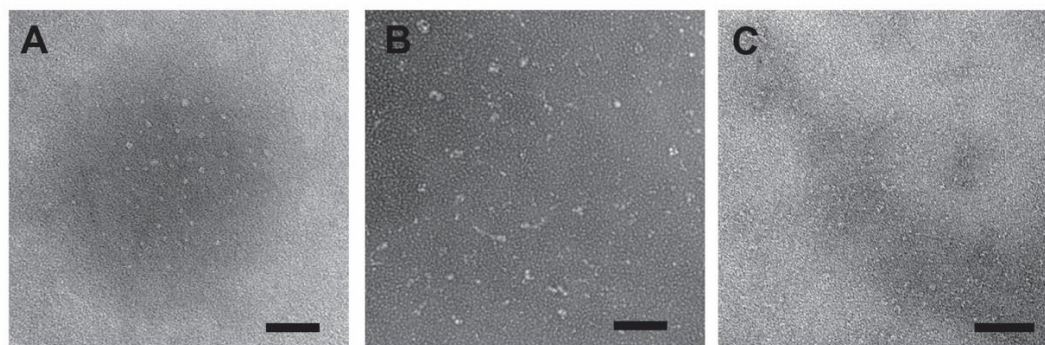


Figure 16 Validation of the presence of BSA in fixed fragmentation of chromatographic elution.

(A) The NIRF of BSA, HA_{20k}-dye conjugates or the combination of BSA and HA_{20k}-dye conjugates determined by the spectrofluorometer. (C-D) The elution histogram of BSA + HA_{20k}-dye conjugates determined by the UV absorbance at 280 nm. (E-F) Bradford protein assay of fixed fractions of interest captured under white light. The corresponding time of elution was labeled in C-D. (G-H) The absorption spectra from 500 nm to 700 nm for bio-rad samples of fractions of interest, absorption maxima was labeled at 595 nm with dashed line.

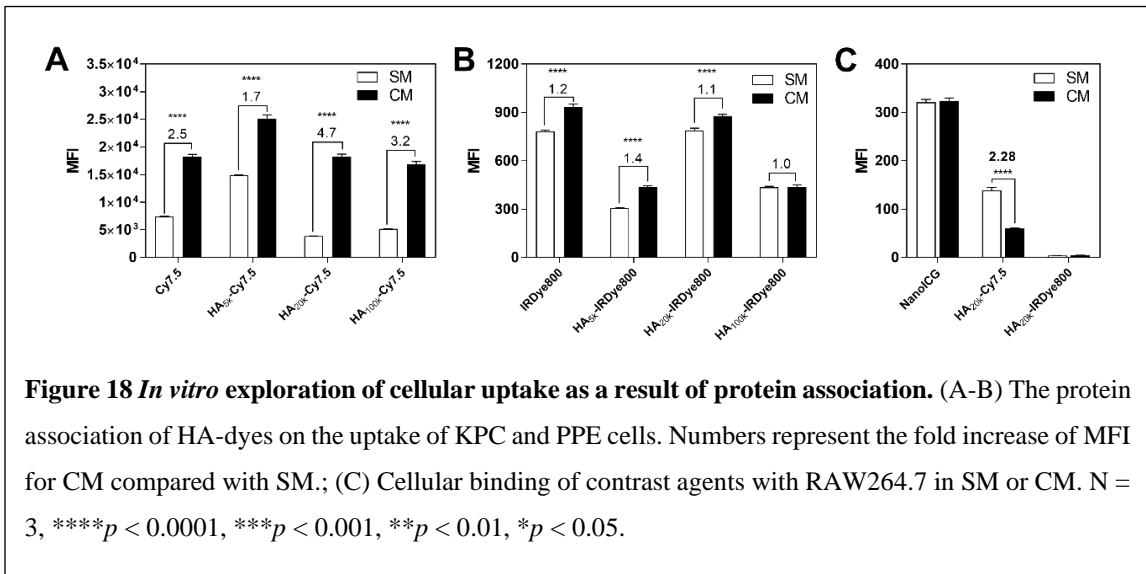
Table 97 NP tracking analysis of BSA and BSA with/without HA-dye conjugates

	Mean diameter (nm)	Concentration (particle/mL)	Theoretical concentration (particle/mL)
BSA	117.9 ± 57.2	7.05×10 ⁸ ± 1.16×10 ⁷	3.01×10 ¹⁵
HA _{20k} -Cy7.5	162.1 ± 50.9	7.34×10 ⁷ ± 1.68×10 ⁶	2.41×10 ¹⁵
HA _{20k} -IRDye800	166.0 ± 65.8	2.35×10 ⁸ ± 1.36×10 ⁷	2.41×10 ¹⁵
BSA+HA _{20k} -Cy7.5	130.2 ± 60.0	2.91×10 ⁸ ± 1.25×10 ⁷	5.42×10 ¹⁵
BSA+HA _{20k} -IRDye800	136.4 ± 66.1	6.69×10 ⁸ ± 1.84×10 ⁷	5.42×10 ¹⁵

**Figure 17 TEM images of BSA (A), BSA mixed with HA_{20k}-Cy7.5 (B), BSA mixed with HA_{20k}-IRDye800 (C) with negative staining, scale bar represents 100 nm.**

Protein adsorption granted the biomaterial with new “biological identity” upon *i.v.* injection, which alters the pharmacokinetic properties and potentially tissue specificity. To explore the existence and biological role of protein association on HA-dyes, cellular association was determined for HA-NIRF with/without serum. Protein binding leads to increased uptake of HA-Cy7.5 for KPC cells, with a fold increase of complete medium (CM) compared to starving medium (SM) is 2-4 for HA-Cy7.5 and 1-2 for HA-IRDye.(**Figure 18A-B**), indicating higher level of protein association for the relatively hydrophobic HA-Cy7.5 as compared to HA-IRDye800. The protein association extent

could be further quantified by the macrophage binding (**Figure 18C**) with/without serum: $66.2 \pm 4.2\%$ of RAW264.7 would bind with HA_{20k}-Cy7.5 without protein association, while only $9.1 \pm 0.4\%$ bound with protein associated HA_{20k}-Cy7.5, suggesting protein plays less important role in mediating macrophage binding. Furthermore, negligible percentage (0.004% in SM and 0.007% in CM) of cells would bind with HA-IRDye800, proves that HA-IRDye800 is less immunogenic as compared with HA-Cy7.5, indicating less RES sequestration.



3.3.3 Biodistribution of HA-NIRF To test the hypothesis that the protein association resulting from dye hydrophobicity/hydrophilicity in combination with HA MW_N could affect the biodistribution pattern, the fluorescence intensity was examined in each organ for both HA-Cy7.5 and HA-IRDye800. The organs of interest: RES organs and clearance organs, were compared between different MW_N of HA-dye to identify the detailed *in vivo* performance. Overall majority of HA-Cy7.5 was accumulated in liver, followed by spleen and kidney, among which, HA_{20k}-Cy7.5 displayed the highest

fluorescence intensity in liver (**Figure 19A-B**). Additionally, hepatic retention of HA_{20k}-Cy7.5 lasts for 96 h (**Figure 20**). On the contrary, HA-IRDye800 did not bind with albumin and was able to retain the small size and hydrophilicity of HA and IRDye800, thus resulting in biodistribution of HA-Dye conjugate, not of albumin (**Figure 19C-D**). When comparing different MW_N of HA conjugated IRDye800, HA_{100k}-IRDye800 tends to be retained in RES organs, whereas HA_{5k} and HA_{20k} conjugated IRDye800 accumulated more so in the kidney, as observed in **Figure 19C-D**.

In the PDAC-bearing mice, higher fluorescence signal was observed in pancreas in the HA-NIRF-treated group compared with dye-treated group with $p < 0.0001$ (**Figure 20**). The fold increase of NIR signal in pancreas was 8-28 for HA-Cy7.5 as compared with Cy7.5; and 8-15 for HA-IRDye800 when compared with IRDye800 (**Table 3-4**). Between individual organs, significantly higher signals were seen in the liver and spleen with the HA-Cy7.5-treated groups, hepatic accumulation is 2-3 times higher for HA-Cy7.5 when compared with Cy7.5, the fold-increase in splenic NIR signal ranges from 5-10 for HA-Cy7.5 when compared to Cy7.5. In comparison, increased uptake was observed in the kidney, femur and stomach due to HA_{5k}-, HA_{20k}-IRDye800. Furthermore, a sharp increase of RES accumulation was observed for HA_{100k}-IRDye800 in addition to renal accumulation. The fold increase of HA-IRDye800 accumulation in bone ranges from 8-16 as compared with IRDye800; the ratio of kidney specificity is 3-4 times higher than that of the free dye.

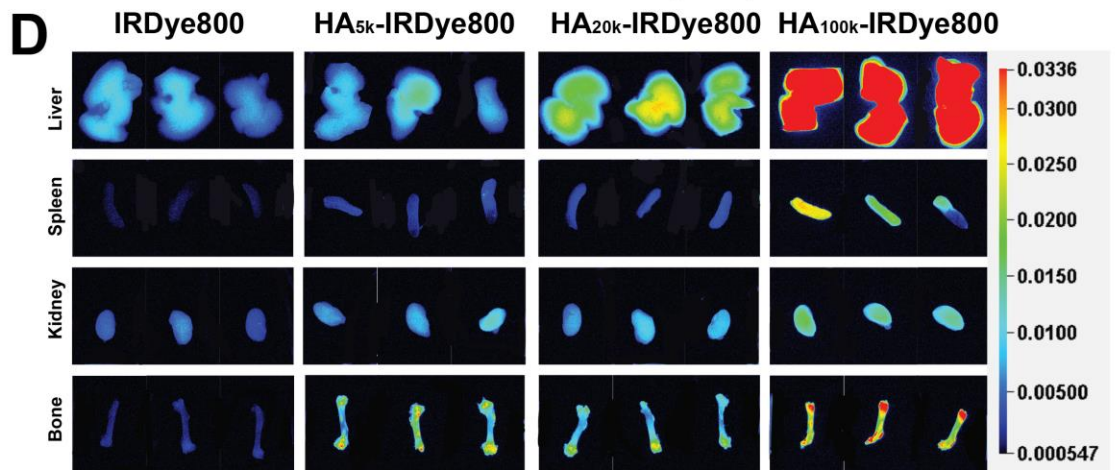
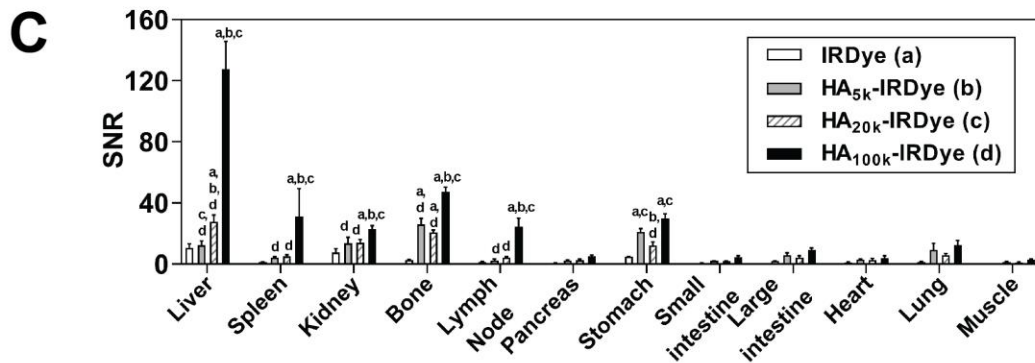
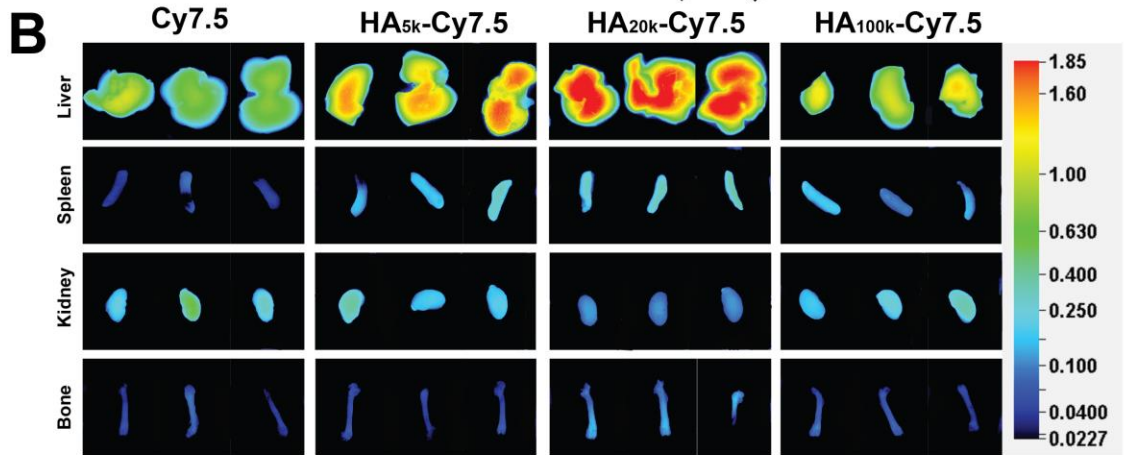
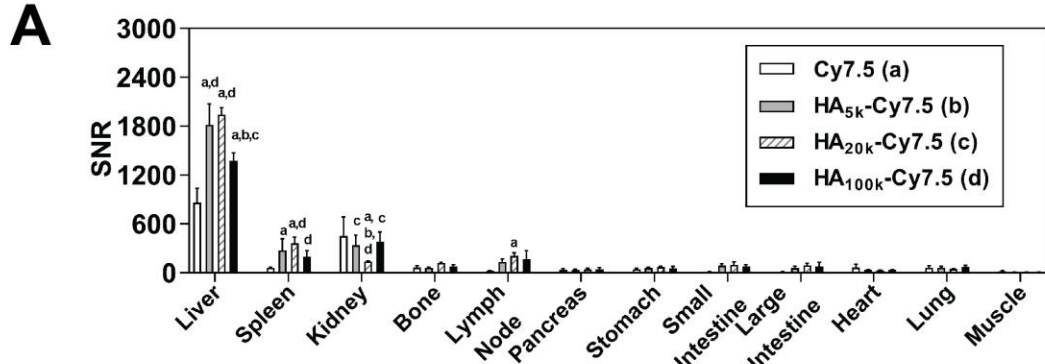


Figure 19 Varied biodistribution between HA-Cy7.5 and HA-IRDye800 in WT C57BL/6 mice 24 h post *i.v.* injection. (A, C) Quantitative organ biodistribution of HA-Cy7.5 and HA-IRDye800 determined by the relative fluorescence of each organ from NIRF images; (B, D) semi-quantitative comparison of different MW_N of HA conjugated dyes accumulation in organs of interest in WT C57BL/6 mice, which demonstrate the predominant elimination route of each contrast agent. Representative images of necropsied organs were acquired with NIR channel of Pearl Trilogy Small Animal Imaging System; borders of images were erased to black to eliminate the interference from the neighboring placed organ samples. $N = 3$, ^a $p < 0.05$ as compared to free dye, ^b $p < 0.05$ as compared to HA_{5k}-dye, ^c $p < 0.05$ as compared to HA_{20k}-dye, ^d $p < 0.05$ as compared to HA_{100k}-dye.

After 4 days clearance, RES retention is observed due to HA-Cy7.5, indicative of macrophage sequestration (data not shown). In summary, HA-Cy7.5 exhibited profound accumulation in liver and spleen, regardless of HA MW_N; whereas low MW_N HA-IRDye800 displayed nearly consistent distribution over bone, lung, spleen, kidney, and stomach, as well as a relative increase of signal in the kidneys, suggesting enhanced distribution volume and urine elimination which were ascribed to the hydrophilic nature of IRDye800 in conjunction with its accordingly low affinity for albumin and small size HA moiety.

3.3.4 Background interference Background organ interference was quantified by dividing the signal of PDAC by the signal of muscle (referential tissue for non-NIR accumulation), stomach, small intestine, liver, spleen and kidneys (surrounding organs or clearance organs). The ratios were plotted in **Figure 20C** and summarized in **Table 3-4**. The SNR of PDAC: muscle was intense due to HA conjugated dye and the ratio remained ≥ 10 after 4 days' clearance. PDAC:organ ratios were also calculated to uncover the impact of clearance routes on the tumor contrast. PDAC signal of HA-Cy7.5 tends to be less-affected by the signal from kidney and stomach, as the average contrast ratio for kidney is 2-7 for HA-Cy7.5 in comparison to 0.12 for Cy7.5. The average contrast by stomach is 5-

7 for HA-Cy7.5 in comparison to 0.36 for Cy7.5 (**Figure 20C, Table 3-4**). However, the PDAC signal of HA-IRDye800-treated group was less influenced by the intestines and liver (**Figure 20C**). The contrast ratio is 8-25 for intestines, and higher than 1 for liver with HA_{5k}- and HA_{20k}-IRDye800. HA_{100k}-IRDye800 exhibited comparable liver contrast with HA-Cy7.5: with an average ratio of 0.3 (**Table 4**). In comparison, the SNR of pancreas in HA-dyes-treated groups, when divided by that of the GI tract, RES organs, and kidneys in WT C57BL/6 mice, is below 1, regardless of contrast agent (Calculated from **Figure 19A, C**).

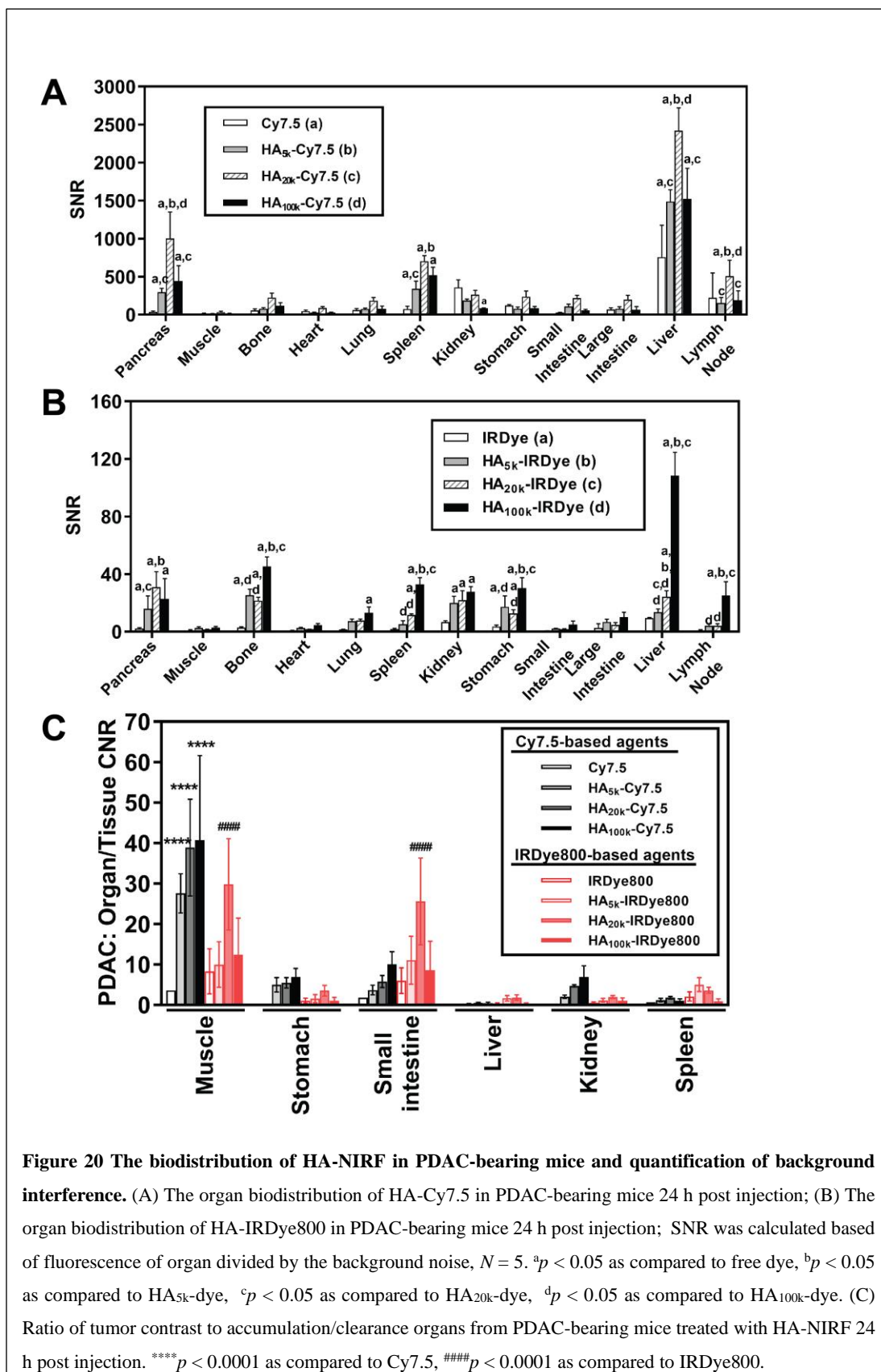


Figure 20 The biodistribution of HA-NIRF in PDAC-bearing mice and quantification of background interference. (A) The organ biodistribution of HA-Cy7.5 in PDAC-bearing mice 24 h post injection; (B) The organ biodistribution of HA-IRDye800 in PDAC-bearing mice 24 h post injection; SNR was calculated based of fluorescence of organ divided by the background noise, $N = 5$. ^a $p < 0.05$ as compared to free dye, ^b $p < 0.05$ as compared to HA_{5k}-dye, ^c $p < 0.05$ as compared to HA_{20k}-dye, ^d $p < 0.05$ as compared to HA_{100k}-dye. (C) Ratio of tumor contrast to accumulation/clearance organs from PDAC-bearing mice treated with HA-NIRF 24 h post injection. **** $p < 0.0001$ as compared to Cy7.5, ##### $p < 0.0001$ as compared to IRDye800.

Table 3 Ratio of HA-Cy7.5-treated pancreas or PDAC fluorescence divided by signal of surrounding organs 24 h post injection (N = 5)

	W.T. C57BL/6				PDAC			
	Cy7.5	HA _{5k} - Cy7.5	HA _{20k} - Cy7.5	HA _{100k} - Cy7.5	Cy7.5	HA _{5k} - Cy7.5	HA _{20k} - Cy7.5	HA _{100k} - Cy7.5
Muscle	2.31±0.50	4.64±1.29	4.46±1.21	4.44±1.27	3.59±1.68	27.56±4.83	33.88±11.98	40.76±20.90
Stomach	0.78±0.31	0.58±0.08	0.60±0.36	0.79±0.12	0.36±0.11	4.98±1.78	5.45±1.28	6.94±2.10
Int	2.38±0.41	0.42±0.20	0.41±0.07	0.62±0.39	1.77±0.75	3.67±1.19	5.77±1.50	10.06±3.09
Liver	0.04±0.01	0.02±0.003	0.02±0.01	0.03±0.01	0.05±0.02	0.25±0.06	0.51±0.11	0.43±0.25
Kidney	0.08±0.01	0.11±0.02	0.29±0.12	0.12±0.04	0.12±0.04	2.02±0.42	4.68±0.28	6.93±2.74
Spleen	0.56±0.17	0.14±0.03	0.12±0.08	0.24±0.12	0.69±0.40	1.18±0.41	1.76±0.32	1.11±0.40

Table 4 Ratio of HA-IRDye800-treated pancreas or PDAC fluorescence divided by signal of surrounding organs 24 h post injection (N = 5)

	W.T. C57BL/6				PDAC			
	IRDye	HA _{5k} - IRDye	HA _{20k} - IRDye	HA _{100k} - IRDye	IRDye	HA _{5k} - IRDye	HA _{20k} - IRDye	HA _{100k} - IRDye
Muscle	3.38±0.85	0.92±0.78	2.26±0.38	1.74±0.59	8.28±5.55	9.96±5.63	29.81±11.2	12.42±9.00
Stomach	0.17±0.03	0.39±0.58	0.23±0.08	0.17±0.05	1.06±0.59	1.54±0.97	3.50±1.32	1.04±0.77
Int	1.47±0.70	0.54±0.50	1.44±0.20	1.14±0.34	6.00±3.17	11.03±5.90	25.56±10.7	8.59±7.16
Liver	0.08±0.03	0.11±0.09	0.09±0.01	0.04±0.01	0.36±0.14	1.65±0.66	1.81±0.69	0.30±0.20
Kidney	0.12±0.02	0.10±0.08	0.19±0.03	0.22±0.06	0.52±0.22	1.14±0.48	1.96±0.34	1.06±0.65
Spleen	0.59±0.10	0.43±0.26	0.51±0.06	0.20±0.10	2.08±1.14	5.01±1.73	3.60±0.72	0.91±0.58

3.3.5 IGS of HA-NIRF in PDAC-bearing mouse model An orthotopic, syngeneic PDAC mouse model was used to demonstrate the tumor contrast efficiency of HA-dyes. The representative FIGS images from HA-dyes displayed marked contrast within pancreas (**Figure 21-22**). Overall, HA-Cy7.5 exhibited higher fluorescence intensity than HA-IRDye800, with visible or apparent background signal from GI content, especially for HA_{20k}-Cy7.5. In comparison, HA-IRDye800 displayed comparable or greater contrast within the tumor-bearing pancreas along with negligible background signal from GI tract. The fold increase of signal intensity when the excitation source is directed at the tumor compared to when the excitation source is directed off the tumor is 0.14 (Cy7.5), 2.10 (HA_{5k}-Cy7.5), 3.59 (HA_{20k}-Cy7.5), 9.17 (HA_{100k}-Cy7.5), as detected at 825 nm, and 0 (IRDye800), 2.17 (HA_{5k}-IRDye800), 663.09 (HA_{20k}-IRDye800), 52.32 (HA_{100k}-IRDye800), as detected at 810 nm (**Figure 22**). The PDAC specificity was maintained for up to 4 days post injection with HA-Cy7.5, but contrast was compromised as time extends for HA-IRDye800, especially for HA_{20k} and HA_{100k} (**Figure 23**). In summary, HA conjugated dyes displayed structure-influenced robust PDAC specificity with tunable GI background signal.

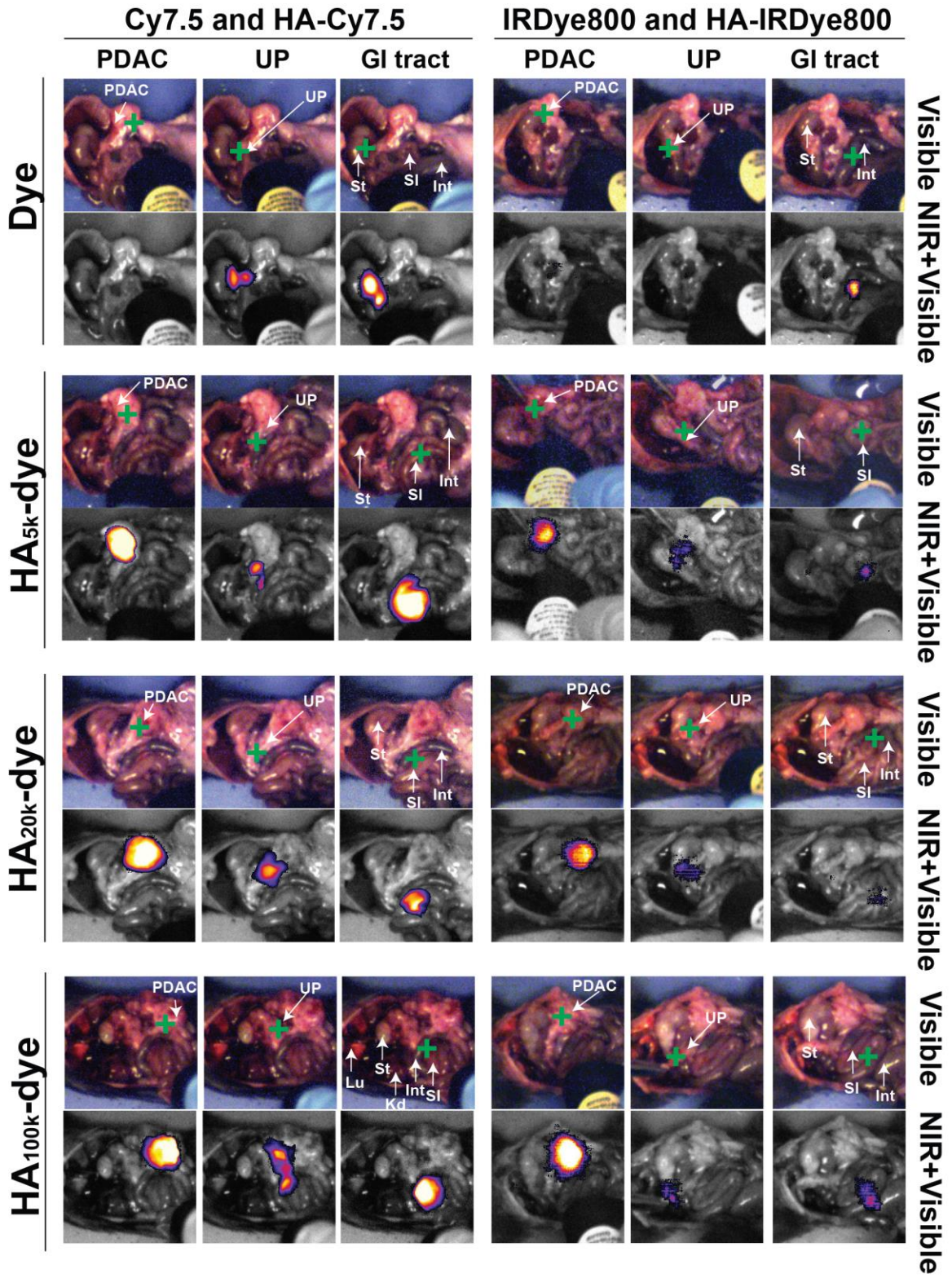


Figure 21 Images from surgical navigation of PDAC with contrast enhancement due to HA-dye and dye 24 h post *i.v.* injection. Livers and spleens were removed due to high background signal from clearance, spleens that were completely involved with PDAC were kept. Two channels (visible with/without NIR) and three spots [Spectropen directed at PDAC, uninvolved pancreas (UP) and (GI)] were displayed for each experimental group: (*Top*) Color images depict orthotopic PDAC and the location of the handheld spectroscopic pen, which provides NIR spectral information and serves as an excitation source for a widefield imaging system; (*Bottom*) NIR signal overlaid onto the grayscale image shows robust enhancement of syngeneic, orthotopic pancreatic cancer, green crosses indicated the directed location of excitation laser. Improved contrast can be observed due to HA conjugated dye but not free dye. PDAC = pancreatic ductal adenocarcinoma, UP = uninvolved pancreas, St = stomach, SI = small intestine, Int = large intestine.

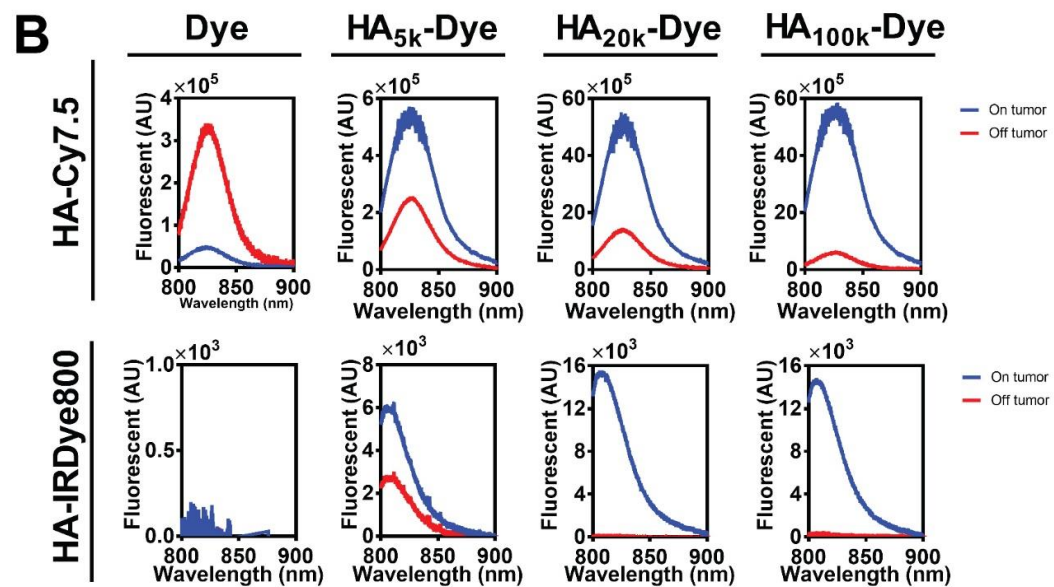
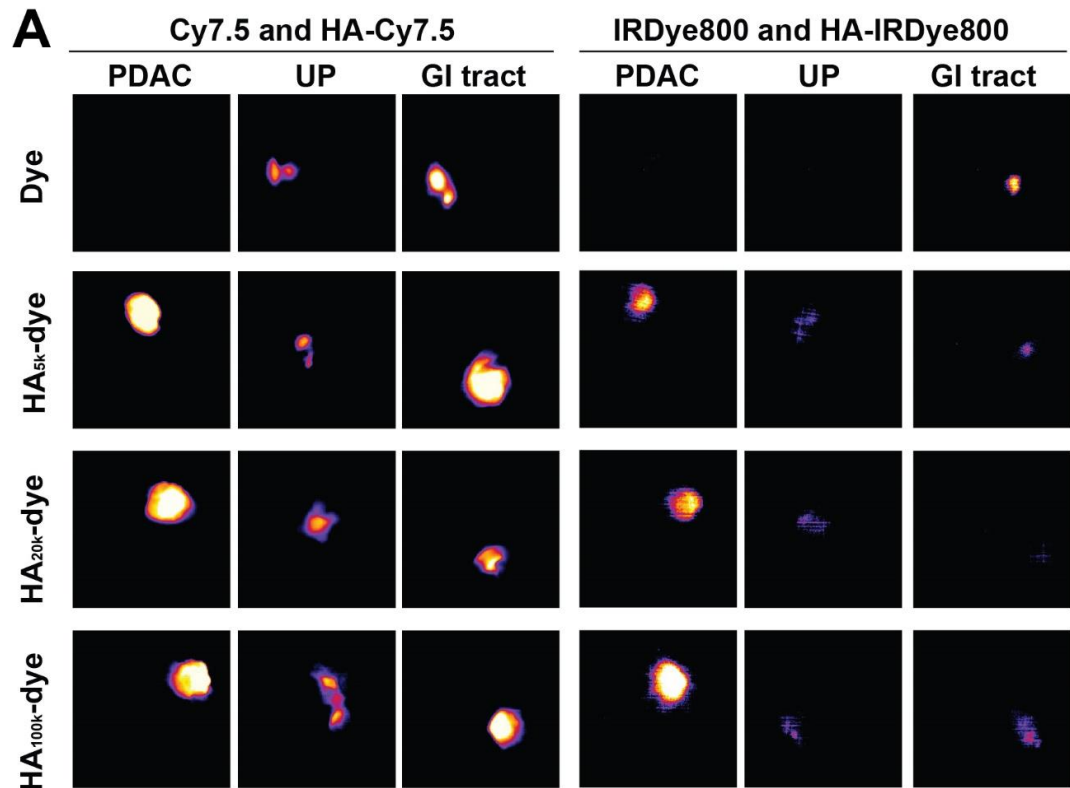


Figure 22 Quantification and quantification of signal from NIR channel that corresponds to **Figure 19**. (A) Pseudo colored (fire) NIRF signal from PDAC, uninvolved pancreas (UP) and GI excited by the Spectropen pointing at green cross in **Figure 5**; (B) spectroscopic signal from PDAC (on tumor, blue) and UP (off tumor, red).

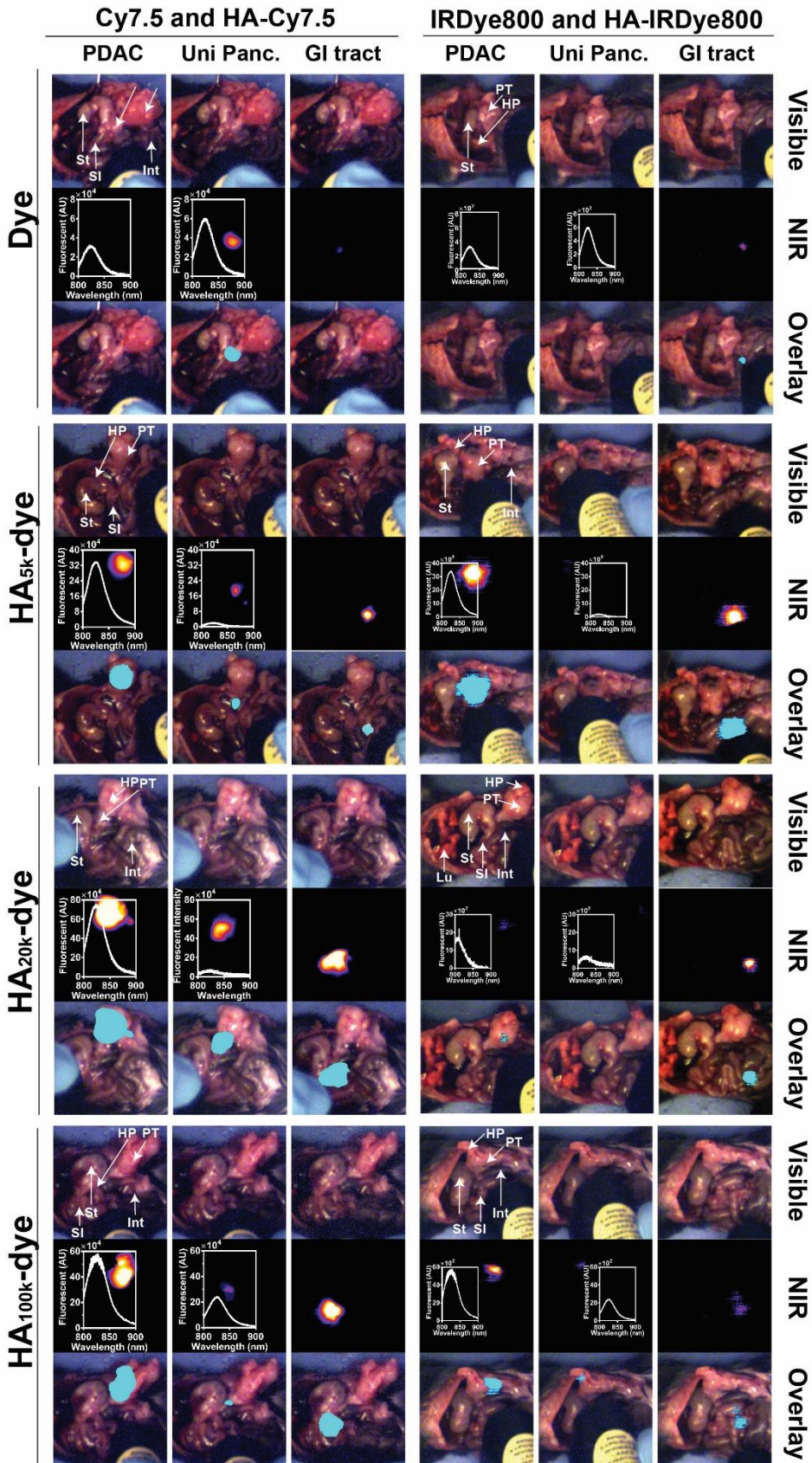


Figure 23 Images from surgical navigation of pancreatic tumor contrast-enhanced with HA-dye 96 h post *i.v.* injection. Livers and spleens were removed due to high background signal from clearance, spleens that completely involved with PDAC were kept. PDAC = pancreatic ductal adenocarcinoma, UP = uninvolved panc, St = stomach, SI = small intestine, Int = large intestine; each group was arranged into three rows: (*Top*) Color images show orthotopic PDAC and the location of the handheld spectroscopic pen, which provides NIR spectral information and serves as an excitation source for a widefield imaging system. (*Middle*) Pseudo-colored signal (fire) in the NIR channel of the widefield imaging system and the spectroscopic signal from within the contrast-enhanced region; (*Bottom*) NIR signal overlaid (cyan) onto the color image shows robust enhancement of syngeneic, orthotopic pancreatic cancer. Contrast enhancement can be observed with HA_{5k}-, HA_{20k}- and HA_{100k}-Cy7.5, HA_{5k}- and HA_{100k}-IRDye800 (see inset middle row).

As observed in **Figure 24A-D**, NIRF images (*Top row*) of the pancreas showed HA_{20k}-dye did not accumulate in the healthy pancreas of WT mice (*left column*) or uninvolved pancreas of PDAC tumor-bearing mice, but accumulated extensively and specifically in the PDAC portion of the pancreas. PDAC-specificity was also observed for HA_{5k}- and HA_{100k}-dyes. The *middle row* on the left quantified fluorescence intensity from the spectroscopic pen at acquisition locations across the pancreas, which matches with fluorescence variation delineated along the red-dashed line shown on the right. The *bottom row* exhibited the NIR signal distribution across longitudinally-sectioned pancreas and corresponding histopathology. PDAC is poorly differentiated but well-perfused by HA_{20k}-dye, as compared with HA_{5k}-dye and HA_{100k}-dye. Signal was not detected in free dye-treated PDAC or healthy pancreas. Contrast was still visible after 4 days of clearance (**Figure 25**), especially for the 100k HA conjugates. In summary, HA conjugated dyes are effective at PDAC probing, with HA_{20k}-dye the most efficient scaffold for PDAC delivery. To compare the contrast enhancement of HA-dye statistically and quantitatively, SNR of PDAC was divided by that of uninvolved pancreas or healthy pancreas from WT mice. As shown in **Figure 24E**, no significant difference of NIRF signal was detected between

uninvolved pancreas and healthy pancreas, regardless of contrast agent treatment. In comparison, a significantly higher signal was detected between PDAC and uninvolved pancreas for HA_{5k}-, HA_{20k}- and HA_{100k}-Cy7.5, HA_{5k}- and HA_{20k}-IRDye800 but not HA_{100k}-IRDye800 treated mice, the contrast ratio (defined by SNR of PDAC/SNR of UP) was labeled in each figure. HA_{20k}-IRDye800 displayed the highest fold increase of 14.04, with $p < 0.001$. HA-Cy7.5 exhibited increased contrast as compared to Cy7.5, regardless of MW_N of HA. Furthermore, enhanced contrast within PDAC pancreas was detectable after 4 days, with a contrast ratio of 3.86 and 5.96 for HA_{20k}-Cy7.5 and HA_{20k}-IRDye800, respectively (**Figure 25**).

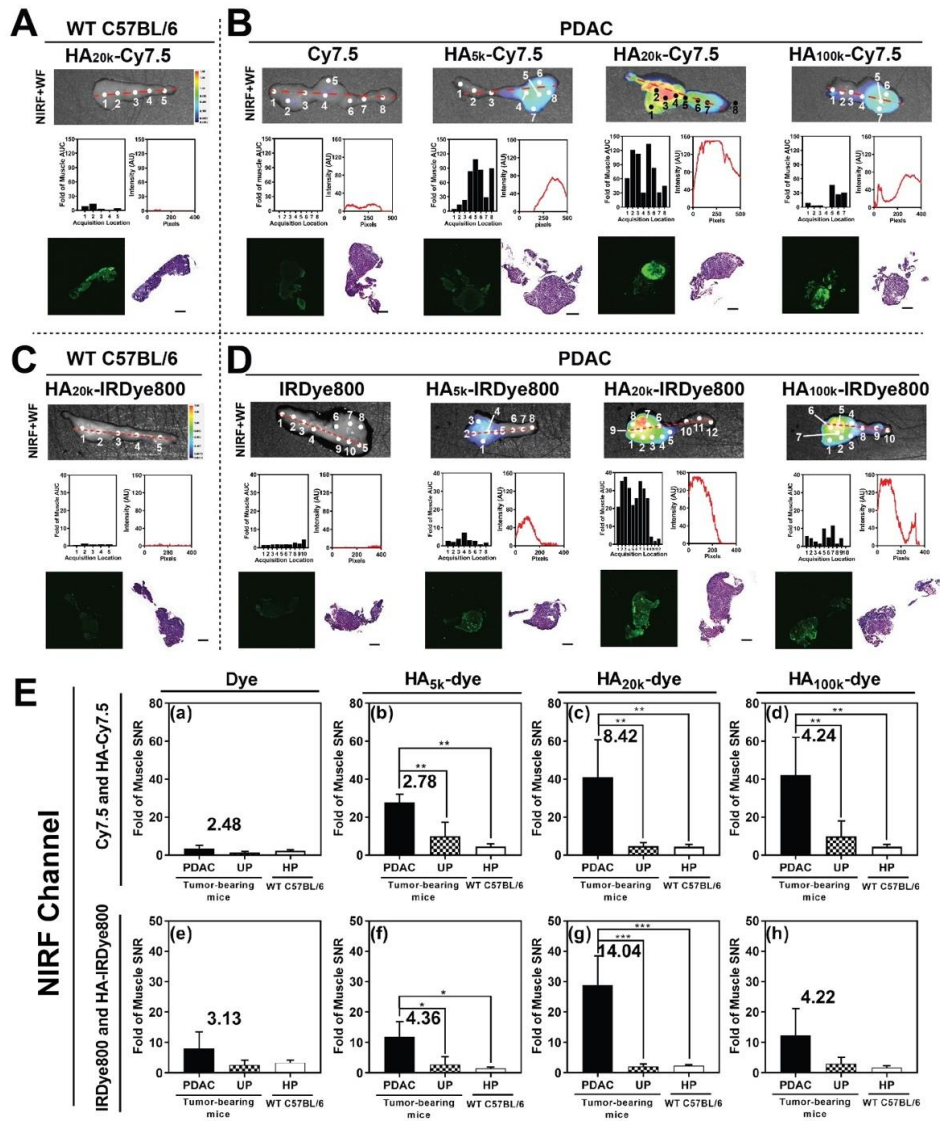
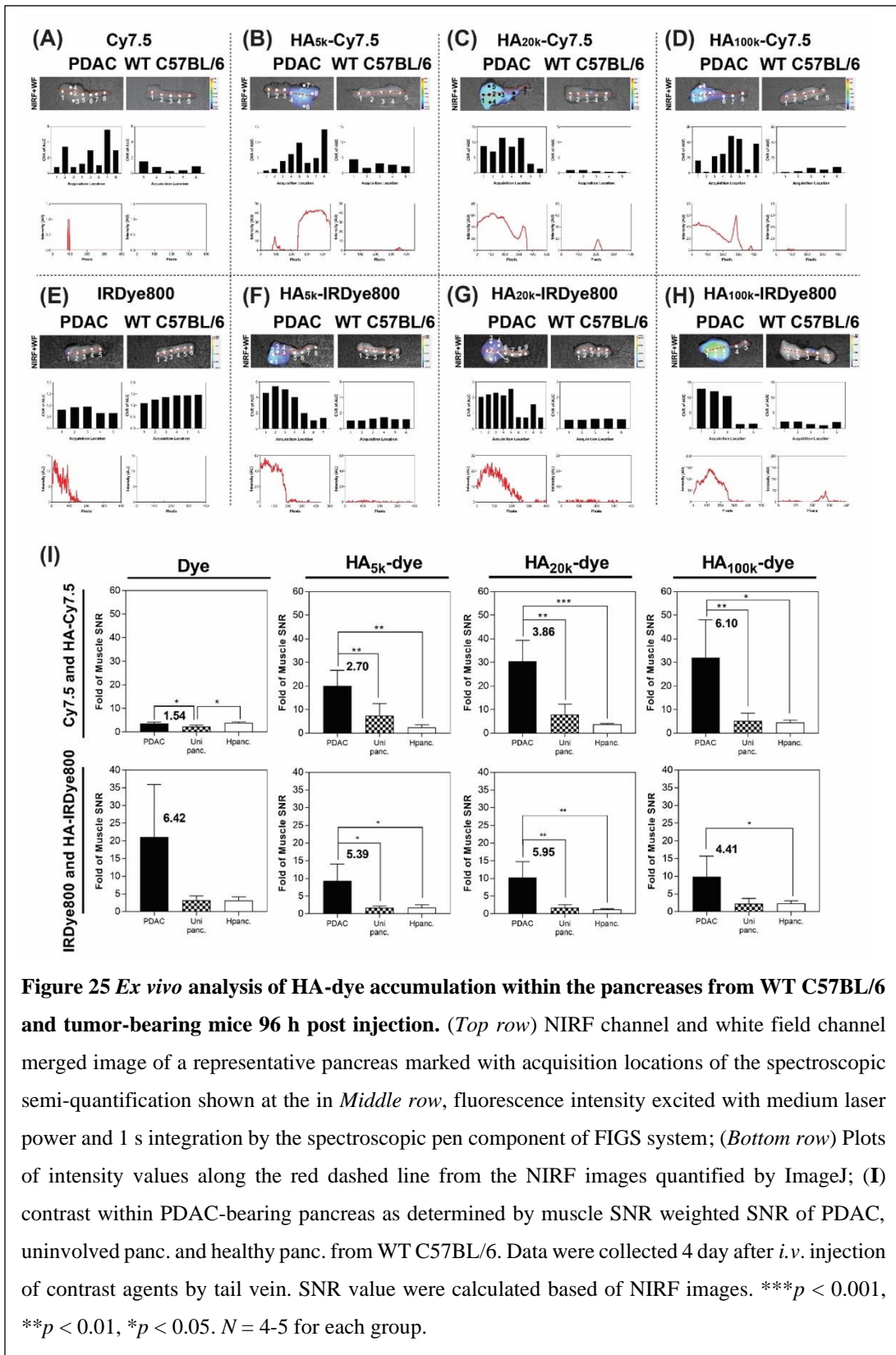
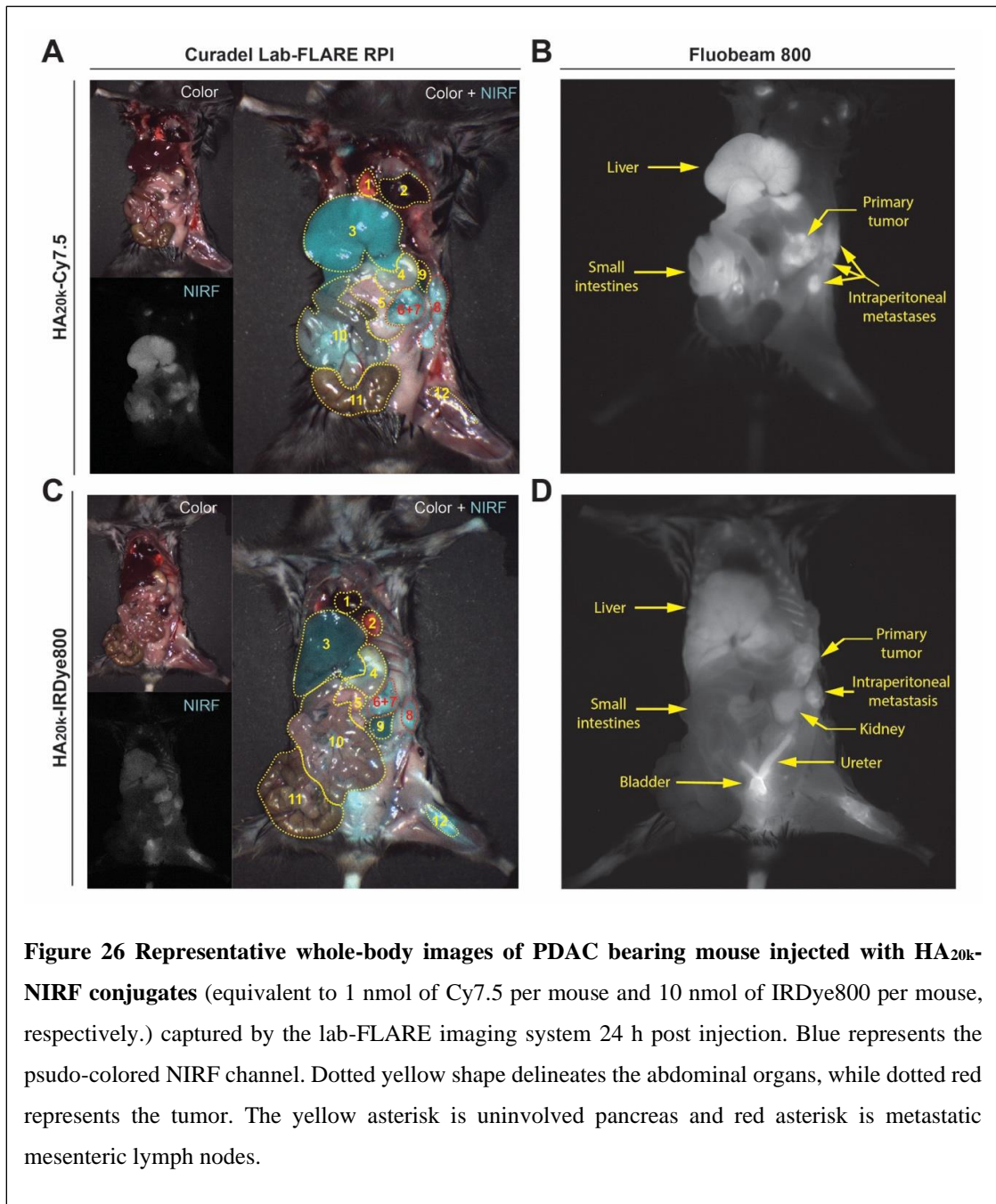


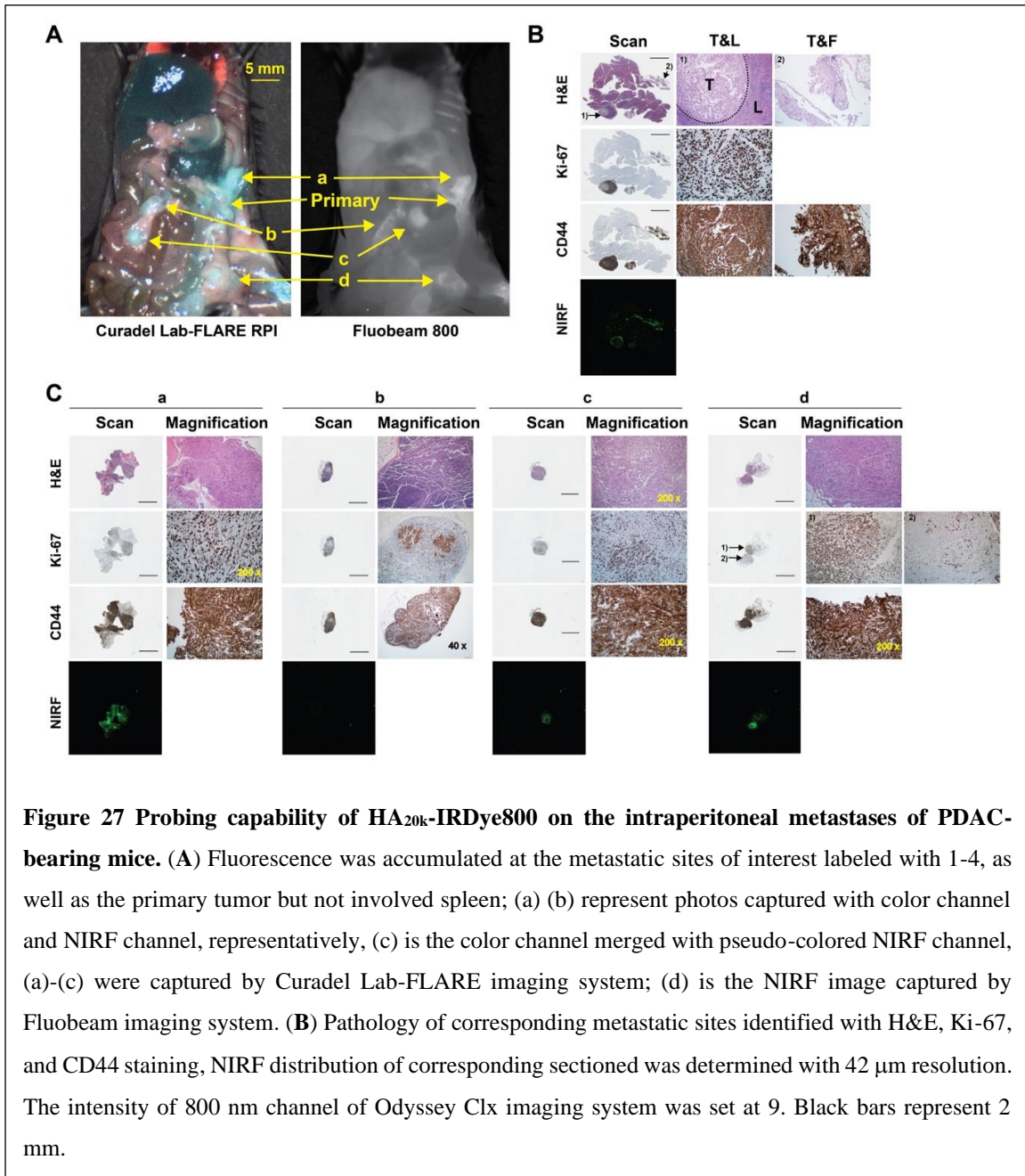
Figure 24 *Ex vivo* analysis of HA-dye accumulation within the pancreases from WT C57BL/6 (A, C) and tumor-bearing mice (B, D, E). HA_{20k}-Cy7.5 and HA_{20k}-IRDye800 treated healthy pancreases were plotted on the left for healthy control. Panel A-D were arranged into three rows for each group: (Top) NIRF and white-field (WF) images of a representative healthy/PDAC-bearing pancreas marked with acquisition locations of the spectroscopic signal shown in middle row; (middle, left) fluorescence intensity excited with medium laser power and 1 s integration time with the excitation laser component of FIGS system; (middle, right) plots of intensity values along the red dashed line from the NIRF images quantified by ImageJ; (bottom, left) scanned image of frozen-sectioned unstained healthy/PDAC-bearing pancreas with NIR channel from Odyssey Clx imaging system; (bottom, right) scanned H&E stained pancreas slides with Panoramic 250 flash series digital scanner, for each group pancreases were sequentially sectioned with unstained slides. All scale bars represent 2 mm; (E) SNR of PDAC, uninvolved pancreas (UP) and healthy pancreas (HP) normalized by muscle SNR that's been treated with (a) Cy7.5, (b) HA_{5k}-Cy7.5, (c) HA_{20k}-Cy7.5, (d) HA_{100k}-Cy7.5, (e) IRDye800, (f) HA_{5k}-IRDye800, (g) HA_{20k}-IRDye800, (h) HA_{100k}-IRDye800. Contrast data was obtained 24 h after *i.v.* injection. SNR values were calculated from NIRF images obtained with the Pearl Trilogy Small Animal Imaging System. ****p* < 0.001, ***p* < 0.01, **p* < 0.05, *N* = 4-5 for each group.





HA_{20k}-NIRF conjugates were able identify abdominal lesions smaller than 7 mm³ and lymphatic metastases (**Figure 27**). The presence of malignant tissue was supported by the hematoxylin and eosin (H&E) and positive staining of Ki-67 (**Figure 27B-C**). To that end, detailed histopathology investigation confirmed contrast enhancement of several

primary and metastatic PDAC malignancies. Sections of the primary lesion demonstrate nodules of epithelioid tumor cells within a peri-pancreatic lymph node and fat, the latter associated with a prominent inflammatory response (**Figure 27B**). The tumor cells demonstrated marked cytologic atypia without definitive glandular formation and adjacent pancreatic parenchyma was unremarkable. Immunostaining revealed that the tumor cells showed strong, diffuse membranous staining for CD44 in the background of expected staining within lymphocytes. While Ki-67 labeled >90% of tumor nuclei. PDAC invasion into soft tissue immediately adjacent to the pancreas had some areas that were more poorly differentiated with foci having a sarcomatoid appearance (**Figure 27C-a**). CD44 stained all tumor cells and Ki-67 labeled approximately 75% of all tumor nuclei. PDAC metastases to adipocytic tissue (**Figure 27C-c**) had consistent morphology and showed diffuse CD44 and strong cytoplasmic staining. Ki-67 labels 50-60% of tumor nuclei. In **Figure 27C-d**, tumor cells are seen involving adipose tissue, surrounding individual adipocytes. Interestingly, there is heterogeneity of morphology with some tumor cells being epithelioid with others having a spindled, sarcomatoid appearance. CD44 strongly labels all tumor cells, which could play a role in HA targeting of these malignancies.



Acute toxicity of HA_{20k}-NIRF was examined to further confirm their translational potential (Figure 28, 29). Upon the administration of HA_{20k}-NIRF conjugates at 20 times of the dose used for imaging, a comprehensive diagnostic profile was determined for indications of toxicities in liver, kidney, bone, GI, pancreas. Disorders including

malnutrition, dehydration, hyperglycemia/hypoglycemia were assessed. A slight increase of BUN for HA_{20k}-IRDye800 could be attributed to its renal clearance (**Figure 28**). Whereas reduced amount of total protein from HA_{20k}-Cy7.5 might be correlated with the strong protein adsorption (**Figure 28**). These aberrancies contradicted with the findings that lungs, kidneys, spleen, and heart were histologically unremarkable by H&E staining (**Figure 29**). Liver sections from each animal demonstrated mild, diffuse microvesicular steatosis within hepatocytes in the absence of lobular/portal inflammation, ballooning degeneration, or apoptosis. Brain sections overall were without abnormality with occasional animals showing scattered red neurons in Purkinje cells within the cerebellum.

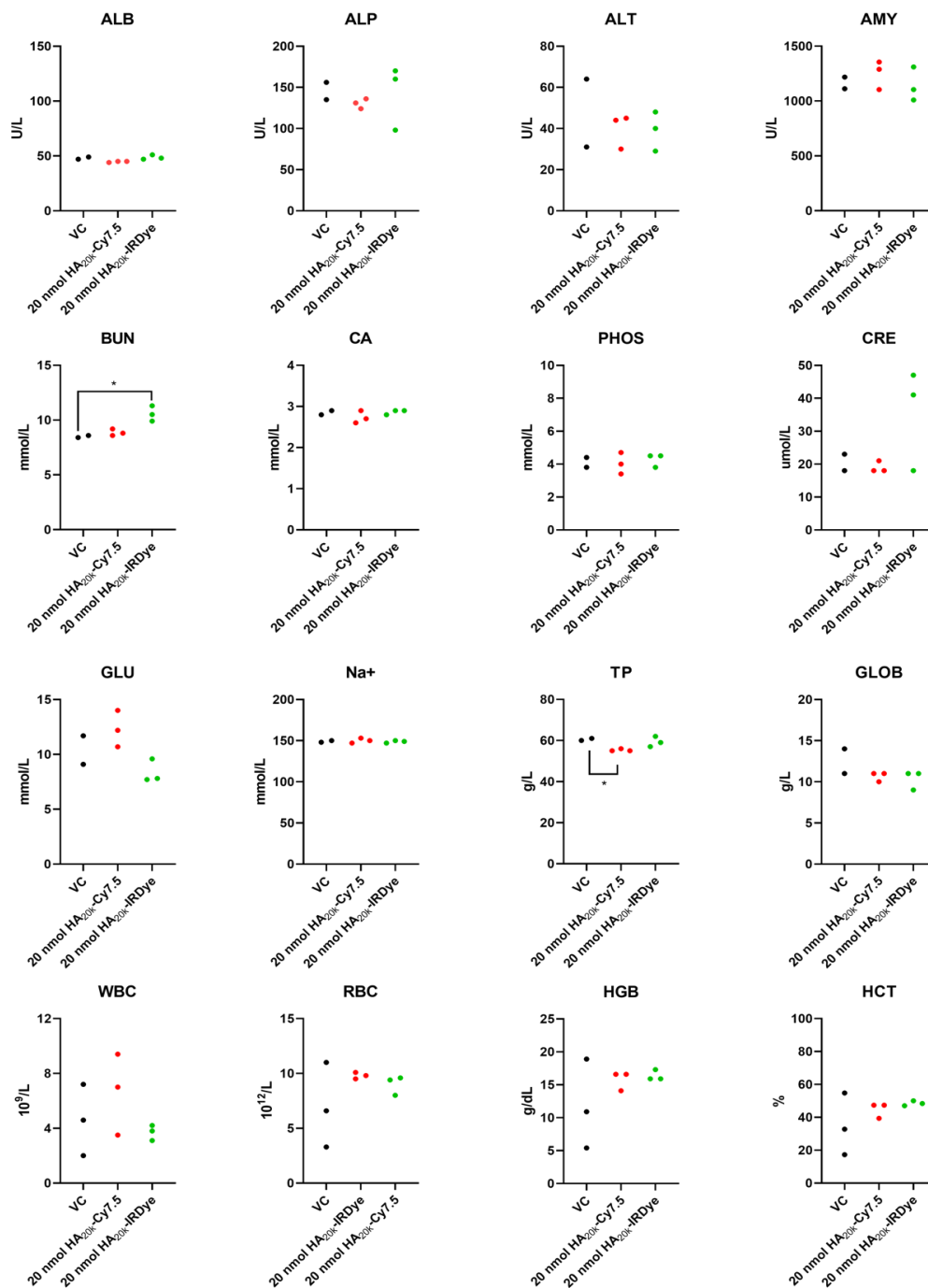
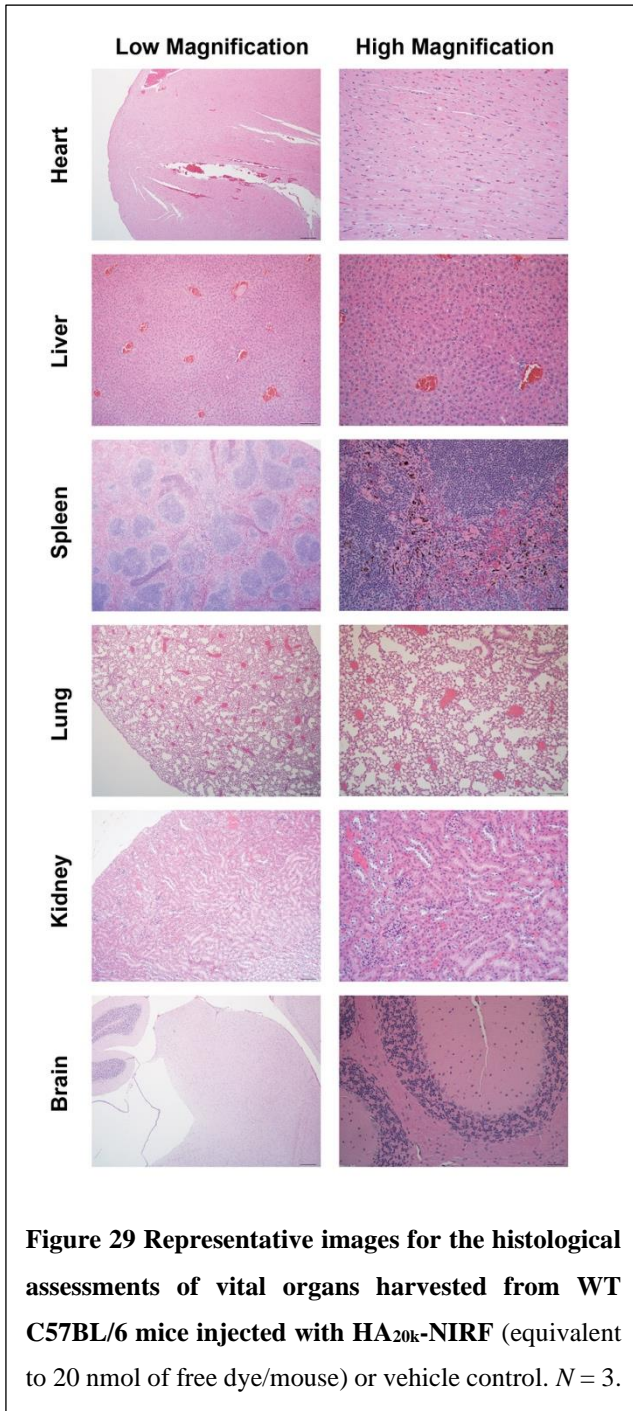


Figure 28 Comprehensive biochemical and hematological assessments for WT C57BL/6 mice injected with HA_{20k}-NIRF (equivalent to 20 nmol of free dye/mouse) or vehicle control for the acute toxicology study. *N* = 3.



3.4 Discussion

Tumor contrast enhancement relies not only on the accumulation of the contrast agent in tumor tissue, but also on the ability of the contrast agent to be removed from healthy surrounding tissues and organs. Accumulation and removal of imaging agent from tissue that is not malignant is the sum of several factors, including native dye clearance mechanism, physico-chemical properties of the contrast agent, and/or for potential phagocytic interaction, which directs agents to organs of RES [260], [261]. Therefore, several important criteria that can be tuned to control the *in vivo* biodistribution of contrast agents [157]. Size and hydrophobicity are decisive factors for kidney elimination and RES sequestration [262]: generally, particles with a hydrodynamic diameter up to 5-7 nm fall below renal filtration threshold and are excreted [263], while particles larger than 200 nm can be trapped in liver and spleen with prolonged retention. Hydrophilicity variation affects the pharmacokinetics of the probes as a result of distinct protein adsorption, which is more likely for hydrophobic than hydrophilic materials [264]. Protein adsorption could mediate the enhanced RES sequestration by promoting opsonization [138], [264], [265]. More importantly, serum protein adsorption increases the apparent hydrodynamic diameter of a hydrophobic molecules by more than 15 nm, which prevents the renal excretion [266]. The optimum pharmacological properties for *in vivo* application include minimum non-specific binding and an adequate retention time in the body preferably followed by fast excretion [267]. A better understanding with regard to how the characteristics of contrast agents influence their *in vivo* behavior is an important step towards designing NIRF biomaterials suitable for molecular imaging applications and for efficient tumor delivery [261].

On the basis of physiological parameters such as hepatic filtration, tissue

extravasation, tissue diffusion, and kidney excretion, it is clear that physical size of imaging agent has a profound impact on its *in vivo* distribution [138], [157] (**Figure 19**). Often macromolecules ($10 \text{ nm} \leq \text{size} \leq 100 \text{ nm}$) [138] afford prolonged blood half-lives to allow time for extravasation out of the vasculature. Nevertheless, small particles exhibited lower background signal due to rapid clearance, but provided less time for the probe to access the tumor [268]. As a linear homopolymer, HA demonstrated MW-dependent biodistribution.[269] Courel *et al.* [270] found the retention of tritiated high MW (HMW)-HA was 40-fold higher than that of HA oligomers on nude mice 5 h post injection; in addition, the highest accumulation was in kidney for HA oligomers and in liver for HMW-HA. Though conjugated with NIR fluorophore, HA-IRDye800 demonstrated consistent MW-dependent biodistribution as HA, (**Figure 19C-D, 20B**) because the large sized HA moiety drives the *in vivo* performance instead of the hydrophilic fluorophore. Whereas the Cy7.5 moiety is entropically favorable to bind with albumin (**Figure 12B, 14B**) with size enhancement, making them excluded from renal filtration and entrapped through hepatic filtration (**Figure 19A-B, 20A**).

Cyanine dyes are capable of forming H-aggregates by hydrophobic interaction, which characterized with hypsochromic absorption and weak fluorescence emission [271]–[273]. As shown in **Figure 12B** (Also in **Figure 13**), the absorption maximum blue-shifted for HA_{5k} and HA_{20k} conjugated Cy7.5 in H₂O, meanwhile the dimer absorption (represented by shoulder peak) becomes more visible as compared to Cy7.5, all suggest intermolecular hydrophobic interaction between Cy7.5 moiety. In comparison, the hydrophilic IRDye800 displayed limited tendency to interact among each other as opposed to with polar solvent molecules by strong ion-dipole interaction between sulfonate groups

and H₂O (**Figure 12C, 13**). The negative charge also acts as obstacle for proximity of heterocyclic rings between dyes, compromising hydrophobic interaction. Therefore, the spectroscopic changes of HA-IRDye800 were not apparent throughout varied solvents.

Non-specific protein adsorption affects the *in vivo* fate of contrast agent which is determined by its topography, composition (hydrophobicity), heterogeneity and potential surface physiochemical properties [274]. The strong binding of a fluorescent probe to albumin alters the pharmacokinetics of the probe, resulting in reduced diffusion into tissues and poor target contrast [275]. Nonuniformity of surface characteristics results in domains that can interact differently with proteins [274]. Berezin *et al.* [275] proved that fluorophore but not targeting moiety, is predominantly responsible for albumin binding of imaging probes. Meanwhile, HA is a biocompatible and safe drug carrier capable of reducing protein adsorption and potentially immunogenicity of the protein corona [201], [202]. Cyanine dyes such as ICG, are able to bind with plasma proteins with high affinity, results in complete extraction by hepatic parachyma and fast elimination into the bile [276], [277]. More importantly, hydrophilic dyes exhibited up to 2 orders of magnitude lower binding constants toward albumin than their hydrophobic counterparts [275]. Beckford *et al.* [278] claimed that increased hydrophobicity of the indolium side chain results in enhanced binding interaction within limitation threshold of steric hindrance. Accordingly, our study demonstrated that HA-Cy7.5 displayed more intensive binding with BSA as compared to HA-IRDye800CW (**Figure 14B-C**), which might attribute to the fact that benzindole is more hydrophobic than indole. Also, ionized sulfonate groups significantly weaken the hydrophobicity of IRDye800. The charged side chain is indicative of low protein binding and high serum stability.

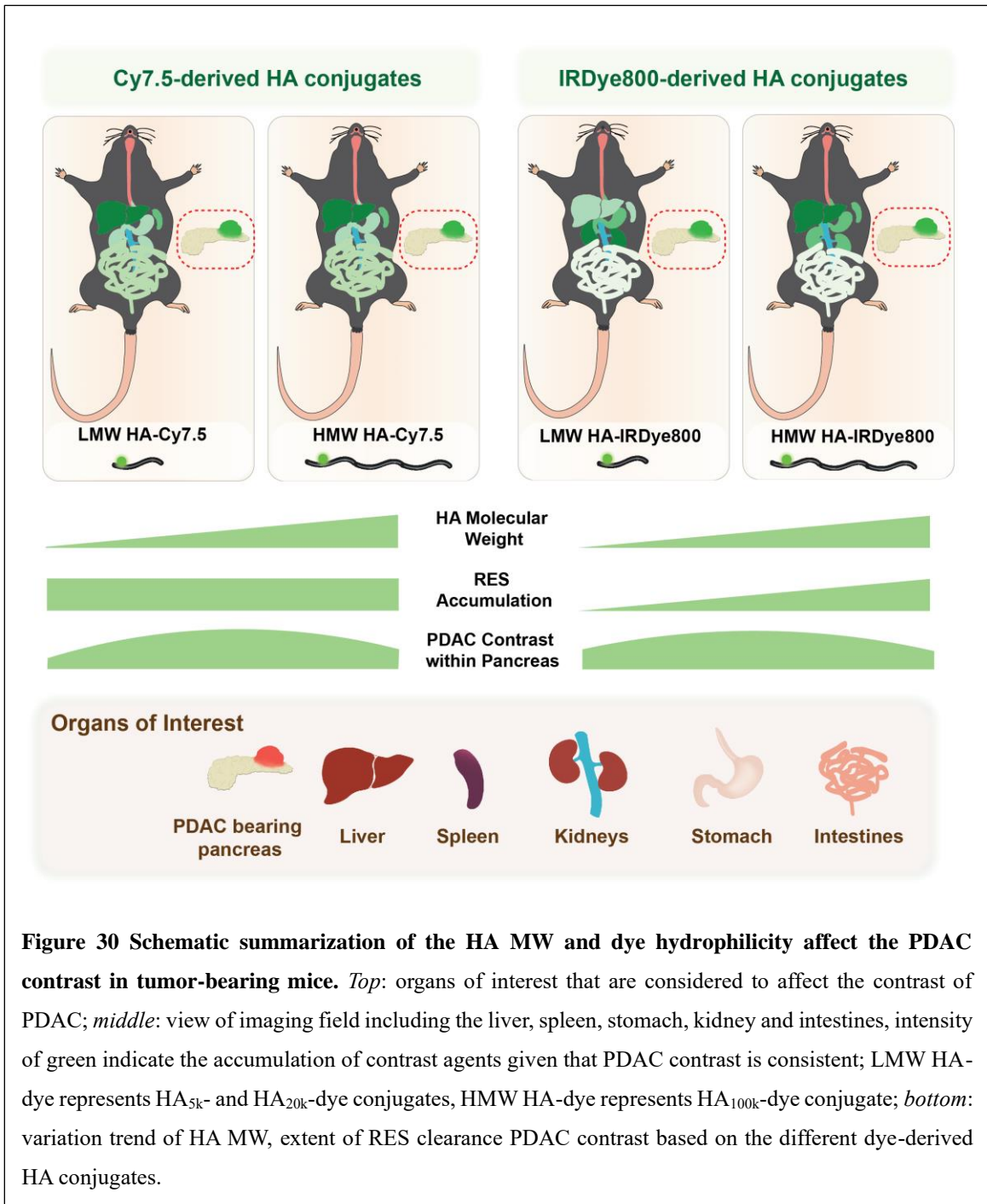
The tumoral retention of HA-dye depends on the interstitial binding of HA moiety after blood circulation and extravasation. Unlike many tumor types, PDAC is hypovascular with collapsed, but intact blood vessels, which is not desirable for EPR effect [279]–[281]. Cabral *et al.* [282] reported that sub-30 nm micelles could penetrate vasculature of pancreatic tumor. The calculated experimental hydrodynamic diameter of 30k HA is 15 nm, while 32 nm for 100k HA [283]. Therefore, HA_{5k}, HA_{20k} conjugated dye are presumed to extravasate more easily than HA_{100k}-dyes, meanwhile vascular bursts could potentially enhance permeability of pancreatic tumor blood vessels for large particles [284]. Additionally, PDAC is characterized with an extensive extracellular HA deposition, which is (34 ± 2.7) ng/mg tissue for normal pancreas in contrast to (420 ± 150) ng/mg for PDAC in *KPC* mice [232], [285], [286]. A wide variety of HA binding molecules (serum-derived HA-binding protein, versican) and receptors (CD44, LYVE-1, RHAMM) contribute to the formation of HA meshwork and anchorage to the cell surface [285]. Followed with extravasation, HA moiety of contrast agents bind to overexpressed CD44 (or potentially other HA binding receptors), which could confine the conjugates in tumor interstitium as opposed to diffusing back into blood vessels. Furthermore, the binding affinity relates with HA MW:HA oligomers with size of 38 disaccharide units (around HA_{20k}) showed higher avidity with CD44 compared with that of 10 disaccharide units (around HA_{5k}) due to multivalent binding [287]. In summary, PDAC vasculature is available for LMW HA-dye's extravasation, and HA-CD44 binding plays a role in retention within tumor, which may be the mechanism of HA-dye's robust contrast in PDAC.

Figure 31 outlines the tuning effects of HA MW and physicochemical properties of dyes on the accumulation of organs of interest. The CNR was defined by the tumor

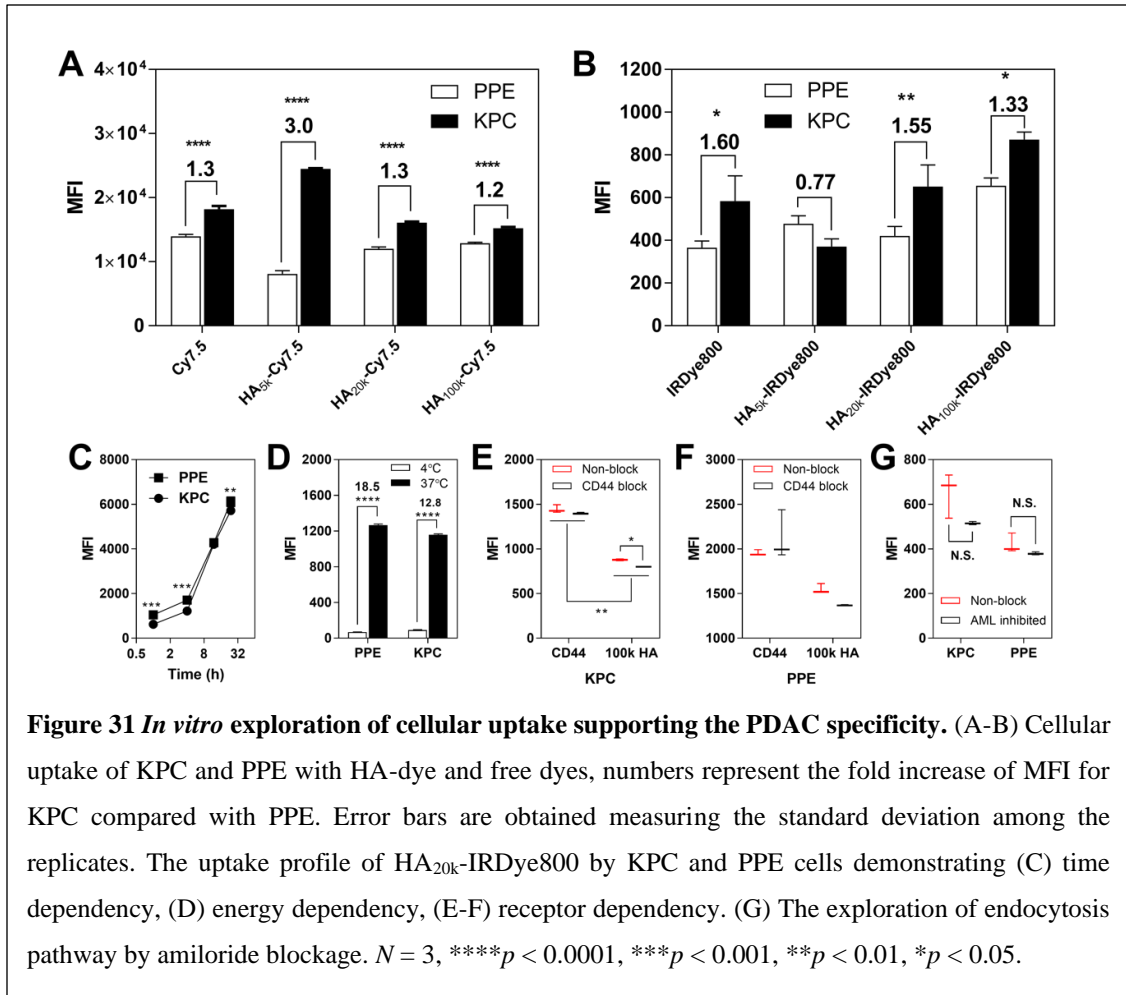
contrast which could be achieved by all the conjugation of HA (insets in the bottom). SNR is tuned to minimize the signal from liver, spleen and GI tracts. The strategy to reroute the native clearance of cyanine dyes from hepatobiliary to renal elimination and ease the RES burden of macromolecules results in the finding of optimized contrast agent (HA_{20k}-IRDye800) with minimal non-specific accumulation in background organs. The dominant factor is size, which could be affected by the HA MW as well as the protein association. As shown with the HA-Cy7.5, protein association with Cy7.5 normalize the biodistribution to the RES sequestered, hepatobiliary eliminated pattern, with marginal variation between different HA MW. Whereas the LMW HA conjugated IRDye800 falls below the renal threshold with reduced accumulation in RES organs, presumably caused by the native small size of LMW HA and hydrophilicity of IRDye800 unfavorable for plasma protein interaction. In summary, HA-dye conjugates provide a simple but versatile platform for imaging pancreatic tumor. Based on that, our study screened a promising contrast agent candidate for clinical translation as well as establishing a foundation for rational probe design, also it concludes the guidelines for efficient delivery of therapeutics to the tumor.

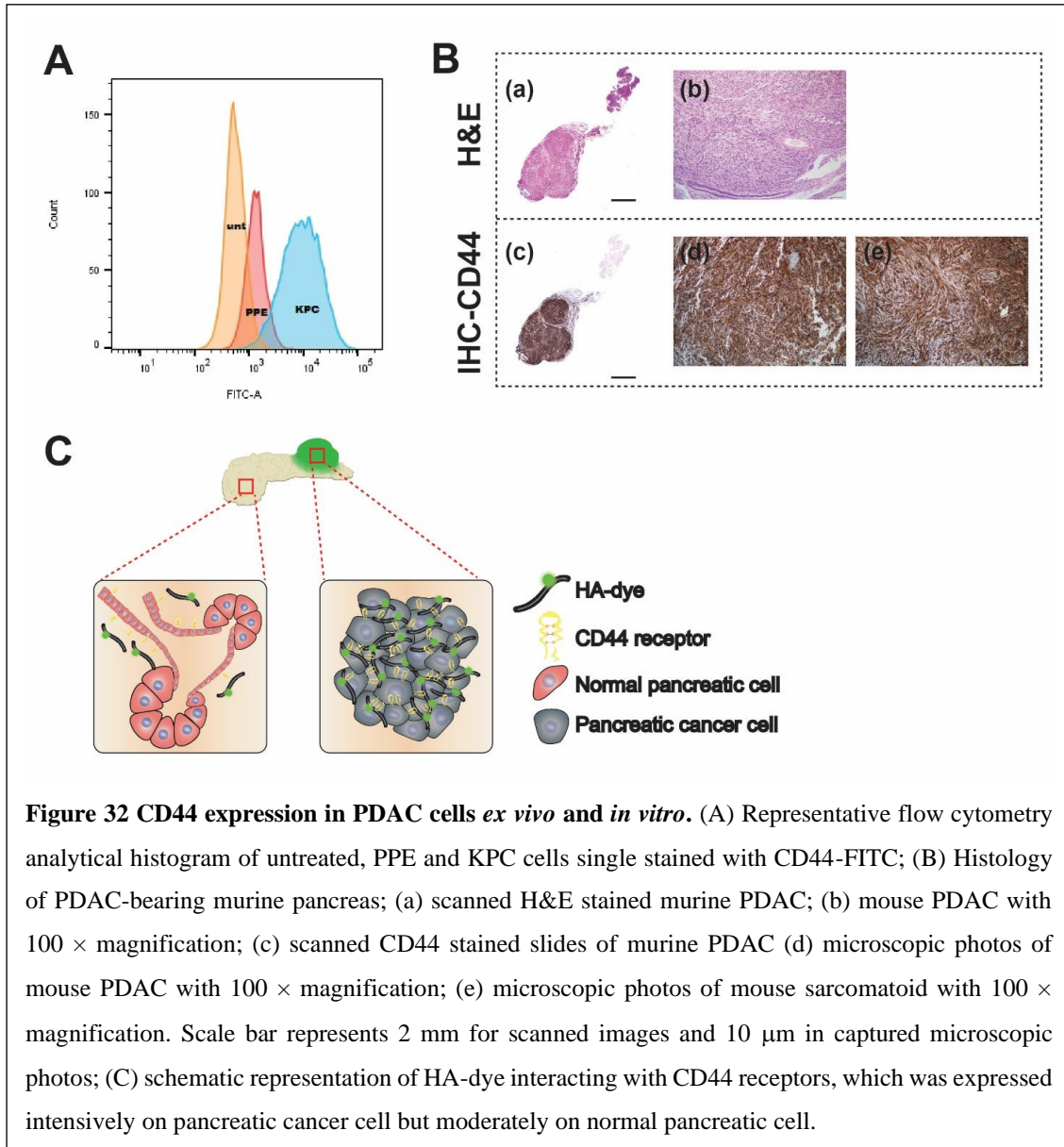
To account for the tumor specificity, we determined if HA-CD44 binding is responsible for the contrast within pancreas. When blocked with 100k HA, uptake of HA_{20k}-IRDye800 was significantly reduced both for KPC and PPE cells with $p < 0.0001$ (**Figure 31A-B**). In addition, uptake of HA_{20k}-IRDye800 is energy-dependent (**Figure 31D**), and not involved with micropincytosis (**Figure 31G**), indicating involvement of receptor-mediated pathway. Finally, uptake efficiency of HA-dyes was evaluated between PPE and KPC cells to support PDAC specificity *ex vivo* and *in vivo* (**Figure 32A-B**). Overall, the uptake efficiency was higher for KPC when compared with PPE under

identical conditions, regardless of HA MW and dyes. The fold increase of MFI for KPC as compared to PPE was 1.3, 3.0, 1.3, 1.2 for Cy7.5, 5k, 20k and 100k HA-Cy7.5, and, 1.6, 0.8, 1.6, 1.3 for IRDye800, 5k, 20k, 100k HA-IRDye800, respectively. The differences, though not as high as observed *in vivo*, were significant. Which matches with the CD44



expression between KPC and PPE cells, CD44 positivity contributes to the endocytosis of HA conjugated dyes for both KPC and PPE, the overexpression of CD44 in KPC favors the clustering of CD44, higher affinity and stronger binding of HA conjugated dyes, thus results in PDAC contrast macroscopically.





CHAPTER 4: PROBING THE CAPABILITY OF HA-BASED CONTRAST AGENTS FOR IDENTIFICATION OF PANCREATIC CANCER METASTASES

4.1 Introduction

Metastasis is the most common cause of death in cancer patients [288]. This is particularly true for pancreatic cancer, in which majority of patients are diagnosed with metastatic disease and few show a sustained response to adjuvant therapy [289]. As a result, patients undergo complete resection and adjuvant therapy often died of the metastatic development [290]. Most of the metastases occur in liver, and thus, patients likely harbor liver occult metastases at the time of surgery [290]. Finding these metastases has prognostic and therapeutic consequence for patients with resectable or boardline resectable PDAC. Therefore, an accurate detection of metastases not only aid with cancer staging and treatment planning, but also help avoid futile resection procedures that greatly decrease the quality of life of a patient that has no hope of being cured. Staging laproscopy and MDCT are reported for detection of intrahepatic occult metastases with controversial outcome [291]–[294]. Houghton *et al.* [295] reported that NIRF imaging is able to map the sentinel lymph node metastases of PDAC with CA19.9-targeted immunoconjugates, they also found that NIRF signal is apparent in numerous micrometastases, indicating NIRF imaging is applicable for imaging of PDAC metastases.

HA_{20k}-IRDye800 were previously reported to be highly efficient for tumor detection in PDAC mouse model with reduced background organ interference and

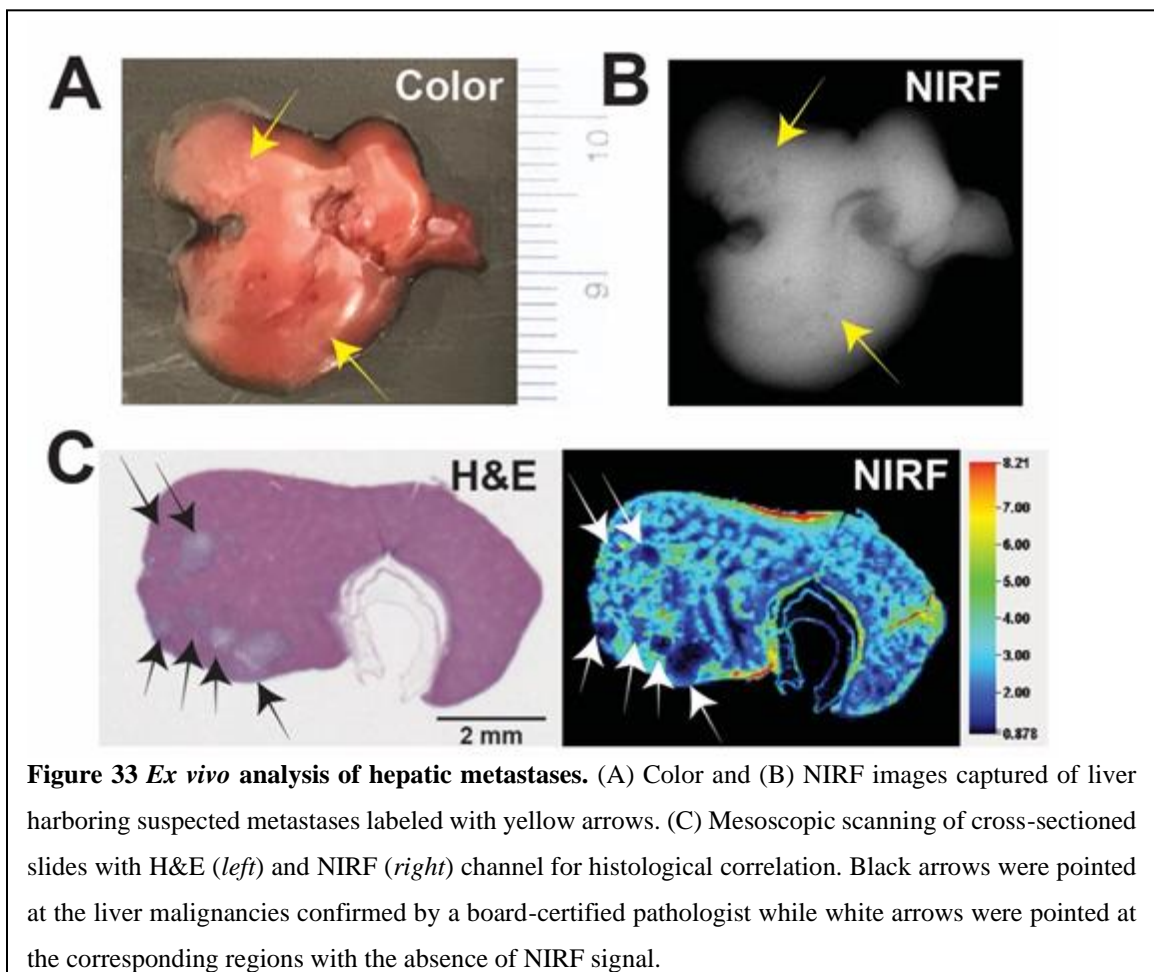
excellent contrast ratio. Furthermore, HA-NIRF conjugates displayed enhanced contrast in the primary tumor, with abdominal signal emphasized in different organs. Herein, we further explore its clinical applicability by using metastases models of PDAC, and determine the signal attenuation under varied metastatic sites.

4.2 Methods

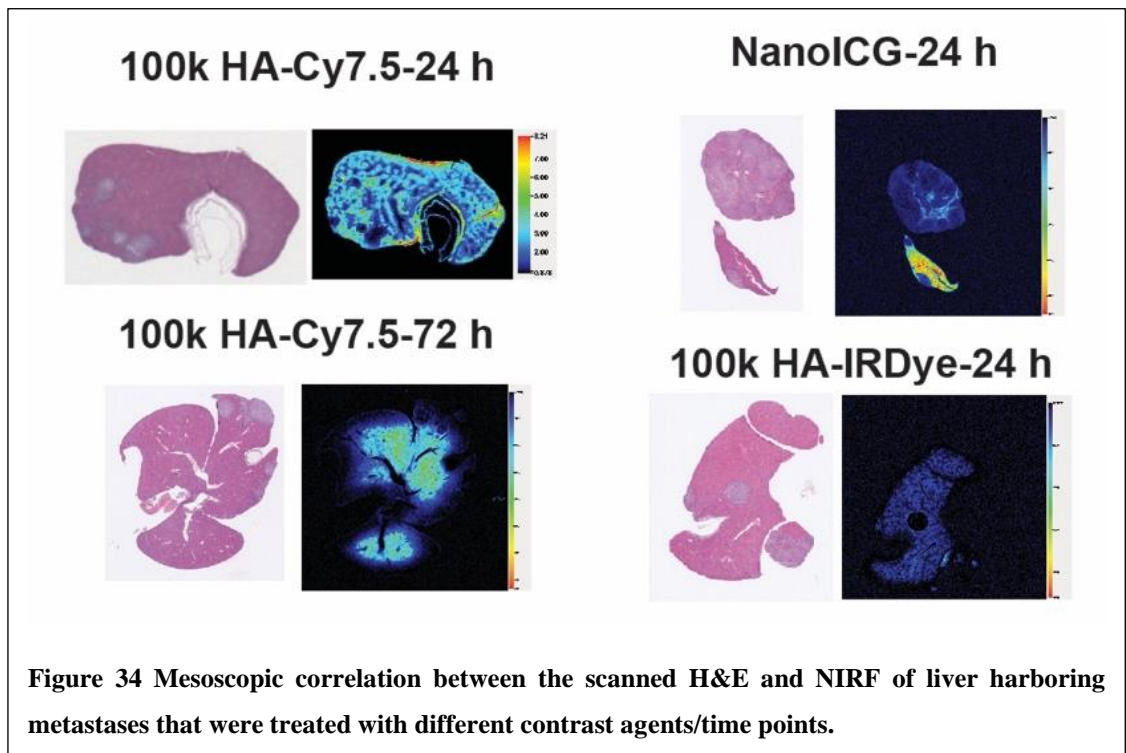
All animal studies were performed under a protocol approved by the UNMC Institutional Animal Care and Use Committee. Procedures were followed in accordance with institutional guidelines per the Guidelines on the Care and Use of Animals for Scientific Purposes. The guidelines were followed to ensure humane care of the animals. 10^6 KPC cells per mouse were injected in to the spleen of WT C57BL/6 mice and allowed to circulate for 1 minute. Vessels supplying the spleen were cauterized, and wound closed. The cells circulated to the liver were allowed to grow for 2-3 weeks [296]. External US imaging provide invaluable real-time data for tracking metastasis formation in liver [297]. Periodically, tumor-bearing mice will be examined with Visual Sonics Vevo 2100 US imaging system (FUJIFILM, Toronto, Canada). Upon the observation of liver metastases, HA_{20k}-Cy7.5, HA_{20k}-IRDye800, HA_{100k}-Cy7.5, HA_{100k}-IRDye800 and NanoICG were *i.v.* injected in tail vein of mouse model and monitored with NIRF setting at 12 h, 24 h and 72 h. To demarcate the areas of specific uptake and demonstrate preferential localization of the HA-based contrast agents, metastases located in the liver will be harvested and fixed with Formalin. Histologic analyses for regions of interest were conducted using hematoxylin and eosin (H&E) staining by a pathologist blinded to experimental conditions. The mesoscopic scan of fluorescence was correlated with histological H&E scan.

4.3 Results

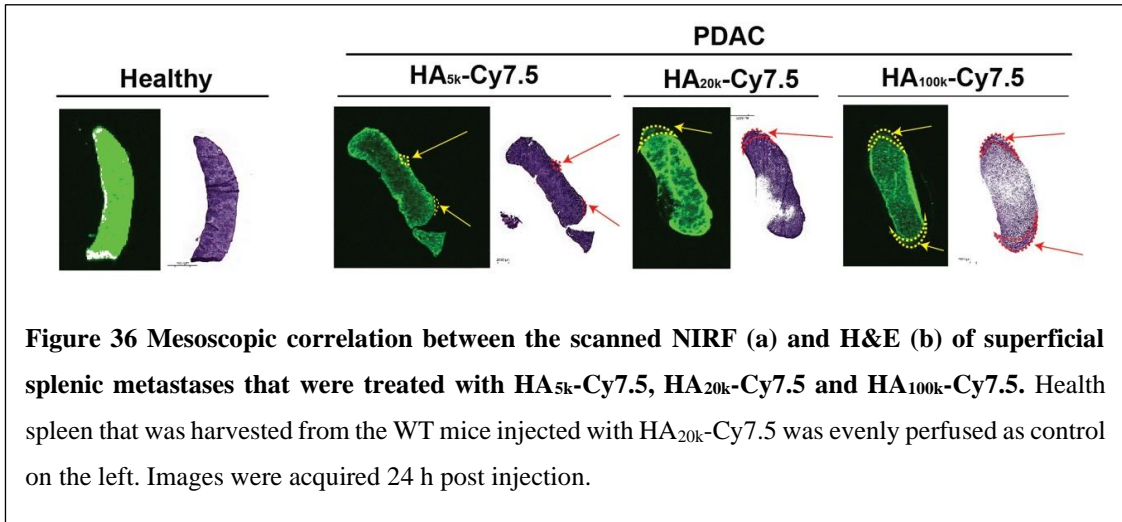
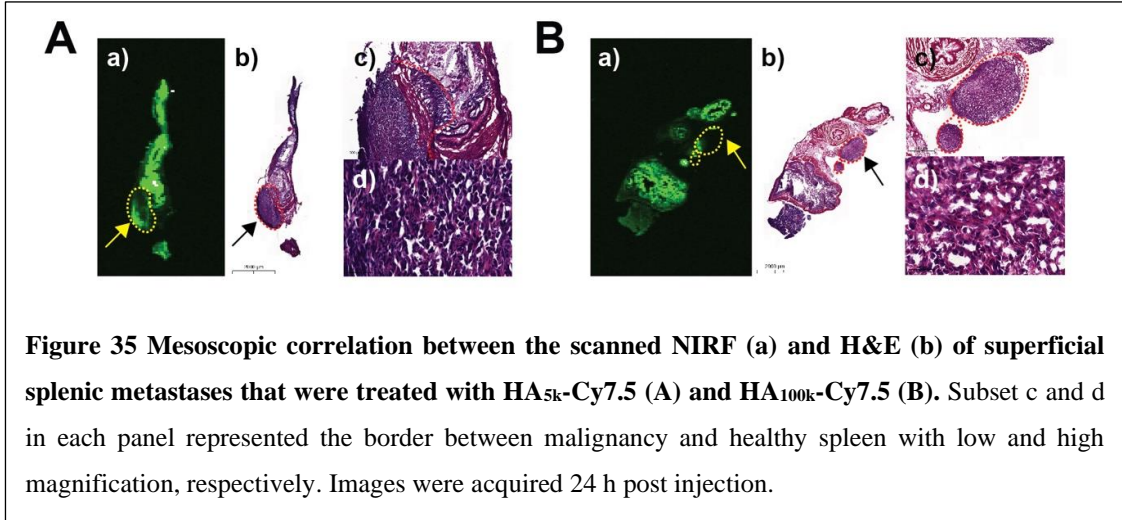
The development of hepatic metastatic model was optimized with gradient concentration (5×10^5 , 1×10^6 and 5×10^6 /mouse) of KPC cells and altered time (2 weeks, 3 weeks and 4 weeks) for tumor growth. When inoculated with 1×10^6 of KPC cells per mouse and developed for 2 weeks, scattered micrometastases with the size of less than 0.5 mm were observable on the surface of the medium lobe (**Figure 33**), which is marginally detectable in the white light field. It is worth mentioning that at this this level of metastases, the aberrancies in liver function were not detected, the malignancies were also non-detectable by transdominal US (data not shown). With the NIRF channel in the intraoperative setting, hypo-contrast of hepatic metastases was observed due to HA_{100k}-



Cy7.5, which was demonstrated to be utmostly accumulated in the liver among all HA-NIRF conjugates. The contrast is able to remain for at least 72 h. As those that tend to be trapped in the liver, HA_{100k}-IRDye800 and NanoICG also demonstrated hypo-contrast in identifying liver malignancies, but with limited contrast ratio due to low quantum yield. **(Figure 33)** In comparison, HA_{20k}-IRDye800 will exhibit no contrast due to minimal hepatic entrapment shown previously. This finding is in accordance with the fact the metabolism of contrast agents correlated with functional areas.



The hypo-contrast was also observed in metastases buried in the stomach (**Figure 35**) and on the surface of the spleen (**Figure 36**) due to HA-Cy7.5. The mesoscopic correlation between NIRF and H&E supported that malignant areas matched with those with the absence of NIRF. Compared with metastatic spots in the stomach wall, the splenic metastases are more frequently observed throughout HA-Cy7.5 groups with hypo-contrast.



4.4 Discussion

Liver is the common site for PDAC micrometastases, yet not considered for surgical resection due to uncontrollable and expansive growth pattern [298]. Therefore, a

specific imaging toolkit for detection of liver metastases will afford accurate staging and prognosis. ICG has been shown to accumulate around hepatic metastasis of pancreatic and colorectal cancers, probably due to retention of indocyanine green in compressed hepatocytes, which is shown by a fluorescent rim [299]. In 16% of patients undergoing pancreatic resection without preclinical detected hepatic metastases, fluorescence imaging revealed micrometastases of at least 1.5 mm, which was confirmed by histopathological examination. By revealing undetected hepatic metastases, NIR fluorescence imaging can further decrease the rate of futile pancreatic resections. However, due to the nonspecificity no tumor-specific targeting can be expected of ICG. Because of the permeation limit of NIR light, this method cannot be used to identify deep hepatic lesions. The utility of this technique is limited to superficial hepatic tumors. However, small lesions at the hepatic surface are likely to be missed by other imaging methods, such as CT, MRI, or US, because of partial volume effects or poor near-field resolution, whereas those conventional modalities are better at detecting deep hepatic lesions. Therefore, fluorescent examination seems to have complementary merits over other imaging techniques and, thus, is worth performing to examine the entire liver in detail [299]. The hypo-contrast demonstrated by the HA-Cy7.5 conjugates in the detection of hepatic metastases is in accordance with the recent clinical trial using Cetaximab-IRDye800 [176], which demonstrated hypo-contrast for the intraoperative detection of liver micrometastases.

CHAPTER 5: FUTURE DIRECTIONS

Due to our prior success in intraoperative imaging of PDAC, further investigation of the mechanism of targeting and the effects of extended systemic exposure is needed for optimizing contrast obtained *in vivo* as well as the PK profile of HA-based macromolecular contrast agents. We hypothesize that high contrast enhancement of HA-dyes is induced by receptor-mediated endocytosis, the difference in expression level of CD44 between KPC cells and healthy pancreatic epithelial cells contributes to the contrast between PDAC and uninvolved pancreas, the total amount of protein associated with HA-dyes is significantly reduced as compared to NanoICG, and the enriched protein species is innate to the RES system that confers the stealth effect of HA-dyes. These assumptions are foundational to the high sensitivity and enhanced pharmacokinetic profiles required for clinical translation of HA-conjugated dyes. Developing a deep understanding of the targeting ability of HA-dye conjugates is paramount for potential use as a biocompatible platform for effective delivery of chemotherapeutic agents to PDAC.

5.1 Research proposed for the near future

This research proposed for the near future seeks to characterize the enhanced contrast obtained when using HA-based NIRF probes for the detection of pancreatic cancer. The in-depth understanding of the fundamental cellular biology leading to contrast enhancement will not only illustrate the translational potential of HA-based contrast agents, but also aid in the future design of other macromolecular contrast agents for PDAC imaging. Investigating the mechanism of uptake from the perspectives of molecular pharmaceutics and physical pharmaceutics support the robustness of tumor-specificity, based on contrast enhancement displayed in a syngeneic, orthotopic PDAC model. Further evaluation of PK

profiles of macromolecular contrast agents would provide another avenue of innovation in this project, expanding impact beyond HA-based agents to other macromolecular contrast agents and improving potential for clinical translation of such formulations.

We expect the NIRF signal from HA-dye conjugates to overlay with the CD44 positive region, especially the triple-positive region, indicating specific uptake in malignant cells. We also expect that the lack of plasma associated proteins significantly reduce the macrophage adhesion while promoting the cellular uptake of KPC-PC for HA-dyes. HA-dyes displayed higher tumor accumulation than NanoICG, as demonstrated in our preliminary data, which we expect is due to lower affinity for plasma proteins with HA-dyes than with NanoICG. We also expect that the enriched proteins associated with HA-dyes, if any, belong to the dysopsonins that shield HA-dyes from being recognized by macrophages.

5.1.1 Preclinical investigation of in vivo performance for HA20k-Cy7.5

and HA20k-IRDye800 with PK study Detailed investigations of the PK properties of imaging agents remain critical to their successful clinical translation [300]. Therefore, the focus herein is to quantitatively elucidate the *in vivo* kinetics of HA-dye to identify optimal dosing strategies to provide the best chance of clinical benefit.

The first step is to investigate whether the HA_{20k}-dye conjugates will be stable in blood. Contrast agents will be incubated with freshly collected whole blood from Sprague-Dawley (SD) rats, and samples will be retrieved at predetermined times. The plasma will be analyzed for visible absorption and fluorescence emission as a function of time.

Simultaneously, I will work on setting and validating the bioanalytical method for the detection of HA_{20k}-dye conjugates on the LC-MS/MS.

The PK profile of HA_{20k}-Cy7.5, HA_{20k}-IRDye800 and free dye will be compared using three SD rats per contrast agent. Repeated blood sampling will be performed using jugular vein catheterization in rats (see detail in vertebrate animals). After the surgery, HA-dye will be injected into the jugular vein, samples will be taken at different time intervals and processed if needed. The kinetic parameters will be estimated with Phoenix WinNonlin (Certara, USA) software with non-linear PK/PD modeling.

5.1.2 Characterization of CD44-mediated cancer cell uptake and subcellular localization of HA-based contrast agents

The targeting mechanisms and specificity of cellular uptake are integral to obtaining contrast in intraoperative imaging. This aim seeks to develop an understanding of multifactorial influences including HA MW, cellular CD44 receptor expression level, temperature dependency, as well as HA blockage on the cellular uptake of HA-dye conjugates. It also seeks to determine the endocytic pathway and intracellular localization of HA-dye conjugates. To investigate ATP dependence on contrast enhancement, KPC cells will be incubated at either 37°C or 4°C along with the HA-dye conjugates. The cellular uptake will then be determined with flow cytometry (FC). Additionally, CD44 dependence will be investigated using corresponding MW of HA to block the CD44 receptors. Samples with blocked CD44 will be compared to those without CD44 blockage to elucidate the degree to which CD44-mediated endocytosis affects uptake of HA-dye conjugates. To further investigate whether HA-dye uptake is dependent on the expression level of CD44, we will compare the uptake between immortalized human pancreatic nestin-expressing (HPNE,

CD44 low expression) cells and KPC (CD44 high expression) cells to determine if high expression of CD44 translates into higher uptake of HA-dye conjugates. To explore the intracellular transporting mechanism of HA-dye conjugates, we will study the effects of membrane entry inhibitors on the cellular internalization of HA-dye conjugates.

The subcellular fate of contrast agents can also influence the ultimate translational applicability, especially for NIRF dyes which may degrade in harsh environments. Confocal scanning laser microscopy will be used to determine the subcellular location of HA-dye conjugates. Samples will be incubated with both HA-dye conjugates and the primary antibody for early endosomal marker Rab5 (anti-Rab5), which will help to determine the subcellular location and fate of HA-dye conjugates.

5.1.3 Gel separation and proteomic analysis of associated proteins of

HA_{20k}-dye conjugates HA_{20k}-dye conjugates at the theoretical plasma concentration will be incubated with an equal volume of pooled mouse plasma (Sigma-Aldrich, P9275) under constant agitation for the formation of HA-dye-protein complexes. The preliminary separation of associated protein from unbound protein will be performed with gel-filtration chromatography [GFC: ÄKTA Pure system (GE Healthcare) equipped with a Superdex 75 10/300 column, UV (collecting at 280 nm to detect protein) and fluorescence ($\lambda_{\text{ex}} = 760$ nm; $\lambda_{\text{em}} = 810$ nm to detect NIRF or HA-NIRF) detectors, and fraction collector in series will be applied for sample elution]. Eluted fractions that are positive for NIR fluorescence will be analyzed by bicinchoninic acid quantification to confirm the presence of protein. The free dyes will be used for negative controls.

The eluted fractions that are positive for NIRF will be precipitated with trichloroacetic acid. A protein pellet will be formed by centrifugation. The pellet will be

pooled for each group, and processed for two-dimensional polyacrylamide gel electrophoresis (2D-PAGE) [301]. The protein of interest (albumin, Complement C3, apolipoprotein A-I, Ig heavy chain alpha, gamma, Ig chain alpha) will be identified and compared between each group. To further analyze the proteome of HA-dye conjugates and dye only associated proteins, the protein pellet (processed as described previously) will be analyzed using a quantitative proteomics approach.

5.1.4 Expected results/Potential problems/Alternatives For the PK study, we expect the HA-dye conjugates are stable in whole blood due to the amide bond, HA-dye conjugates will have prolonged blood half-lives as compared with that of free dye, of which, HA-Cy7.5 will exhibit the most extended blood retention. Volume of distribution is expected to be significantly higher for HA-IRDye800 compared to HA-Cy7.5, as HA-IRDye800 is a hydrophilic polymeric derivative. Potential difficulties include stability of HA-dye in the blood, as hyaluronidase exist in the blood which degrade the HA to oligomers, so NIRF signal may not represent the original HA-based dye. The alternative strategy is to run GFC to separate NIRF-positive elutions and determine the time span for HA stability. 2) As far as the endocytic analysis, a higher level of NIRF will be co-localized with CD44 positive regions from *ex vivo* analysis of tissue as compared to other groups. We expect a significantly higher amount of CD44 positivity and NIRF uptake in KPC cells as compared with HPNE, and higher uptake with higher temperature and increased HA MW. The CD44-mediated internalization might occur via the lipid raft-mediated endocytosis pathway. HA-dye residues might be found in endo-lysosomal vesicles. 3) We expect that more protein will be associated with HA_{20k}-Cy7.5 conjugate compared to

HA_{20k}-IRDye800, and a higher level of complement protein and apolipoprotein will be associated with HA-Cy7.5.

5.2 New strategies proposed for PDAC therapy

Through our preliminary data and the experiments proposed in Aim 1, we anticipate robust tumor imaging of PDAC. However, eradication of PDAC is the ultimate goal of my research, which remains challenging due to tumor heterogeneity and therapy resistance [302]–[304]. In the next step, I will particularly focus on immunotherapy because it is superior than other therapeutic modalities at multiple aspects for sustained anti-tumor response, among which, immune checkpoint blockade (ICB) is a common denominator approach for improving T cell response [305], [306]. However, pancreatic cancer is poorly immunogenic and the tumor microenvironment contributes to immune tolerance [307]. Desmoplastic reaction, featured with hyaluronan and collagen deposition, contributes to immunosuppression of pancreatic cancer both biochemically and mechanically, and thus become a potential combinational target for immunotherapy [308]–[312]. Either pharmacological or genetic targeting for dense matrix depletion lacks evidence for sensitizing immunotherapy, but the combination of both create strategies for efficient disturbance of immunosuppressive matrix [175], [313]. Therefore, my third research aim will be to develop immunotherapy-based combinational strategies for the treatment of advanced, resistant pancreatic tumor, including exploring delivery strategies for genetic targeting and determination of anti-tumor immune response.

Tumors are heterogeneous and ever-evolving, so drugs that are designed to kill cancer cells directly by targeting cell intrinsic pathways inherently select for resistant clones that lead to relapse [306]. Clinical data confirms that stimulating a patient's natural

antitumor immune response can cure relapsed, refractory patients with difficult-to-treat cancers who have exhausted other treatment options [306], [314], [315]. Immunotherapy by immune checkpoint blockade (ICB) is a promising approach to activate therapeutic antitumor immunity and can bring long-lasting clinical benefits [316], but only a fraction of patients respond to treatment and significant immune-related adverse events exist [317], [318]. ICB improved the therapeutic outcome in melanoma and lung cancer [319]–[322], which might be related to their high mutational load-induced antigen presentation [323], [324]. However, other solid tumors that carry less mutational burden, are resistant to ICB due to inadequate T cell infiltration and stroma-associated immune suppression [325], [326]. Meanwhile, ICB-based combinational therapeutic interventions are extensively explored [327]–[329], but remains challenging due to the poor delivery and distribution of ICB in the tumor. Specifically, tumors undergo significant remodeling that results in high cross-linked and dense extracellular matrix, which increases interstitial fluid pressure, constricts both tumor lymphatics and tumor blood vessels as a “binding site barrier” [330]. Of importance, dense matrix led to failure of several strategies aimed at improving effector T cell infiltration by blocking their entry into tumor bed [331], [332]. Hence, normalizing the tumor matrix and microvasculature using extracellular matrix-degrading enzymes, extracellular matrix antagonists, and anti-angiogenic therapies hold promise for improving the entry and penetration of ICB [333], [334].

Pancreatic cancer is unique from an immunological perspective with the hallmark of dense desmoplastic reaction [308]–[310], in which hyaluronic acid and collagen contribute to solid stress [311]. The dense matrix exerts both mechanical and biochemical effects on immunosuppression and drug delivery [312]. Although depletion of cancer-

associated fibroblast induce vessel perfusion, it results in tumor metastasis and immune suppression in pancreatic cancer [335], [336]. Au *et al.* summarized that collagenase promotes dispersion of larger molecules and nanoparticles, whereas hyaluronidase is more effective for small molecules [337], [338]. Furthermore, collagenase promote T cell penetration, indicating its relevance with immuno-therapy [337]. However, there's a lack of knowledge on how the blood perfusion facilitates ICB in PDAC. Based on the background above, I hypothesize that collagenase and hyaluronidase could convert desmoplastic tumors from ICB-resistant to ICB-sensitive for pancreatic tumors and would improve the antitumoral immune response by enhancing the blood perfusion. To test my hypothesis, I intend to pursue immuno-oncological research to answer the following fundamental questions: (1) What would be the best delivery strategies for hyaluronidase and collagenase to reduce collateral damage/risk of tumor progression? (2) How to decide the matrix modeling window that facilitates the ICB? (3) Will the anti-tumor efficiency improve post desmoplasia depletion? (4) Will genetic targeting create a synergistic effect with pharmacologic targeting for eradicating dense matrix?

Cancer treatment by ICB can bring long-lasting clinical benefits, but only a fraction of patients respond to treatment [317]. In order to sensitize the pancreatic cancer immunosuppressive microenvironment with ICB, I propose to deplete the hyaluronan and collagen-the major component for the dense matrix-through pharmacological and genetic targeting, and explore the anti-tumor immunity by 1) determining deliver strategies of matrix-depleting agents; 2) determine the time-frame of matrix remodeling for ICB; 3) investigate the immune responsive cell populations and cytokines; 4) synergistic effect of combining the genetic and pharmacologic matrix-depletion for ICB. My hypothesis is that

by pharmacological and genetic targeting of matrix-depletion, pancreatic tumor will be responsive for ICB as demonstrated by reduced immunosuppressive cells, and increased level of effector T cells and immune cytokines.

5.2.1 To determine the optimized delivery strategies for hyaluronidase, collagenase Though bacteriophage vector was reported for the co-delivery of hyaluronidase and collagenase [339], it raises concerns for immune responses. Poly (Lactic-*co*-glycolid)-*b*-polyethylene glycol (PLGA-PEG) polymer-based delivery system was reported for the delivery of collagenase and recombinant human hyaluronidase PH20 (rHuPH20) with high efficiency and biocompatibility [340], [341]. Therefore, it holds promise for enzyme loading without interfering with IBC.

Preparation of PLGA-PEG loaded hyaluronidase and collagenase (NPhc), hyaluronidase (NPh) and collagenase (NPc) will be similar as previously reported [341]. The thiolated enzymes will be conjugated, followed by a protective layer of fabricated PEG for prolonging the half-life of enzymes. The conjugated unit of enzymes will be determined by a microtiter-based assay for HA and collagen degradation. Fluorophores will be entrapped for imaging detection (NPhc-DiD) as mentioned in 2.2.

Catalytic efficiency of NPhc: The enzymatic efficiency will be investigated with the pancreatic tumor spheroids. Using the previous report, 3-D tumor spheroids of MIAPaCa-2 and PANC-1 will be developed [342]. The type I collagen and HA in the supernatants of cells before and after NPhc treatment will be quantified using enzyme-linked immunosorbent assay (ELISA) for HA and Sirius Red assay for collagen, respectively [339].

Dorsal skinfold window chamber tumor model [343] will be applied with PANC-1 cells in BALB/c nude mice, for the *in vivo* determination of perfusion after matrix depletion. NPh, NPc and a vehicle control will be used as the controls for NPhc. The time frame of NPhc might be different than free enzymes, which will be adjusted accordingly. The number of vessels that are opened for NPhc will be compared with NPh, NPc, vehicle control and/or free enzymes.

5.2.2 To decide the time frame of matrix modeling for ICB perfusion

The dynamic change of tumor remodeling requires efficient therapeutic deliveries within the optimal modeling time frame [175]. PANC-1 cells will be implanted in nude mice to determine the biodistribution. DiD-encapsulated NPhc will be injected into the tumor-bearing mice in 2.1.3 via orthotopic implantation. Upon the injection of DiD encapsulated NP, NPh, NPc, NPhc, the tumor will be harvested at different time intervals. Immunohistochemical (IHC) analysis of HA, collagen, CD31, and fluorescence signal of tumor with IVIS will be used to determine the optimal time for matrix depletion. ICB will be administered according to the predetermined optimal time. IHC of HA, collagen and fluorescent signal will be used to visualize the desmoplastic breakage.

5.2.3 To investigate the delivery efficiency for the antitumor immunotherapy

To define the application and mechanism of extracellular-depleted ICB, we will examine the immune response by quantifying cellular subsets and cytokines of interest. We will also use an advanced tumor model to study survival and molecular responses.

Mouse model of primary and metastases C57BL/6 mice will be inoculated with Panc02 cells either in the pancreatic tail as a primary tumor or in the hemi-spleen as an

advanced tumor model [344]. The NPhc will be injected 2 weeks post tumor implantation. 24 h post NPhc injection, anti-mouse PD-1, anti-mouse PD-L1 or IgG control will be administered. The groups will include: NP+IgG, NPhc+IgG, NP+ICB, and NPhc+ICB. The treatments will be given 3 times in 9 days and the mice will be monitored 3 times a week for survival studies.

Analysis of infiltrating lymphocytes Murine livers and spleens will be mashed, centrifuged and suspended in Percoll density gradient media for identification of the lymphocyte layer. Cells will be labelled with CD3, CD8, CD4, CD25 and Foxp3 for the identification of regulatory T cells (Treg) and effector T cells.

Determination of intracellular interferon gamma (IFN γ) isolated liver infiltrating lymphocytes and splenocytes will be enriched for CD8 cells using CD8 negative isolation kits. Golgistop will be added to the enriched cells, followed by the incubation of antibodies for CD8, CD4 and a live marker. The IFN γ antibody will be added for FC assays. An ELISA for mouse IFN γ will also be applied on the CD8 enriched cells for quantification.

5.2.4 Exploration of genetic targeting of fibrosis with ICB In addition to pharmacologic targeting of desmoplasia; genetic targeting of fibrotic signaling has been proved to be efficient for reducing immunosuppressive cells, but failed in the clinical trial as single treatment [313]. Extracellular matrix deposition is a complex process and intervention from multi-aspects to break the matrix. Therefore, the combination of pharmacological and genetic targeting will be of interest to potentiate immunotherapy and become a promising strategy to achieve durable regression of PDAC. We specifically choose the focal adhesion kinase (FAK) as the genetic targeting [313], and hypothesize the

synergistic effect will be induced with NPhc for ICB. The combination of FAK inhibitor with NPhc and ICB will be explored with KPC and the more aggressive KPPC (*p48-Cre;LSL-Kras^{G12D};Trp53^{flox/flox}*) mice. The FAK inhibitor will be physically entrapped in the NPhc, named NPhck. The treatment will be applied to KPC-derived orthotopic model on C57BL/6 mice for preliminary evaluation, then using KPC and KPPC mice for the detailed evaluation of immunotherapy. The detailed assessment includes *ex vivo analysis of* cytokine profile (ELISA), the population of myeloid-derived suppressor cells, tumor-associated macrophages and Treg (FC and immunohistology). The survival time, tumor burden and body weight will also be recorded.

5.2.5 Expected results: I expect successful completion of the experiments proposed in Aim 2 will lead to a clear understanding of the desmoplastic depletion for sensitizing the PDAC with ICB. I also expect that the co-delivery of pharmacological and genetic targeting agents of fibrosis will be synergistic for perturbing tumor stasis and favoring the T cell infiltration. Specifically, the PEG-PLGA delivery of hyaluronidase and collagenase to tumor sites could disrupt the extracellular matrix of PDAC which would release solid stress. The perfusion time frame will be determined with PK/PD in Aim 2.2, which we predict will be 24 h. The immunosuppression of advanced PDAC will be reversed by the release of solid stress from the tumor resulting in an improved immune response, as evidenced by improved CD8 T cell infiltration, secreted cytokines, and reduced population of immune suppressive cells. The combination of pharmacological and genetic targeted depletion of matrix will synergistically reverse the fibrosis of PDAC for ICB intervention, both in an orthotopic model and KPC mice.

To obtain the skills necessary to complete these aims, I will acquire information about gene editing ethics, gene knockout strategy, and the mechanism for breeding select types of transgenic mice. I will also investigate methods for discovering relevant target signaling pathways, as well as developing technical skills such as ELISA, tumor spheroid culturing, quantification of cytokines and subcellular population of interest.

5.2.6 The challenges and alternatives would include: 1) the stability and efficacy of NPnc might be compromised in the systemic circulation. Size-induced splenic and hepatic uptake would raise concerns for the delivery efficiency of enzymes, antigen presentation and T cell activation in the spleen. 2) hyaluronidase and collagenase exist in tumors, which might enhance tumor progress, and cause collateral damage in healthy organs. Thus, the stealth coating of PEG will need manipulation in terms of MW, concentration and reaction time for the optimal delivery efficiency. Localized delivery might be another alternative, for example, the peritumoral delivery of PLGA-PEG-PLGA gel for the sustained release of enzymes [340]. 3) the basal state of the mouse immune system might be affected by the husbandry condition of the pathogen, which could cause significant individual differences in basal cytokine levels and lymphocyte populations. The alternative is to keep the mice in specific pathogen free conditions, and use the same mouse model for determining the basal immunogenic parameters. 4) FAK is not a genetic target specific for eradicating collagen and hyaluronic acid, but HAS2 [345], ROCK2 [346] were reported to regulate the synthesis of hyaluronic acid and collagen, which might be of value for specific genetic targeting.

Common classification of anticancer agents includes kinase inhibitors, therapeutic antibodies, antibody-drug conjugates, immunotherapies and chemotherapies. The kinase

target include epidermal growth factor receptor [347], phosphatidylinositide 3-kinase [348], [349], mitogen-activated extracellular signal regulated kinase kinase [350]. Currently, there are four chemotherapy drugs approved by the US FDA for the treatment of pancreatic cancer: ABRASANE (albumin-bound paclitaxel), Gemzar (gemcitabine), 5-FU (fluorouracil) and ONIVYDE (irinotecan liposome injection). In addition, FOLFIRINOX, a combination of three chemotherapy drugs (5-FU/leucovorin, irinotecan and oxaliplatin) is commonly used in the treatment of metastatic pancreatic adenocarcinoma due to the positive response in a Phase 3 trial. There are reports of new chemotherapeutics that reported to treat advanced pancreatic cancer but end in failure: metformin [351], nanoliposomal irinotecan in combination with fluorouracil and folinic acid [352].

Cancer immune evasion is observed in PDAC [353]. Immunotherapy is ineffective for PDAC due to multiple reasons: first, cancer cell-specific CD8⁺ T cells did not respond to two immunological checkpoint antagonists that promote the function of T cells: anti-cytotoxic T-lymphocyte-associated protein 4 (α -CTLA-4) and α -programmed cell death 1 ligand 1 (α -PD-L1) [354]. Second is the poor antigenicity. As the key initial step of launching effective anti-tumor immunity, antigenicity is inferred by the mutational landscape [355]. PDAC has 30-40 mutations per tumor as compared to 160-170 for colorectal cancer [356]. Third, leukocyte invasion was dominated by immunosuppressive cell types, such as tumor-associated macrophages, myeloid-derived suppressor cells and Treg cells.

The discovery of the perfect target and translation of molecular-targeted imaging to the clinic remains challenging due to the need for specific exogenous imaging agents in order to image the biochemical process of interest. The discovery and validation of such

imaging targets is time-consuming and expensive, and rarely results in a clinically useful agent. Many of the imaging probes reported to be efficacious in animal models have failed to reach the clinic and are still in the investigational stage [357], [358]. Unfortunately, the extensive approval process of the FDA makes it impossible to quickly test imaging probes in a clinical pilot study in order to determine effectiveness in humans and thus save resources and concentrate on more promising probes [359]. In addition, the added value of molecularly-targeted imaging to patient benefit still needs to be proven before wide-spread use of this technique is expected. This needs to be accomplished by increasing the number of human trials using a standardized technique to demonstrate safety and effectiveness. Although this is still far from current reality, the bulk of preclinical studies and the first successful clinical studies show that more wide-spread clinical use is on the horizon.

5.3 Challenges to translate new molecularly targeted contrast agents into the clinic

It is expected that ongoing complementary research on new biomarker and imaging-based approaches will result in earlier detection of pancreatic cancer in the future. However, one of the challenges in developing new molecular imaging-based approaches with novel contrast agents is the inability to fail quickly and early during the contrast agent development process, in particular during the costly phases of clinical testing. Ideally, once a new contrast agent has shown to be safe and effective in preclinical studies, the agent should be quickly tested in pilot clinical trials to assess its efficacy in patients. If the agent continues to show promise in the clinical setting, its development could be expedited, whereas its development could be halted immediately upon disappointing results. This recognition of quick and early failure would give researchers the opportunity to save

resources and concentrate their efforts on the most promising contrast agent candidates to be moved through the different phases of clinical trials. However, since molecular imaging agents are treated as drugs by the FDA, they must undergo the same lengthy approval process as any other drug. This does not allow for quick go or no-go decisions for many contrast agents.

Fortunately, for PET contrast agents that are injected with trace amounts (defined as $\leq 100 \mu\text{g}$ for imaging agents and 30 nmol for protein products), an exploratory investigative new drug application (IND) pathway had been introduced by the FDA, allowing translation into early first-in-human phase 0 clinical trials, with less requirements for preclinical animal testing than it is typically needed for a traditional IND [52]. A cost-effective pipeline for obtaining traditional IND approvals from FDA to allow timely translation of new PET agents was recently reported [360]. Through this pipeline, a traditional IND for a PET probe can be obtained within 7 months at a cost of approximately \$50 000, if safety and toxicity assessment are obtained for several agents conjointly and by using the internal and nonprofit facilities. The cost was estimated at \$150,000 per agent using contract research organizations [360]. Though there is less experience in clinical translation for molecularly targeted contrast agents other than PET agents, this example shows that the FDA approval process for molecular contrast agents can be expedited through a team effort. It is expected that similar pipelines could be developed for other types of contrast agents in the future, and the experience from this process could be leveraged to expedite translating similar or next-generation US contrast agents into the clinic [360].

5.4 Novel imaging of molecular targets is an emerging area crucial to the development of targeted drugs

Targeted drugs hold great promise for the treatment of malignant tumors. However, there are several challenges for efficient evaluation of these drugs in preclinical and clinical studies. These challenges include identifying the biologically active concentration and dose schedule, selecting the patients likely to benefit from the treatment, monitoring inhibition of the targeted protein or pathway, and assessing the response of the tumor to therapeutics. Although anatomic imaging will remain important, molecular imaging provides several new opportunities to make the process of drug development more efficient. Various techniques for molecular imaging that enable noninvasive and quantitative imaging are now available to aid development and evaluation of new drugs for the treatment of cancer. In the following paragraphs, we will discuss the integration of molecular imaging into the process of drug development and how molecular imaging can address key questions in the preclinical and clinical evaluation of new targeted drugs. Examples include imaging of the expression and inhibition of drug targets, noninvasive tissue pharmacokinetics, and early assessment of the tumor response [361].

Targeted drugs have been used to treat a variety of common human solid tumors, including breast cancer, colorectal cancer, and non-small-cell lung cancer (NSCLC). Diverse integrated signaling pathways are involved in the development and progression of these malignancies, each of which is genetically heterogeneous. Consequently, inhibition of one specific pathway is likely to be efficacious only in small subsets of patients who share a specific tumor subtype. For example, in unselected patients with metastatic breast cancer, the response rate to the anti-HER2 antibody trastuzumab is less than 10% [362].

Low response rates have also been reported for EGFR and mammalian target of rapamycin (mTOR) kinase inhibitors in patients with NSCLC [363] and renal cell carcinoma [364], respectively. Therefore, patient stratification to identify potential responders would be of great benefit. For breast cancer, identification of probable responders to trastuzumab therapy by use of immunohistochemical (IHC) staining of HER2 facilitated approval of this drug and its widespread use for the treatment of HER2-positive breast cancer [362].

When new targeted drugs enter clinical trials, comparable benefit are not always achievable throughout cancer types. Moreover, sensitivity to new drugs might not purely rely on the overexpression of target proteins. Moreover, it might be based on factors such as specific mutations of the target molecule, loss of negative regulators of its activity, and other regulatory, redundant and/or compensatory tumor responses that are not currently understood. An inability to identify the appropriate patient subsets complicates drug development when “go-no go” decisions are made according to the response rates in relatively small phase II studies. In such studies, poorly defined study populations might lead to an apparent drug failure because of the large fraction of non-responders that dilute the positive drug effect on subpopulations detected by the study. The inability to properly identify appropriate patient subsets is confounded by the fact that the conventional size criteria used to assess tumor responses might not be applicable for some targeted drugs, since durable responses to targeted drugs might be cytostatic rather than cytotoxic and are thus not associated with tumor shrinkage. As a consequence, standard response criteria, which defines a response as a decrease in tumor size, are of limited reliability in assessing the response to this class of drugs.

Targeted-molecular imaging provides strategy that could address expression of the target protein, drug–target protein interactions and drug effects in both preclinical studies. In addition, it reduces the costs of drug development [365], stratify patient populations and monitor therapeutic efficacy. With regard to the clinical setting, the two key imaging techniques that will be emphasized are PET and MRI. For preclinical studies, specialized imaging devices that include small-animal PET, SPECT instrumentation, small-animal MRI, and optical imaging devices for fluorescence and bioluminescence, are currently available for studies of rodents and other animal species. In addition to identify targets, these devices enable pharmacokinetic and pharmacodynamic studies in animal models of cancer and in humans.

Although there is little doubt that small-animal imaging will facilitate the development of targeted drugs and imaging agents, drug targets can be species-specific. For example, CEA is not expressed in mice. The monoclonal antibody bevacizumab, which targets VEGF, binds specifically to human but not the mouse VEGF. In such cases, the results of clinical imaging studies might differ from those obtained from animal models. In the paragraphs that followed, we present selected examples to illustrate the applications of molecular imaging, focusing on how molecular imaging can potentially contribute to “go–no go” decisions earlier in the process of drug development.

5.4.1 Imaging of target expression

Expression of the protein or proteins targeted by a drug can generally be assessed by standard IHC. Tissue samples for IHC analysis, however, are frequently available only from the primary tumor, which might have a different phenotype and drug response than metastatic lesions. By the time patients enter clinical trials, expression of the target protein,

or its function, may have changed considerably. For example, Linden *et al.* [366] studied 47 patients with recurrent breast cancer. At the time of diagnosis, all primary tumors were estrogen receptor (ER) positive. However, only 23% of the patients achieved an objective response to salvage hormonal therapy. Whereas the degree of binding of the radiolabeled estrogen analog [¹⁸F]fluoroestradiol (FES) to ERs in metastatic tumors, as measured by PET, was predictive of the tumor response. Specifically, none of the patients lacking focal FES tumor binding responded to therapy, whereas 34% of patients with FES tumor binding responded to salvage hormonal therapy. Thus, FES-PET can be used to identify patient subgroups that, despite expression of ERs in the primary tumor, are unlikely to benefit from anti-estrogen therapy because the metastatic tumors are ER negative.

Besides identifying differences in expression of target proteins inter-patiently, molecular imaging can also show intra-patient heterogeneity of the expression target proteins. For instance, lesion-to-lesion differences in the expression of $\alpha\beta3$ integrin in a patient with metastatic soft tissue sarcoma was reported [367]. Currently, the levels of expression of target proteins are determined by analysis of tumor biopsies. In patients with metastatic disease, analysis of tumor biopsies allows evaluation of only a small part of the total tumor mass. The assessment of the expression of protein targets by use of biopsies might, therefore, be misleading, since $\alpha\beta3$ integrin was highly expressed in the primary tumor but not in the pulmonary metastases.

Currently, only a limited number of molecular targets can be imaged in clinical studies because of the restricted number of available probes [361]. Most molecular targets are expressed at nanomolar range in the tumor tissue, which presents a challenge for the development of ligands. Many potential probes not only bind with their targets with high

avidity but also demonstrate considerable nonspecific binding that resulted in unfavorable pharmacokinetic properties for *in vivo* imaging. Reducing nonspecific binding and optimizing the pharmacokinetic properties have been major challenges in the development of new imaging probes.

5.4.2 Tissue pharmacokinetics

PET imaging has been used to study the pharmacokinetics of several anticancer drugs, for example the radiolabeled humanized anti-VEGF antibody HuMV833 [368]. Jayson and co-authors used PET imaging with an iodinated drug analog to study the pharmacokinetic properties of this antiangiogenic drug [369]. To quantify the drug concentrations in the organ and tumor, labeled antibodies were administered for PET imaging at 24 h and 48 h. The study revealed important differences in drug uptake, clearance and biological activity between primary tumors and metastatic lesions. Some primary tumors exhibited clearance rates that were three times faster than those of metastatic tumors, even within the same patient. Substantial differences in the rates of drug clearance from the tumor were also observed among different patients and tumor types. This heterogeneous pharmacokinetic response might explain the lack of effectiveness of treatment in some patients. The study also revealed discrepancies between the plasma pharmacokinetics of the drug and the rate of drug clearance from tumors, as determined by PET. In patients with multiple lesions, intra-tumoral drug concentrations varied up to 3.4-fold [369]. This variance indicates that plasma pharmacokinetics cannot be used to predict intratumoral drug concentrations.

Tansi *et al.* [370] reported development of NIRF immune-liposomes as quick, effective and more reliable setup to validate the macroscopic and subcellular

biodistribution of contrast agents in freshly excised animal organs. Confocal microscopic imaging of freshly excised organs can detect the subcellular localization of fluorescent probes, which could be correlated to the observations made by macroscopic imaging. Such approach will be highly beneficial to many researchers involved in nano-drug design or in fluorescence-based studies on disease pathogenesis. With that, single-cell and subcellular pharmacokinetic imaging allows insight into drug action *in vivo*.

5.4.3 Measuring target inhibition

Noninvasive assessment of the target inhibition is important at various stages of drug development. In phase I studies, assessment of target inhibition can define the biologically active dose of a new drug for further phase II and III studies. Traditionally, the dose of a cancer drug chosen for further investigation has been determined by the maximum tolerated dose (MTD) in phase I studies. Pathway-targeted drugs, however, frequently cause limited acute adverse effects. The biologically active dose might be substantially lower than the MTD. Furthermore, classic cytotoxic agents are administered over a relatively brief period of time, with the intent to eradicate tumor cells. By contrast, many pathway-targeted drugs are developed as oral treatments for long-term use and are designed to inhibit tumor growth. Dosing these drugs at the MTD might result in unnecessary toxicity. Moreover, the effectiveness of some targeted drugs may actually decrease at higher doses, owing to off-target effects on other biologically active molecules.

In phase II studies, new drugs commonly fail to produce the desired responses for two reasons. First, the dose schedule might be inadequate indicating that the target might not be inhibited. This fact should not lead to “no go” decisions before exploring the outcome of optimizing the dose or schedule of administration. Second, drugs might inhibit

the target but might not affect tumor growth if the target is not essential. This should lead to “no go” decisions.

If the probes used in imaging bind to the same target as the drug, inhibition of the target can be monitored by imaging the blocking of probe uptake by the study drug. Similarly, inhibition of enzymatic activity can also be visualized by imaging probes that are substrates of specific enzymes. Napp *et al.* [371] determined the activity of matriptase, evaluate molecular efficacy of synthetic matriptase inhibitors in an orthotopic mouse model of AsPC-1 PDAC with time-domain NIRF imaging, which can be successfully used to separate fluorescence signals that derived from the applied probe from the autofluorescence background. By using optical imaging in combination with a fluorescently labeled antibody directed against matriptase and an activatable probe, expression and activity of this enzyme in tumors was determined *in vivo*. By measuring increase in fluorescence intensity over bladder we could clearly detect cleavage of the substrate and thereby activity of matriptase. Matriptase activity can be inhibited *in vivo* for at least 24 h by using different synthetic active-site directed enzyme inhibitors, apparent on reduced fluorescence intensities over bladder.

5.4.4 Assessment of tumor response to therapy

Imaging tumors and their response to treatment is valuable toward early assessment of therapy in patients with cancer. Imaging technology to detect molecular changes in the asymmetry of phospholipid distribution in the cell membrane bilayer is a growing field of preclinical and clinical research to detect tumors and measure responses to therapy. Phosphatidylserine (PS) is the most abundant anionic aminophospholipid present in the cell membrane of all mammalian cells and is located in the inner leaflet of the cell

membrane of normal healthy cells. Recently, Zhao *et al.* [372] used NIR optical imaging, the use of a F(ab')₂ fragment of PGN635 labeled with the NIR fluorescent dye IRDye 800CW, was used to demonstrate tumor uptake in a model of rat glioma and enhancement of probe uptake by irradiation of tumors. Furthermore, Gong *et al.* sought to explore the usage of PGN650-IRDye800 as an imaging agent to monitor the exposure of PS in tumors and to assess responses to chemotherapy. Measurement of PS exposure in response to chemotherapy was assessed using human breast and prostate tumor xenografts in mice. In both tumor models, elevated levels of PS were detected in tumors following administration of docetaxel, which was confirmed by *ex vivo* imaging of tumors and fluorescence microscopy. PGN650 may be a useful probe to detect PS that exposed in tumors and to monitor enhanced PS exposure to optimize anti-tumor efficacy [373].

Despite improved tissue penetration as compared to visible light, an essential limitation of utilizing NIR fluorescence imaging intraoperatively is its inability to visualize structures deeper than approximately 5-8 mm below the surface [92]. As a result of this limitation, the field has been shifting towards developing a combination of different forms of imaging modalities, as reported by Tummers *et al.* [176] in the clinical trial of image-guided PDAC resection. Furthermore, multimodal imaging modalities also have significant potential when used as an integrated diagnostic and intraoperative technology, since this can overcome limitations of the individual modalities. The restricted tissue penetration of light limits the use of optical imaging probes. By use of NIRF reporters, tissue penetration of several centimeters has been achieved in experimental studies, albeit with increasing attenuation with depth [374]. Furthermore, image reconstruction algorithms are now being developed to produce tomographic imaging in animal models, with the goal of quantitative

assessment of regional concentrations of fluorescent reporters [374]. Near-infrared fluorescence imaging might, in the future, have a role in clinical studies of superficial tumors or tumors accessible by endoscopy.

REFERENCES

- [1] J. Ferlay *et al.*, “Estimating the global cancer incidence and mortality in 2018: GLOBOCAN sources and methods,” *Int. J. Cancer*, vol. 144, no. 8, p. ijc.31937, Dec. 2018.
- [2] O. Strobel, J. Neoptolemos, D. Jäger, and M. W. Büchler, “Optimizing the outcomes of pancreatic cancer surgery,” *Nat. Rev. Clin. Oncol.*, p. 1, Oct. 2018.
- [3] S. Idachaba *et al.*, “A Review of Pancreatic Cancer: Epidemiology, Genetics, Screening, and Management.,” *Open access Maced. J. Med. Sci.*, vol. 7, no. 4, pp. 663–671, Feb. 2019.
- [4] A. McGuigan, P. Kelly, R. C. Turkington, C. Jones, H. G. Coleman, and R. S. McCain, “Pancreatic cancer: A review of clinical diagnosis, epidemiology, treatment and outcomes.,” *World J. Gastroenterol.*, vol. 24, no. 43, pp. 4846–4861, Nov. 2018.
- [5] F. Bray, J. Ferlay, I. Soerjomataram, R. L. Siegel, L. A. Torre, and A. Jemal, “Global cancer statistics 2018: GLOBOCAN estimates of incidence and mortality worldwide for 36 cancers in 185 countries,” *CA. Cancer J. Clin.*, vol. 68, no. 6, pp. 394–424, Nov. 2018.
- [6] P. Rawla, T. Sunkara, and V. Gaduputi, “Epidemiology of Pancreatic Cancer: Global Trends, Etiology and Risk Factors.,” *World J. Oncol.*, vol. 10, no. 1, pp. 10–27, Feb. 2019.
- [7] D. M. Parkin, L. Boyd, and L. C. Walker, “16. The fraction of cancer attributable to lifestyle and environmental factors in the UK in 2010,” *Br. J. Cancer*, vol. 105,

- no. S2, pp. S77–S81, Dec. 2011.
- [8] W. C. Willett, “Diet and Cancer,” *Oncologist*, vol. 5, no. 5, pp. 393–404, Oct. 2000.
- [9] M. Ezzati, S. J. Henley, A. D. Lopez, and M. J. Thun, “Role of smoking in global and regional cancer epidemiology: Current patterns and data needs,” *Int. J. Cancer*, vol. 116, no. 6, pp. 963–971, Oct. 2005.
- [10] J. M. Genkinger *et al.*, “A pooled analysis of 14 cohort studies of anthropometric factors and pancreatic cancer risk,” *Int. J. Cancer*, vol. 129, no. 7, pp. 1708–1717, Oct. 2011.
- [11] M. Hidalgo *et al.*, “Addressing the challenges of pancreatic cancer: Future directions for improving outcomes,” *Pancreatology*, vol. 15, no. 1, pp. 8–18, Jan. 2015.
- [12] M. S. D. De La Cruz, A. P. Young, M. T. Ruffin IV, and M. T. Ruffin, “Diagnosis and management of pancreatic cancer,” *Am. Fam. Physician*, vol. 89, no. 8, pp. 626–632, Apr. 2014.
- [13] R. L. Siegel, K. D. Miller, and A. Jemal, “Cancer statistics, 2018,” *CA. Cancer J. Clin.*, vol. 68, no. 1, pp. 7–30, Jan. 2018.
- [14] R. L. Siegel, K. D. Miller, and A. Jemal, “Cancer statistics, 2017,” *CA. Cancer J. Clin.*, vol. 67, no. 1, pp. 7–30, Jan. 2017.
- [15] R. B. Reynolds and J. Folloder, “Clinical Management of Pancreatic Cancer,” *J. Adv. Pract. Oncol.*, vol. 5, no. 5, pp. 356–64, 2014.
- [16] D. Chatterjee *et al.*, “Histologic grading of the extent of residual carcinoma

following neoadjuvant chemoradiation in pancreatic ductal adenocarcinoma,” *Cancer*, vol. 118, no. 12, pp. 3182–3190, Jun. 2012.

- [17] J.-Y. Jang *et al.*, “A prospective randomized controlled study comparing outcomes of standard resection and extended resection, including dissection of the nerve plexus and various lymph nodes, in patients with pancreatic head cancer.,” *Ann. Surg.*, vol. 259, no. 4, pp. 656–64, Apr. 2014.
- [18] M. Klauss *et al.*, “Value of three-dimensional reconstructions in pancreatic carcinoma using multidetector CT: initial results.,” *World J. Gastroenterol.*, vol. 15, no. 46, pp. 5827–32, Dec. 2009.
- [19] J. C. Wong and D. S. K. Lu, “Staging of pancreatic adenocarcinoma by imaging studies.,” *Clin. Gastroenterol. Hepatol.*, vol. 6, no. 12, pp. 1301–8, Dec. 2008.
- [20] F. Safi, R. Roscher, R. Bittner, B. Schenkluhn, H. P. Dopfer, and H. G. Beger, “High sensitivity and specificity of CA 19-9 for pancreatic carcinoma in comparison to chronic pancreatitis. Serological and immunohistochemical findings.,” *Pancreas*, vol. 2, no. 4, pp. 398–403, 1987.
- [21] P. Tummala, O. Junaidi, and B. Agarwal, “Imaging of pancreatic cancer: An overview.,” *J. Gastrointest. Oncol.*, vol. 2, no. 3, pp. 168–74, Sep. 2011.
- [22] G. Barugola *et al.*, “Resectable pancreatic cancer: who really benefits from resection?,” *Ann. Surg. Oncol.*, vol. 16, no. 12, pp. 3316–22, Dec. 2009.
- [23] A. Stathis and M. J. Moore, “Advanced pancreatic carcinoma: current treatment and future challenges.,” *Nat. Rev. Clin. Oncol.*, vol. 7, no. 3, pp. 163–72, Mar. 2010.

- [24] S. Pandit, H. Samant, K. Kohli, H. M. Shokouh-Amiri, G. Wellman, and G. B. Zibari, "Incidental liver metastasis in pancreatic adenocarcinoma," *J. Surg. Case Reports*, vol. 2019, no. 3, Mar. 2019.
- [25] C. Finlayson *et al.*, "Intraoperative ultrasound does not improve detection of liver metastases in resectable pancreatic cancer," *Am. J. Surg.*, vol. 175, no. 2, pp. 99–101, Feb. 1998.
- [26] C. S. Verbeke, "Resection margins and R1 rates in pancreatic cancer--are we there yet?," *Histopathology*, vol. 52, no. 7, pp. 787–96, Jun. 2008.
- [27] C. S. Verbeke, D. Leitch, K. V Menon, M. J. McMahon, P. J. Guillou, and A. Anthoney, "Redefining the R1 resection in pancreatic cancer.," *Br. J. Surg.*, vol. 93, no. 10, pp. 1232–7, Oct. 2006.
- [28] J. Bachmann, C. W. Michalski, M. E. Martignoni, M. W. Büchler, and H. Friess, "Pancreatic resection for pancreatic cancer.," *HPB (Oxford)*, vol. 8, no. 5, pp. 346–51, 2006.
- [29] P. Tummala, T. Howard, and B. Agarwal, "Dramatic Survival Benefit Related to R0 Resection of Pancreatic Adenocarcinoma in Patients With Tumor ≤ 25 mm in Size and ≤ 1 Involved Lymph Nodes," *Clin. Transl. Gastroenterol.*, vol. 4, no. 3, p. e33, Mar. 2013.
- [30] C. S. Verbeke and I. P. Gladhaug, "Resection margin involvement and tumour origin in pancreatic head cancer," *Br. J. Surg.*, vol. 99, no. 8, pp. 1036–1049, Aug. 2012.
- [31] J.-F. Zhang *et al.*, "Influence of perineural invasion on survival and recurrence in

- patients with resected pancreatic cancer.,” *Asian Pac. J. Cancer Prev.*, vol. 14, no. 9, pp. 5133–9, 2013.
- [32] A. D. Newton *et al.*, “Intraoperative Near-infrared Imaging Can Identify Neoplasms and Aid in Real-time Margin Assessment During Pancreatic Resection,” *Ann. Surg.*, vol. 270, no. 1, pp. 12–20, Jul. 2019.
- [33] N. C. Balci and R. C. Semelka, “Radiologic diagnosis and staging of pancreatic ductal adenocarcinoma.,” *Eur. J. Radiol.*, vol. 38, no. 2, pp. 105–12, May 2001.
- [34] P. F. Laeseke, R. Chen, R. B. Jeffrey, T. A. Brentnall, and J. K. Willmann, “Combining in Vitro Diagnostics with in Vivo Imaging for Earlier Detection of Pancreatic Ductal Adenocarcinoma: Challenges and Solutions.,” *Radiology*, vol. 277, no. 3, pp. 644–61, Dec. 2015.
- [35] M. Topazian *et al.*, “Interobserver agreement for EUS findings in familial pancreatic-cancer kindreds,” *Gastrointest. Endosc.*, vol. 66, no. 1, pp. 62–67, Jul. 2007.
- [36] N. A. Ahmad *et al.*, “Interobserver agreement among endosonographers for the diagnosis of neoplastic versus non-neoplastic pancreatic cystic lesions,” *Gastrointest. Endosc.*, vol. 58, no. 1, pp. 59–64, Jul. 2003.
- [37] H. J. Lee, Y. Il Yoon, and Y. J. Bae, “Theragnostic ultrasound using microbubbles in the treatment of prostate cancer.,” *Ultrason. (Seoul, Korea)*, vol. 35, no. 4, pp. 309–17, Oct. 2016.
- [38] T. Annese, R. Tamma, S. Ruggieri, and D. Ribatti, “Angiogenesis in Pancreatic Cancer: Pre-Clinical and Clinical Studies.,” *Cancers (Basel)*, vol. 11, no. 3, Mar.

2019.

- [39] J. J. Rychak *et al.*, “Microultrasound molecular imaging of vascular endothelial growth factor receptor 2 in a mouse model of tumor angiogenesis,” *Mol. Imaging*, vol. 6, no. 5, pp. 289–96.
- [40] M. A. Pysz *et al.*, “Vascular endothelial growth factor receptor type 2-targeted contrast-enhanced US of pancreatic cancer neovasculature in a genetically engineered mouse model: potential for earlier detection,” *Radiology*, vol. 274, no. 3, pp. 790–9, Mar. 2015.
- [41] S. Pochon *et al.*, “BR55: A Lipopeptide-Based VEGFR2-Targeted Ultrasound Contrast Agent for Molecular Imaging of Angiogenesis,” *Invest. Radiol.*, vol. 45, no. 2, pp. 89–95, Feb. 2010.
- [42] K. Foygel *et al.*, “Detection of pancreatic ductal adenocarcinoma in mice by ultrasound imaging of thymocyte differentiation antigen 1,” *Gastroenterology*, vol. 145, no. 4, pp. 885-894.e3, Oct. 2013.
- [43] O. F. Kaneko and J. K. Willmann, “Ultrasound for molecular imaging and therapy in cancer,” *Quant. Imaging Med. Surg.*, vol. 2, no. 2, pp. 87–97, Jun. 2012.
- [44] J. H. Kim *et al.*, “Visually Isoattenuating Pancreatic Adenocarcinoma at Dynamic-Enhanced CT: Frequency, Clinical and Pathologic Characteristics, and Diagnosis at Imaging Examinations,” *Radiology*, vol. 257, no. 1, pp. 87–96, Oct. 2010.
- [45] S. S. Ahn, M.-J. Kim, J.-Y. Choi, H.-S. Hong, Y. E. Chung, and J. S. Lim, “Indicative findings of pancreatic cancer in prediagnostic CT,” *Eur. Radiol.*, vol. 19, no. 10, pp. 2448–2455, Oct. 2009.

- [46] S. H. Kim, A. Kamaya, and J. K. Willmann, "CT perfusion of the liver: principles and applications in oncology.," *Radiology*, vol. 272, no. 2, pp. 322–44, Aug. 2014.
- [47] L. Delrue, P. Blanckaert, D. Mertens, E. Cesmeli, W. P. Ceelen, and P. Duyck, "Assessment of Tumor Vascularization in Pancreatic Adenocarcinoma Using 128-Slice Perfusion Computed Tomography Imaging," *J. Comput. Assist. Tomogr.*, vol. 35, no. 4, pp. 434–438, Jul. 2011.
- [48] M. Klau *et al.*, "Computed Tomography Perfusion Analysis of Pancreatic Carcinoma," *J. Comput. Assist. Tomogr.*, vol. 36, no. 2, pp. 237–242, 2012.
- [49] B. N. Patel, J. V. Thomas, M. E. Lockhart, L. L. Berland, and D. E. Morgan, "Single-source dual-energy spectral multidetector CT of pancreatic adenocarcinoma: Optimization of energy level viewing significantly increases lesion contrast," *Clin. Radiol.*, vol. 68, no. 2, pp. 148–154, Feb. 2013.
- [50] X. Montet *et al.*, "Improved Visualization of Vessels and Hepatic Tumors by Micro-Computed Tomography (CT) Using Iodinated Liposomes," *Invest. Radiol.*, vol. 42, no. 9, pp. 652–658, Sep. 2007.
- [51] S. Mukundan *et al.*, "A Liposomal Nanoscale Contrast Agent for Preclinical CT in Mice," *Am. J. Roentgenol.*, vol. 186, no. 2, pp. 300–307, Feb. 2006.
- [52] M. F. Kircher and J. K. Willmann, "Molecular Body Imaging: MR Imaging, CT, and US. Part II. Applications," *Radiology*, vol. 264, no. 2, pp. 349–368, Aug. 2012.
- [53] N. H. Gilinsky, P. C. Bornman, A. H. Girdwood, and I. N. Marks, "Diagnostic yield of endoscopic retrograde cholangiopancreatography in carcinoma of the

- pancreas,” *Br. J. Surg.*, vol. 73, no. 7, pp. 539–543, Jul. 1986.
- [54] M. Menges, M. M. Lerch, and M. Zeitz, “The double duct sign in patients with malignant and benign pancreatic lesions,” *Gastrointest. Endosc.*, vol. 52, no. 1, pp. 74–77, Jul. 2000.
- [55] B. Vachiranubhap, Y. H. Kim, N. C. Balci, and R. C. Semelka, “Magnetic Resonance Imaging of Adenocarcinoma of the Pancreas,” *Top. Magn. Reson. Imaging*, vol. 20, no. 1, pp. 3–9, Feb. 2009.
- [56] W. Schima, A. Ba-Ssalamah, P. Goetzinger, M. Scharitzer, and C. Koelblinger, “State-of-the-Art Magnetic Resonance Imaging of Pancreatic Cancer,” *Top. Magn. Reson. Imaging*, vol. 18, no. 6, pp. 421–429, Dec. 2007.
- [57] N. L. Kelekis and R. C. Semelka, “MRI of pancreatic tumors,” *Eur. Radiol.*, vol. 7, no. 6, pp. 875–886, Jul. 1997.
- [58] S. P. Kauhanen *et al.*, “A Prospective Diagnostic Accuracy Study of 18F-Fluorodeoxyglucose Positron Emission Tomography/Computed Tomography, Multidetector Row Computed Tomography, and Magnetic Resonance Imaging in Primary Diagnosis and Staging of Pancreatic Cancer,” *Ann. Surg.*, vol. 250, no. 6, pp. 957–963, Dec. 2009.
- [59] S. Bipat *et al.*, “Ultrasonography, Computed Tomography and Magnetic Resonance Imaging for Diagnosis and Determining Resectability of Pancreatic Adenocarcinoma,” *J. Comput. Assist. Tomogr.*, vol. 29, no. 4, pp. 438–445, Jul. 2005.
- [60] A. Dzik-Jurasz *et al.*, “Diffusion MRI for prediction of response of rectal cancer to

- chemoradiation,” *Lancet*, vol. 360, no. 9329, pp. 307–308, Jul. 2002.
- [61] T. Ichikawa *et al.*, “High- b Value Diffusion-Weighted MRI for Detecting Pancreatic Adenocarcinoma: Preliminary Results,” *Am. J. Roentgenol.*, vol. 188, no. 2, pp. 409–414, Feb. 2007.
- [62] K. Nasu *et al.*, “Hepatic Metastases: Diffusion-weighted Sensitivity-encoding versus SPIO-enhanced MR Imaging,” *Radiology*, vol. 239, no. 1, pp. 122–130, Apr. 2006.
- [63] N. Muraoka *et al.*, “Apparent diffusion coefficient in pancreatic cancer: Characterization and histopathological correlations,” *J. Magn. Reson. Imaging*, vol. 27, no. 6, pp. 1302–1308, May 2008.
- [64] M. Takeuchi, K. Matsuzaki, H. Kubo, and H. Nishitani, “High- b -value diffusion-weighted magnetic resonance imaging of pancreatic cancer and mass-forming chronic pancreatitis: preliminary results,” *Acta radiol.*, vol. 49, no. 4, pp. 383–386, May 2008.
- [65] R. Fattahi *et al.*, “Pancreatic diffusion-weighted imaging (DWI): Comparison between mass-forming focal pancreatitis (FP), pancreatic cancer (PC), and normal pancreas,” *J. Magn. Reson. Imaging*, vol. 29, no. 2, pp. 350–356, Feb. 2009.
- [66] N. Kartalis, T. L. Lindholm, P. Aspelin, J. Permert, and N. Albiin, “Diffusion-weighted magnetic resonance imaging of pancreas tumours,” *Eur. Radiol.*, vol. 19, no. 8, pp. 1981–1990, Aug. 2009.
- [67] O. Henriksen, “MR spectroscopy in clinical research,” *Acta Radiol.*, vol. 35, no. 2, pp. 96–116, Mar. 1994.

- [68] S. G. Cho *et al.*, “Differentiation of Chronic Focal Pancreatitis From Pancreatic Carcinoma by In Vivo Proton Magnetic Resonance Spectroscopy,” *J. Comput. Assist. Tomogr.*, vol. 29, no. 2, pp. 163–169, Mar. 2005.
- [69] X. Ma *et al.*, “The Metabolic Features of Normal Pancreas and Pancreatic Adenocarcinoma,” *J. Comput. Assist. Tomogr.*, vol. 35, no. 5, pp. 539–543, Sep. 2011.
- [70] D. Kozłowska, P. Foran, P. MacMahon, M. J. Shelly, S. Eustace, and R. O’Kennedy, “Molecular and magnetic resonance imaging: The value of immunoliposomes,” *Adv. Drug Deliv. Rev.*, vol. 61, no. 15, pp. 1402–1411, Dec. 2009.
- [71] M. Tan, X. Wu, E.-K. Jeong, Q. Chen, D. L. Parker, and Z.-R. Lu, “An effective targeted nanoglobular manganese(II) chelate conjugate for magnetic resonance molecular imaging of tumor extracellular matrix,” *Mol. Pharm.*, vol. 7, no. 4, pp. 936–43, Aug. 2010.
- [72] C. Xu and S. Sun, “Superparamagnetic nanoparticles as targeted probes for diagnostic and therapeutic applications,” *Dalton Trans.*, no. 29, pp. 5583–91, Aug. 2009.
- [73] X. Chen *et al.*, “Plectin-1 Targeted Dual-modality Nanoparticles for Pancreatic Cancer Imaging,” *EBioMedicine*, vol. 30, pp. 129–137, Apr. 2018.
- [74] K. A. Kelly *et al.*, “Targeted nanoparticles for imaging incipient pancreatic ductal adenocarcinoma,” *PLoS Med.*, vol. 5, no. 4, p. e85, Apr. 2008.
- [75] L. Yang *et al.*, “Single chain epidermal growth factor receptor antibody conjugated

nanoparticles for in vivo tumor targeting and imaging.,” *Small*, vol. 5, no. 2, pp. 235–43, Feb. 2009.

- [76] S. S. Gambhir, J. Czernin, J. Schwimmer, D. H. Silverman, R. E. Coleman, and M. E. Phelps, “A tabulated summary of the FDG PET literature.,” *J. Nucl. Med.*, vol. 42, no. 5 Suppl, pp. 1S-93S, May 2001.
- [77] S. N. Reske *et al.*, “Overexpression of glucose transporter 1 and increased FDG uptake in pancreatic carcinoma.,” *J. Nucl. Med.*, vol. 38, no. 9, pp. 1344–8, Sep. 1997.
- [78] S. Bang *et al.*, “The Clinical Usefulness of 18-Fluorodeoxyglucose Positron Emission Tomography in the Differential Diagnosis, Staging, and Response Evaluation After Concurrent Chemoradiotherapy for Pancreatic Cancer,” *J. Clin. Gastroenterol.*, vol. 40, no. 10, pp. 923–929, Nov. 2006.
- [79] D. Lytras *et al.*, “Positron Emission Tomography Does Not Add to Computed Tomography for the Diagnosis and Staging of Pancreatic Cancer,” *Dig. Surg.*, vol. 22, no. 1–2, pp. 55–62, 2005.
- [80] E. Singer *et al.*, “Differential diagnosis of benign and malign pancreatic masses with 18F-fluorodeoxyglucose-positron emission tomography recorded with a dual-head coincidence gamma camera,” *Eur. J. Gastroenterol. Hepatol.*, vol. 19, no. 6, pp. 471–478, Jun. 2007.
- [81] S. Seo *et al.*, “Contribution of 18F-fluorodeoxyglucose positron emission tomography to the diagnosis of early pancreatic carcinoma,” *J. Hepatobiliary Pancreat. Surg.*, vol. 15, no. 6, pp. 634–639, Nov. 2008.

- [82] J. Ruf *et al.*, “Detection of recurrent pancreatic cancer: Comparison of FDG-PET with CT/MRI,” *Pancreatology*, vol. 5, no. 2–3, pp. 266–272, Jan. 2005.
- [83] C. Sperti, C. Pasquali, S. Bissoli, F. Chierichetti, G. Liessi, and S. Pedrazzoli, “Tumor Relapse after Pancreatic Cancer Resection is Detected Earlier by 18-FDG PET than by CT,” *J. Gastrointest. Surg.*, vol. 14, no. 1, pp. 131–140, Jan. 2010.
- [84] A. Sendler *et al.*, “Preoperative Evaluation of Pancreatic Masses with Positron Emission Tomography Using 18F-fluorodeoxyglucose: Diagnostic Limitations,” *World J. Surg.*, vol. 24, no. 9, pp. 1121–1129, Sep. 2000.
- [85] S. Tang *et al.*, “Usefulness of 18F-FDG PET, combined FDG-PET/CT and EUS in diagnosing primary pancreatic carcinoma: A meta-analysis,” *Eur. J. Radiol.*, vol. 78, no. 1, pp. 142–150, Apr. 2011.
- [86] D. Delbeke and W. H. Martin, “PET and PET/CT for Pancreatic Malignancies,” *Surg. Oncol. Clin. N. Am.*, vol. 19, no. 2, pp. 235–254, Apr. 2010.
- [87] M. Yoshimoto *et al.*, “Characterization of acetate metabolism in tumor cells in relation to cell proliferation: acetate metabolism in tumor cells,” *Nucl. Med. Biol.*, vol. 28, no. 2, pp. 117–22, Feb. 2001.
- [88] C. Zhao *et al.*, “Imaging a pancreatic carcinoma xenograft model with 11C-acetate: A comparison study with 18F-FDG,” *Nucl. Med. Commun.*, vol. 30, no. 12, pp. 971–977, Dec. 2009.
- [89] L. G. Flores *et al.*, “Detection of pancreatic carcinomas by imaging lactose-binding protein expression in peritumoral pancreas using [18F]fluoroethyl-deoxylactose PET/CT,” *PLoS One*, vol. 4, no. 11, p. e7977, Nov. 2009.

- [90] S. H. Hausner *et al.*, “Targeted in vivo imaging of integrin $\alpha v \beta 6$ with an improved radiotracer and its relevance in a pancreatic tumor model.,” *Cancer Res.*, vol. 69, no. 14, pp. 5843–50, Jul. 2009.
- [91] A. Chakrabarti *et al.*, “Radiohybridization PET imaging of KRAS G12D mRNA expression in human pancreas cancer xenografts with [64Cu]DO3A-peptide nucleic acid-peptide nanoparticles,” *Cancer Biol. Ther.*, vol. 6, no. 6, pp. 948–956, Jun. 2007.
- [92] A. L. Vahrmeijer, M. Hutteman, J. R. van der Vorst, C. J. H. van de Velde, and J. V Frangioni, “Image-guided cancer surgery using near-infrared fluorescence.,” *Nat. Rev. Clin. Oncol.*, vol. 10, no. 9, pp. 507–18, Sep. 2013.
- [93] O. I. Olubiya *et al.*, “Intraoperative Magnetic Resonance Imaging in Intracranial Glioma Resection: A Single-Center, Retrospective Blinded Volumetric Study,” *World Neurosurg.*, vol. 84, no. 2, pp. 528–536, Aug. 2015.
- [94] T. Nagaya, Y. A. Nakamura, P. L. Choyke, and H. Kobayashi, “Fluorescence-Guided Surgery.,” *Front. Oncol.*, vol. 7, p. 314, 2017.
- [95] J. B. Kruskal and R. A. Kane, “Intraoperative ultrasonography of the pancreas: techniques and clinical applications.,” *Surg. Technol. Int.*, vol. 6, pp. 49–57, 1997.
- [96] M. R. M. Sun, D. D. Brennan, J. B. Kruskal, and R. A. Kane, “Intraoperative ultrasonography of the pancreas.,” *Radiographics*, vol. 30, no. 7, pp. 1935–53, Nov. 2010.
- [97] S. Hata *et al.*, “Value of visual inspection, bimanual palpation, and intraoperative ultrasonography during hepatic resection for liver metastases of colorectal

- carcinoma.,” *World J. Surg.*, vol. 35, no. 12, pp. 2779–87, Dec. 2011.
- [98] S. B. Mondal, S. Gao, N. Zhu, R. Liang, V. Gruev, and S. Achilefu, “Real-time fluorescence image-guided oncologic surgery.,” *Adv. Cancer Res.*, vol. 124, pp. 171–211, 2014.
- [99] T. Conroy *et al.*, “FOLFIRINOX versus gemcitabine for metastatic pancreatic cancer.,” *N. Engl. J. Med.*, vol. 364, no. 19, pp. 1817–25, May 2011.
- [100] C. R. Ferrone *et al.*, “Radiological and surgical implications of neoadjuvant treatment with FOLFIRINOX for locally advanced and borderline resectable pancreatic cancer.,” *Ann. Surg.*, vol. 261, no. 1, pp. 12–7, Jan. 2015.
- [101] G. A. Coté, J. Smith, S. Sherman, and K. Kelly, “Technologies for imaging the normal and diseased pancreas.,” *Gastroenterology*, vol. 144, no. 6, pp. 1262–71.e1, Jun. 2013.
- [102] Y. Wang and Q. Cui, “[Recent advances in gene change of pancreatic cancer].,” *Zhongguo Yi Xue Ke Xue Yuan Xue Bao.*, vol. 26, no. 1, pp. 79–82, Feb. 2004.
- [103] S. Jones *et al.*, “Core signaling pathways in human pancreatic cancers revealed by global genomic analyses.,” *Science*, vol. 321, no. 5897, pp. 1801–6, Sep. 2008.
- [104] H. C. Harsha *et al.*, “A compendium of potential biomarkers of pancreatic cancer.,” *PLoS Med.*, vol. 6, no. 4, p. e1000046, Apr. 2009.
- [105] M. van Oosten, L. M. Crane, J. Bart, F. W. van Leeuwen, and G. M. van Dam, “Selecting Potential Targetable Biomarkers for Imaging Purposes in Colorectal Cancer Using TArget Selection Criteria (TASC): A Novel Target Identification Tool.,” *Transl. Oncol.*, vol. 4, no. 2, pp. 71–82, Apr. 2011.

- [106] S. Wachsmann-Hogiu, T. Weeks, and T. Huser, “Chemical analysis in vivo and in vitro by Raman spectroscopy—from single cells to humans,” *Curr. Opin. Biotechnol.*, vol. 20, no. 1, pp. 63–73, Feb. 2009.
- [107] M. L. James and S. S. Gambhir, “A Molecular Imaging Primer: Modalities, Imaging Agents, and Applications,” *Physiol. Rev.*, vol. 92, no. 2, pp. 897–965, Apr. 2012.
- [108] V. W. Pike, “Positron-emitting radioligands for studies in vivo—probes for human psychopharmacology,” *J. Psychopharmacol.*, vol. 7, no. 2, pp. 139–158, Mar. 1993.
- [109] C. Halldin, B. Gulyás, O. Langer, and L. Farde, “Brain radioligands—state of the art and new trends,” *Q. J. Nucl. Med.*, vol. 45, no. 2, pp. 139–52, Jun. 2001.
- [110] M. Longmire, P. L. Choyke, and H. Kobayashi, “Clearance properties of nano-sized particles and molecules as imaging agents: considerations and caveats,” *Nanomedicine*, vol. 3, no. 5, pp. 703–717, Oct. 2008.
- [111] V. Torchilin, *Handbook of targeted delivery of imaging agents*. 1995.
- [112] S. Lee, J. Xie, and X. Chen, “Peptides and Peptide Hormones for Molecular Imaging and Disease Diagnosis,” *Chem. Rev.*, vol. 110, no. 5, pp. 3087–3111, May 2010.
- [113] M. Schottelius and H.-J. Wester, “Molecular imaging targeting peptide receptors,” *Methods*, vol. 48, no. 2, pp. 161–177, Jun. 2009.
- [114] A. K. Sato, M. Viswanathan, R. B. Kent, and C. R. Wood, “Therapeutic peptides: technological advances driving peptides into development,” *Curr. Opin.*

Biotechnol., vol. 17, no. 6, pp. 638–642, Dec. 2006.

- [115] P. Vlieghe, V. Lisowski, J. Martinez, and M. Khrestchatisky, “Synthetic therapeutic peptides: science and market,” *Drug Discov. Today*, vol. 15, no. 1–2, pp. 40–56, Jan. 2010.
- [116] A. J. Beer *et al.*, “Comparison of integrin $\alpha V\beta 3$ expression and glucose metabolism in primary and metastatic lesions in cancer patients: a PET study using ^{18}F -galacto-RGD and ^{18}F -FDG,” *J. Nucl. Med.*, vol. 49, no. 1, pp. 22–9, Jan. 2008.
- [117] Q. T. Nguyen *et al.*, “Surgery with molecular fluorescence imaging using activatable cell-penetrating peptides decreases residual cancer and improves survival,” *Proc. Natl. Acad. Sci. U. S. A.*, vol. 107, no. 9, pp. 4317–22, Mar. 2010.
- [118] C. Bremer, C.-H. Tung, and R. Weissleder, “In vivo molecular target assessment of matrix metalloproteinase inhibition,” *Nat. Med.*, vol. 7, no. 6, pp. 743–748, Jun. 2001.
- [119] L. E. Edgington *et al.*, “Noninvasive optical imaging of apoptosis by caspase-targeted activity-based probes,” *Nat. Med.*, vol. 15, no. 8, pp. 967–973, Aug. 2009.
- [120] S. C. Drew *et al.*, “Optical Imaging Detects Apoptosis in the Brain and Peripheral Organs of Prion-Infected Mice,” *J. Neuropathol. Exp. Neurol.*, vol. 70, no. 2, pp. 143–150, Feb. 2011.
- [121] S. Guhlke, H.-J. Wester, C. Bruns, and G. Stöcklin, “(2-[^{18}F]fluoropropionyl-(d)phe1)-octreotide, a potential radiopharmaceutical for quantitative somatostatin receptor imaging with PET: Synthesis, radiolabeling, in vitro validation and

- biodistribution in mice,” *Nucl. Med. Biol.*, vol. 21, no. 6, pp. 819–825, Aug. 1994.
- [122] C. Decristoforo, L. Melendez-Alafort, J. K. Sosabowski, and S. J. Mather, “^{99m}Tc-HYNIC-[Tyr3]-octreotide for imaging somatostatin-receptor-positive tumors: preclinical evaluation and comparison with ¹¹¹In-octreotide,” *J. Nucl. Med.*, vol. 41, no. 6, pp. 1114–9, Jun. 2000.
- [123] C. Van de Wiele *et al.*, “Technetium-99m RP527, a GRP analogue for visualisation of GRP receptor-expressing malignancies: a feasibility study,” *Eur. J. Nucl. Med.*, vol. 27, no. 11, pp. 1694–1699, Nov. 2000.
- [124] J. Schuhmacher *et al.*, “GRP receptor-targeted PET of a rat pancreas carcinoma xenograft in nude mice with a ⁶⁸Ga-labeled bombesin(6-14) analog,” *J. Nucl. Med.*, vol. 46, no. 4, pp. 691–9, Apr. 2005.
- [125] P. Mäding, F. Füchtner, and F. Wüst, “Module-assisted synthesis of the bifunctional labelling agent N-succinimidyl 4-[¹⁸F]fluorobenzoate ([¹⁸F]SFB),” *Appl. Radiat. Isot.*, vol. 63, no. 3, pp. 329–332, Sep. 2005.
- [126] P. R. Bouchard, R. M. Hutabarat, and K. M. Thompson, “Discovery and Development of Therapeutic Aptamers,” *Annu. Rev. Pharmacol. Toxicol.*, vol. 50, no. 1, pp. 237–257, Feb. 2010.
- [127] K. W. Thiel and P. H. Giangrande, “Therapeutic Applications of DNA and RNA Aptamers,” *Oligonucleotides*, vol. 19, no. 3, pp. 209–222, Sep. 2009.
- [128] B. Tavitian, F. Ducongé, R. Boisgard, and F. Dollé, “In Vivo Imaging of Oligonucleotidic Aptamers,” Humana Press, Totowa, NJ, 2009, pp. 241–259.
- [129] C. Younes, R. Boisgard, and B. Tavitian, “Labelled Oligonucleotides as

- Radiopharmaceuticals: Pitfalls, Problems and Perspectives,” *Curr. Pharm. Des.*, vol. 8, no. 16, pp. 1451–1466, Jul. 2002.
- [130] P. Chames, M. Van Regenmortel, E. Weiss, and D. Baty, “Therapeutic antibodies: successes, limitations and hopes for the future.,” *Br. J. Pharmacol.*, vol. 157, no. 2, pp. 220–33, May 2009.
- [131] G. Malviya, F. Conti, M. Chianelli, F. Scopinaro, R. A. Dierckx, and A. Signore, “Molecular imaging of rheumatoid arthritis by radiolabelled monoclonal antibodies: new imaging strategies to guide molecular therapies,” *Eur. J. Nucl. Med. Mol. Imaging*, vol. 37, no. 2, pp. 386–398, Feb. 2010.
- [132] T. Olafsen and A. M. Wu, “Antibody Vectors for Imaging,” *Semin. Nucl. Med.*, vol. 40, no. 3, pp. 167–181, May 2010.
- [133] J. V Jokerst, T. Lobovkina, R. N. Zare, and S. S. Gambhir, “Nanoparticle PEGylation for imaging and therapy,” *Nanomedicine*, vol. 6, no. 4, pp. 715–728, Jun. 2011.
- [134] F. Liang and B. Chen, “A Review on Biomedical Applications of Single-Walled Carbon Nanotubes,” *Curr. Med. Chem.*, vol. 17, no. 1, pp. 10–24, Jan. 2010.
- [135] X. Gao, Y. Cui, R. M. Levenson, L. W. K. Chung, and S. Nie, “In vivo cancer targeting and imaging with semiconductor quantum dots,” *Nat. Biotechnol.*, vol. 22, no. 8, pp. 969–976, Aug. 2004.
- [136] S. Keren, C. Zavaleta, Z. Cheng, A. de la Zerda, O. Gheysens, and S. S. Gambhir, “Noninvasive molecular imaging of small living subjects using Raman spectroscopy,” *Proc. Natl. Acad. Sci. U. S. A.*, vol. 105, no. 15, pp. 5844–9, Apr.

2008.

- [137] O. Veiseh *et al.*, “Inhibition of Tumor-Cell Invasion with Chlorotoxin-Bound Superparamagnetic Nanoparticles,” *Small*, vol. 5, no. 2, pp. 256–264, Dec. 2008.
- [138] F. Alexis, E. Pridgen, L. K. Molnar, and O. C. Farokhzad, “Factors Affecting the Clearance and Biodistribution of Polymeric Nanoparticles,” *Mol. Pharm.*, vol. 5, no. 4, pp. 505–515, Aug. 2008.
- [139] M. Ogawa *et al.*, “Dual-Modality Molecular Imaging Using Antibodies Labeled with Activatable Fluorescence and a Radionuclide for Specific and Quantitative Targeted Cancer Detection,” *Bioconjug. Chem.*, vol. 20, no. 11, pp. 2177–2184, Nov. 2009.
- [140] W. B. Edwards *et al.*, “Agonist–Antagonist Dilemma in Molecular Imaging: Evaluation of a Monomolecular Multimodal Imaging Agent for the Somatostatin Receptor,” *Bioconjug. Chem.*, vol. 19, no. 1, pp. 192–200, Jan. 2008.
- [141] † Anurag Mishra *et al.*, “A New Class of Gd-Based DO3A-Ethylamine-Derived Targeted Contrast Agents for MR and Optical Imaging,” 2006.
- [142] A. Louie, “Multimodality Imaging Probes: Design and Challenges,” *Chem. Rev.*, vol. 110, no. 5, pp. 3146–3195, May 2010.
- [143] O. C. Boerman and W. J. G. Oyen, “Multimodality probes: amphibian cars for molecular imaging,” *J. Nucl. Med.*, vol. 49, no. 8, pp. 1213–4, Aug. 2008.
- [144] C. Csontos, I. Kolosova, and A. D. Verin, “Regulation of vascular endothelial cell barrier function and cytoskeleton structure by protein phosphatases of the PPP family,” *Am. J. Physiol. Cell. Mol. Physiol.*, vol. 293, no. 4, pp. L843–L854, Oct.

2007.

- [145] H. S. Choi *et al.*, “Renal clearance of quantum dots,” *Nat. Biotechnol.*, vol. 25, no. 10, pp. 1165–1170, Oct. 2007.
- [146] A. Goel *et al.*, “Genetically engineered tetravalent single-chain Fv of the pancarcinoma monoclonal antibody CC49: improved biodistribution and potential for therapeutic application.,” *Cancer Res.*, vol. 60, no. 24, pp. 6964–71, Dec. 2000.
- [147] N. P. Alazraki *et al.*, “Sentinel node staging of early breast cancer using lymphoscintigraphy and the intraoperative gamma detecting probe.,” *Radiol. Clin. North Am.*, vol. 39, no. 5, pp. 947–56, viii, Sep. 2001.
- [148] T. Barrett, P. L. Choyke, and H. Kobayashi, “Imaging of the lymphatic system: new horizons,” *Contrast Media Mol. Imaging*, vol. 1, no. 6, pp. 230–245, Nov. 2006.
- [149] M. Hamidi, A. Azadi, and P. Rafiei, “Pharmacokinetic Consequences of Pegylation,” *Drug Deliv.*, vol. 13, no. 6, pp. 399–409, Jan. 2006.
- [150] W. M. Deen, M. J. Lazzara, and B. D. Myers, “Structural determinants of glomerular permeability,” *Am. J. Physiol. Physiol.*, vol. 281, no. 4, pp. F579–F596, Oct. 2001.
- [151] M. Ohlson, J. Sörensson, and B. Haraldsson, “A gel-membrane model of glomerular charge and size selectivity in series,” *Am. J. Physiol. Physiol.*, vol. 280, no. 3, pp. F396–F405, Mar. 2001.
- [152] L. F. Prescott, J. A. McAuslane, and S. Freestone, “The concentration-dependent disposition and kinetics of inulin.,” *Eur. J. Clin. Pharmacol.*, vol. 40, no. 6, pp.

619–24, 1991.

- [153] H. Kobayashi *et al.*, “L-lysine effectively blocks renal uptake of 125I- or 99mTc-labeled anti-Tac disulfide-stabilized Fv fragment.,” *Cancer Res.*, vol. 56, no. 16, pp. 3788–95, Aug. 1996.
- [154] A. P. Chapman, P. Antoniw, M. Spitali, S. West, S. Stephens, and D. J. King, “Therapeutic antibody fragments with prolonged in vivo half-lives,” *Nat. Biotechnol.*, vol. 17, no. 8, pp. 780–783, Aug. 1999.
- [155] E. Wiener *et al.*, “Dendrimer-based metal chelates: A new class of magnetic resonance imaging contrast agents,” *Magn. Reson. Med.*, vol. 31, no. 1, pp. 1–8, Jan. 1994.
- [156] H. KOBAYASHI and M. BRECHBIEL, “Nano-sized MRI contrast agents with dendrimer cores,” *Adv. Drug Deliv. Rev.*, vol. 57, no. 15, pp. 2271–2286, Dec. 2005.
- [157] S. A. Hilderbrand and R. Weissleder, “Near-infrared fluorescence: application to in vivo molecular imaging,” *Curr. Opin. Chem. Biol.*, vol. 14, no. 1, pp. 71–79, Feb. 2010.
- [158] M. Thompson *et al.*, “Understanding biophysicochemical interactions at the nano–bio interface,” *Nat. Mater.*, vol. 8, no. 7, pp. 543–557, Jul. 2009.
- [159] H. Kobayashi *et al.*, “The pharmacokinetic characteristics of glycolated humanized anti-Tac Fabs are determined by their isoelectric points.,” *Cancer Res.*, vol. 59, no. 2, pp. 422–30, Jan. 1999.
- [160] E. Kuntz and H. Kuntz, *Hepatology, Principles and practice: history, morphology,*

biochemistry, diagnostics, clinic, therapy. 2006.

- [161] E. de Boer *et al.*, “Optical innovations in surgery.,” *Br. J. Surg.*, vol. 102, no. 2, pp. e56-72, Jan. 2015.
- [162] J. R. van der Vorst *et al.*, “Near-infrared fluorescence-guided resection of colorectal liver metastases.,” *Cancer*, vol. 119, no. 18, pp. 3411–8, Sep. 2013.
- [163] S. L. Troyan *et al.*, “The FLARE™ Intraoperative Near-Infrared Fluorescence Imaging System: A First-in-Human Clinical Trial in Breast Cancer Sentinel Lymph Node Mapping,” *Ann. Surg. Oncol.*, vol. 16, no. 10, pp. 2943–2952, Oct. 2009.
- [164] G. M. van Dam *et al.*, “Intraoperative tumor-specific fluorescence imaging in ovarian cancer by folate receptor- α targeting: first in-human results.,” *Nat. Med.*, vol. 17, no. 10, pp. 1315–9, Sep. 2011.
- [165] J. R. van der Vorst *et al.*, “Dose optimization for near-infrared fluorescence sentinel lymph node mapping in patients with melanoma.,” *Br. J. Dermatol.*, vol. 168, no. 1, pp. 93–8, Jan. 2013.
- [166] M. Hutteman *et al.*, “Optimization of near-infrared fluorescent sentinel lymph node mapping for vulvar cancer.,” *Am. J. Obstet. Gynecol.*, vol. 206, no. 1, pp. 89.e1–5, Jan. 2012.
- [167] L. M. A. Crane *et al.*, “Intraoperative near-infrared fluorescence imaging for sentinel lymph node detection in vulvar cancer: first clinical results.,” *Gynecol. Oncol.*, vol. 120, no. 2, pp. 291–5, Feb. 2011.
- [168] L. M. A. Crane *et al.*, “Intraoperative multispectral fluorescence imaging for the

- detection of the sentinel lymph node in cervical cancer: a novel concept.," *Mol. imaging Biol.*, vol. 13, no. 5, pp. 1043–9, Oct. 2011.
- [169] J. R. van der Vorst *et al.*, "Optimization of near-infrared fluorescent sentinel lymph node mapping in cervical cancer patients.," *Int. J. Gynecol. Cancer*, vol. 21, no. 8, pp. 1472–8, Nov. 2011.
- [170] J. X. Jiang *et al.*, "Optimization of the enhanced permeability and retention effect for near-infrared imaging of solid tumors with indocyanine green.," *Am. J. Nucl. Med. Mol. Imaging*, vol. 5, no. 4, pp. 390–400, 2015.
- [171] J. D. Predina *et al.*, "A clinical trial of intraoperative near-infrared imaging to assess tumor extent and identify residual disease during anterior mediastinal tumor resection," *Cancer*, vol. 125, no. 5, pp. 807–817, Mar. 2019.
- [172] A. D. Newton *et al.*, "Optimization of Second Window Indocyanine Green for Intraoperative Near-Infrared Imaging of Thoracic Malignancy," *J. Am. Coll. Surg.*, vol. 228, no. 2, pp. 188–197, Feb. 2019.
- [173] C. E. S. Hoogstins *et al.*, "Image-Guided Surgery in Patients with Pancreatic Cancer: First Results of a Clinical Trial Using SGM-101, a Novel Carcinoembryonic Antigen-Targeting, Near-Infrared Fluorescent Agent," *Ann. Surg. Oncol.*, vol. 25, no. 11, pp. 3350–3357, Oct. 2018.
- [174] W. S. Tummers, J. K. Willmann, B. A. Bonsing, A. L. Vahrmeijer, S. S. Gambhir, and R.-J. Swijnenburg, "Advances in Diagnostic and Intraoperative Molecular Imaging of Pancreatic Cancer," *Pancreas*, vol. 47, no. 6, pp. 675–689, Jul. 2018.
- [175] L. Miao, C. M. Lin, and L. Huang, "Stromal barriers and strategies for the delivery

- of nanomedicine to desmoplastic tumors,” *J. Control. Release*, vol. 219, pp. 192–204, Dec. 2015.
- [176] W. S. Tummers *et al.*, “Intraoperative Pancreatic Cancer Detection using Tumor-Specific Multimodality Molecular Imaging,” *Ann. Surg. Oncol.*, vol. 25, no. 7, pp. 1880–1888, Jul. 2018.
- [177] D. Gao *et al.*, “A near-infrared phthalocyanine dye-labeled agent for integrin $\alpha\beta6$ -targeted theranostics of pancreatic cancer,” *Biomaterials*, vol. 53, pp. 229–238, Jun. 2015.
- [178] C. Zhang, R. Kimura, L. Abou-Elkacem, J. Levi, L. Xu, and S. S. Gambhir, “A Cystine Knot Peptide Targeting Integrin $\alpha\beta6$ for Photoacoustic and Fluorescence Imaging of Tumors in Living Subjects.,” *J. Nucl. Med.*, vol. 57, no. 10, pp. 1629–1634, Oct. 2016.
- [179] Z. Cruz-Monserrate *et al.*, “Detection of pancreatic cancer tumours and precursor lesions by cathepsin E activity in mouse models,” *Gut*, vol. 61, no. 9, pp. 1315–1322, Sep. 2012.
- [180] W. R. Abd-Elgaliel, Z. Cruz-Monserrate, C. D. Logsdon, and C.-H. Tung, “Molecular imaging of Cathepsin E-positive tumors in mice using a novel protease-activatable fluorescent probe.,” *Mol. Biosyst.*, vol. 7, no. 12, pp. 3207–3213, Dec. 2011.
- [181] R. Weissleder, C. H. Tung, U. Mahmood, and A. Bogdanov, “In vivo imaging of tumors with protease-activated near-infrared fluorescent probes.,” *Nat. Biotechnol.*, vol. 17, no. 4, pp. 375–8, Apr. 1999.

- [182] A. Hellebust and R. Richards-Kortum, “Advances in molecular imaging: targeted optical contrast agents for cancer diagnostics,” *Nanomedicine (Lond)*, vol. 7, no. 3, pp. 429–45, Mar. 2012.
- [183] M. J. Whitley *et al.*, “A mouse-human phase 1 co-clinical trial of a protease-activated fluorescent probe for imaging cancer,” *Sci. Transl. Med.*, vol. 8, no. 320, p. 320ra4, Jan. 2016.
- [184] W. C. Johnston *et al.*, “Total pancreatectomy for pancreatic ductal adenocarcinoma: review of the National Cancer Data Base,” *HPB*, vol. 18, no. 1, pp. 21–28, Jan. 2016.
- [185] S. P. Cleary *et al.*, “Prognostic factors in resected pancreatic adenocarcinoma: Analysis of actual 5-year survivors¹ 1No competing interests declared,” *J. Am. Coll. Surg.*, vol. 198, no. 5, pp. 722–731, May 2004.
- [186] H. Manuel, M. Hidalgo, and H. Manuel, “Pancreatic Cancer,” *N Engl J Med.*, vol. 362, no. 17, pp. 1605–1617, Apr. 2010.
- [187] J. R. van der Vorst, “Near-infrared fluorescence imaging of a solitary fibrous tumor of the pancreas using methylene blue,” *World J. Gastrointest. Surg.*, vol. 4, no. 7, p. 180, 2012.
- [188] H. H. J. M. Handgraaf *et al.*, “Current and future intraoperative imaging strategies to increase radical resection rates in pancreatic cancer surgery,” *BioMed Res.*, vol. 2014, no. Article ID 890230, p. 8 pages, Jul. 2014.
- [189] D. W. Nelson, T. H. Blanchard, M. W. Causey, J. F. Homann, and T. A. Brown, “Examining the accuracy and clinical usefulness of intraoperative frozen section

- analysis in the management of pancreatic lesions,” *Am. J. Surg.*, vol. 205, no. 5, pp. 613–617, 2013.
- [190] M. Trajkovic-Arsic *et al.*, “Multimodal Molecular Imaging of Integrin $\alpha_3\beta_1$ for In Vivo Detection of Pancreatic Cancer,” *J. Nucl. Med.*, vol. 55, no. 3, pp. 446–451, 2014.
- [191] C.-H. Quek and K. W. Leong, “Near-Infrared Fluorescent Nanoprobes for in Vivo Optical Imaging,” *Nanomaterials*, vol. 2, no. 4, pp. 92–112, 2012.
- [192] M. McElroy *et al.*, “Imaging of primary and metastatic pancreatic cancer using a fluorophore-conjugated anti-CA19-9 antibody for surgical navigation,” *World J Surg*, vol. 32, no. 6, pp. 1057–1066, Jun. 2008.
- [193] J. V Frangioni, “In vivo near-infrared fluorescence imaging,” *Curr. Opin. Chem. Biol.*, vol. 7, no. 5, pp. 626–34, 2003.
- [194] K. Welsher, S. P. Sherlock, and H. Dai, “Deep-tissue anatomical imaging of mice using carbon nanotube fluorophores in the second near-infrared window,” *Proc. Natl. Acad. Sci.*, vol. 108, no. 22, pp. 8943–8948, 2011.
- [195] C. A. Metildi *et al.*, “Ratiometric Activatable Cell-Penetrating Peptides Label Pancreatic Cancer, Enabling Fluorescence-Guided Surgery, Which Reduces Metastases and Recurrence in Orthotopic Mouse Models,” *Ann. Surg. Oncol.*, vol. 22, no. 6, pp. 2082–2087, 2015.
- [196] L. Yang *et al.*, “Molecular Imaging of Pancreatic Cancer in an Animal Model Using Targeted Multifunctional Nanoparticles,” *Gastroenterology*, vol. 136, no. 5, pp. 1514-1525.e2, 2009.

- [197] N. Kosaka *et al.*, “In vivo stable tumor-specific painting in various colors using dehalogenase-based protein-tag fluorescent ligands,” *Bioconjug. Chem.*, vol. 20, no. 7, pp. 1367–1374, 2009.
- [198] J. Lesley, N. English, A. Perschl, J. Gregoroff, and R. Hyman, “Variant cell lines selected for alterations in the function of the hyaluronan receptor CD44 show differences in glycosylation,” *J. Exp. Med.*, vol. 182, no. 2, pp. 431–7, Aug. 1995.
- [199] S. Ilangumaran, B. Borisch, and D. C. Hoessli, “Signal Transduction via CD44: Role of Plasma Membrane Microdomains,” *Leuk. Lymphoma*, vol. 35, no. 5–6, pp. 455–469, Jan. 1999.
- [200] Q. Zhao *et al.*, “Dual-stimuli responsive hyaluronic acid-conjugated mesoporous silica for targeted delivery to CD44-overexpressing cancer cells,” *Elsevier*.
- [201] M. H. Ramadan, J. E. Prata, O. Karácsony, G. Dunér, and N. R. Washburn, “Reducing Protein Adsorption with Polymer-Grafted Hyaluronic Acid Coatings,” *Langmuir*, vol. 30, no. 25, pp. 7485–7495, Jul. 2014.
- [202] A. Almalik *et al.*, “Hyaluronic Acid Coated Chitosan Nanoparticles Reduced the Immunogenicity of the Formed Protein Corona,” *Sci. Rep.*, vol. 7, no. 1, p. 10542, Dec. 2017.
- [203] M. Van Beek, L. Jones, and H. Sheardown, “Hyaluronic acid containing hydrogels for the reduction of protein adsorption,” *Biomaterials*, vol. 29, no. 7, pp. 780–789, Mar. 2008.
- [204] M. van Beek, A. Weeks, L. Jones, and H. Sheardown, “Immobilized hyaluronic acid containing model silicone hydrogels reduce protein adsorption,” *J. Biomater.*

Sci. Polym. Ed., vol. 19, no. 11, pp. 1425–1436, Jan. 2008.

- [205] M. Ogawa, N. Kosaka, P. L. Choyke, and H. Kobayashi, “In vivo Molecular Imaging of Cancer with a Quenching Near-Infrared Fluorescent Probe Using Conjugates of Monoclonal Antibodies and Indocyanine Green,” *Cancer Res*, vol. 69, no. 4, pp. 1268–1272, 2009.
- [206] T. Hill, S. Kelkar, N. Wojtynek, and J. Soucek, “Near Infrared Fluorescent Nanoparticles Derived from Hyaluronic Acid Improve Tumor Contrast for Image-Guided Surgery,” *Theranostics*, vol. 6, no. 13, pp. 2314–2328, 2016.
- [207] T. Ishizawa, N. Fukushima, J. Shibahara, and K. Masuda, “Real-Time Identification of Liver Cancers by Using Indocyanine Green Fluorescent Imaging,” *Cancer*, 2009.
- [208] M. A. Solis, Y. H. Chen, T. Y. Wong, V. Z. Bittencourt, Y. C. Lin, and L. L. H. Huang, “Hyaluronan regulates cell behavior: A potential niche matrix for stem cells,” *Biochemistry Research International*. 2012.
- [209] D. A. Paul Bulpitt, “New strategy for chemical modification of hyaluronic acid: Preparation of functionalized derivatives and their use in the formation of novel biocompatible hydrogels,” *J. Biomed. Mater. Res.*, vol. 47, no. 2, pp. 152–169, 1999.
- [210] G. D. Prestwich, D. M. Marecak, J. F. Marecek, K. P. Vercruyse, and M. R. Ziebell, “Controlled chemical modification of hyaluronic acid: synthesis, applications, and biodegradation of hydrazide derivatives,” *J. Control. Release*, vol. 53, no. 1–3, pp. 93–103, 1998.

- [211] T. K. Hill *et al.*, “Indocyanine green-loaded nanoparticles for image-guided tumor surgery,” *Bioconjug. Chem.*, vol. 26, no. 2, pp. 294–303, 2015.
- [212] M. A. Dobrovolskaia and S. E. McNeil, “Understanding the correlation between in vitro and in vivo immunotoxicity tests for nanomedicines,” *J. Control. Release*, vol. 172, no. 2, pp. 456–466, 2013.
- [213] H. Tsutsumida, “RNA Interference Suppression of MUC1 Reduces the Growth Rate and Metastatic Phenotype of Human Pancreatic Cancer Cells,” *Clin. Cancer Res.*, vol. 12, no. 10, pp. 2976–2987, 2006.
- [214] A. M. Mohs *et al.*, “Hand-held spectroscopic device for in vivo and intraoperative tumor detection: Contrast enhancement, detection sensitivity, and tissue penetration,” *Anal. Chem.*, vol. 82, no. 21, pp. 9058–9065, 2010.
- [215] A. Mohs *et al.*, “An integrated widefield imaging and spectroscopy system for contrast enhanced, image-guided research of tumors,” *IEEE Trans. Biomed. Eng.*, vol. 62, no. 5, pp. 1416–1424, 2015.
- [216] V. Saxena and M. Sadoqi, “of Indocyanine Green in Polymeric Nanoparticulate Systems,” *Microscope*, vol. 74, no. 1, pp. 29–38, 2004.
- [217] E. M. Chung, M. D. Travis, and R. M. Conran, “Pancreatic Tumors in Children: Radiologic-Pathologic Correlation,” *RadioGraphics*, vol. 26, no. 4, pp. 1211–1238, 2006.
- [218] F. Dosio, S. Arpicco, B. Stella, and E. Fattal, “Hyaluronic acid for anticancer drug and nucleic acid delivery,” *Adv. Drug Deliv. Rev.*, vol. 97, pp. 204–236, 2015.
- [219] J. J. Water, Y. Kim, M. J. Maltesen, H. Franzyk, C. Foged, and H. M. Nielsen,

- “Hyaluronic acid-based nanogels produced by microfluidics-facilitated self-assembly improves the safety profile of the cationic host defense peptide novicidin,” *Pharm. Res.*, vol. 32, no. 8, pp. 2727–2735, 2015.
- [220] J. Huang *et al.*, “Biodegradable self-assembled nanoparticles of poly (d,l-lactide-co-glycolide)/hyaluronic acid block copolymers for target delivery of docetaxel to breast cancer,” *Biomaterials*, vol. 35, no. 1, pp. 550–566, 2014.
- [221] Y. Liu, J. Sun, P. Zhang, and Z. He, “Amphiphilic polysaccharide-hydrophobicized graft polymeric micelles for drug delivery nanosystems,” *Curr. Med. Chem.*, vol. 18, no. 17, pp. 2638–48, 2011.
- [222] S. Misra *et al.*, “Hyaluronan-CD44 interactions as potential targets for cancer therapy,” *FEBS J.*, vol. 278, pp. 1429–1443, 2011.
- [223] H. Maeda, H. Nakamura, and J. Fang, “The EPR effect for macromolecular drug delivery to solid tumors: Improvement of tumor uptake, lowering of systemic toxicity, and distinct tumor imaging in vivo,” *Adv. Drug Deliv. Rev.*, vol. 65, no. 1, pp. 71–79, 2013.
- [224] R. Gallagher *et al.*, “Characterization of the continuous, differentiating myeloid cell line (HL-60) from a patient with acute promyelocytic leukemia,” *Blood*, vol. 54, no. 3, pp. 713–733, 1979.
- [225] C. M. McKee *et al.*, “Hyaluronan (HA) fragments induce chemokine gene expression in alveolar macrophages: The role of HA size and CD44,” *J. Clin. Invest.*, vol. 98, no. 10, pp. 2403–2413, 1996.
- [226] C. C. Termeer *et al.*, “Oligosaccharides of Hyaluronan Are Potent Activators of

- Dendritic Cells,” *J. Immunol.*, vol. 165, no. 4, pp. 1863–1870, 2000.
- [227] D. Peer and R. Margalit, “Loading mitomycin C inside long circulating hyaluronan targeted nano-liposomes increases its antitumor activity in three mice tumor models,” *Int. J. Cancer*, vol. 108, no. 5, pp. 780–789, 2004.
- [228] S. Qhattal, T. Hye, A. Alali, and X. Liu, “Hyaluronan Polymer Length , Grafting Density , and Surface Poly (ethylene glycol) Coating Influence in Vivo Circulation and Tumor Targeting of Hyaluronan-grafted liposomes,” *ACS Nano*, vol. 8, no. 6, pp. 5423–5440, 2015.
- [229] X. Han *et al.*, “Stealth CD44-targeted hyaluronic acid supramolecular nanoassemblies for doxorubicin delivery: Probing the effect of uncovalent pegylation degree on cellular uptake and blood long circulation,” *J. Control. Release*, vol. 197, pp. 29–40, 2015.
- [230] M. Bouvet *et al.*, “Real-Time optical imaging of primary tumor growth and multiple metastatic events in a pancreatic cancer orthotopic model,” *Cancer Res.*, vol. 62, no. 5, pp. 1534–1540, 2002.
- [231] E. Ruoslahti, S. N. Bhatia, and M. J. Sailor, “Targeting of drugs and nanoparticles to tumors,” *J. Cell Biol.*, vol. 188, no. 6, pp. 759–768, 2010.
- [232] N. Sato, S. Kohi, K. Hirata, and M. Goggins, “Role of hyaluronan in pancreatic cancer biology and therapy: Once again in the spotlight,” *Cancer Sci.*, vol. 107, no. 5, pp. 569–575, May 2016.
- [233] F. Gebauer, M. Kemper, G. Sauter, P. Prehm, and U. Schumacher, “Is hyaluronan deposition in the stroma of pancreatic ductal adenocarcinoma of prognostic

- significance?,” *PLoS One*, vol. 12, no. 6, p. e0178703, 2017.
- [234] K. M. Wong, K. J. Horton, A. L. Coveler, S. R. Hingorani, and W. P. Harris, “Targeting the Tumor Stroma: the Biology and Clinical Development of Pegylated Recombinant Human Hyaluronidase (PEGPH20),” *Curr. Oncol. Rep.*, vol. 19, no. 7, p. 47, 2017.
- [235] J. Kim and Y. Park, “Improved Antitumor Efficacy of Hyaluronic Acid-Complexed Paclitaxel Nanoemulsions in Treating Non-Small Cell Lung Cancer,” *Biomol. Ther. (Seoul)*, vol. 25, no. 4, pp. 411–416, 2017.
- [236] Z. Lu, J. Su, Z. Li, Y. Zhan, and D. Ye, “Hyaluronic acid-coated, prodrug-based nanostructured lipid carriers for enhanced pancreatic cancer therapy,” *Drug Dev. Ind. Pharm.*, vol. 43, no. 1, pp. 160–170, Jan. 2017.
- [237] “Hyaluronic acid-green tea catechin micellar nanocomplexes: Fail-safe cisplatin nanomedicine for the treatment of ovarian cancer without off-target toxicity,” *Biomaterials*, vol. 148, pp. 41–53, Dec. 2017.
- [238] J. Wang *et al.*, “The effect of dual-functional hyaluronic acid-vitamin E succinate micelles on targeting delivery of doxorubicin,” *Int. J. Nanomedicine*, vol. 11, pp. 5851–5870, 2016.
- [239] N. V. Rao *et al.*, “Recent developments in hyaluronic acid-based nanomedicine for targeted cancer treatment,” *Expert Opin. Drug Deliv.*, vol. 13, no. 2, pp. 239–252, Feb. 2016.
- [240] I. Garrido-Laguna and M. Hidalgo, “Pancreatic cancer: from state-of-the-art treatments to promising novel therapies,” *Nat. Rev. Clin. Oncol.*, vol. 12, no. 6, pp.

319–334, Jun. 2015.

- [241] K. Bao, J. H. Lee, H. Kang, G. K. Park, G. El Fakhri, and H. S. Choi, “PSMA-targeted contrast agents for intraoperative imaging of prostate cancer.,” *Chem. Commun. (Camb)*, vol. 53, no. 10, pp. 1611–1614, Feb. 2017.
- [242] K. Bao *et al.*, “Charge and hydrophobicity effects of NIR fluorophores on bone-specific imaging.,” *Theranostics*, vol. 5, no. 6, pp. 609–17, 2015.
- [243] H. Hyun *et al.*, “700-nm Zwitterionic Near-Infrared Fluorophores for Dual-Channel Image-Guided Surgery.,” *Mol. Imaging Biol.*, vol. 18, no. 1, pp. 52–61, Feb. 2016.
- [244] E. A. Owens, M. Henary, G. El Fakhri, and H. S. Choi, “Tissue-Specific Near-Infrared Fluorescence Imaging,” *Acc. Chem. Res.*, vol. 49, no. 9, pp. 1731–1740, Sep. 2016.
- [245] E. A. Owens, S. Lee, J. Choi, M. Henary, and H. S. Choi, “NIR fluorescent small molecules for intraoperative imaging,” *Wiley Interdiscip. Rev. Nanomedicine Nanobiotechnology*, vol. 7, no. 6, pp. 828–838, Nov. 2015.
- [246] Y. Ye and X. Chen, “Integrin targeting for tumor optical imaging.,” *Theranostics*, vol. 1, pp. 102–26, 2011.
- [247] H. S. Choi *et al.*, “Synthesis and In Vivo Fate of Zwitterionic Near-Infrared Fluorophores,” *Angew. Chemie Int. Ed.*, vol. 50, no. 28, pp. 6258–6263, Jul. 2011.
- [248] S. Achilefu, “The Insatiable Quest for Near-Infrared Fluorescent Probes for Molecular Imaging,” *Angew. Chemie Int. Ed.*, vol. 49, no. 51, pp. 9816–9818, Dec. 2010.

- [249] B. Ballou *et al.*, “Tumor labeling in vivo using cyanine-conjugated monoclonal antibodies,” *Cancer Immunol. Immunother.*, vol. 41, no. 4, pp. 257–263, Jul. 1995.
- [250] H. S. Choi *et al.*, “Targeted zwitterionic near-infrared fluorophores for improved optical imaging,” *Nat. Biotechnol.*, vol. 31, no. 2, pp. 148–153, Feb. 2013.
- [251] L. Barstow and R. E. Small, “Liver Function Assessment by Drug Metabolism,” *Pharmacother. J. Hum. Pharmacol. Drug Ther.*, vol. 10, no. 4, pp. 280–288, Jul. 1990.
- [252] H. S. Choi *et al.*, “Design considerations for tumour-targeted nanoparticles,” *Nat. Nanotechnol.*, vol. 5, no. 1, pp. 42–47, Jan. 2010.
- [253] V. Ntziachristos, C. Bremer, and R. Weissleder, “Fluorescence Imaging With Near-Infrared Light: New Technological Advances That Enable In Vivo Molecular Imaging,” *Eur Radiol*, vol. 13, no. 1, pp. 195–208, 2003.
- [254] A. Becker *et al.*, “Receptor-targeted optical imaging of tumors with near-infrared fluorescent ligands,” *Nat. Biotechnol.*, vol. 19, no. 4, pp. 327–331, Apr. 2001.
- [255] Y. Hiroshima *et al.*, “Hand-held high-resolution fluorescence imaging system for fluorescence-guided surgery of patient and cell-line pancreatic tumors growing orthotopically in nude mice,” *J. Surg. Res.*, vol. 187, no. 2, pp. 510–517, Apr. 2014.
- [256] B. Qi *et al.*, “Indocyanine green loaded hyaluronan-derived nanoparticles for fluorescence-enhanced surgical imaging of pancreatic cancer,” *Nanomedicine Nanotechnology, Biol. Med.*, vol. 14, no. 3, pp. 769–780, Apr. 2018.
- [257] A. M. Mohs *et al.*, “Hyaluronic acid formulation of near infrared fluorophores

- optimizes surgical imaging in a prostate tumor xenograft,” *Acta Biomater.*, vol. 75, pp. 323–333, 2018.
- [258] M. A. Kelkar S, Hill T, Marini F, S. S. Kelkar, T. K. Hill, F. C. Marini, and A. M. Mohs, “Near infrared fluorescent nanoparticles based on hyaluronic acid: Self-assembly, optical properties, and cell interaction,” *Acta Biomater.*, vol. 36, pp. 112–121, May 2016.
- [259] D. Chen, S. Ganesh, W. Wang, and M. Amiji, “Plasma protein adsorption and biological identity of systemically administered nanoparticles,” *Nanomedicine*, vol. 12, no. 17, pp. 2113–2135, Sep. 2017.
- [260] H. Arami, A. Khandhar, D. Liggitt, and K. M. Krishnan, “In vivo delivery, pharmacokinetics, biodistribution and toxicity of iron oxide nanoparticles,” *Chem. Soc. Rev.*, vol. 44, no. 23, pp. 8576–8607, Nov. 2015.
- [261] Z. Yang *et al.*, “Pharmacokinetics and biodistribution of near-infrared fluorescence polymeric nanoparticles,” *Nanotechnology*, vol. 20, no. 16, p. 165101, Apr. 2009.
- [262] T. M., “Understanding Biophysicochemical Interactions at the NanoÀ Bio Interface,” *Nat. Mater.*, vol. 8, p. 543, 2009.
- [263] N. Kamaly, J. C. He, D. A. Ausiello, and O. C. Farokhzad, “Nanomedicines for renal disease: current status and future applications,” *Nat. Rev. Nephrol.*, vol. 12, no. 12, pp. 738–753, Dec. 2016.
- [264] A. Vonarbourg, C. Passirani, P. Saulnier, and J.-P. Benoit, “Parameters influencing the stealthiness of colloidal drug delivery systems,” *Biomaterials*, vol. 27, no. 24, pp. 4356–4373, Aug. 2006.

- [265] A. Chonn, S. Semple, P. C.-J. of B. Chemistry, and U. 1992, “Association of blood proteins with large unilamellar liposomes in vivo. Relation to circulation lifetimes,” *ASBMB*.
- [266] H. Choi, W. Liu, P. Misra, E. Tanaka, ... J. Z.-N., and undefined 2007, “Renal clearance of quantum dots,” *nature.com*.
- [267] M. Grabolle, J. Pauli, R. Brehm, and U. Resch-Genger, “Structural control of dye–protein binding, aggregation and hydrophilicity in a series of asymmetric cyanines,” *Dye. Pigment.*, vol. 103, pp. 118–126, Apr. 2014.
- [268] N. Hoshyar, S. Gray, H. Han, and G. Bao, “The effect of nanoparticle size on in vivo pharmacokinetics and cellular interaction,” *Nanomedicine (Lond.)*, vol. 11, no. 6, pp. 673–92, Mar. 2016.
- [269] L. Y. Qiu and Y. H. Bae, “Polymer Architecture and Drug Delivery,” *Pharm. Res.*, vol. 23, no. 1, pp. 1–30, Jan. 2006.
- [270] M.-N. Courel, C. Maingonnat, P. Bertrand, C. Chauzy, F. Smadja-Joffe, and B. Delpech, “Biodistribution of injected tritiated hyaluronic acid in mice: a comparison between macromolecules and hyaluronic acid-derived oligosaccharides,” *n vivo (Athens, Greece)*, vol. 18, no. 2, pp. 181–7, 2004.
- [271] H. v. Berlepsch and C. Böttcher, “H-Aggregates of an Indocyanine Cy5 Dye: Transition from Strong to Weak Molecular Coupling,” *J. Phys. Chem. B*, vol. 119, no. 35, pp. 11900–11909, Sep. 2015.
- [272] F. Würthner, T. E. Kaiser, and C. R. Saha-Möller, “J-Aggregates: From Serendipitous Discovery to Supramolecular Engineering of Functional Dye

- Materials,” *Angew. Chemie Int. Ed.*, vol. 50, no. 15, pp. 3376–3410, Apr. 2011.
- [273] A. S. Tatikolov and S. M. B. Costa, “Effects of normal and reverse micellar environment on the spectral properties, isomerization and aggregation of a hydrophilic cyanine dye,” *Chem. Phys. Lett.*, vol. 346, no. 3–4, pp. 233–240, Oct. 2001.
- [274] K. C. Dee, D. A. Puleo, and R. Bizios, *An Introduction To Tissue-Biomaterial Interactions*. New York, USA: John Wiley & Sons, Inc., 2002.
- [275] M. Y. Berezin *et al.*, “Rational Approach To Select Small Peptide Molecular Probes Labeled with Fluorescent Cyanine Dyes for in Vivo Optical Imaging,” *Biochemistry*, vol. 50, no. 13, pp. 2691–2700, Apr. 2011.
- [276] B. E. Schaafsma *et al.*, “The clinical use of indocyanine green as a near-infrared fluorescent contrast agent for image-guided oncologic surgery,” *J. Surg. Oncol.*, vol. 104, no. 3, pp. 323–332, Sep. 2011.
- [277] E. Levesque, E. Martin, D. Dudau, C. Lim, G. Dhonneur, and D. Azoulay, “Current use and perspective of indocyanine green clearance in liver diseases,” *Anaesth. Crit. Care Pain Med.*, vol. 35, no. 1, pp. 49–57, Feb. 2016.
- [278] G. Beckford, E. Owens, M. Henary, and G. Patonay, “The solvatochromic effects of side chain substitution on the binding interaction of novel tricarbocyanine dyes with human serum albumin,” *Talanta*, vol. 92, pp. 45–52, Apr. 2012.
- [279] A. Rhim, P. Oberstein, D. Thomas, E. M.-C. cell, and undefined 2014, “Stromal elements act to restrain, rather than support, pancreatic ductal adenocarcinoma,” *Elsevier*.

- [280] S. Taurin, H. Nehoff, K. G.-J. of controlled Release, and U. 2012, “Anticancer nanomedicine and tumor vascular permeability; where is the missing link?,” *J. Control. Release*, vol. 164, no. 3, pp. 265–275, 2012.
- [281] A. A. K. Iyer, G. Khaled, J. Fang, H. Maeda, H. M.-D. discovery Today, and U. 2006, “Exploiting the enhanced permeability and retention effect for tumor targeting,” *drug discov today*, vol. 11, no. 17–18, pp. 812–8, Sep. 2006.
- [282] H. Cabral *et al.*, “Accumulation of sub-100 nm polymeric micelles in poorly permeable tumours depends on size,” *Nat. Nanotechnol.*, vol. 6, no. 12, pp. 815–823, Dec. 2011.
- [283] C. Kuehl *et al.*, “Hyaluronic Acid Molecular Weight Determines Lung Clearance and Biodistribution after Instillation,” *Mol. Pharm.*, vol. 13, no. 6, pp. 1904–14, 2016.
- [284] Y. Matsumoto *et al.*, “Vascular bursts enhance permeability of tumour blood vessels and improve nanoparticle delivery,” *Nat. Nanotechnol.*, vol. 11, no. 6, pp. 533–538, Jun. 2016.
- [285] N. Itano, L. Zhuo, and K. Kimata, “Impact of the hyaluronan-rich tumor microenvironment on cancer initiation and progression,” *Cancer Sci.*, vol. 99, no. 9, pp. 1720–1725, Sep. 2008.
- [286] C. C. C. DuFort *et al.*, “Interstitial pressure in pancreatic ductal adenocarcinoma is dominated by a gel-fluid phase,” *Biophys J.*, vol. 110, no. 9, pp. 2106–19, May 2016.
- [287] J. Lesley, V. Hascall, M. Tammi, R. H.-J. of B. Chemistry, and U. 2000,

- “Hyaluronan binding by cell surface CD44,” *J. Biol. Chem.*, vol. 275, pp. 26967–26975, 2000.
- [288] D. X. Nguyen, P. D. Bos, and J. Massagué, “Metastasis: from dissemination to organ-specific colonization,” *Nat. Rev. Cancer*, vol. 9, no. 4, pp. 274–284, Apr. 2009.
- [289] S. Yachida *et al.*, “Distant metastasis occurs late during the genetic evolution of pancreatic cancer,” *Nature*, vol. 467, no. 7319, pp. 1114–1117, Oct. 2010.
- [290] T. E. Newhook *et al.*, “Adjuvant Trametinib Delays the Outgrowth of Occult Pancreatic Cancer in a Mouse Model of Patient-Derived Liver Metastasis,” *Ann. Surg. Oncol.*, vol. 23, no. 6, pp. 1993–2000, Jun. 2016.
- [291] M. Suker, B. G. Koerkamp, F. A. Eskens, J. J. Nuyttens, and C. H. J. van Eijck, “High yield of occult metastases during staging laparoscopy for locally advanced pancreatic cancer,” *HPB*, vol. 18, pp. e356–e357, Apr. 2016.
- [292] T. Ito *et al.*, “The diagnostic advantage of EOB-MR imaging over CT in the detection of liver metastasis in patients with potentially resectable pancreatic cancer,” *Pancreatology*, vol. 17, no. 3, pp. 451–456, May 2017.
- [293] H. Handgraaf *et al.*, “Staging laparoscopy with ultrasound and near-infrared fluorescence imaging to detect occult pancreatic metastases,” *Pancreatology*, vol. 17, no. 3, p. S71, Jul. 2017.
- [294] Z. V. Fong *et al.*, “Reappraisal of Staging Laparoscopy for Patients with Pancreatic Adenocarcinoma: A Contemporary Analysis of 1001 Patients,” *Ann. Surg. Oncol.*, vol. 24, no. 11, pp. 3203–3211, Oct. 2017.

- [295] J. L. Houghton *et al.*, “Site-specifically labeled CA19.9-targeted immunoconjugates for the PET, NIRF, and multimodal PET/NIRF imaging of pancreatic cancer,” *Proc. Natl. Acad. Sci. U. S. A.*, vol. 112, no. 52, pp. 15850–5, Dec. 2015.
- [296] E. N. Savariar *et al.*, “Real-time in vivo molecular detection of primary tumors and metastases with ratiometric activatable cell-penetrating peptides,” *Cancer Res.*, vol. 73, no. 2, pp. 855–64, Jan. 2013.
- [297] M. Yang *et al.*, “Whole-body optical imaging of green fluorescent protein-expressing tumors and metastases,” 1999.
- [298] S. Yachida and C. A. Jacobuzio-Donahue, “The Pathology and Genetics of Metastatic Pancreatic Cancer,” 2009.
- [299] N. Yokoyama *et al.*, “Real-time detection of hepatic micrometastases from pancreatic cancer by intraoperative fluorescence imaging,” *Cancer*, vol. 118, no. 11, pp. 2813–2819, Jun. 2012.
- [300] C. G. England *et al.*, “Preclinical Pharmacokinetics and Biodistribution Studies of ⁸⁹Zr-Labeled Pembrolizumab,” *J. Nucl. Med.*, vol. 58, no. 1, pp. 162–168, Jan. 2017.
- [301] L. Koontz, “TCA Precipitation,” *Methods Enzymol.*, vol. 541, pp. 3–10, Jan. 2014.
- [302] F. Janku, “Tumor heterogeneity in the clinic: is it a real problem?,” *Ther. Adv. Med. Oncol.*, vol. 6, no. 2, pp. 43–51, Mar. 2014.
- [303] M. Jamal-Hanjani, S. A. Quezada, J. Larkin, and C. Swanton, “Translational Implications of Tumor Heterogeneity CME Staff Planners’ Disclosures,” *Clin*

Cancer Res, vol. 21, no. 6, 2015.

- [304] M. Hölzel, A. Bovier, and T. Tüting, “Plasticity of tumour and immune cells: a source of heterogeneity and a cause for therapy resistance?,” *Nat. Rev. Cancer*, vol. 13, no. 5, pp. 365–376, May 2013.
- [305] S. L. Topalian, C. G. Drake, and D. M. Pardoll, “Immune Checkpoint Blockade: A Common Denominator Approach to Cancer Therapy,” *Cancer Cell*, vol. 27, no. 4, pp. 450–461, Apr. 2015.
- [306] M. S. Goldberg, “Immunoengineering: How Nanotechnology Can Enhance Cancer Immunotherapy,” *Cell*, vol. 161, no. 2, pp. 201–204, Apr. 2015.
- [307] D. Laheru and E. M. Jaffee, “Immunotherapy for pancreatic cancer — science driving clinical progress,” *Nat. Rev. Cancer*, vol. 5, no. 6, pp. 459–467, Jun. 2005.
- [308] P. R. Kunk, T. W. Bauer, C. L. Slingluff, and O. E. Rahma, “From bench to bedside a comprehensive review of pancreatic cancer immunotherapy,” *J. Immunother. Cancer*, vol. 4, no. 1, p. 14, Dec. 2016.
- [309] D. I. Jodrell *et al.*, “Hyaluronan impairs vascular function and drug delivery in a mouse model of pancreatic cancer,” *Gut*, vol. 62, no. 1, pp. 112–120, Jan. 2013.
- [310] M. Topalovski and R. A. Brekken, “Matrix control of pancreatic cancer: New insights into fibronectin signaling,” *Cancer Lett.*, vol. 381, no. 1, pp. 252–8, 2016.
- [311] V. P. Chauhan *et al.*, “Angiotensin inhibition enhances drug delivery and potentiates chemotherapy by decompressing tumour blood vessels,” *Nat. Commun.*, vol. 4, p. 2516, 2013.
- [312] M. Weniger, K. C. Honselmann, and A. S. Liss, “The Extracellular Matrix and

- Pancreatic Cancer: A Complex Relationship.,” *Cancers (Basel)*., vol. 10, no. 9, Sep. 2018.
- [313] H. Jiang *et al.*, “Targeting focal adhesion kinase renders pancreatic cancers responsive to checkpoint immunotherapy,” *Nat. Med.*, vol. 22, no. 8, pp. 851–860, Aug. 2016.
- [314] O. Fuge, N. Vasdev, P. Allchorne, and J. S. Green, “Immunotherapy for bladder cancer.,” *Res. reports Urol.*, vol. 7, pp. 65–79, 2015.
- [315] J. Nakajima *et al.*, “A phase I study of adoptive immunotherapy for recurrent non-small-cell lung cancer patients with autologous $\gamma\delta$ T cells☆☆☆,” *Eur. J. Cardio-Thoracic Surg.*, vol. 37, no. 5, pp. 1191–1197, May 2010.
- [316] D. M. Pardoll, “The blockade of immune checkpoints in cancer immunotherapy,” *Nat. Rev. Cancer*, vol. 12, no. 4, pp. 252–264, Apr. 2012.
- [317] P. Jiang *et al.*, “Signatures of T cell dysfunction and exclusion predict cancer immunotherapy response,” *Nat. Med.*, vol. 24, no. 10, pp. 1550–1558, Oct. 2018.
- [318] M. A. Postow, R. Sidlow, and M. D. Hellmann, “Immune-Related Adverse Events Associated with Immune Checkpoint Blockade,” *N. Engl. J. Med.*, vol. 378, no. 2, pp. 158–168, Jan. 2018.
- [319] S.-Y. Li *et al.*, “Restoring anti-tumor functions of T cells via nanoparticle-mediated immune checkpoint modulation,” *J. Control. Release*, vol. 231, pp. 17–28, Jun. 2016.
- [320] C. Wang, Y. Ye, G. M. Hochu, H. Sadeghifar, and Z. Gu, “Enhanced Cancer Immunotherapy by Microneedle Patch-Assisted Delivery of Anti-PD1 Antibody,”

Nano Lett., vol. 16, no. 4, pp. 2334–2340, Apr. 2016.

- [321] A. Kosmidis *et al.*, “Biomimetic Biodegradable Artificial Antigen Presenting Cells Synergize with PD-1 Blockade to Treat Melanoma HHS Public Access,” *Biomaterials*, vol. 118, pp. 16–26, 2017.
- [322] A. W. Li *et al.*, “A facile approach to enhance antigen response for personalized cancer vaccination,” *Nat. Mater.*, vol. 17, no. 6, pp. 528–534, Jun. 2018.
- [323] N. A. Rizvi *et al.*, “Mutational landscape determines sensitivity to PD-1 blockade in non-small cell lung cancer,” *Science (80-.)*, vol. 348, no. 6230, pp. 124–128, Apr. 2015.
- [324] M. S. Rooney, S. A. Shukla, C. J. Wu, G. Getz, and N. Hacohen, “Molecular and Genetic Properties of Tumors Associated with Local Immune Cytolytic Activity,” *Cell*, vol. 160, no. 1–2, pp. 48–61, Jan. 2015.
- [325] F. Dammeijer, S. P. Lau, C. H. J. van Eijck, S. H. van der Burg, and J. G. J. V. Aerts, “Rationally combining immunotherapies to improve efficacy of immune checkpoint blockade in solid tumors,” *Cytokine Growth Factor Rev.*, vol. 36, pp. 5–15, Aug. 2017.
- [326] X. Zhao and S. Subramanian, “Intrinsic Resistance of Solid Tumors to Immune Checkpoint Blockade Therapy,” *Cancer Res.*, vol. 77, no. 4, pp. 817–822, Feb. 2017.
- [327] H. Nakashima *et al.*, “Modeling tumor immunity of mouse glioblastoma by exhausted CD8⁺ T cells,” *Sci. Rep.*, vol. 8, no. 1, p. 208, Dec. 2018.
- [328] M. Sade-Feldman *et al.*, “Defining T Cell States Associated with Response to

Checkpoint Immunotherapy in Melanoma,” *Cell*, vol. 175, no. 4, pp. 998-1013.e20, Nov. 2018.

- [329] M. W. LaFleur, Y. Muroyama, C. G. Drake, and A. H. Sharpe, “Inhibitors of the PD-1 Pathway in Tumor Therapy.,” *J. Immunol.*, vol. 200, no. 2, pp. 375–383, 2018.
- [330] M. U. Mushtaq *et al.*, “Tumor matrix remodeling and novel immunotherapies: the promise of matrix-derived immune biomarkers,” *J. Immunother. Cancer*, vol. 6, no. 1, p. 65, Dec. 2018.
- [331] E. Lanitis, D. Dangaj, M. Irving, and G. Coukos, “Mechanisms regulating T-cell infiltration and activity in solid tumors,” *Ann. Oncol.*, vol. 28, no. suppl_12, pp. xii18–xii32, Dec. 2017.
- [332] I. Melero, A. Rouzaut, G. T. Motz, G. Coukos, and A. Liations:, “T-Cell and NK-Cell Infiltration into Solid Tumors: A Key Limiting Factor for Efficient Cancer Immunotherapy,” *Cancer Discov.*, vol. 4, no. 5, pp. 522–6, 2014.
- [333] D. M. Francis and S. N. Thomas, “Progress and opportunities for enhancing the delivery and efficacy of checkpoint inhibitors for cancer immunotherapy,” *Adv. Drug Deliv. Rev.*, vol. 114, pp. 33–42, May 2017.
- [334] R. K. Jain and T. Stylianopoulos, “Delivering nanomedicine to solid tumors,” *Nat. Rev. Clin. Oncol.*, vol. 7, no. 11, pp. 653–664, Nov. 2010.
- [335] V. M. Weaver *et al.*, “Depletion of Carcinoma-Associated Fibroblasts and Fibrosis Induces Immunosuppression and Accelerates Pancreas Cancer with Reduced Survival,” *Cancer Cell*, vol. 25, no. 6, pp. 719–734, 2014.

- [336] A. D. Rhim *et al.*, “Stromal Elements Act to Restrain, Rather Than Support, Pancreatic Ductal Adenocarcinoma,” *Cancer Cell*, vol. 25, no. 6, pp. 735–747, 2014.
- [337] J. L.-S. Au, B. Z. Yeung, M. G. Wientjes, Z. Lu, and M. G. Wientjes, “Delivery of cancer therapeutics to extracellular and intracellular targets: Determinants, barriers, challenges and opportunities,” *Adv. Drug Deliv. Rev.*, vol. 97, pp. 280–301, Feb. 2016.
- [338] L. Eikenes, I. Tufto, E. A. Schnell, A. Bjørkøy, and C. D. L. Davies, “Effect of collagenase and hyaluronidase on free and anomalous diffusion in multicellular spheroids and xenografts,” *Anticancer Res.*, vol. 30, no. 2, pp. 359–368, 2010.
- [339] T. Yata, E. L. Q. Lee, K. Suwan, N. Syed, P. Asavarut, and A. Hajitou, “Modulation of extracellular matrix in cancer is associated with enhanced tumor cell targeting by bacteriophage vectors,” *Mol. Cancer*, vol. 14, no. 1, p. 110, Dec. 2015.
- [340] A. Pan *et al.*, “Localized co-delivery of collagenase and trastuzumab by thermosensitive hydrogels for enhanced antitumor efficacy in human breast xenograft,” *Drug Deliv.*, vol. 25, no. 1, pp. 1495–1503, Nov. 2018.
- [341] J. Deng *et al.*, “Hyaluronidase Embedded in Nanocarrier PEG Shell for Enhanced Tumor Penetration and Highly Efficient Antitumor Efficacy,” *Nano Lett.*, vol. 16, no. 5, pp. 3268–3277, 2016.
- [342] Z. Wen, Q. Liao, Y. Hu, L. You, L. Zhou, and Y. Zhao, “A spheroid-based 3-D culture model for pancreatic cancer drug testing, using the acid phosphatase

- assay.," *Brazilian J. Med. Biol. Res. = Rev. Bras. Pesqui. medicas e Biol.*, vol. 46, no. 7, pp. 634–42, Jul. 2013.
- [343] I. Tufto, R. Hansen, D. Byberg, K. H. H. Nygaard, J. Tufto, and C. de L. Davies, "The effect of collagenase and hyaluronidase on transient perfusion in human osteosarcoma xenografts grown orthotopically and in dorsal skinfold chambers.," *Anticancer Res.*, vol. 27, no. 3B, pp. 1475–81.
- [344] K. Yoshimura *et al.*, "A Preclinical Murine Model of Hepatic Metastases," *J. Vis. Exp.*, no. 91, p. 51677, Sep. 2014.
- [345] T. D. Camenisch *et al.*, "Disruption of hyaluronan synthase-2 abrogates normal cardiac morphogenesis and hyaluronan-mediated transformation of epithelium to mesenchyme.," *J. Clin. Invest.*, vol. 106, no. 3, pp. 349–60, Aug. 2000.
- [346] A. V Pinho *et al.*, "ROCK signaling promotes collagen remodeling to facilitate invasive pancreatic ductal adenocarcinoma tumor cell growth," *EMBO Mol. Med.*, vol. 9, no. 2, pp. 198–218, 2017.
- [347] M. J. Moore *et al.*, "Erlotinib Plus Gemcitabine Compared With Gemcitabine Alone in Patients With Advanced Pancreatic Cancer: A Phase III Trial of the National Cancer Institute of Canada Clinical Trials Group," 2007.
- [348] Ng SSW, M. S. Tsao, S. Chow, and D. W. Hedley, "Inhibition of phosphatidylinositide 3-kinase enhances gemcitabine-induced apoptosis in human pancreatic cancer cells.," *Cancer Res.*, vol. 60, no. 19, pp. 5451–5, Oct. 2000.
- [349] T. Asano, Y. Yao, J. Zhu, D. Li, J. L. Abbruzzese, and S. A. G. Reddy, "The PI 3-kinase/Akt signaling pathway is activated due to aberrant Pten expression and

targets transcription factors NF- κ B and c-Myc in pancreatic cancer cells,”
Oncogene, vol. 23, no. 53, pp. 8571–8580, Nov. 2004.

[350] J. Rinehart *et al.*, “Multicenter Phase II Study of the Oral MEK Inhibitor, CI-1040, in Patients With Advanced Non-Small-Cell Lung, Breast, Colon, and Pancreatic Cancer,” 2004.

[351] S. Kordes *et al.*, “Metformin in patients with advanced pancreatic cancer: a double-blind, randomised, placebo-controlled phase 2 trial,” *Lancet Oncol.*, vol. 16, no. 7, pp. 839–847, Jul. 2015.

[352] A. Wang-Gillam *et al.*, “Nanoliposomal irinotecan with fluorouracil and folinic acid in metastatic pancreatic cancer after previous gemcitabine-based therapy (NAPOLI-1): a global, randomised, open-label, phase 3 trial,” *Lancet*, vol. 387, no. 10018, pp. 545–557, Feb. 2016.

[353] D. S. Vinay *et al.*, “Immune evasion in cancer: Mechanistic basis and therapeutic strategies,” *Semin. Cancer Biol.*, vol. 35, pp. S185–S198, Dec. 2015.

[354] C. Feig *et al.*, “Targeting CXCL12 from FAP-expressing carcinoma-associated fibroblasts synergizes with anti-PD-L1 immunotherapy in pancreatic cancer.”

[355] R. J. Torphy, Y. Zhu, and R. D. Schulick, “Immunotherapy for pancreatic cancer: Barriers and breakthroughs.” *Ann. Gastroenterol. Surg.*, vol. 2, no. 4, pp. 274–281, Jul. 2018.

[356] B. Vogelstein *et al.*, “Cancer genome landscapes.” *Science*, vol. 339, no. 6127, pp. 1546–58, Mar. 2013.

[357] I. W. Mak, N. Evaniew, and M. Ghert, “Lost in translation: animal models and

- clinical trials in cancer treatment.,” *Am. J. Transl. Res.*, vol. 6, no. 2, pp. 114–8, 2014.
- [358] J. R. Lindner and J. Link, “Molecular Imaging in Drug Discovery and Development,” *Circ. Cardiovasc. Imaging*, vol. 11, no. 2, Feb. 2018.
- [359] W. S. Tummers *et al.*, “Regulatory Aspects of Optical Methods and Exogenous Targets for Cancer Detection.,” *Cancer Res.*, vol. 77, no. 9, pp. 2197–2206, May 2017.
- [360] S. Mosessian *et al.*, “INDs for PET Molecular Imaging Probes—Approach by an Academic Institution,” *Mol. Imaging Biol.*, vol. 16, no. 4, pp. 441–448, Aug. 2014.
- [361] W. A. Weber, J. Czernin, M. E. Phelps, and H. R. Herschman, “Technology Insight: novel imaging of molecular targets is an emerging area crucial to the development of targeted drugs.,” *Nat. Clin. Pract. Oncol.*, vol. 5, no. 1, pp. 44–54, Jan. 2008.
- [362] C. L. Vogel *et al.*, “Efficacy and Safety of Trastuzumab as a Single Agent in First-Line Treatment of *HER2* -Overexpressing Metastatic Breast Cancer,” *J. Clin. Oncol.*, vol. 20, no. 3, pp. 719–726, Feb. 2002.
- [363] F. A. Shepherd *et al.*, “Erlotinib in Previously Treated Non–Small-Cell Lung Cancer,” *N. Engl. J. Med.*, vol. 353, no. 2, pp. 123–132, Jul. 2005.
- [364] M. B. Atkins *et al.*, “Randomized Phase II Study of Multiple Dose Levels of CCI-779, a Novel Mammalian Target of Rapamycin Kinase Inhibitor, in Patients With Advanced Refractory Renal Cell Carcinoma,” *J. Clin. Oncol.*, vol. 22, no. 5, pp. 909–918, Mar. 2004.

- [365] P. Workman *et al.*, “Minimally Invasive Pharmacokinetic and Pharmacodynamic Technologies in Hypothesis-Testing Clinical Trials of Innovative Therapies,” *JNCI J. Natl. Cancer Inst.*, vol. 98, no. 9, pp. 580–598, May 2006.
- [366] H. M. Linden *et al.*, “Quantitative Fluoroestradiol Positron Emission Tomography Imaging Predicts Response to Endocrine Treatment in Breast Cancer,” *J. Clin. Oncol.*, vol. 24, no. 18, pp. 2793–2799, Jun. 2006.
- [367] A. J. Beer *et al.*, “Biodistribution and pharmacokinetics of the alphavbeta3-selective tracer 18F-galacto-RGD in cancer patients.,” *J. Nucl. Med.*, vol. 46, no. 8, pp. 1333–41, Aug. 2005.
- [368] O. Hutchinson, D. Collingridge, H. Barthel, P. Price, and E. Aboagye, “Pharmacokinetics of Radiolabelled Anticancer Drugs for Positron Emission Tomography,” *Curr. Pharm. Des.*, vol. 9, no. 11, pp. 917–929, Apr. 2003.
- [369] G. C. Jayson *et al.*, “Molecular Imaging and Biological Evaluation of HuMV833 Anti-VEGF Antibody: Implications for Trial Design of Antiangiogenic Antibodies,” *JNCI J. Natl. Cancer Inst.*, vol. 94, no. 19, pp. 1484–1493, Oct. 2002.
- [370] F. L. Tansi *et al.*, “A fast and effective determination of the biodistribution and subcellular localization of fluorescent immunoliposomes in freshly excised animal organs.,” *BMC Biotechnol.*, vol. 17, no. 1, p. 8, Dec. 2017.
- [371] J. Napp *et al.*, “Time-domain in vivo near infrared fluorescence imaging for evaluation of matriptase as a potential target for the development of novel, inhibitor-based tumor therapies,” *Int. J. Cancer*, vol. 127, no. 8, pp. 1958–1974, Oct. 2010.

- [372] D. Zhao, J. H. Stafford, H. Zhou, and P. E. Thorpe, “Near-infrared Optical Imaging of Exposed Phosphatidylserine in a Mouse Glioma Model,” *Transl. Oncol.*, vol. 4, no. 6, pp. 355–364, Dec. 2011.
- [373] J. Gong *et al.*, “Measuring response to therapy by near-infrared imaging of tumors using a phosphatidylserine-targeting antibody fragment,” *Mol. Imaging*, vol. 12, no. 4, pp. 244–56, Jun. 2013.
- [374] V. Ntziachristos, C.-H. Tung, C. Bremer, and R. Weissleder, “Fluorescence molecular tomography resolves protease activity in vivo,” *Nat. Med.*, vol. 8, no. 7, pp. 757–761, Jul. 2002.

CURRICULUM VITAE

EDUCATION

Aug. 2015 – Present

Doctor of Philosophy

Pharmaceutical Sciences
University of Nebraska Medical Center
Omaha, NE

Graduate Research: Hyaluronic-acid based near-infrared fluorescent contrast agents for intraoperative imaging

Mentor: Dr. Aaron Mohs, Ph.D.

Aug. 2012 – Jul. 2015

Master of Science

Pharmaceutical Sciences
Sichuan University
Chengdu, Sichuan

Dissertation: Renal-targeted triptolide aminoglycoside conjugates for lowering systemic toxicities of triptolide.

Mentor: Dr. Zhirong Zhang, Ph.D.

Aug. 2008 – Jul. 2012

Bachelor of Science

Pharmacy
Sichuan University
Chengdu, Sichuan

Undergraduate Research: Brain-specific delivery of dopamine mediated by N, N-dimethyl amino group for the treatment of Parkinson's disease.

Mentor: Dr. Zhirong Zhang, Ph.D.

RESEARCH EXPERIENCE

Department of Pharmaceutical Sciences, University of Nebraska Medical Center,
Omaha, NE

Doctoral Research

2015-present

Research Advisor: Dr. Aaron Mohs

- Conducted, presented and published lab-scale surgical detection of nanoformulated imaging agents with an orthotopic murine model of pancreatic cancer, as well as comprehensive *in vitro* and *in vivo* toxicological evaluation.
- Developed patentable methodology for tuning biodistribution by controlling the physiochemical properties of the contrast agent platform. Identified tumor-specific and

potentially-translatable contrast agents for guiding tumor resection, which has supported a collaborative funding application with melanoma research groups.

- Proficient at IV and IP administration, organ dissection, tissue collection and frozen tissue section of 300+ mice and 100+ rats for graduate projects.
- Self-trained and managed the day-to-day running of the AKTA Pure Chromatography System (GE Health), and coupled it with a fluorescence detector to determine protein association with contrast agents for interpreting the mechanism of altered biodistribution.
- Established peer-to-peer collaboration with researchers from Wake Forest Institute of Regenerative Medicine and UNMC Eppley Cancer Institute with active involvement from the NCI's SPORE program in pancreatic cancer.

Department of Pharmaceutical Sciences, Sichuan University,
Chengdu, Sichuan

Graduate Research

2012-2015

Research Advisor: Dr. Zhirong Zhang

- Worked as an independent medicinal chemist extensively designing, setting up and validating aminoglycosylation of diterpeneoid triepoxide as an efficient 7-step chemical modification of triptolide for improving its druggability.
- Tested the pre-clinical characteristics of self-synthesized triptolide-aminoglucoside including serum stability, pharmacokinetics and tissue biodistribution with pre-verified LC-MS/MS assay.
- Designed, investigated and published the protective effect of triptolide-aminoglucoside in a rodent model of renal ischemia/reperfusion injury, and evaluated the multi-organ toxicities with biochemical analysis, histology and flow cytometry.
- Extensive training in brain-targeted modification of Dopamine and L-Dopa, *in vitro* stability, release mechanism and bioassay verification with LC-MS/MS for the improved treatment of Parkinson's disease.
- Assisted in biosample processing of brain-targeted Pyrilamine-derivatives for pharmacokinetic and biodistribution studies.

Department of Pharmaceutical Sciences, Sichuan University,
Chengdu, Sichuan

Undergraduate Research

2011-2012

Research Advisor: Dr. Zhirong Zhang

Investigated the *In vitro* and *in vivo* release mechanism of Dopamine-derived prodrugs for determining delivery efficiency to the brain.

PUBLICATIONS

A) Published/Preparing Journal Article

1. **Qi B**, Crawford AJ, Wojtynek NE, Talmon GA, Ly QP, Hollingsworth MA, Mohs AM. Tuning hyaluronic acid for delivery to pancreatic cancer for optimized intraoperative imaging. *In revision*.
2. **Qi B**, Crawford AJ, Wojtynek NE, Holmes MB, Soucek JJ, Almeida-Porada G, Ly QP, Cohen SM, Hollingsworth MA, Mohs AM. Indocyanine green loaded hyaluronan-derived NPs for fluorescence-enhanced surgical imaging of pancreatic cancer. *Nanomedicine* **2018**;14:769-780. PMID: 29325740
3. Soucek JJ, Wojtynek NE, Payne WM, Holmes MB, Dutta S, **Qi B**, Datta K, LaGrange CA, Mohs AM. Optimized hyaluronic acid formulation of near infrared fluorophores for surgical detection of a prostate tumor xenograft. *Acta Biomater.* **2018**; 75:323-333. PMID: 29890268
4. Soucek JJ, Davis AL, Hill TK, Holmes MB, **Qi B**, Singh PK, Kridel SJ, Mohs AM. Combination treatment with orlistat-containing NPs and taxanes is synergistic and enhances microtubule stability in taxane-resistant prostate cancer cells. *Mol Cancer Ther.* **2017**;16(9):1819- 1830. PMID: 28615298
5. Wang X, **Qi B**, Su, H, Li, J, Sun, X, He L, Fu Y, Zhang Z. Pyrillamine-sensitive proton-coupled organic cation (H⁺/OC) antiporter for brain-specific drug delivery. *Journal of Controlled Release.* **2017**;254, 34-43. PMID: 28351667
6. **Qi B**, Wang X, Zhou Y, Han Q, He L, Gong T, Sun X, Zhang Z. A renal-targeted triptolide aminoglycoside (TPAG) conjugate for lowering systemic toxicities of triptolide. *Fitoterapia.* **2014**;103, 242-251. PMID: 25869848
7. Li Y, Zhou Y, **Qi B**, Gong T, Sun X, Fu Y, Zhang Z. Brain-specific delivery of dopamine mediated by N, N-dimethyl amino group for the treatment of Parkinson's disease. *Molecular pharmaceutics*, **2014**;11(9), 3174-3185. PMID: 25072272

B) Abstracts and Preliminary Communications (Presenter underlined)

1. **Qi B**, Crawford AJ, Cohen SM, Ly QP, Hollingsworth HA, Mohs AM. Surgical imaging of pancreatic cancer using near infrared fluorescent hyaluronic acid nanomaterials. American Association for Cancer Research Annual Meeting; Chicago, IL, April 2018. *Poster*.
2. **Qi B**, Hill TK, Crawford AJ, Wojtynek NE, Hollingsworth MA, Mohs AM. Tumor enhancement for fluorescent surgical navigation by near infrared hyaluronic acid conjugates. NanoDDS 2017, Ann Arbor, MI, September 2017. *Poster*.

PRESENTATIONS

1. **Qi B**, Crawford AJ, Wojtynek NE, Ly P, Hollingsworth MA, Mohs AM. Intraoperative pancreatic cancer imaging using hyaluronic acid conjugates tuned for minimized background signal. GI/Pancreas SPORE Workshop; Omaha, NE, October 2018. *Poster*.
2. **Qi B**, Crawford AJ, Wojtynek NE, Ly P, Hollingsworth MA, Mohs AM. Intraoperative pancreatic cancer imaging using hyaluronic acid conjugates tuned for minimized background signal. World Molecular Imaging Congress; Seattle, WA, September 2018. *Podium Presentation*. ***Seclected for Women in Molecular Imaging Network Scholar and awarded Student travel stipend**.
3. **Qi B**, Crawford AJ, Holmes MB, Wojtynek NE, Soucek JJ, Almeida-Porada G, Hollingsworth MA, Mohs AM. Indocyanine green loaded hyaluronan-derived NPs for fluorescence- enhanced surgical imaging of an orthotopic pancreatic cancer model. World Molecular Imaging Congress; Philadelphia, PA, September 2017. *Podium Presentation*.
4. **Qi B**, Crawford AJ, Holmes MB, Wojtynek NE, Soucek JJ, Almeida-Porada G, Hollingsworth MA, Mohs AM. Indocyanine green loaded hyaluronan-derived NPs for fluorescence- enhanced surgical imaging of an orthotopic pancreatic cancer model. UNMC Biopharmaceutical Research & Development Symposium; Omaha, NE, September 2017. *Poster*.

AWARDS AND HONORS

2019	University nominee for NIH/NCI F99/K00 fellowship
2018-2019	Chair-elected, UNMC student chapter of American Association of Pharmaceutical Sciences (AAPS)
2018	Student Travel Stipend awarded by the World Molecular Imaging Congress for the excellency of abstract
2018	Women in Molecular Imaging Network Scholar by the World Molecular Imaging Network Leadership Committee
2017-2018	Treasurer, UNMC student chapter of American Association of Pharmaceutical Sciences (AAPS)
2016-2019	Research Assistantship, University of Nebraska Medical Center
2015-2019	Graduate Research Fellowship, China Scholarship Council
2015-2016	Teaching Assistantship, University of Nebraska Medical Center
2012-2015	National Graduate Scholarship-awarded by Chinese Ministry of Education and Sichuan University for academic excellence and leadership

2009-2011 National Recognition Scholarship for Undergraduate Students-awarded by Chinese Ministry of Education and Sichuan University, based on academic achievements, service and leadership.

TEACHING ACTIVITIES

2015-2016 **Teaching Assistant**, University of Nebraska Medical Center
Course: Introduction to Pharmaceutical Sciences, PHSC 550
Pharmaceutical Biochemistry, PHSC 520
Duties: Prepared for lectures handouts, graded assignments, exams and organized Q&A sessions with students

2017 **Mentor for Undergraduate thesis**, University of Nebraska Medical Center
Student: Ziling Zhao
Program: Pharmaceutical Science (China Pharmaceutical University)

REVELENT SKILLS

- Organic synthesis (small molecule, polymer)
- UV-Vis spectroscopy, fluorescence spectroscopy
- DLS, NMR, TEM
- Flow cytometry
- ELISA
- Colony-forming assay
- Orthotopic tumor model induction
- LC-MS/MS
- GFC
- Jugular vein catheterization
- Near-infrared fluorescence imaging
- Biochemical analysis
- Tissue processing and cryostat sectioning
- Fluorescence and confocal microscopy
- Adobe Illustrator
- Chemdraw
- DAS 3.0
- FlowJo
- ImageJ
- GraphPad Prism
- Photoshop

MEMBERSHIPS IN PROFESSIONAL SOCIETIES

American Association of Pharmaceutical Scientists (AAPS)
World Molecular Imaging Society (WMIS)
American Association for the Advancement of Science (AAAS)